The Pennsylvania State University
The Graduate School
Department of Aerospace Engineering

MULTI-POINT INVERSE DESIGN OF ISOLATED AIRFOILS AND AIRFOILS IN CASCADE IN INCOMPRESSIBLE FLOW

A Thesis in
Aerospace Engineering

by

Michael Scott Selig

Submitted in Partial Fulfillment
of the Requirements
for the Degree of

Doctor of Philosophy

May 1992

We approve the thesis of Michael Scott Selig.

Date of Signature

[redacted] March 11, 1992

Mark D. Maughmer
Associate Professor of Aerospace Engineering
Thesis Advisor
Chair of Committee

[redacted] March 12, 1992

Lyle N. Long
Assistant Professor of Aerospace Engineering

[redacted] 3/11/92

Philip J. Morris
Boeing Professor of Aerospace Engineering

[redacted] March 11, 1992

Gary S. Settles
Professor of Mechanical Engineering

[redacted] 3/12/92

Dennis K. McLaughlin
Professor of Aerospace Engineering
Head of the Department of Aerospace Engineering

ABSTRACT

This thesis describes a multi-point inverse design method for airfoils and one for cascades. In the present sense, inverse design is taken to mean the problem of finding the shape which corresponds to the desired set of aerodynamic and geometric characteristics. These include the pitching moment, maximum thickness ratio, part of the velocity distribution or boundary-layer flow physics, for example, the shape-factor, skin-friction or linear stability amplification factor distribution. Specifically, the airfoil or cascade blade to be determined is divided into a desired number of segments along each of which either the desired velocity distribution or boundary-layer development is prescribed together with, if desired, the maximum thickness ratio, etc. The solution is formulated through the use of conformal mapping and a direct integral boundary-layer technique resulting in a system of nonlinear equations which are solved through multi-dimensional Newton iteration. It is shown that certain integral constraints, continuity constraints and stagnation point velocity distribution relations must be satisfied in order for the inverse problem to be well-posed. The satisfaction of these conditions may be handled conveniently. This makes the practical application of the method feasible. Several example airfoils and cascades are presented to illustrate the two inverse methods.

A solution to the direct analysis problem for the velocity distributions about airfoils and cascades is also discussed. The current approach to both analysis problems differs significantly from the standard approaches such as those based on Theodorsen's method. The airfoil or cascade is mapped to the circle by one transformation that is expressed in derivative form so that the velocity distribution follows directly. Also, an exact solution to the flow through an infinite cascade is presented based on a mapping which has close ties to the Joukowski transformation. As compared with

Gostelow's method, exact solutions can be obtained in a straightforward way. Finally, extensions of the theory to the inverse design of radial cascades, semi-infinite bodies and channels are discussed briefly.

TABLE OF CONTENTS

LIST OF FIGURES

LIST OF TABLES

LIST OF SYMBOLS

a	= location of vortex-source relative to ζ-coordinate system
a_m, b_m	= Fourier series coefficients
a_{jk}, b_j	= coefficients for integral constraints and trailing-edge continuity condition
A	= modulus of a
b	= location of vortex-source relative to ζ'-coordinate system
B	= modulus of b; path of integration in cascade plane
c	= airfoil chord; location of stagnation point on the generating circle relative to ζ'-coordinate system
c_0, c_1, c_2	= complex coefficients in mapping
c_D	= dissipation coefficient
c_f	= skin friction coefficient
c_l, $c_{l_{max}}$	= airfoil lift coefficient and maximum lift coefficient
c_{m_0}	= zero-lift pitching moment coefficient
$c_{m_{c/4}}$	= pitching moment coefficient about airfoil quarter-chord point
C	= modulus of c; path of integration in circle plane
D^*	= dissipation correlation function
$f(\zeta)$	= regular function outside circle
$F(z)$, $F(\zeta)$	= complex potential function in physical and circle plane
$g(\zeta)$	= regular function outside circle
$g(\phi)$, $h(\phi)$	= positive, non-zero functions on unit circle
H_{12}, H_{32}	= shape factors, δ_1/δ_2 and δ_3/δ_2
i	= index
I	= total number of segments; integral in Appendix B

j = index

J = integral in Appendix B

k, k_i = index; strength of function $S(\phi)$

k_1, k_2, k_3 = coefficients used in analysis of airfoils and cascades

K = main recovery parameter

K_H = closure recovery parameter

K_S = trailing-edge thickness parameter

L = airfoil lift

M = number of sharp corners in $P(\phi)$

$M_{c/4}$ = airfoil moment about quarter-chord point

M_O = airfoil moment about the origin in airfoil plane

n = index; linear stability amplification factor

N = $2N$ number of equiangular points about the circle; number of blades in radial cascade

p = value of generic desired parameter in Newton iteration

$P(\phi)$ = harmonic function on circle

$\hat{P}(\phi)$ = estimate of $P(\phi)$ in analysis problem

$\overline{P}(\phi)$ = smooth part of $P(\phi)$

$P(r,\phi)$ = real part of $f(\zeta)$

q_I, q_O = inlet and outlet flow speed tangential to the cascade front

$q^*(\phi)$, $\overline{q}^*(\phi)$ = multi-point design inlet and outlet tangential flow distribution

Q = source strength

$Q(\phi)$ = conjugate harmonic function on circle

$\hat{Q}(\phi)$ = estimate of $Q(\phi)$ in analysis problem

$Q(r,\phi)$ = imaginary part of $f(\zeta)$

r = modulus of ζ

R = airfoil chord Reynolds number (vc/ν)

R_i = $\vec{R}$ vector components; Reynolds number for segment

$\vec{R}$ = residue vector used in Newton iteration

R_{δ_1}, R_{δ_2} = Reynolds numbers ($v\delta_1/\nu$ and $v\delta_2/\nu$)

s = arc length about airfoil or cascade blade; cascade spacing

s_i = arc length for a given segment junction ϕ_i

s_{max} = maximum arc length about airfoil or cascade blade

$\tilde{s}_i$ = relative arc length for segment

$\tilde{s}_i^n$ = points in terms of $\tilde{s}_i$ corresponding to spline supports in $\tilde{\phi}_i$

$S(\phi)$ = part of $P(\phi)$ with sharp corners

t/c = maximum thickness ratio of airfoil or cascade blade

$T(\phi)$ = conjugate harmonic function to $S(\phi)$

$T(\phi,i)$, $T(i,j)$ = functions used in Appendix B

u = flow speed normal to the cascade front

u_I, u_O = inlet and outlet flow speed normal to the cascade front

U_i = $\vec{U}$ vector components

$\vec{U}$ = vector of inverse design parameters used for iteration

$U(i)$, $U(\phi,i)$ = functions used in Appendix B

v = velocity distribution normalized by freestream; boundary-layer edge velocity

v_i = velocity level for segment

v_T = trailing edge velocity for cascade

$v^*(\phi)$ = multi-point design velocity distribution

$v_0^*(\phi)$ = single-point design velocity distribution at zero-lift

$v_\alpha^*(\phi)$ = single-point design velocity distribution at angle of attack α

$\tilde{v}_i(\tilde{s}_i)$ = relative design velocity distribution in terms of $\tilde{s}_i$

$\tilde{v}_i(\tilde{\phi}_i)$ = relative design velocity distribution in terms of $\tilde{\phi}_i$

V = airfoil freestream flow

V_i, $\overline{V}_i$ = design inlet and outlet flow speed for cascade-blade segment

V_I, V_O = inlet and outlet flow speed for cascade

$V^*(\phi)$, $\overline{V}^*(\phi)$ = multi-point design inlet and outlet flow distribution

w = velocity about circle used in Appendix A

$w(\phi)$ = total recovery function

$w_F(\phi)$ = trailing-edge recovery function

$w_S(\phi)$ = closure recovery function

$w_W(\phi)$ = main recovery function

x_i = chordwise location for a given segment junction ϕ_i

$x(\phi)$, $y(\phi)$ = airfoil coordinates to be translated by the amounts δx and δy

z = physical-plane complex coordinate $(x + iy)$

z_c = value of z about the airfoil or cascade-blade

z' = intermediate-plane between circle and physical plane

α = angle of attack relative to zero-lift angle of attack; argument of a

α_i = design angle of attack for airfoil segment

$\alpha^*(\phi)$ = multi-point design angle of attack distribution

β_{ZL} = cascade zero-lift flow angle

β_i, $\overline{\beta}_i$ = design inlet and outlet flow angle for cascade-blade segment

β_I, β_O = cascade inlet and outlet flow angle

$\beta^*(\phi)$, $\overline{\beta}^*(\phi)$ = multi-point design inlet and outlet flow angle distribution

γ = stagnation point arc limit for given angle of attack α

Γ = circulation for isolated airfoil problem

$\Gamma(\phi)$ = function used in Appendix D

Γ_I, Γ_O = inlet and outlet circulation strengths for cascade

$\Gamma^*(\phi)$, $\overline{\Gamma}^*(\phi)$ = multi-point design inlet and outlet circulation distribution

$\delta_1, \delta_2, \delta_3$ = displacement, momentum and energy thicknesses

δx, δy = airfoil coordinate corrections

Δs = denotes an increment in s

ϵ = trailing-edge angle parameter

ϵ^* = skin-friction correlation function

ζ = circle-plane complex coordinate $(\xi + i\eta)$

ζ_c = value of ζ about the circle in ζ-axes

ζ_T = location of stagnation point on generating circle

ζ' = circle coordinate with respect to ζ'-axes

ζ'_c = value of ζ' about the circle in ζ-axes $(\xi_c + i\,\eta_c)$

$\theta(\phi)$ = surface angle about airfoil or cascade blade

$\hat{\theta}(\phi)$ = estimate of $\theta(\phi)$ in analysis problem

$\theta^*(\phi)$ = flow angle direction about airfoil or cascade blade

λ = constant in evaluating airfoil pitching moment

μ = main recovery parameter; index; generating circle offset relative to ζ-coordinate system

ν = index; kinematic viscosity

$\nu(\phi)$ = function used in Appendix D

$\pi^*(\phi)$ = step function

ρ = fluid density

ρ_j = constants used in Appendix D

σ = cascade solidity (c/s)

σ_j = kernel used in Appendix D

$\tau(\phi)$ = function used in Appendix D

ϕ = arc limit in circle plane; argument of ζ

ϕ_0, ϕ_I = arc limits in circle plane ($\phi_0 \equiv 0$ and $\phi_I \equiv 2\pi$)

ϕ_F = trailing-edge recovery arc limit

ϕ_i = arc limit for segment

$\phi_{i\,L}$ = leading-edge arc limit

ϕ_S = closure recovery arc limit

ϕ_{W^-} = main recovery arc limit ($\phi_{W^-} \equiv \phi_1$ and $\overline{\phi}_{W^-} \equiv \phi_{I-1}$)

$\tilde{\phi}_i$ = relative arc limit for segment

$\tilde{\phi}_i^n$ = location of spline support defining function in terms of $\tilde{\phi}_i$

χ = cascade stagger angle

ψ = variable of integration; argument of b

ω = relaxation factor; argument of c

Superscripts:

$\tilde{}$ = relative to beginning of segment

$-$ = lower-surface quantity; conjugate; outlet flow quantity

Subscripts:

i = value for segment or at arc limit ϕ_i; integration path

$+$ = from positive side

$-$ = from negative side

Special Notations:

$(\hat{})^i$ = estimate i

$(\hat{})^{i+1}$ = estimate $i+1$

$)^+$ = approach from positive side

$)^-$ = approach from negative side

ACKNOWLEDGMENTS

Several individuals played vital roles in the successful completion of this thesis. Prof. Mark D. Maughmer has contributed greatly to this work by offering valuable insight into the design problem. This, together with our many fruitful discussions on topics not related directly to this thesis, has influenced positively my thinking on topics in applied aerodynamics. Prof. Philip J. Morris, Prof. Lyle N. Long and Prof. Gary S. Settles as members of my Ph.D. committee made many helpful suggestions during the course of this work. My collaboration with Dr. Paolo Dini on topics related to airfoil design and analysis helped to guide the direction of this research. I am indebted to Prof. Richard Eppler for having established a method for multi-point inverse airfoil design that lead in part to the current theory for multi-point inverse cascade design. Also, his comments regarding the use of his computer program were helpful in verifying the implementation of the cascade theory.

I express my deepest gratitude to my wife, Lisa, for her encouragement and patience offered during the conduct of this research.

Finally, this research was supported under the NASA Graduate Student Researchers Program through the NASA Langley Research Center (NGT-50341). The helpful suggestions of the grant monitors, Mr. Dan M. Somers and Mr. John R. Dagenhart of the NASA Langley Research Center, is gratefully acknowledged.

Chapter 1

INTRODUCTION

The purpose of this thesis is to describe the development of a practical inverse design method for airfoils and one for cascades in incompressible flow. To place the present work in perspective, it is helpful to start by discussing the state of affairs at the Langley Memorial Aeronautical Laboratory in the early 1930s. Eastman N. Jacobs and his co-workers had just finished work on a systematic, empirical approach to airfoil design and development (Jacobs, Ward and Pinkerton 1933), but the tremendous practical implications of improvements in aerodynamic efficiency attainable through extended runs of laminar flow continued to spur interest in airfoil research.

This research into laminar flow airfoils developed along two paths. First, what type of velocity distribution would give rise to sustained runs of laminar flow, and, second, how might this velocity distribution be transformed into an airfoil shape. Only after attending the Fifth Volta Congress in Rome and having been inspired by discussions with B. Meville Jones and Sir Goeffrey I. Taylor did Jacobs realize that laminar flow would probably be sustained by a continuous run of increasing velocity (Hansen 1987). With regard to the latter question, that of how to transform this velocity distribution to an airfoil shape, Jacobs thought that Theodorsen's method for airfoil analysis (Theodorsen 1931) could be used as the basis of the design method by inverting the analysis process. With some contributions made by Theodorsen and Garrick (1933), the approach proved possible and eventually lead to the development of a series of low-drag laminar-flow airfoils, namely the NACA 6-series airfoils (Jacobs 1939) that are still applied today. Jacobs's design method,

although crude by present standards, was the first of what have come to be known as inverse airfoil design methods—methods which form the basis of modern airfoil design methodology.

Surprisingly, the inverse approach of Jacobs was initially received by considerable skepticism among the group of theoreticians at Langley, and, even after it proved successful, it was never fully appreciated. Ira H. Abbott who worked with Jacobs at the time and who later took part in compiling and publishing the airfoil work done at the NACA (Abbott, Von Doenhoff and Stivers 1945; Abbott and Von Doenhoff 1959) said (Abbott 1980):

> We were told that even the statement of the problem was mathematical nonsense with the implication that it was our ignorance that encourages us. (pp. 23–24)

In the mind of E. I. Garrick, this view had hardly changed when he later wrote (Garrick 1952):

> In the opinion of the writer several difficulties arise or exist in defining this problem to satisfy both the mathematician and the aerodynamicist. For one thing, attempts have not been successful in making precise statements of the problem in regard to uniqueness, closure, proper trailing edge, leading edge contours, avoidance of grotesque nonstreamline figures most likely to be subject to separated flow, or of no physical significance as figures eight (or worse). For another, the prescription of pressure distributions with respect to a reference chord leads to nonuniqueness; and prescription with regard to normals to the boundary surface leads to undefiniteness, since the physical boundaries are being sought. Another difficulty is the fact that our insight and knowledge of flow behavior are not developed to the point that an exactly defined desirable pressure distribution can be specified. (p. 145)

Predictably, these attitudes did not foster continued growth in airfoil research at Langley as high-speed aerodynamics came into the forefront in the 1940s and 1950s. Interestingly, Barger (1974, 1975*a*,*b*) in a series of NASA reports extended the inverse method of Jacobs, but it was never received with much enthusiasm. Other more powerful methods had come into favor.

These more powerful methods were based on conformal mapping (like Jacobs's method) and had their origin in Europe, notably Mangler (1938) in Germany and Lighthill (1945*a*) in Britain. It is not clear if Jacobs's work had any direct impact in these developments; chances are it did not since Jacobs never fully published his approach and only few details exist (Theodorsen and Garrick 1933; Theodorsen 1944). These new methods of Mangler and Lighthill showed clearly for the first time that the velocity distribution specified around the airfoil could not be entirely arbitrary. Specifically, they showed that the velocity distribution had to satisfy three important integral constraints: one in order to guarantee compatibility with the freestream velocity and two in order to ensure closure of the airfoil profile. While these theories did much to dispell doubts about the theoretical soundness of the inverse approach, practical application was hampered severely by the lengthy calculations involved in obtaining the final airfoil shape; it was said that a skilled mathematician could perform the calculations in approximately 20 hours. Thus, most of the early work done following the theory of Mangler and Lighthill was focused primarily on improving the numerical solution, both its speed and accuracy (Peebles 1947; Glauert 1947; Timman 1951; Peebles and Parkin 1956). Starting in the 1960s emphasis had shifted towards practical application through the use of the computer (Nonweiler 1968; Ingen 1969; Arlinger 1970; Strand 1974; Polito 1974).

By the 1970s, the inverse approach had matured into a very powerful tool for design, but it was not without shortcomings—shortcomings that still exist today. The all-important integral constraints are expressed in terms of the velocity distribution around the airfoil not as a function of arc length but as a function of the angular coordinate around the circle from which the airfoil is mapped. In other words, the desired velocity distribution can only be specified indirectly as a function of the circle angular coordinate. Iterative techniques, however, were introduced by Arlinger (1970) and James in 1970, as discussed by Liebeck (1990), so that the desired velocity distribution could be specified from the outset, subject of course to the integral constraints.

From the need to satisfy the integral constraints arises a different problem. Since there are three integral constraints, it is necessary to introduce into the specified velocity distribution three, free parameters in order to satisfy them. Many successful ways have been devised to do this. A difficulty occurs when the values determined for these free parameters lead to unrealistic velocity distributions which in turn correspond to unrealistic airfoils, for instance, crossed airfoils or figure of eights as referred to by Garrick (1952). Essentially, all practical inverse methods employ some kind of iterative technique to overcome this difficulty.

Finally, the last shortcoming pertains not to the application of the method but to the theory itself. Methods based on the theory of Mangler and Lighthill may be regarded as single-point inverse airfoil design methods; that is, the desired velocity distribution is prescribed at a single angle of attack. The fact is that many airfoils must operate over a range—not at a single point. Whether or not an airfoil designed by a single-point method satisfies multi-point design requirements must be determined through post-design analysis at the operating conditions of interest.

Consequently, the single-point design methods tend to be very tedious if multi-point design requirements are imposed. Although design by this single-point method has lead to many successful airfoils, a theory that has the explicit capability of handling multi-point design requirements from the outset is favored.

While efforts were underway in the 1950s to improve the numerical techniques of the single-point design methods, Eppler published his theory for multi-point design (Eppler 1957). Since this time, the method has been improved and made readily available as a computer program (Eppler and Somers 1980*a,b*; Eppler 1990). To this day the program enjoys increasingly widespread use. The Eppler method allows the airfoil to be divided into a desired number of segments along each of which the velocity distribution is prescribed together with the design angle of attack at which the velocity is to be achieved. In this way, multi-point design requirements can be satisfied during the actual design effort, not iteratively through post-design analysis. Despite the versatility of the method as a practical design tool, the actual theory has received very little attention; notable exceptions are Miley (1974), Ormsbee and Maughmer (1984) and Selig and Maughmer (1991). Miley (1974) applied the Eppler method to the design of low Reynolds number airfoils, and Ormsbee and Maughmer (1984) derived necessary conditions and integral constraints for the attainment of finite trailing-edge pressure gradients. The contributions made by Selig and Maughmer (1991) will be discussed in this thesis.

The 1950s also marked the beginning of new efforts aimed at the more precise definition of the velocity distribution in order to control the boundary-layer behavior and thereby control aerodynamic performance. In this respect, Wortmann (1955, 1957, 1961) and Eppler (1960, 1963*a,b*, 1969) made significant progress during the development of low-drag laminar-flow airfoils for sailplane applications. Most im-

portantly, the design philosophy of Wortmann regarding the turbulent pressure recovery, specifically the philosophy that the boundary layer should avoid separation everywhere by a constant margin, was supported by the experiments of Stratford (1959). Subsequently, these findings, taken to the extreme, were applied by Liebeck and Ormsbee (1970) and Liebeck (1976, 1978) in the design of a special class of high-lift low-drag airfoils and also by Miley (1974) in the design of airfoils for low Reynolds number applications. Out of developments such as these, it became evident the one desirable way to approach viscous design was to prescribe the margin by which the boundary layer avoids separation, specifically the boundary-layer shape factor (Henderson 1978; Goettsching 1988) which itself is a measure of the tendency of the boundary layer to separation. In other cases, it has been desirable to achieve other boundary-layer distributions in order to control such things as laminar flow, transition location, laminar and turbulent separation, stall characteristics, cavitation, etc. (Viken 1980; Shen and Eppler 1981; Maughmer and Somers 1989).

Most often, a desired boundary-layer development is achieved indirectly by performing a boundary-layer analysis of the prescribed velocity distribution and comparing the particular boundary-layer development with what is desired. If agreement is not satisfactory, the velocity distribution is modified interactively until agreement is reached. Since this approach is rather tedious, there has been some movement toward developing methods that allow the desired boundary-layer distribution to be prescribed directly from which ultimately the profile shape is derived (Henderson 1978; McMasters and Henderson 1979; Goettsching 1988). The procedure involves first finding the velocity distribution corresponding to the desired boundary-layer development through the use of an inverse boundary-layer technique. Second, through an inverse design method, the corresponding profile shape

is determined from the velocity distribution. Such methods, however, have not been adopted widely mainly for three reasons. First, the resulting velocity distribution from the inverse boundary-layer method will not satisfy the necessary three integral constraints automatically. Thus, some adjustment to the velocity distribution must be made, and, afterwards, the desired boundary-layer development will no longer be achieved exactly. Second, it is not always possible to express the boundary-layer equations in terms of the desired boundary-layer development. Third, although these methods are suitable for single-point design, it is unclear how to formulate the method for multi-point design.

It should be mentioned that an alternative approach to airfoil design is through optimization (Hicks and Vanderplaats 1977; Sobieczky 1989; Ghielmi *et al.* 1989; Drela 1990*a*; Sorensen 1991). Optimization formulations by their very nature have the particular potential advantage of taking into account all the relevant considerations in the areas of aerodynamics, structures, and stability and control just to name a few. Ironically, therein lies its very weakness. In a consideration of the multi-disciplinary nature of the design problem, it becomes necessary to define a suitable object function and constraints. What determines the best object function and appropriate constraints, however, is usually not known beforehand but rather only becomes known after the design process is well underway. Research into expert systems will probably aid in this definition process, but practical application is far from becoming a reality. For the time being, the airfoil designer will remain a key element in the design process and inverse techniques will be the tool of choice.

The significant contribution of the current research pertains to the development of a method that allows for the prescription of either the velocity distribution or boundary-layer development in a multi-point fashion. In addition, single parame-

ters like the airfoil maximum thickness and the zero-lift pitching moment may be prescribed—parameters which usually can only be specified in optimization formulations. After having specified the desired set of characteristics, the airfoil shape is determined by coupling an incompressible, potential-flow, inverse airfoil design method with a direct boundary-layer analysis method and solving the resulting nonlinear system of equations via a multi-dimensional Newton iteration technique. Details of the method (Selig and Maughmer 1991*a*,*b*) and example airfoils are given in Chapter 2. Also described in Chapter 2 is a new potential-flow airfoil-analysis method based on conformal mapping.

The principles applied in the design of isolated airfoils can also be applied in an analogous manner to cascades. Lighthill (1945*b*) was the first to show, through the use of conformal mapping, that in the design of an infinite cascade of airfoils the velocity distribution had to satisfy three integral constraints as with the isolated airfoil, albeit the constraints are considerably more complicated. In fact, application of the theory is difficult enough so that relatively few have ventured to apply Lighthill's method (Crooks and Howard 1954; Johnson 1957; Ruzicka and Spacek 1981). Part of the difficulty stems from the use of two mappings rather than one, and part comes from the evaluation of the resulting integral constraints. It seems that efforts at cascade design by conformal mapping methods have been all but abandoned. Methods based on singularity distributions are by far most common (e.g., Wilkinson 1969; Schwering 1970; Lewis 1982).

A drawback of the Lighthill method and methods based on singularity distributions is that they are only capable of solving the single-point inverse cascade design problem. As with the isolated airfoil, there is a strong interest in solving the multi-point design problem. To address this need, a theory for a multi-point

inverse cascade design has been formulated and is presented in Chapter 3. As with Lighthill's method, conformal mapping is used. The difference is that instead of involving two mappings only one is used. The resulting integral constraints are expressed in such a way that their evaluation is relatively straightforward. Also given in Chapter 3 is a simple theory for the generation of exact solutions to the flow through an infinite cascade and a new potential-flow cascade-analysis method based on conformal mapping. Chapter 4 gives suggestions for future work. Finally, conclusions are presented in Chapter 5.

Chapter 2

ISOLATED AIRFOILS

This chapter is made up of three, main parts related to isolated airfoils. In section 2.1, a potential-flow multi-point inverse airfoil design method is presented. The method forms the basis of a fairly general inverse airfoil design tool for incompressible flow. Viscous design aspects are considered in section 2.2. Finally, it is shown in section 2.3 that the theory developed in section 2.1 can be used to solve the analysis problem; that of finding the velocity distribution about a given airfoil shape.

2.1 THE POTENTIAL FLOW INVERSE DESIGN PROBLEM

As discussed in the introduction, the preferred way of solving the inverse airfoil design problem for incompressible flow is through conformal mapping. This preference is derived from the fact that the flow around an arbitrary airfoil may be mapped to the flow about a circle. The flow in this circle plane is easily determined; it only remains to determine the mapping. How this mapping is actually determined depends on the type of problem being solved. The Joukowski airfoil problem is one for which the mapping is specified. From this mapping both the airfoil shape and the flow about this airfoil are determined. For the analysis problem of an arbitrary airfoil, the task becomes that of finding the mapping which takes the circle to the airfoil. From this mapping follows the velocity distribution. Lastly, there is the inverse problem. The object is to determine the mapping not from the airfoil shape but from the specified airfoil velocity distribution. In this case, it is most convenient

to solve not for the mapping, per se, but for the mapping derivative since this can be related directly to the specified velocity distribution. This is the approach taken by Mangler (1938), Lighthill (1945*a*), Eppler (1957) and several others afterwards.

This section begins with a consideration of an extension of the Eppler theory (1957). In particular, the mapping is assumed to be of the form capable of mapping the circle to an airfoil with either a cusped or finite trailing-edge angle. Eppler (1957) only considers the cusped airfoil case. Furthermore, a new solution procedure is developed which allows for prescriptions of desired parameters, such as the pitching moment, maximum thickness ratio and velocity distribution $v(s)$. In section 2.2, this solution technique is generalized to include viscous design. In what follows, the integral constraints for multi-point inverse airfoil design are derived through the use of conformal mapping. Also, continuity conditions on the velocity distribution are shown to result from specifying the velocity distribution in a piecewise (multi-point) fashion. Example airfoils, not meant for practical application, are finally presented to illustrate the use of the basic theory and the implementation of the Newton iteration in design.

2.1.1 Conformal Mapping and Conditions on the Mapping

The complex potential for uniform flow of unit velocity at angle of attack α about a unit circle in the ζ-plane is given by

$$F(\zeta) = e^{-i\alpha}\zeta + \frac{e^{i\alpha}}{\zeta} + \frac{i\Gamma}{2\pi}\ln\zeta \tag{2.1}$$

where $\Gamma = 4\pi \sin\alpha$ so as to satisfy the Kutta condition by fixing the rear stagnation point at $\zeta = 1$. The front stagnation point is then located at $\phi = \gamma = \pi + 2\alpha$. To obtain the flow about an arbitrary airfoil in the z-plane, the flow about the circle in the ζ-plane is mapped via $z = z(\zeta)$ as illustrated in figure 2-1.

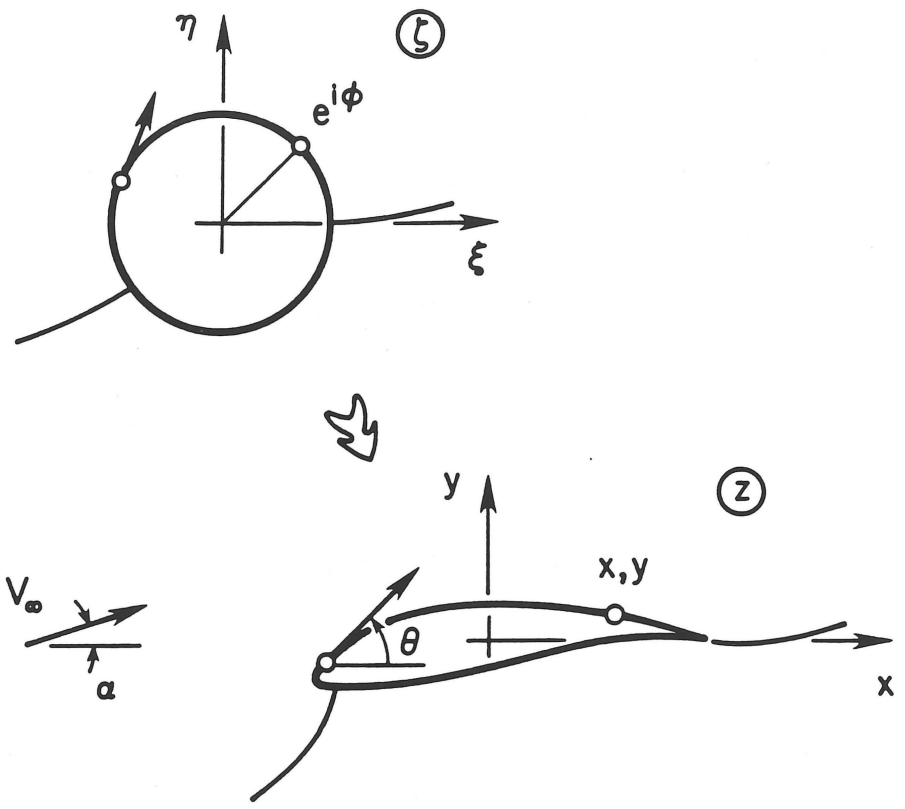

Figure 2-1 Mapping from circle to airfoil plane.

The mapping must satisfy three conditions: the airfoil trailing-edge angle must be finite, the flow at infinity must be unaltered, and the airfoil contour must close. These latter two conditions lead ultimately to the integral constraints for multi-point inverse airfoil design. The mapping is assumed to be of the form

$$\frac{dz}{d\zeta} = \left(1 - \frac{1}{\zeta}\right)^{1-\epsilon} \exp \sum_{m=0}^{\infty} (a_m + ib_m)\zeta^{-m} \tag{2.2}$$

where, for a convergent power series, it is required that $|\zeta| \geq 1$. As discussed by James (1971), the Schwarz-Christoffel factor $(1-1/\zeta)^{1-\epsilon}$ guarantees an airfoil with a trailing-edge angle of $\pi\epsilon$. Taking $\epsilon = 0$ for a cusped airfoil yields the transformation used by Eppler (1957).

To determine the remaining conditions on the mapping, it is helpful to expand equation (2.2) as

$$\frac{dz}{d\zeta} = e^{a_0+ib_0}\left(1 + \frac{a_1 - 1 + \epsilon + ib_1}{\zeta} + \cdots\right) \tag{2.3}$$

The condition that the flow at infinity be unaltered is expressed as

$$\lim_{\zeta\to\infty} \frac{dz}{d\zeta} = 1 \tag{2.4}$$

which is only satisfied if

$$a_0 = 0 \quad \text{and} \quad b_0 = 0 \tag{2.5a, b}$$

The condition that the airfoil be closed can be written as

$$\oint_{C_z} dz = \oint_{C_\zeta} \frac{dz}{d\zeta} d\zeta = 0 \tag{2.6}$$

where C_z and C_ζ are about the airfoil and the circle, respectively. From equation (2.3), this condition is only satisfied if

$$a_1 = 1 - \epsilon \quad \text{and} \quad b_1 = 0 \tag{2.7a, b}$$

If the intent were merely to generate an airfoil, one could stop here. The series $\sum(a_m + ib_m)\zeta^{-m}$ could be truncated, and the coefficients could be set arbitrarily with the simple exception that $a_0 = b_0 = b_1 = 0$ and $a_1 = 1 - \epsilon$. The mapping would satisfy all of the necessary conditions and would produce an airfoil with the desired trailing-edge angle $\pi\epsilon$. The motivating factor to continue comes from the desire to specify not the series coefficients explicitly but rather the velocity in a multi-point fashion about the airfoil.

2.1.2 Relation between the Mapping and the Complex Velocity

The problem at hand is to relate the desired velocity distribution about the airfoil to the series coefficients of the mapping. To this end, the complex velocity in the z-plane is expressed as

$$\frac{dF}{dz} = ve^{-i\theta} \tag{2.8}$$

which on the boundary of the unit circle, $\zeta = e^{i\phi}$, becomes

$$\left.\frac{dF}{dz}\right|_{\zeta=e^{i\phi}} = v(\phi)e^{-i\theta(\phi)} \tag{2.9}$$

Obtaining the real and imaginary parts of equation (2.9) for later use is facilitated by taking its natural logarithm. This, however, requires special consideration since $v(\phi)$ is negative along the lower surface aft of the leading-edge stagnation point as shown in figure 2-2. This problem is alleviated by taking the absolute value, $|v(\phi)| = v^*(\phi)$. In so doing, the flow direction must jump by π at the leading-edge stagnation point and by $\pi\epsilon$ at the trailing edge. To reflect these jumps, $\theta(\phi)$ is replaced by $\theta^*(\phi)$. Now

$$\left.\frac{dF}{dz}\right|_{\zeta=e^{i\phi}} = v^*(\phi)e^{-i\theta^*(\phi)} \tag{2.10}$$

and taking the natural logarithm yields

$$\left.\ln\left(\frac{dF}{dz}\right)\right|_{\zeta=e^{i\phi}} = \ln v^*(\phi) - i\theta^*(\phi) \tag{2.11}$$

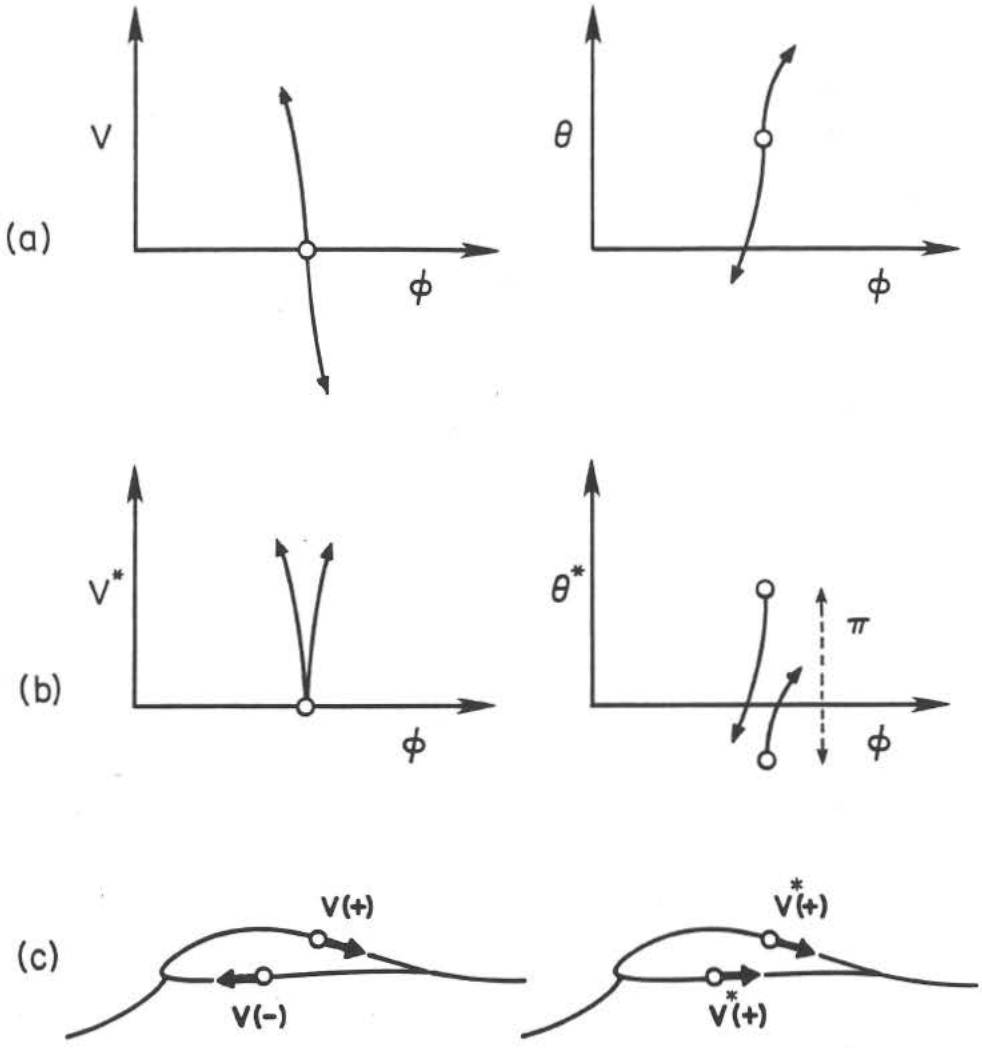

Figure 2-2 Relation between $v(\phi)$ and $v^*(\phi)$: (a) velocity $v(\phi)$ and flow angle $\theta(\phi)$ near the stagnation point, (b) velocity $v^*(\phi)$ and flow angle $\theta^*(\phi)$ near the stagnation point and (c) velocity $v(\phi)$ and $v^*(\phi)$ at two points on the airfoil.

To relate $v^*(\phi)$ and $\theta^*(\phi)$ to the series coefficients, the complex velocity is written alternatively as

$$\left.\frac{dF}{dz}\right|_{\zeta=e^{i\phi}} = \frac{dF/d\zeta|_{\zeta=e^{i\phi}}}{dz/d\zeta|_{\zeta=e^{i\phi}}} \tag{2.12}$$

The numerator $dF/d\zeta|_{\zeta=e^{i\phi}}$ is simply the known flow over the circle given by

$$\left.\frac{dF}{d\zeta}\right|_{\zeta=e^{i\phi}} = 4\sin(\phi/2)\,\cos(\phi/2-\alpha^*(\phi))e^{-i(\phi-\pi/2)} \tag{2.13}$$

The reason for writing the angle of attack as $\alpha^*(\phi)$ will be explained in section 2.1.5. Since the factor $\cos(\phi/2-\alpha^*(\phi))$ is negative for $\pi+2\alpha^*(\phi)<\phi<2\pi$, the complex velocity about the circle is, in preparation for taking its natural logarithm, alternatively written as

$$\left.\frac{dF}{d\zeta}\right|_{\zeta=e^{i\phi}} = 4\sin(\phi/2)\,|\cos(\phi/2-\alpha^*(\phi))|e^{-i(\phi-\pi/2-\pi^*(\phi))} \tag{2.14}$$

where

$$\pi^*(\phi) = \begin{cases} 0, & 0\le\phi\le\pi+2\alpha^*(\phi) \\ \pi, & \pi+2\alpha^*(\phi)\le\phi\le 2\pi \end{cases} \tag{2.15}$$

for $0\le\phi\le 2\pi$. The step function $\pi^*(\phi)$ is introduced in order to account properly for the jumps in the flow direction at the front and rear stagnation points on the circle.

From equation (2.2), the derivative of the mapping function on the unit circle is

$$\left.\frac{dz}{d\zeta}\right|_{\zeta=e^{i\phi}} = (1-e^{-i\phi})^{1-\epsilon}\exp\sum_{m=0}^{\infty}(a_m+ib_m)\,e^{-im\phi} \tag{2.16}$$

or

$$= (1-e^{-i\phi})^{1-\epsilon}e^{P(\phi)+iQ(\phi)} \tag{2.17}$$

where

$$P(\phi)+iQ(\phi) \equiv \sum_{m=0}^{\infty}(a_m\cos m\phi+b_m\sin m\phi)+i\sum_{m=0}^{\infty}(b_m\cos m\phi-a_m\sin m\phi) \tag{2.18}$$

Using equations (2.14) and (2.17) and taking the natural logarithm of equation (2.12), the following result is obtained

$$\ln\left(\frac{dF}{dz}\right)\Big|_{\zeta=e^{i\phi}} = -\ln\left\{\frac{(2\sin\phi/2)^{-\epsilon}}{2|\cos(\phi/2-\alpha^*(\phi))|}\right\}$$
$$+i\left[\pi^*(\phi)-\phi/2+\epsilon(\pi/2-\phi/2)\right]-P(\phi)-iQ(\phi) \qquad (2.19)$$

Equating equations (2.11) and (2.19) gives the important result

$$P(\phi)+iQ(\phi) = -\ln\left\{\frac{(2\sin\phi/2)^{-\epsilon}v^*(\phi)}{2|\cos(\phi/2-\alpha^*(\phi))|}\right\}$$
$$+i\left[\theta^*(\phi)+\pi^*(\phi)-\phi/2+\epsilon(\pi/2-\phi/2)\right] \qquad (2.20)$$

It is seen from equation (2.20) that the specification of the velocity $v^*(\phi)$ and angle of attack $\alpha^*(\phi)$ determines $P(\phi)$ uniquely. Alternatively, the specification of the airfoil flow direction $\theta^*(\phi)$ and $\alpha^*(\phi)$ determines $Q(\phi)$ uniquely. From either $P(\phi)$ or $Q(\phi)$, the corresponding conjugate harmonic function may be determined through the Poisson integral exterior to the unit circle, that is,

$$P(\phi)+iQ(\phi) = -\frac{1}{2\pi}\int_0^{2\pi} Q(\psi)\cot\frac{\psi-\phi}{2}\,d\psi + i\,\frac{1}{2\pi}\int_0^{2\pi} P(\psi)\cot\frac{\psi-\phi}{2}\,d\psi \qquad (2.21)$$

A discussion of how $Q(\phi)$ is determined numerically from $P(\phi)$ is given in section 2.1.7.3.

2.1.3 Airfoil Coordinates

Once $P(\phi)$ and $Q(\phi)$ are known, the airfoil coordinates may be computed by equating the expression

$$\frac{dz}{d\zeta}\Big|_{\zeta=e^{i\phi}} = \frac{dz/d\phi}{d\zeta/d\phi} = -ie^{-i\phi}\left(\frac{dx}{d\phi}+i\frac{dy}{d\phi}\right) \qquad (2.22)$$

with equation (2.17). After some manipulation, this gives

$$x(\phi) + iy(\phi) = -\int (2\sin\phi/2)^{1-\epsilon} e^{P(\phi)} e^{i[\phi/2 - \epsilon(\pi/2-\phi/2)+Q(\phi)]}\, d\phi \qquad (2.23)$$

The airfoil coordinates, $x(\phi)$ and $y(\phi)$, are then obtained through quadrature.

2.1.4 Airfoil Lift and Moment

By the Blasius relations, the airfoil lift and moment are given by

$$L = \frac{1}{2}\rho\, Re\left\{\oint_{C_z}\left(\frac{dF}{dz}\right)^2 dz\right\} \quad \text{and} \quad M_O = \frac{1}{2}\rho\, Re\left\{\oint_{C_z}\left(\frac{dF}{dz}\right)^2 z\, dz\right\} \quad (2.24a, b)$$

where the lift acts perpendicular to the freestream and the moment is taken as positive in the clockwise direction. The contour C_z is any closed curve which encloses the airfoil. It is well known that equation (2.24a) leads to

$$L = \rho V \Gamma \qquad (2.25)$$

Since $\Gamma = 4\pi \sin\alpha$, the lift coefficient becomes

$$c_l = \frac{L}{\frac{1}{2}\rho V^2 c} = \frac{4\pi\rho V \sin\alpha}{\frac{1}{2}\rho V^2 c} \qquad (2.26)$$

Taking $V = 1$, as is consistent with equation (2.1), gives

$$c_l = \frac{8\pi \sin\alpha}{c} \qquad (2.27)$$

Typically, the airfoil as computed by equation (2.22) has $c \approx 4$. Using this approximation for the chord and assuming a small angle of attack gives $c_l \approx 2\pi\alpha$. Consequently, specifying an angle of attack α is essentially like specifying the lift coefficient.

Equation (2.24b) for the moment is evaluated by taking C_z to be the contour about the airfoil itself; however, the integral (2.24b) is evaluated not in the airfoil plane but in the circle plane. Using the relations

$$\frac{dF}{dz} = \frac{dF/d\zeta}{dz/d\zeta} \qquad \text{and} \qquad dz = \frac{dz}{d\zeta}d\zeta \tag{2.28a, b}$$

expression (2.24b) becomes

$$M_O = \frac{1}{2}\rho\, Re\left\{\oint_{C_\zeta}\left(\frac{dF}{d\zeta}\right)^2 \frac{z(\zeta)}{dz/d\zeta}\, d\zeta\right\} \tag{2.29}$$

where the contour C_z has been mapped into the contour C_ζ about the unit circle.

Evaluation of the moment begins with the determination of the integrand in equation (2.29). From equation (2.1), it is found that

$$\frac{dF}{d\zeta} = e^{-i\alpha}\left(1-\frac{1}{\zeta}\right)\left(1-\frac{e^{i\gamma}}{\zeta}\right) \tag{2.30}$$

which yields

$$\left(\frac{dF}{d\zeta}\right)^2 = e^{-2i\alpha}\left[1-\frac{2(1+e^{i\gamma})}{\zeta}+\frac{2e^{i\gamma}+(1+e^{i\gamma})^2}{\zeta^2}-\frac{2e^{i\gamma}(1+e^{i\gamma})}{\zeta^3}+\frac{e^{2i\gamma}}{\zeta^4}\right] \tag{2.31}$$

From equation (2.2), it is found upon expansion that

$$\frac{dz}{d\zeta} = 1+\frac{\lambda}{\zeta^2}+\cdots \tag{2.32}$$

where

$$\lambda = \frac{1}{2}(\epsilon-1)+a_2+ib_2 \tag{2.33}$$

Inverting equation (2.32) gives

$$\frac{1}{dz/d\zeta} = 1-\frac{\lambda}{\zeta^2}+\cdots \tag{2.34}$$

and integrating equation (2.32) gives

$$z = \zeta - \frac{\lambda}{\zeta} + \cdots \tag{2.35}$$

where the constant of integration has been taken as zero for convenience. Combining equations (2.31), (2.34) and (2.35) produces

$$\left(\frac{dF}{d\zeta}\right)^2 \frac{z(\zeta)}{dz/d\zeta} = e^{-2i\alpha}\left[\zeta - 2(1+e^{i\gamma}) + \frac{2e^{i\gamma} + (1+e^{i\gamma})^2 - 2\lambda}{\zeta} + \cdots\right] \tag{2.36}$$

so that

$$\oint_{C_\zeta} \left(\frac{dF}{d\zeta}\right)^2 \frac{z(\zeta)}{dz/d\zeta}\, d\zeta = 2\pi i\{e^{-2i\alpha}[2e^{i\gamma} + (1+e^{i\gamma})^2 - 2\lambda]\} \tag{2.37}$$

Taking the real part of equation (2.37) according to equation (2.29) finally gives

$$M_O = 2\pi\rho\,[b_2 \cos 2\alpha - (a_2 - 1/2 + \epsilon/2)\sin 2\alpha] \tag{2.38}$$

where, from the Euler formulas for the Fourier series coefficients which define the mapping derivative [equation (2.2)]

$$a_2 = \frac{1}{\pi}\int_0^{2\pi} P(\phi)\cos 2\phi\, d\phi \qquad \text{and} \qquad b_2 = \frac{1}{\pi}\int_0^{2\pi} P(\phi)\sin 2\phi\, d\phi \tag{2.39a, b}$$

The moment as given by equation (2.38) is, as previously stated, the moment about the origin in the airfoil plane. Following standard convention, however, it is desired that the moment be about the airfoil quarter-chord point. Equation (2.23) upon integration provides the airfoil shape relative to an additive constant of integration and does not therefore locate the airfoil in proper reference to the origin. In order to find the moment about the airfoil quarter-chord point, the first step is to locate the airfoil in proper reference to the origin and then to resolve the lift and moment at the origin into a lift and moment at the quarter-chord point. The latter problem is solved through simple statics, while the former one requires

some ingenuity if it is to be solved short of determining the entire mapping $z(\zeta)$—a task which would be computationally expensive.

A straight-forward procedure for finding the proper placement of the airfoil relative to the origin starts by dividing equation (2.35) by ζ to yield

$$\frac{z(\zeta)}{\zeta} = 1 - \frac{\lambda}{\zeta^2} + \cdots \tag{2.40}$$

Integration of this equation about the unit circle as

$$\oint_{C_\zeta} \frac{z(\zeta)}{\zeta}\, d\zeta = \oint_{C_\zeta} \left(1 - \frac{\lambda}{\zeta^2} + \cdots\right) d\zeta \tag{2.41}$$

gives, upon integration of the right hand side,

$$\oint_{C_\zeta} \frac{z(\zeta)}{\zeta}\, d\zeta = 0 \tag{2.42}$$

On the unit circle, this becomes

$$\int_0^{2\pi} \frac{x(\phi) + iy(\phi)}{e^{i\phi}}\, ie^{i\phi}\, d\phi = 0 \tag{2.43}$$

or

$$\int_0^{2\pi} x(\phi)\, d\phi = 0 \qquad \text{and} \qquad \int_0^{2\pi} y(\phi)\, d\phi = 0 \tag{2.44a, b}$$

In words, the airfoil coordinates must satisfy equations (2.44*a,b*) or else the airfoil is not placed in proper reference to the origin. Realizing that the airfoil as computed by equation (2.23) will not satisfy these equations automatically (since the additive constant is not known a priori), corrections can be introduced as

$$x(\phi) = \hat{x}(\phi) + \delta x \qquad \text{and} \qquad y(\phi) = \hat{y}(\phi) + \delta y \tag{2.45a, b}$$

where $\hat{x}(\phi)$ and $\hat{y}(\phi)$ are the airfoil coordinates as computed through equation (2.23) and δx and δy are the corrections. Substituting equations (2.45*a,b*) into (2.44*a,b*) yields the correction equations

$$\delta x = -\frac{1}{2\pi}\int_0^{2\pi} \hat{x}(\phi)\, d\phi \qquad \text{and} \qquad \delta y = -\frac{1}{2\pi}\int_0^{2\pi} \hat{y}(\phi)\, d\phi \tag{2.46a, b}$$

Once having solved for δx and δy, the airfoil may be translated by equations (2.45a,b).

With the airfoil in proper reference to the origin, the moment about the quarter-chord point $M_{c/4}$ can be found. The pitching-moment coefficient about the quarter-chord point $c_{m_{c/4}}$ is given by

$$c_{m_{c/4}} = \frac{M_{c/4}}{\frac{1}{2}\rho V^2 c^2} = \frac{2M_{c/4}}{\rho c^2} \tag{2.47}$$

using $V = 1$. For the special case of zero lift ($\alpha = 0$), it is not necessary to correct the airfoil coordinates by δx and δy because the point about which the moment is taken is arbitrary. In this special case, the zero-lift pitching-moment coefficient c_{m_0} becomes through equation (2.38)

$$c_{m_0} = \frac{M_O(\alpha = 0)}{\frac{1}{2}\rho V^2 c^2} = \frac{4\pi b_2}{c^2} \tag{2.48}$$

2.1.5 Multi-Point Design Capability of the Theory

For discussion, $P(\phi)$ given by equation (2.20) is rewritten as

$$P(\phi) = -\ln\left\{\frac{(2\sin\phi/2)^{-\epsilon} v^*(\phi)}{2|\cos(\phi/2 - \alpha^*(\phi))|}\right\} \tag{2.49}$$

The function $P(\phi)$ depends only on ϕ and is defined by specification of $v^*(\phi)$ and $\alpha^*(\phi)$, now termed the design velocity distribution and the corresponding design angle of attack *distribution*. For single-point design, as in Lighthill's theory (1945a), $\alpha^*(\phi)$ is zero while $v^*(\phi)$ is a continuous specified function. It is not necessary, however, that $v^*(\phi)$ and $\alpha^*(\phi)$ be continuous functions; rather, it is only necessary that $P(\phi)$ be continuous. Therefore, in order to maintain a continuous function $P(\phi)$, a discontinuity in $v^*(\phi)$ between two segments must be compensated by a corresponding discontinuity in $\alpha^*(\phi)$. Consequently, the airfoil may be divided

into any number of segments along which the velocity $v^*(\phi)$ and angle of attack $\alpha^*(\phi)$ are given. Practical considerations for multi-point design dictate that over each segment of the airfoil $\alpha^*(\phi)$ be constant while $v^*(\phi)$ may vary in order to obtain some desired velocity distribution over the given segment at the design angle of attack. This process of specifying $v^*(\phi)$ for different segments of the airfoil at different angles of attack $\alpha^*(\phi)$ easily allows for multi-point design. This is the most important result of the theory: discrete segments of the airfoil may be designed for different angles of attack, or more generally each segment may be designed for a different operating condition (Reynolds number, angle of attack, etc.). This result will be illustrated later by example.

2.1.6 Constraints and Special Considerations

2.1.6.1 Integral Constraints

As with any inverse airfoil design formulation, the specification of the velocity distribution is not completely arbitrary. Since the function $P(\phi)$ can be expressed as a Fourier series where $Q(\phi)$ is the conjugate series, the conditions on the mapping coefficients, equations $(2.5a,b)$ and $(2.7a,b)$, give rise to integral constraints on both $P(\phi)$ and $Q(\phi)$. The integral constraints on $P(\phi)$ come from the first three coefficients of the Fourier series representation for $P(\phi)$, that is, from equations $(2.5a)$, $(2.7a,b)$ and (2.18)

$$a_0 = \frac{1}{2\pi}\int_0^{2\pi} P(\phi)\,d\phi \qquad = 0 \tag{2.50a}$$

$$a_1 = \frac{1}{\pi}\int_0^{2\pi} P(\phi)\cos\phi\,d\phi \;= 1-\epsilon \tag{2.50b}$$

$$b_1 = \frac{1}{\pi}\int_0^{2\pi} P(\phi)\sin\phi\,d\phi \;= 0 \tag{2.50c}$$

Likewise, the three integral constraints on $Q(\phi)$ are

$$b_0 = \frac{1}{2\pi}\int_0^{2\pi} Q(\phi)\,d\phi = 0 \tag{2.51a}$$

$$b_1 = \frac{1}{\pi}\int_0^{2\pi} Q(\phi)\cos\phi\,d\phi = 0 \tag{2.51b}$$

$$-a_1 = \frac{1}{\pi}\int_0^{2\pi} Q(\phi)\sin\phi\,d\phi = \epsilon - 1 \tag{2.51c}$$

Considering the expressions for $P(\phi)$ and $Q(\phi)$, it is seen that equations (2.50a–c) are integral constraints on $v^*(\phi)$ and $\alpha^*(\phi)$, while equations (2.51a–c) are integral constraints on $\theta^*(\phi)$ and $\alpha^*(\phi)$.

As could be anticipated, the preceding integral constraints are closely related to several others found in the literature. In fact, they are thought to be the most general form of the integral constraints for incompressible inverse airfoil design. For cusped airfoils, the integral constraints on $P(\phi)$ are equivalent to those of Eppler (1957) when $\epsilon = 0$. Eppler does not give or discuss the integral constraints on $Q(\phi)$ because these integral constraints are not a necessary step in the formulation.

For single-point design in which the angle of attack α is constant, the integral constraints reduce to those of Strand (1973) given for $v_\alpha^*(\phi)$ and $\theta_\alpha^*(\phi)$ by

$$\int_0^{2\pi} \ln v_\alpha^*(\phi) \begin{Bmatrix} 1 \\ \cos\phi \\ \sin\phi \end{Bmatrix} d\phi = \begin{Bmatrix} 0 \\ -2\pi\sin^2\alpha \\ \pi\sin 2\alpha \end{Bmatrix} \tag{2.52}$$

and

$$\int_0^{2\pi} \theta_\alpha^*(\phi) \begin{Bmatrix} 1 \\ \cos\phi \\ \sin\phi \end{Bmatrix} d\phi = \begin{Bmatrix} 2\pi\alpha \\ -\pi\sin 2\alpha \\ -2\pi\sin^2\alpha \end{Bmatrix} \tag{2.53}$$

In verifying equation (2.53), the integration must be performed in two parts for a given angle of attack α. The first part is from the trailing edge $\phi = 0$ to the stagnation point $\gamma = \pi + 2\alpha$ with the integrand $Q(\phi) = \theta_\alpha^*(\phi) - \phi/2 + \epsilon(\pi/2 - \phi/2)$.

The second part of the integration is from the stagnation point to the trailing edge $\phi = 2\pi$ with $Q(\phi) = \theta^*_\alpha(\phi) + \pi - \phi/2 + \epsilon(\pi/2 - \phi/2)$.

For a single-point design at zero-lift where $\alpha^*(\phi) = 0$ and $v^*(\phi) = v^*_0(\phi)$, the integral constraints on $P(\phi)$ reduce to

$$\int_0^{2\pi} \ln v^*_0(\phi) \left\{ \begin{array}{c} 1 \\ \cos\phi \\ \sin\phi \end{array} \right\} d\phi = \left\{ \begin{array}{c} 0 \\ 0 \\ 0 \end{array} \right\} \tag{2.54}$$

as presented by Lighthill (1945*a*). It is not well known that these last integral constraints commonly attributed to Lighthill were derived earlier by Mangler (1938). Furthermore, as noted by Mangler, essentially the same conditions were found even earlier by Betz (1934) and, for the most part, by Weinig (1929).

2.1.6.2 Continuity Constraints

For multi-point design, the requirement that $P(\phi)$ be continuous introduces a *continuity* equation on $P(\phi)$ at each arc limit between segments where there is a jump in $v^*(\phi)$ and a corresponding jump in $\alpha^*(\phi)$. This condition of continuity between segments is expressed as

$$P_+(\phi_i) = P_-(\phi_i) \tag{2.55}$$

or

$$\frac{v^*_+(\phi_i)}{|\cos(\phi_i/2 - \alpha^*_+(\phi_i))|} = \frac{v^*_-(\phi_i)}{|\cos(\phi_i/2 - \alpha^*_-(\phi_i))|} \tag{2.56}$$

where ϕ_i is the arc limit between segments i and $i+1$. An alternative and more physical derivation of the continuity constraints is presented in Appendix A. This condition of continuity is not strictly necessary. For instance, the design velocity distribution could jump discontinuously at a point on the airfoil and thereby model suction (Lighthill 1945*a*; Glauert 1947) or blowing on the airfoil surface. Such airfoil

flows will not be considered here, and $P(\phi)$ is required to be continuous as indicated previously.

2.1.6.3 Limiting Behavior of the Velocity Distribution in the Vicinity of the Stagnation Points

The velocity distribution must satisfy not only the integral constraints and continuity conditions, but in the vicinity of the stagnation points it must go to zero in a special way. This may be seen through equation (2.20) which gives

$$v^*(\phi) = (2\sin\phi/2)^\epsilon\, 2|\cos(\phi/2 - \alpha^*(\phi))|e^{-P(\phi)} \tag{2.57}$$

Stagnation points will always occur at the forward stagnation point $\phi = \gamma = \pi + 2\alpha^*(\phi)$ and, when $\epsilon \neq 0$, at the trailing edge $\phi = 0$, $\phi = 2\pi$. According to equation (2.57), the velocity in the vicinity of the trailing edge must go to zero as

$$\lim_{\phi_+ \to 0} v^*(\phi) \sim (\sin\phi/2)^\epsilon\, g_+(\phi) \tag{2.58a}$$

$$\lim_{\phi_- \to 2\pi} v^*(\phi) \sim (\sin\phi/2)^\epsilon\, g_-(\phi) \tag{2.58b}$$

where $g_+(\phi)$ and $g_-(\phi)$ are positive, non-zero functions. James (1971) obtained the same theoretical trailing-edge velocity relation in an effort to understand the airfoil trailing-edge curvature singularity. Similarly, from equation (2.57), the velocity in the vicinity of the forward stagnation point must go to zero as

$$\lim_{\phi_+ \to \gamma} v^*(\phi) \sim |\cos(\phi/2 - \alpha^*(\phi))|\, h_+(\phi) \tag{2.59a}$$

$$\lim_{\phi_- \to \gamma} v^*(\phi) \sim |\cos(\phi/2 - \alpha^*(\phi))|\, h_-(\phi) \tag{2.59b}$$

where the forward stagnation point γ is at $\pi + 2\alpha^*(\phi)$ and where $h_+(\phi)$ and $h_-(\phi)$ are positive, non-zero functions.

2.1.7 Numerical Implementation

The conditions on the mapping function which lead to the integral constraints on $P(\phi)$ require that the specification of $P(\phi)$, using $v^*(\phi)$ and $\alpha^*(\phi)$, must contain at least three, free parameters to be determined by solution. For each segment, another free parameter must be introduced to satisfy the continuity constraint on $P(\phi)$ between segments. All of the necessary free parameters are introduced in a way that facilitates the numerical solution, that allows for implementation into the multi-dimensional Newton iteration, and that permits the design of practical airfoils.

2.1.7.1 Specification of the Velocity Distribution

The four-segment airfoil depicted in figure 2-3 is given as an example. The design velocity distribution and the design angle of attack distribution for each segment are prescribed piecewise as follows:

$$\begin{aligned} v^*(\phi) &= v_1\, w(\phi) \\ \alpha^*(\phi) &= \alpha_1 \qquad\qquad 0 \le \phi \le \phi_1 \end{aligned} \tag{2.60a}$$

$$\begin{aligned} v^*(\phi) &= v_2 + \tilde{v}_2(\tilde{\phi}_2) \\ \alpha^*(\phi) &= \alpha_2 \qquad\qquad \phi_1 \le \phi \le \phi_2 \end{aligned} \tag{2.60b}$$

$$\begin{aligned} v^*(\phi) &= v_3 + \tilde{v}_3(\tilde{\phi}_3) \\ \alpha^*(\phi) &= \alpha_3 \qquad\qquad \phi_2 \le \phi \le \phi_3 \end{aligned} \tag{2.60c}$$

$$\begin{aligned} v^*(\phi) &= v_4\, \overline{w}(\phi) \\ \alpha^*(\phi) &= \alpha_4 \qquad\qquad \phi_3 \le \phi \le 2\pi \end{aligned} \tag{2.60d}$$

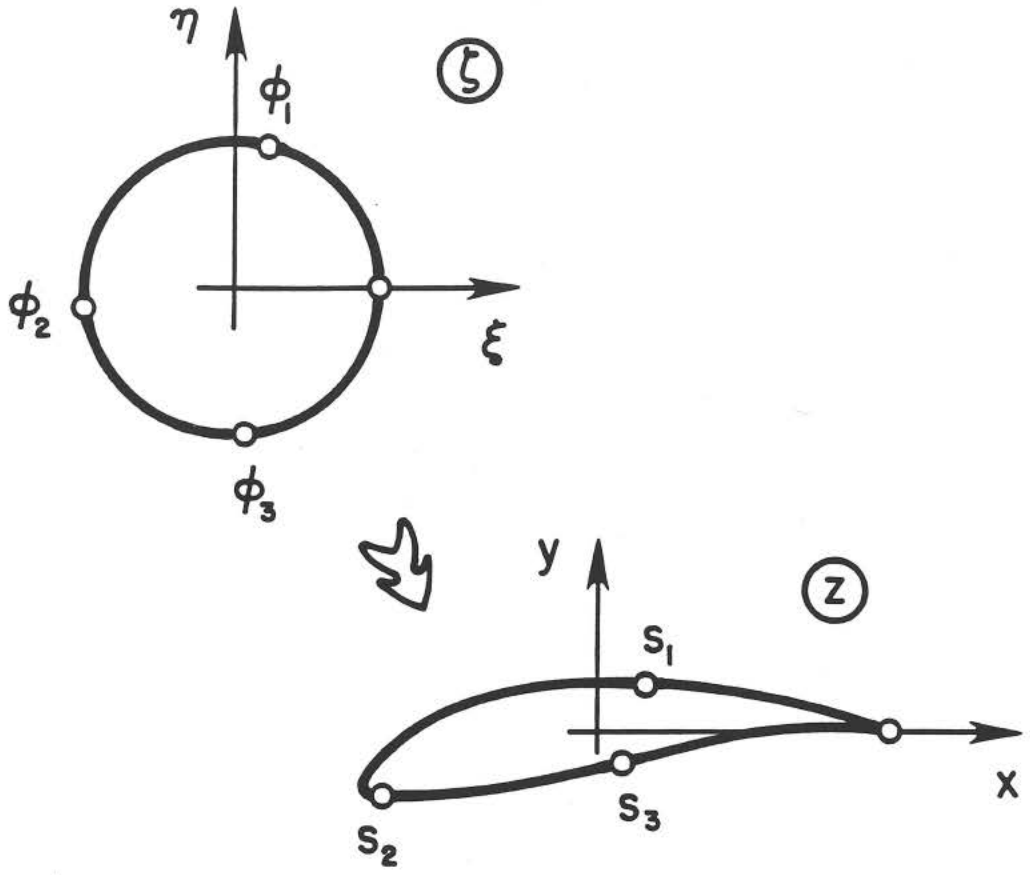

Figure 2-3 Circle divided into four segments and mapped to a four-segment airfoil.

where $\tilde{\phi}_2 = \phi - \phi_1$ and $\tilde{\phi}_3 = \phi - \phi_2$. The velocities v_i and the design angles of attack α_i are constant along their respective segments, while $\tilde{v}_i(\tilde{\phi}_i)$, $w(\phi)$ and $\overline{w}(\phi)$ all vary with ϕ. The velocity function $w(\phi)$ is termed the upper-surface recovery function, while $\overline{w}(\phi)$ is the corresponding function for the lower surface. The special notation ($\tilde{}$) will be discussed later. Although only four segments are presented here, the method is general enough to handle any number of intermediate segments of the type $v^*(\phi) = v_i + \tilde{v}_i(\tilde{\phi}_i)$.

The upper-surface recovery function is defined by

$$w(\phi) = w_{W\cdot}^{-\mu}(\phi)\, w_S^{K_H}(\phi)\, w_F^{\epsilon}(\phi), \qquad 0 \le \phi \le \phi_1 \tag{2.61}$$

where

$$w_{W\cdot}(\phi) = 1 + K\left(\frac{\cos\phi - \cos\phi_{W\cdot}}{1 + \cos\phi_{W\cdot}}\right), \qquad 0 \le \phi \le \phi_{W\cdot} \tag{2.62a}$$

$$w_S(\phi) = \begin{cases} 1 - 0.36\left(\dfrac{\cos\phi - \cos\phi_S}{1 - \cos\phi_S}\right)^2, & 0 \le \phi \le \phi_S \\ 1, & \phi_S \le \phi \le \phi_{W\cdot} \end{cases} \tag{2.62b}$$

$$w_F(\phi) = \begin{cases} \dfrac{\sin\phi/2}{\sin\phi_F/2}, & 0 \le \phi \le \phi_F \\ 1, & \phi_F \le \phi \le \phi_{W\cdot} \end{cases} \tag{2.62c}$$

with $\phi_{W\cdot} \equiv \phi_1$. The lower-surface recovery function $\overline{w}(\phi)$ is of the same form except that $w_{W\cdot}(\phi)$, $w_S(\phi)$, $w_F(\phi)$ and the parameters μ, K_H, K, $\phi_{W\cdot}$, ϕ_S and ϕ_F are replaced by $\overline{w}_{W\cdot}(\phi)$, $\overline{w}_S(\phi)$, $\overline{w}_F(\phi)$, $\overline{\mu}$, $\overline{K}_H$, $\overline{K}$, $\overline{\phi}_{W\cdot} \equiv \phi_3$, $\overline{\phi}_S$ and $\overline{\phi}_F$.

The first two contributions to the recovery functions, $w_{W\cdot}(\phi)$ and $w_S(\phi)$, appear in the Eppler formulation (1957) while the last contribution, $w_F(\phi)$, is new and must be introduced to satisfy the trailing-edge velocity relations (2.58*a*,*b*). For a typical airfoil design $\phi_{W\cdot} > \phi_S > \phi_F$; for instance, $\phi_{W\cdot} = 100°, \phi_S = 30°$ and $\phi_F = 15°$. In this case, the first factor $w_{W\cdot}^{-\mu}(\phi)$ controls the main part of the recovery. The second factor $w_S^{K_H}(\phi)$ controls to a great extent the velocity distribution in the vicinity

of the trailing edge which, in turn, affects the shape of the airfoil near the trailing edge as will be discussed in section 2.1.9. Using the values for the arcs limits given previously and taking $\mu = 0.3$, $K_H = 0.1$, $\epsilon = 0$, $K = 1$ gives the total recovery function shown in figure 2-4. As seen from the figure, the component functions only take effect over their respective arc limits. Since in this example $c = 0$, the airfoil has a cusped trailing edge. An airfoil with a 10° trailing-edge angle, for instance, requires $\epsilon = 1/18$. In this case the recovery function now produces a zero trailing-edge velocity as shown in figure 2-5.

As shown in figure 2-6 for a segment $\phi_{i-1} < \phi < \phi_i$, it is possible to select a design angle of attack such that the stagnation point falls on that segment since $\gamma = \pi + 2\alpha_i$. In this case, it is necessary to follow the forward stagnation point velocity relations (2.59*a*,*b*). Because the forward stagnation point moves with the angle of attack, however, it is possible to specify the design angle of attack such that the stagnation point falls outside of the segment. In this case, the forward stagnation point velocity relation is bypassed. This is the approach adopted by Eppler and followed here. Considering all segments, the condition that the stagnation point falls outside of the segment (either ahead of it or behind) is met by requiring

$$\frac{\phi_1 - \pi}{2} < \alpha_1 < \frac{\pi}{2} \tag{2.63a}$$

$$-\frac{\pi}{2} < \alpha_2 < \frac{\phi_1 - \pi}{2} \quad \text{or} \quad \frac{\phi_2 - \pi}{2} < \alpha_2 < \frac{\pi}{2} \tag{2.63b}$$

$$-\frac{\pi}{2} < \alpha_3 < \frac{\phi_2 - \pi}{2} \quad \text{or} \quad \frac{\phi_3 - \pi}{2} < \alpha_3 < \frac{\pi}{2} \tag{2.63c}$$

$$-\frac{\pi}{2} < \alpha_4 < \frac{\phi_3 - \pi}{2} \tag{2.63d}$$

In the design of a typical airfoil, these conditions are met easily.

A non-constant design velocity distribution over each intermediate segment is introduced through the velocity functions $\tilde{v}_i(\tilde{\phi}_i)$. This capability is not considered

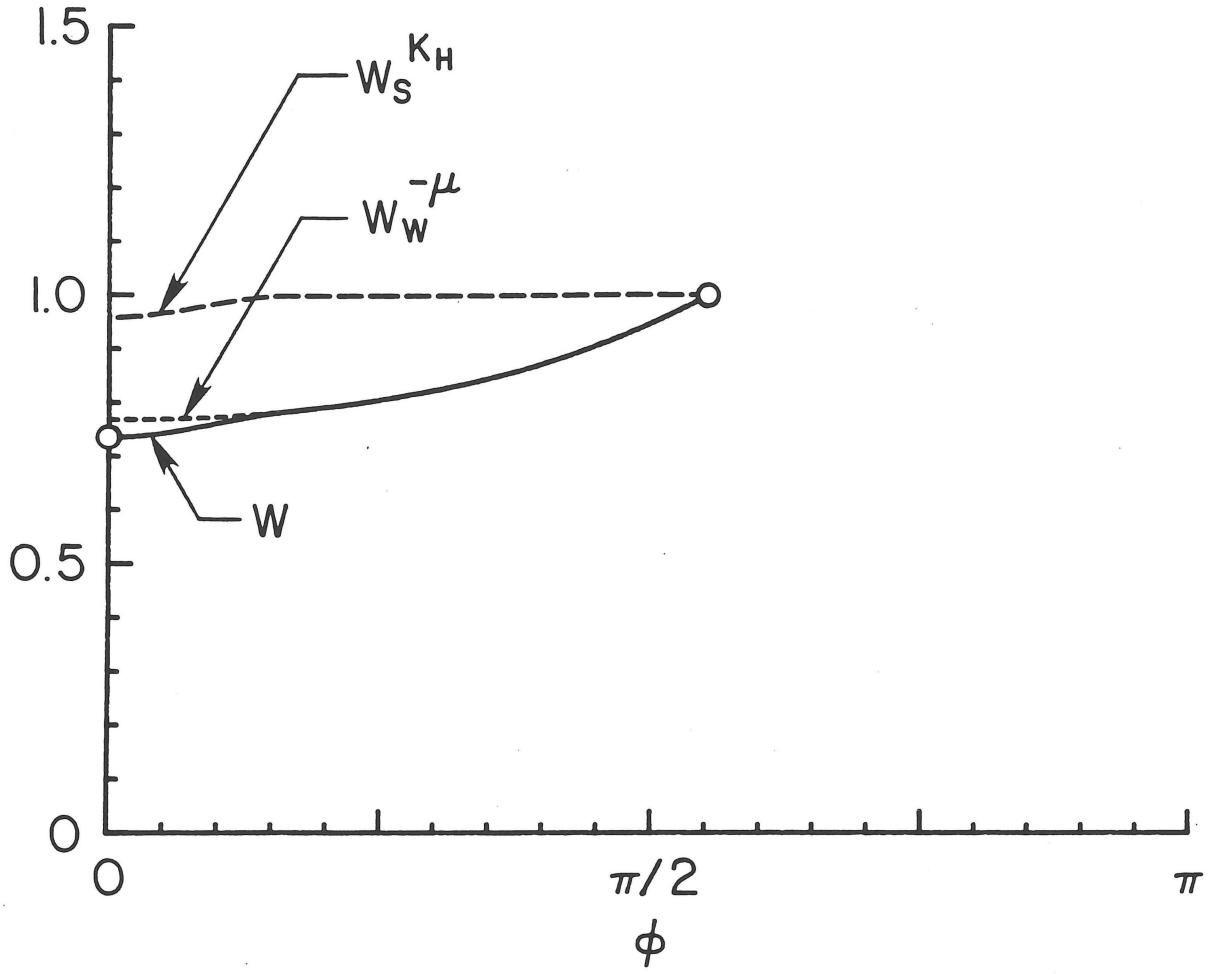

Figure 2-4 Component recovery functions and total recovery function for $\phi_W = 100°$, $\phi_S = 20°$, $\mu = 0.3$, $K_H = 0.1$, $\epsilon = 0$, and $K = 1$ corresponding to an airfoil with a cusped trailing edge.

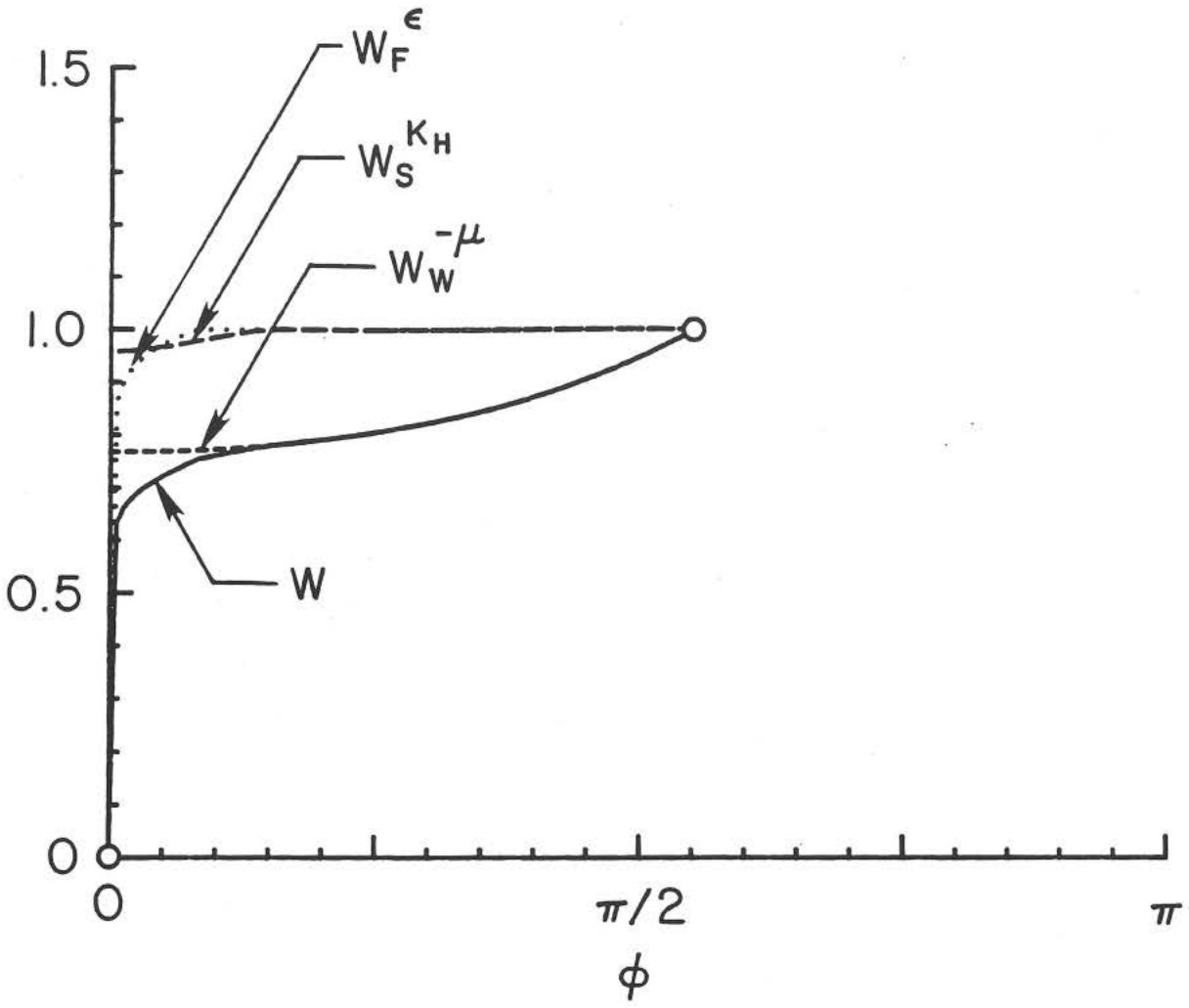

Figure 2-5 Component recovery functions and total recovery function for $\phi_W = 100°$, $\phi_S = 20°$, $\phi_F = 10°$, $\mu = 0.3$, $K_H = 0.1$, $\epsilon = 1/18$ and $K = 1$ corresponding to an airfoil with a 10° trailing-edge angle.

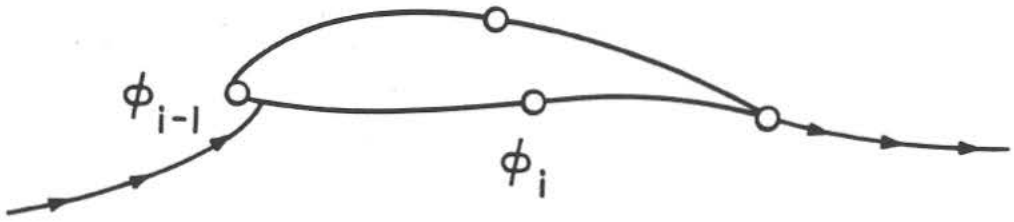

Figure 2-6 Example where the leading-edge stagnation point falls on the segment at the segment design angle of attack.

in the Eppler solution formulation. The notation ($\bar{}$) is used to indicate the value relative to the beginning of the segment i. Thus, as drawn in figure 2-7, $\tilde{\phi}_i$ is the relative arc limit for the segment. Likewise the velocity $\tilde{v}_i(\tilde{\phi}_i)$ is the velocity relative to the beginning of the segment such that

$$\tilde{v}_i(\tilde{\phi}_i = 0) = 0 \tag{2.64}$$

as indicated in figure 2-7. In equations (2.60*b*,*c*), v_i is as a result of equation (2.64) the velocity at the beginning of an intermediate segment i. Appropriately, v_i and $\tilde{v}_i(\tilde{\phi}_i)$ are respectively termed the velocity level and the relative design velocity distribution for an intermediate segment i. Consistent with the approach of avoiding a forward stagnation point on a segment, it is required that $v^*(\phi) > 0$ or

$$v^*(\phi) = v_i + \tilde{v}_i(\tilde{\phi}_i) > 0 \tag{2.65}$$

The relative design velocity functions $\tilde{v}_i(\tilde{\phi}_i)$ may be piecewise linear, cubic spline, or analytic functions and thereby offer a great deal of freedom in the design and especially in the Newton iteration scheme discussed later.

2.1.7.2 Governing Equations for the Inverse Design Problem

Substituting the expressions for $v^*(\phi)$ and $\alpha^*(\phi)$, equations (2.60*a*–*d*), into the three integral constraints on $P(\phi)$ leads to

$$a_{11}\mu + a_{12}\overline{\mu} + a_{13}K_H + a_{14}\overline{K}_H = b_1 \tag{2.66a}$$

$$a_{21}\mu + a_{22}\overline{\mu} + a_{23}K_H + a_{24}\overline{K}_H = b_2 \tag{2.66b}$$

$$a_{31}\mu + a_{32}\overline{\mu} + a_{33}K_H + a_{34}\overline{K}_H = b_3 \tag{2.66c}$$

Detailed expressions for the coefficients are given in Appendix B.

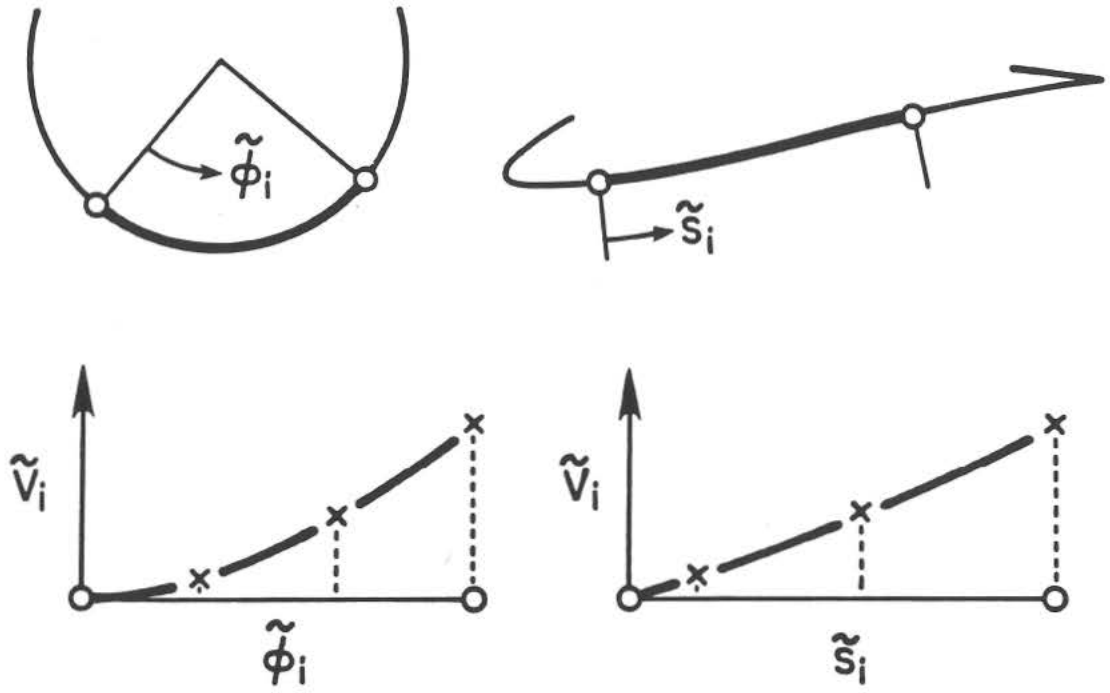

Figure 2-7 Splined relative velocity distribution in terms of the circle coordinate $\tilde{\phi}_i$ and $\tilde{s}_i$ for the resulting airfoil.

It is of interest to note that the integral constraints on $P(\phi)$ are much easier to evaluate than those on $\ln v_\alpha^*(\phi)$, as done through equations (2.52a) or (2.54) in, for example, Lighthill (1945a), Glauert (1947), Timman (1951), Nonweiler (1968), Ingen (1969), Arlinger (1970) and Strand (1973). At the stagnation points, $\ln v_\alpha^*(\phi)$ is singular while the singularities of $P(\phi)$ are removable owing to the velocity relations in the vicinity of the stagnation points. Hence, $P(\phi)$ is bounded in contrast to $\ln v_\alpha^*(\phi)$.

Continuity of $P(\phi)$ at the trailing edge gives

$$a_{41}\mu + a_{42}\overline{\mu} + a_{43}K_H + a_{44}\overline{K}_H = b_4 \tag{2.66d}$$

where the coefficients are again given in Appendix B. Continuity between the segments at ϕ_1, ϕ_2, and ϕ_3 requires further that

$$\frac{v_2}{|\cos(\phi_1/2 - \alpha_2)|} = \frac{v_1}{|\cos(\phi_1/2 - \alpha_1)|} \tag{2.67a}$$

$$\frac{v_3}{|\cos(\phi_2/2 - \alpha_3)|} = \frac{v_2 + \tilde{v}_2(\tilde{\phi}_2 = \phi_2 - \phi_1)}{|\cos(\phi_2/2 - \alpha_2)|} \tag{2.67b}$$

$$\frac{v_4}{|\cos(\phi_3/2 - \alpha_4)|} = \frac{v_3 + \tilde{v}_3(\tilde{\phi}_3 = \phi_3 - \phi_2)}{|\cos(\phi_3/2 - \alpha_3)|} \tag{2.67c}$$

Thus, there are seven equations to satisfy for an airfoil with four segments. Consequently, all but seven parameters can be specified.

Due to the convenient linearity of equations (2.66a-d) with respect to μ, $\overline{\mu}$, K_H and $\overline{K}_H$, it is natural to select these parameters as four of the required seven unknowns. Through the continuity equations (2.67a-c), it is easiest to give any single velocity level, say v_1, and from it compute the remaining velocity levels: v_2, v_3 and v_4. Therefore, a solution to the inverse airfoil problem can be determined by specifying all of the design variables except the seven which are unknown: μ, $\overline{\mu}$,

K_H, $\overline{K}_H$, v_2, v_3 and v_4. In summary, all of the design variables (besides ϵ) for a four-segment airfoil are listed in table 2-1 below.

Table 2-1: Inverse Design Parameters for a Four-Segment Airfoil

i	ϕ	$\alpha^*(\phi)$	$v^*(\phi)$
1	$[0, \phi_1]$	α_1	$v_1, w(\phi; \phi_{TE}, \phi_S, \phi_F, K, \mu, K_H)$
2	$[\phi_1, \phi_2]$	α_2	$v_2, \tilde{v}_2(\tilde{\phi}_2)$
3	$[\phi_2, \phi_3]$	α_3	$v_3, \tilde{v}_3(\tilde{\phi}_3)$
4	$[\phi_3, 2\pi]$	α_4	$v_4, \overline{w}(\phi; \overline{\phi}_{TE}, \overline{\phi}_S, \overline{\phi}_F, \overline{K}, \overline{\mu}, \overline{K}_H)$

2.1.7.3 Numerical Determination of the Mapping

After having satisfied the integral constraints, the functions $v^*(\phi)$ and $\alpha^*(\phi)$ are known and $P(\phi)$ may be formed. Then, through the Poisson integral, $Q(\phi)$ is determined and the airfoil coordinates can be obtained through equation (2.23). Some discussion on the calculation of $Q(\phi)$ from $P(\phi)$ is necessary. Many methods of solution exist in the literature, but the most suitable method is that of Watson (1945) and Garrick (1952) which was subsequently improved by Eppler (1957) for the special circumstances of the present inverse formulation.

As an overview, the methods of Watson and Garrick involve first the approximation of the harmonic function $P(\phi)$ by a truncated Fourier series. Then, through a procedure that amounts to performing two fast-Fourier transforms (Eppler 1990), the conjugate harmonic function $Q(\phi)$ is determined. If $P(\phi)$ is smooth, the fit of the Fourier series is good and the subsequent calculation of $Q(\phi)$ is accurate. If instead $P(\phi)$ has sharp corners, that is, a discontinuity in its slope, the fit of the Fourier series will be poor through the points near the sharp corners and $Q(\phi)$ will show oscillations much like the Gibbs phenomenon. It so happens, as will be shown later, that $P(\phi)$ in the present formulation can have sharp corners, with the one at the leading-edge arc limit usually having the largest slope discontinuity. To take into account these sharp corners, $P(\phi)$ can be decomposed into the sum of a smooth

part and a part containing the sharp corners. The conjugate function $Q(\phi)$ is then simply the sum of the conjugate function to the smooth part (obtained numerically) and the conjugate function to the part containing the sharp corners (obtained analytically). This is the procedure used by Eppler to account for the sharp corner at the leading edge. In the present case, a general procedure is used to take into account all of the sharp corners so as to improve further the numerical accuracy of the calculation of $Q(\phi)$.

To begin with, the harmonic function $P(\phi)$ is expressed as

$$P(\phi) = \overline{P}(\phi) + S(\phi) \tag{2.68}$$

where $\overline{P}(\phi)$ is the smooth part and $S(\phi)$ is the part containing the sharp corners. In order to ensure that $\overline{P}(\phi)$ is smooth the derivative

$$\frac{d\overline{P}(\phi)}{d\phi} = \frac{dP(\phi)}{d\phi} - \frac{dS(\phi)}{d\phi} \tag{2.69}$$

must be continuous. Consider a single sharp corner of $P(\phi)$ located at ϕ_i as indicated in figure 2-8. An infinitesimal distance to the left of ϕ_i, the derivative is expressed as

$$\left.\frac{d\overline{P}(\phi)}{d\phi}\right)^{-} = \left.\frac{dP(\phi)}{d\phi}\right)^{-} - \left.\frac{dS(\phi)}{d\phi}\right)^{-} \tag{2.70a}$$

while to the right

$$\left.\frac{d\overline{P}(\phi)}{d\phi}\right)^{+} = \left.\frac{dP(\phi)}{d\phi}\right)^{+} - \left.\frac{dS(\phi)}{d\phi}\right)^{+} \tag{2.70b}$$

In order for $d\overline{P}(\phi)/d\phi$ to be continuous through ϕ_i, it must be true that

$$\left.\frac{d\overline{P}(\phi)}{d\phi}\right)^{-} = \left.\frac{d\overline{P}(\phi)}{d\phi}\right)^{+} \tag{2.71}$$

or from equations (2.70a,b)

$$\left.\frac{dP(\phi)}{d\phi}\right)^{-} - \left.\frac{dS(\phi)}{d\phi}\right)^{-} = \left.\frac{dP(\phi)}{d\phi}\right)^{+} - \left.\frac{dS(\phi)}{d\phi}\right)^{+} \tag{2.72}$$

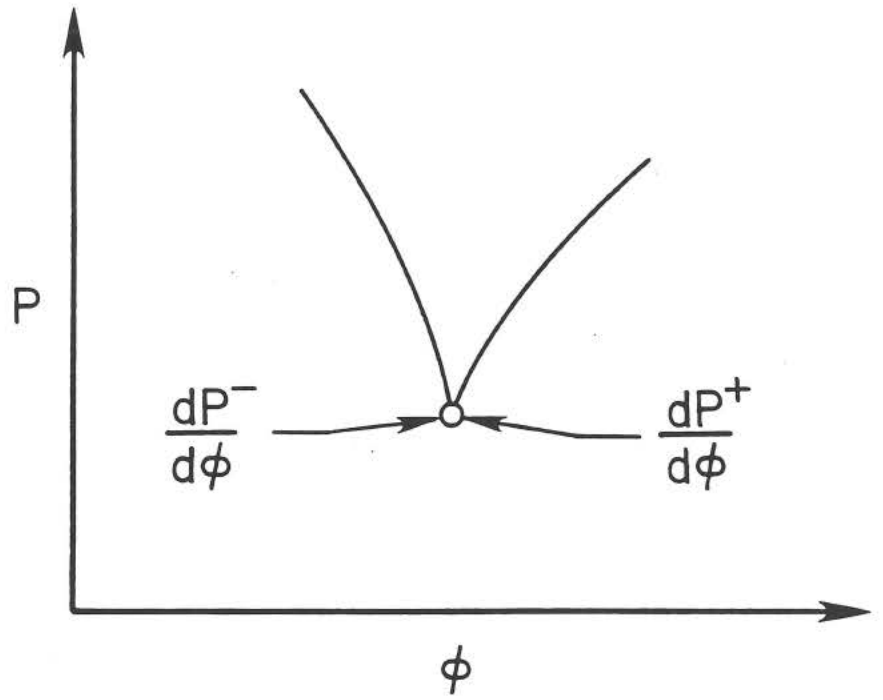

Figure 2-8 Sharp corner of $P(\phi)$ located at ϕ_i and slopes infinitesimally to the left and right of ϕ_i.

Introducing

$$S(\phi) = k \left| \sin\left(\frac{\phi - \phi_i}{2}\right) \right| \tag{2.73}$$

gives

$$\frac{dS(\phi)}{d\phi}\Big)^{-} = -\frac{k}{2}\cos\left(\frac{\phi - \phi_i}{2}\right)\Big|_{\phi=\phi_i} = -\frac{k}{2} \tag{2.74a}$$

and

$$\frac{dS(\phi)}{d\phi}\Big)^{+} = \frac{k}{2}\cos\left(\frac{\phi - \phi_i}{2}\right)\Big|_{\phi=\phi_i} = \frac{k}{2} \tag{2.74b}$$

Thus, the condition for smoothness through the point ϕ_i becomes, from equations (2.74*a*,*b*) and equation (2.72),

$$k = \frac{dP(\phi)}{d\phi}\Big)^{+} - \frac{dP(\phi)}{d\phi}\Big)^{-} \tag{2.75}$$

Considering all sharp corners involves adding more functions of the form of equation (2.73) to equation (2.68) with the constants k determined by equation (2.75). Thus, for M sharp corners, it may be written in general that

$$S(\phi) = \sum_{i=1}^{M} k_i \left| \sin\left(\frac{\phi - \phi_i}{2}\right) \right| \tag{2.76}$$

where

$$k_i = \frac{dP(\phi)}{d\phi}\Big)^{+}_{\phi=\phi_i} - \frac{dP(\phi)}{d\phi}\Big)^{-}_{\phi=\phi_i} \tag{2.77}$$

evaluated at each sharp corner. The location of these sharp corners and the values of the derivative $dP(\phi)/d\phi$ at these locations is determined from equation (2.20) and equations (2.60*a*–*d*) which gives

$$\frac{dP(\phi)}{d\phi} = -\frac{1}{2}\tan(\phi/2 - \alpha^*(\phi)) - \frac{1}{v^*(\phi)}\frac{dv^*(\phi)}{d\phi} - \frac{\mu K}{w_W(\phi)}\frac{\sin\phi}{1+\cos\phi_W}$$

$$-\frac{0.72K_H}{w_S(\phi)}\left[\frac{\cos\phi - \cos\phi_S}{(1-\cos\phi_S)^2}\right]\sin\phi - \frac{\epsilon}{2}\frac{\cos\phi/2}{\sin\phi/2} \tag{2.78}$$

The first term on the right hand side makes a contribution for each segment, and the second term only makes a contribution on the intermediate segments for which $\tilde{v}(\phi)$ is prescribed. The remaining three terms contribute in the recovery region, both for the upper and lower surface, although only the upper-surface terms are expressed for brevity. The third term affects the derivative over the entire recovery region, the fifth only over the closure region, and the fourth only over the finite trailing-edge recovery region.

From equation (2.21), the conjugate harmonic function is given by

$$Q(\phi) = \frac{1}{2\pi}\int_0^{2\pi} P(\psi)\cot\frac{\psi-\phi}{2}\,d\psi \tag{2.79}$$

which through equation (2.68) and (2.76) becomes

$$= \frac{1}{2\pi}\int_0^{2\pi} \overline{P}(\psi)\cot\frac{\psi-\phi}{2}\,d\psi + \sum_{i=1}^{M}\frac{k_i}{2\pi}\int_0^{2\pi}\left|\sin\left(\frac{\phi-\phi_i}{2}\right)\right|\cot\frac{\psi-\phi}{2}\,d\psi \tag{2.80}$$

or

$$= \overline{Q}(\phi) + \sum_{i=1}^{M} T_i(\phi) \tag{2.81}$$

Following Eppler (1957), $\overline{Q}(\phi)$ is determined at $2N$ equiangular values

$$\phi_\nu = \frac{\nu\pi}{N}, \qquad \nu = 0,1,2,\ldots,2N-1 \tag{2.82}$$

from values

$$\overline{P}_\nu = \overline{P}(\phi_\nu) \tag{2.83}$$

by

$$\overline{Q}_\nu = \overline{Q}(\phi_\nu) = \frac{1}{N}\sum_{\mu=1}^{N-1}(\overline{P}_{\nu+\mu} - \overline{P}_{\nu-\mu})\cot\frac{\mu\pi}{2N}, \qquad \mu = \text{ odd values only} \tag{2.84}$$

The conjugate harmonic functions T_i are given analytically by

$$T_i(\phi) = -\frac{2k_i}{\pi}\sin\left(\frac{\phi-\phi_i}{2}\right)\ln\left|\tan\left(\frac{\phi-\phi_i}{4}\right)\right| \tag{2.85}$$

which can be evaluated at the values ϕ_ν to give $T_{\nu\,i}$. Finally

$$Q_\nu = \overline{Q}_\nu + \sum_{i=1}^{M} T_{\nu\,i} \tag{2.86}$$

which, together with P_ν, is used to find the airfoil coordinates.

2.1.8 An Example Airfoil

As an example of the method, a simple four-segment airfoil with a cusped trailing edge is presented. This airfoil and the others that follow in section 2.1.9 are not intended for any practical application; rather, they merely serve as examples to illustrate the capabilities of the method. After specifying $\epsilon = 0$ to give a cusped trailing edge, together with everything listed in table 2-1 except the seven unknowns, equations (2.66) and (2.67) can be solved. The solution yields μ, $\overline{\mu}$, K_H and $\overline{K}_H$ such that the recovery functions $w(\phi)$ and $\overline{w}(\phi)$, plotted in figure 2-9 (a), are defined completely. Also shown in figure 2-9 (a) are the prescribed relative velocity functions $\tilde{v}_2(\tilde{\phi}_2)$ and $\tilde{v}_3(\tilde{\phi}_3)$ satisfying the requirement that $\tilde{v}_i(\tilde{\phi}_i = 0) = 0$. The velocity function $\tilde{v}_2(\tilde{\phi}_2)$ is defined by a cubic spline of four points, and $\tilde{v}_3(\tilde{\phi}_3)$ is prescribed as linear. With $w(\phi)$, $\tilde{v}_2(\tilde{\phi}_2)$, $\tilde{v}_3(\tilde{\phi}_3)$ and $\overline{w}(\phi)$ known and v_2, v_3 and v_4 found from the solution of the system, the complete design velocity distribution $v^*(\phi)$, shown in figure 2-9 (b), is obtained. Through equation (2.20), $\alpha^*(\phi)$ and $v^*(\phi)$ are used to form $P(\phi)$ which is plotted in figure 2-10. The jumps in $\alpha^*(\phi)$ which are compensated by jumps in $v^*(\phi)$, such that $P(\phi)$ remains continuous, are seen in figures 2-9 (b), 2-9 (c) and 2-10. As determined by the method discussed in section 2.1.7.3, the conjugate harmonic function $Q(\phi)$ is found and is also shown in figure 2-10. Airfoil coordinates are then computed using $P(\phi)$ and $Q(\phi)$. The airfoil profile together with the velocity distributions at $\alpha = 0°$, $5°$, $10°$ and $15°$ are shown in figure 2-11.

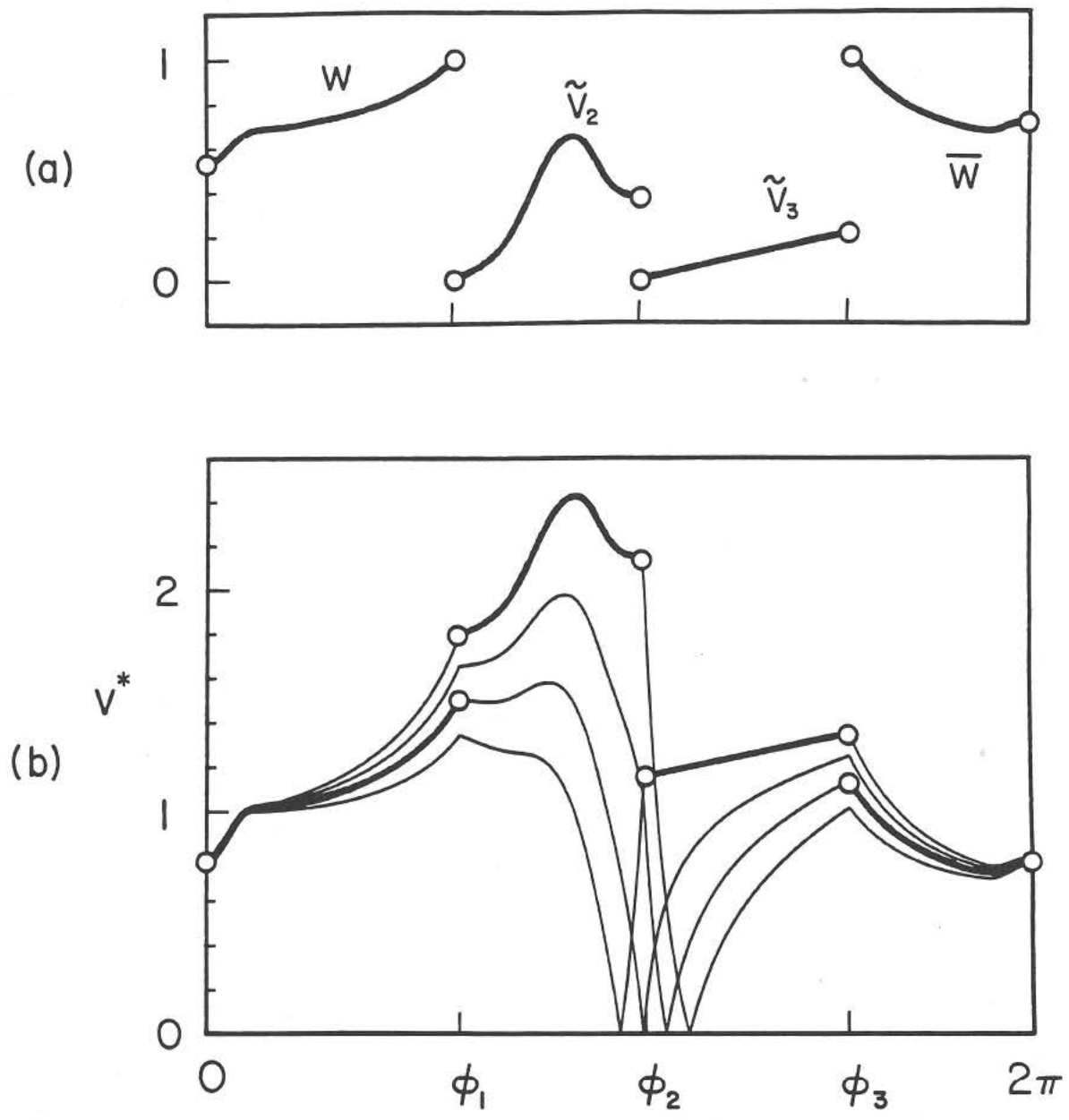

Figure 2-9 Special velocity functions and design velocity and angle of attack distributions for a four-segment airfoil.

(figure continues)

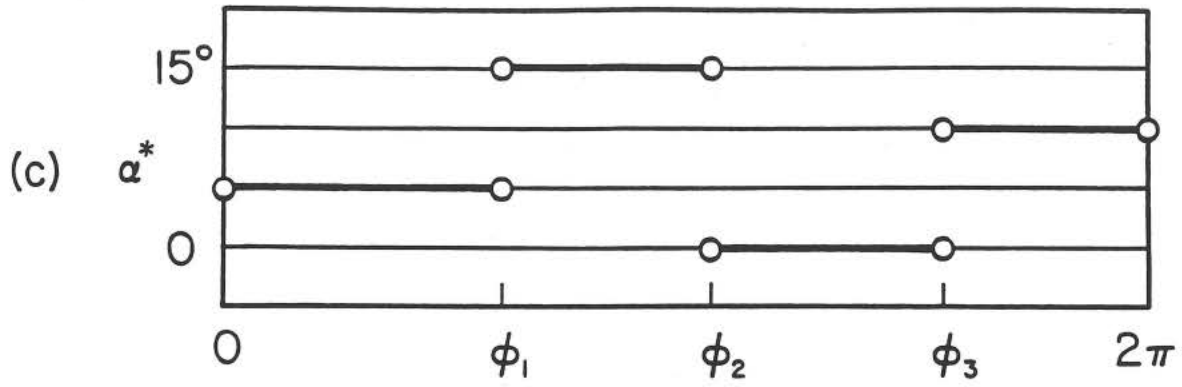

Figure 2-9 Continued.

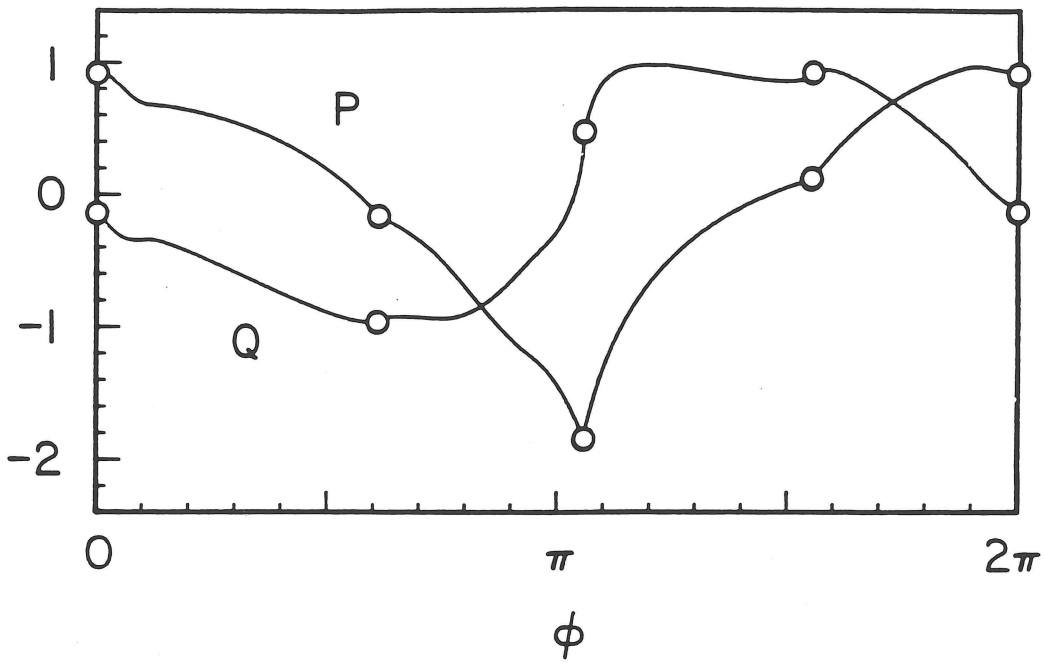

Figure 2-10 Harmonic functions $P(\phi)$ and $Q(\phi)$.

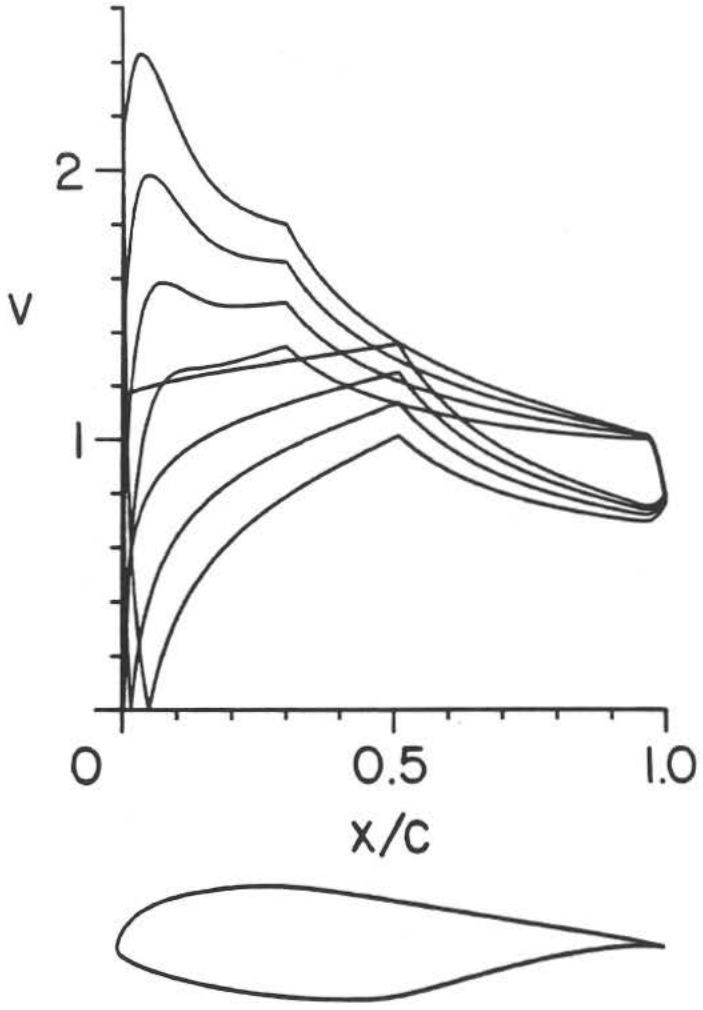

Figure 2-11 Airfoil and velocity distributions at $\alpha = 0°$, 5°, 10°, and 15°.

To serve as a check on the numerical implementation of the theory, an airfoil designed by the method can be analyzed for its velocity distributions to see if they match the velocity distribution used in the inverse method to derive the airfoil shape. For analysis, the Eppler program (Eppler and Somers 1980*a*; Eppler 1988, 1990) is used. The panel method employs parabolically distributed vorticity and satisfies the boundary conditions at the panel end points with high-order approximations used for the influence of panel vorticity on itself. To verify the code predictions, the velocity distribution for a Joukowski airfoil (generated using a circle offset of $\mu = -0.08 + i\,0.06$) was predicted for $\alpha = 6°$ and is compared with the exact solution in figure 2-12. Using double precision, the agreement is quite good with an RMS difference of 0.000449, where RMS $= \sqrt{\sum_{i=1}^{N}(v_{1_i} - v_{2_i})^2/N}$. In this case, v_{1_i} refers to the velocity at a point on the Joukowski airfoil, and v_{2_i} is the velocity as predicted by the panel-method analysis. In figure 2-13, the velocity distributions at $\alpha = 0°$, $5°$, $10°$ and $15°$ for the airfoil shown in figure 2-11 are compared with predictions from the panel method. Again, the agreement is quite good with RMS differences of 0.000139, 0.000138, 0.000136 and 0.000133 for $\alpha = 0°$, $5°$, $10°$ and $15°$, respectively.

2.1.9 Example Airfoils with Multi-Dimensional Newton Iteration

Fundamentally, it is required for the inverse problem that the design velocity distribution $v^*(\phi)$ and design angle of attack distribution $\alpha^*(\phi)$ satisfy the integral constraints, continuity constraints and stagnation point velocity relations. In the design of any practical airfoil, however, additional requirements are usually imposed. For example, the airfoil thickness ratio and pitching moment may be prescribed, and the airfoil certainly must not cross over itself. Also, it may be desirable to specify the velocity distribution as a function of the arc length s. Furthermore, as discussed

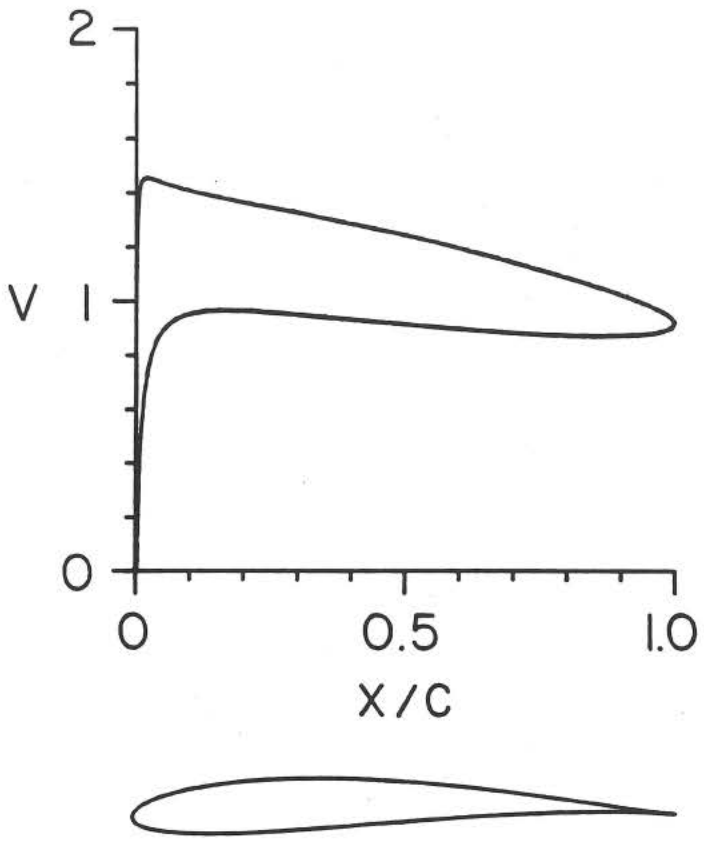

Figure 2-12 Comparison between an exact Joukowski airfoil velocity distribution and that predicted by the Eppler program for $\alpha = 6°$.

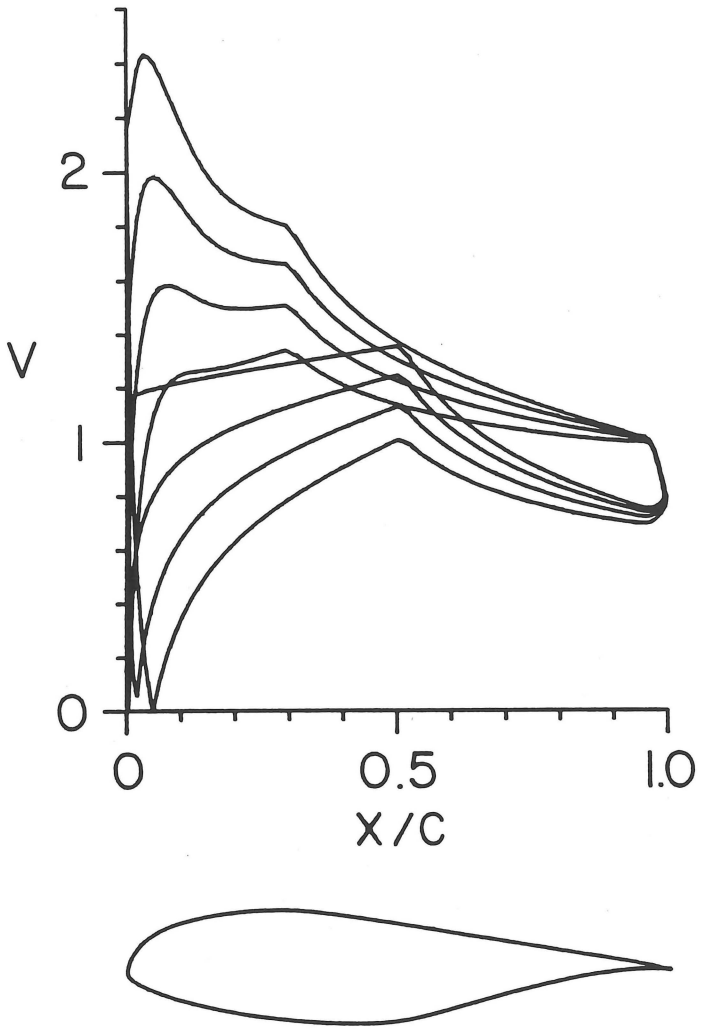

Figure 2-13 Velocity distributions as predicted by the Eppler program and compared with inverse solution for the airfoil shown in figure 2-11.

in Chapter 1, it is usually desirable to specify the boundary-layer development in order to control performance.

For the purpose of discussion, consider the case where a desired zero-lift pitching-moment coefficient is to be achieved. From equations (2.48) and (2.39b), it is then necessary to satisfy the equation

$$c_{m_0} = \frac{4}{c^2} \int_0^{2\pi} P(\phi) \sin 2\phi \, d\phi \tag{2.87}$$

where the value of c_{m_0} is given. This equation represents an additional integral constraint which $P(\phi)$ must then satisfy. Thus, an additional inverse design parameter (from table 2-1) must be relaxed to satisfy the system of equations which now includes the integral constraints, continuity constraints and pitching-moment equation (2.87).

Crossed airfoils are not excluded from the solution in any closed-form mathematical way. Figures 2-14(a,b), for example, show an airfoil which was designed to have a constant velocity along the forward upper surface at 15° and a constant velocity along the forward lower surface at 0°. Even though the airfoil satisfies all the fundamental conditions, the airfoil is crossed. The problem stems from the high, trailing-edge velocity ratio. By empirical observation, the trailing-edge velocity ratio of finite-thickness, uncrossed airfoils is always less than one. Many inverse methods make use of this fact and allow for the adjustment of an inverse design parameter in order to match a specified trailing-edge velocity ratio. One shortcoming of this approach is that thicker airfoils generally have lower trailing-edge velocities than thinner ones, but the airfoil thickness is not known a priori, thereby making it difficult to preassign the proper trailing-edge velocity ratio. Also, the specification of the trailing-edge velocity ratio is not a viable option for the design of airfoils having a finite trailing-edge angle for which the trailing-edge velocity is always zero.

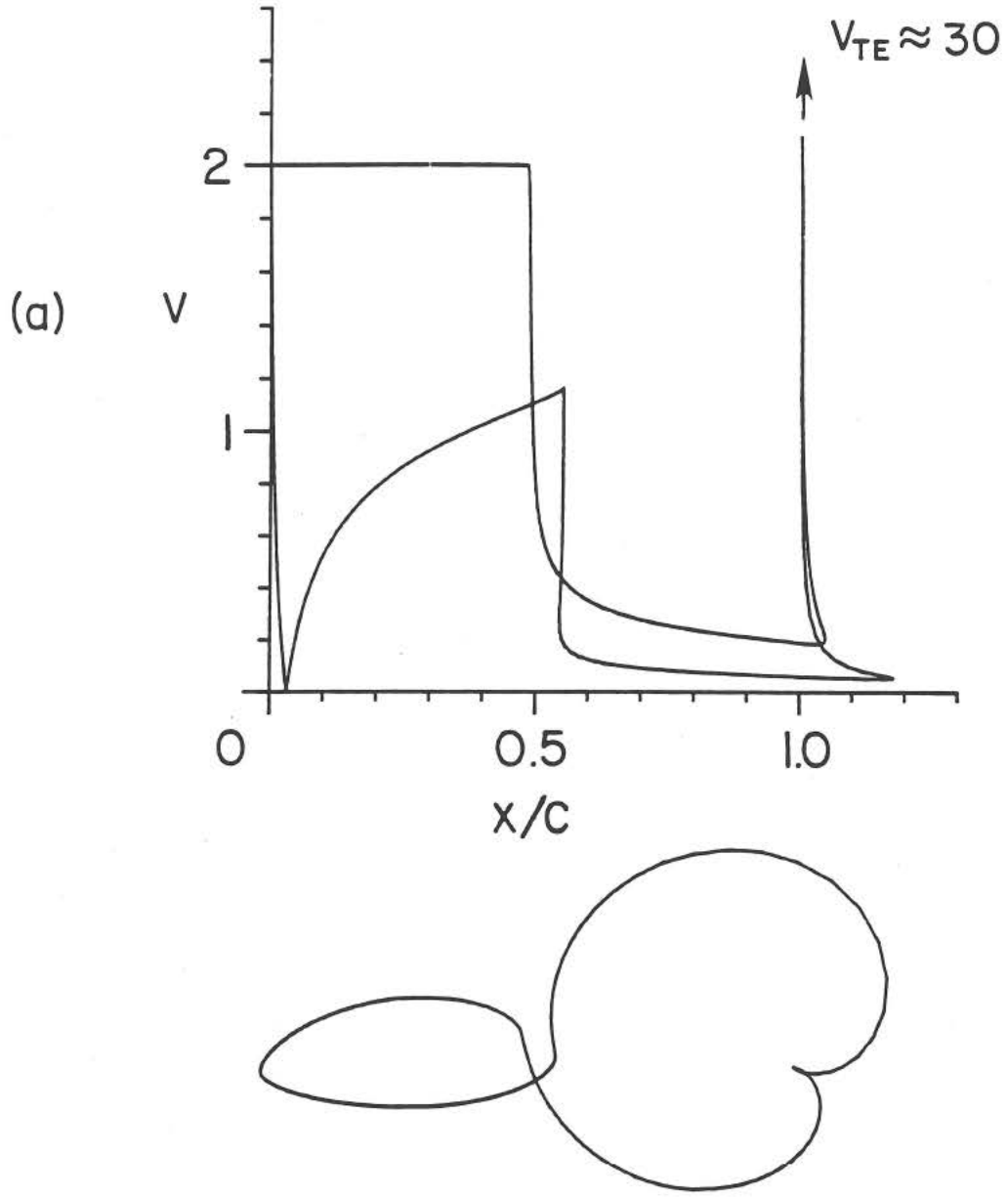

Figure 2-14 Example of a crossed airfoil with high trailing-edge velocity ratio for (a) $\alpha = 15°$ and (b) $\alpha = 0°$.

(figure continues)

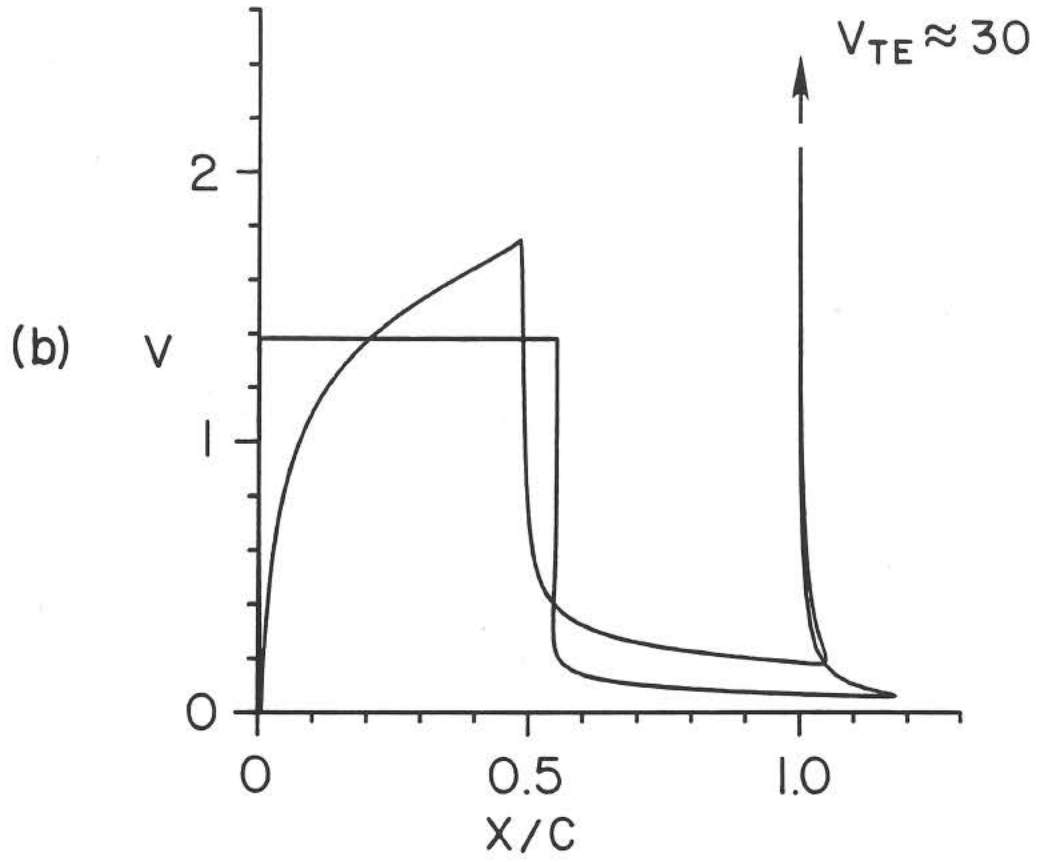

Figure 2-14 Continued.

Besides the value of the trailing-edge velocity ratio, much can be deduced from the character of the velocity distribution in the vicinity of the trailing edge. Figure 2-15 shows the trailing-edge velocity distribution and the trailing-edge shape for three, symmetric, 8% thick, cusped airfoils at 5° angle of attack. Only the last 25% of chord is shown, and the vertical y/c-scale has been expanded to five times that of the x/c-scale. The trend is that the larger the drop in velocity (i.e. pressure recovery) at the trailing edge, the thicker the airfoil in the vicinity of the trailing edge (e.g, case *a*). If there is no drop in the velocity, the trailing edge is very thin (e.g., case *b*). If the velocity shows an increase, the airfoil is usually crossed (e.g., case *c* and case shown in figure 2-14). While these comments are specific to symmetric airfoils such as those shown in figure 2-15, the same trends are observed for non-symmetric airfoils as long as the *net* velocity drop is considered. For example, if the velocity decreases on the upper surface by the same amount that it increases on the lower surface, there is a zero net velocity drop, and the airfoil will in such instance be thin at the trailing edge.

The trend just identified must be translated into an equation if crossed airfoils are to be avoided in the design process. The high, trailing-edge velocity ratio for the airfoil shown in figure 2-14 is produced by the large negative values of K_H ($K_H = -12.62$) and $\overline{K}_H$ ($\overline{K}_H = -16.64$) which control the closure recovery functions $w_S^{K_H}(\phi)$ and $\overline{w}_S^{\overline{K}_H}(\phi)$. If K_H and $\overline{K}_H$ are small positive quantities (for example, 0.2), then the trailing-edge velocity distribution will decrease slightly as shown in figure 2-15 (*a*). If they are both zero, there will be no decrease or increase in the velocity as shown in figure 2-15 (*b*). For negative values, the velocity will increase—figure 2-15 (*c*) being a mild case and figure 2-14 (*a*) extreme.

Practical experience has shown that normal trailing-edge velocity distributions

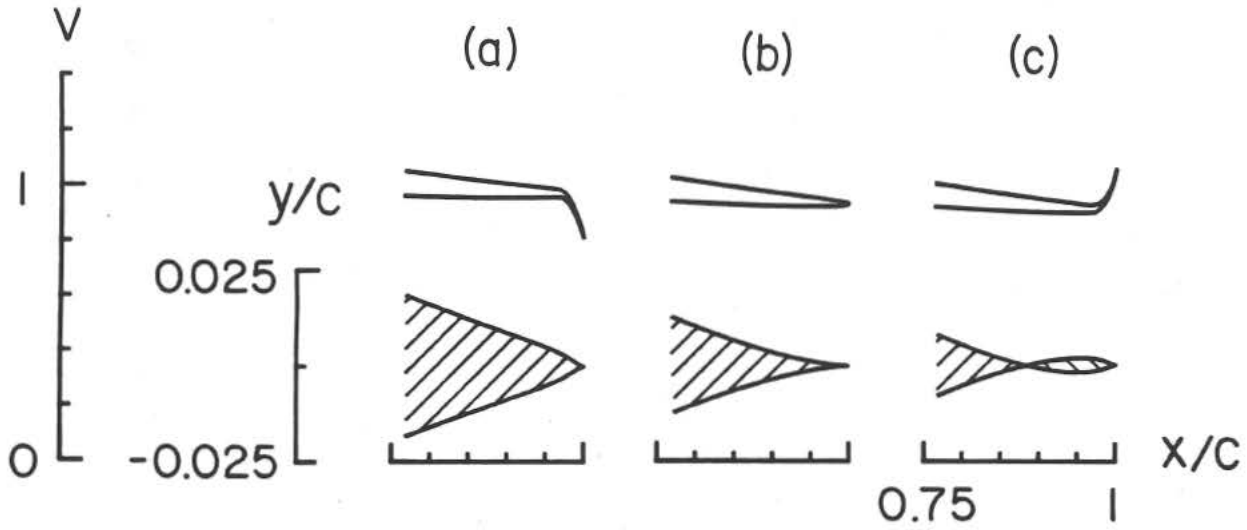

Figure 2-15 Impact of the trailing-edge velocity distribution on the shape of the trailing edge.

are determined not so much by the individual values of K_H and $\overline{K}_H$ but by their sum $K_H + \overline{K}_H$. If the sum is in the range 0.0 to 0.8, normal trailing-edge shapes are produced—the smaller the sum in this range, the thinner the airfoil in the vicinity of the trailing edge. Thus, as in the Eppler method (1957, 1990),

$$K_S = K_H + \overline{K}_H \tag{2.88}$$

serves as a useful equation to control the trailing-edge velocity distribution. Thus, by specification of K_S, crossed airfoils can be avoided and a desired trailing-edge thickness can be achieved.

If an airfoil is to have a specified trailing-edge thickness parameter K_S and zero-lift pitching-moment coefficient, the system of equations includes the integral constraints (three equations), the continuity constraints (four equations for a four-segment airfoil) and equations (2.87) and (2.88). Since there are now two additional equations, two more parameters (in addition to μ, $\overline{\mu}$, K_H, $\overline{K}_H$ and all v_i's except one) must be identified as unknowns. It might be possible to select parameters from table 2-1 or introduce new parameters which would allow the system of equations to be solved directly without recourse to iteration, but, as more equations are added to the system (as will be demonstrated), this rapidly reaches a point of diminishing returns. It is best to resort immediately to an iterative solution technique. To this end, multi-dimensional Newton iteration is used.

For a prescribed K_S and c_{m_0}, equations (2.87) and (2.88) are represented as

$$R_1 = K_S - (K_H + \overline{K}_H) \tag{2.89a}$$

$$R_2 = c_{m_0} - \frac{4}{c^2} \int_0^{2\pi} P(\phi) \sin 2\phi \, d\phi \tag{2.89b}$$

where R_1 and R_2 are the residues which are driven to zero by Newton iteration on parameters U_1 and U_2 taken from the inverse design parameters listed in table 2-1.

For each additional quantity prescribed, there will be an additional residue equation R_i and a parameter U_i admitted for iteration. In general, it is desired that

$$\vec{R}(\vec{U}) = 0 \tag{2.90}$$

Taylor series expansion of $\vec{R}(\vec{U})$ gives

$$\vec{R}(\vec{U})^{n+1} = \vec{R}(\vec{U})^n + \delta\vec{U}\left[\frac{\partial\vec{R}}{\partial\vec{U}}\right]^n + \frac{1}{2}\delta\vec{U}^2\left[\frac{\partial^2\vec{R}}{\partial\vec{U}^2}\right]^n + \cdots \tag{2.91}$$

where n is the current solution and $n+1$ is the solution after the step $\delta\vec{U}$. Neglect of all terms higher than first order and taking $\vec{R}(\vec{U})^{n+1} = 0$ as desired gives

$$\left[\frac{\partial\vec{R}}{\partial\vec{U}}\right]^n \delta\vec{U} = -\vec{R}(\vec{U})^n \tag{2.92}$$

This may be solved to give $\delta\vec{U}$ which may then be used to update the solution

$$\vec{U}^{n+1} = \vec{U}^n + \omega\,\delta\vec{U} \tag{2.93}$$

where ω is a relaxation factor to be discussed later. Based on this solution vector $\vec{U}^{n+1}$, the residue $\vec{R}(\vec{U})^{n+1}$ can be evaluated to see if it is within a prespecified tolerance. If $\vec{R}(\vec{U})^{n+1}$ is not within the tolerance, $\vec{U}^n$ and $\vec{R}(\vec{U})^n$ are replaced by $\vec{U}^{n+1}$ and $\vec{R}(\vec{U})^{n+1}$ and the process is repeated until the tolerance is achieved.

The iteration process begins by adding a small perturbation sequentially to each of the selected inverse design parameters used for iteration. The basic inverse equations (2.66) and (2.67) are then solved after which the residues are evaluated. The change in the residues is monitored to form the Jacobian $\partial\vec{R}/\partial\vec{U}$ which is then used to find the step size $\delta\vec{U}$. If the Newton scheme attempts to take a step $\delta\vec{U}$ which is too large, the convergence of the solution can be disrupted. To prevent this from happening, a maximum step size for any of the unknowns $\vec{U}$ can be preset.

If any of the predicted step sizes at any point in the iteration exceeds a preset maximum (a maximum which is determined through experience with the method), then a fractional step ($\omega\,\delta\vec{U}$) is taken to avoid exceeding a maximum. Another detail is that in the design of a new airfoil, the iterative process is taken in stages. In a typical case, K_S is first satisfied in order for the airfoil to be uncrossed. Then c_{m_0} is sometimes specified to bring the airfoil into a normal range. After this, any additional Newton equations may be added in a logical order.

The Newton iteration process is depicted schematically in figures 2-16 (a–c). The basic approach is shown in figure 2-16 (a). Figure 2-16 (b) details the method used to determine the Jacobian, and figure 2-16 (c) details the check for convergence.

To demonstrate the capability of the Newton iteration procedure, an airfoil is to be designed such that $K_S = 0.5$ (to produce an uncrossed and normal trailing-edge shape), $c_{m_0} = -0.2$ and $t/c = 15\%$. The airfoil shown in figure 2-14 is used as the first guess in the Newton iteration procedure. As mentioned, the process is taken in stages, the first of which is to satisfy $K_S = 0.5$ so that the airfoil becomes uncrossed. This is done by iterating on the leading-edge arc limit ϕ_2 to result in the airfoil shown in figure 2-17 (a). Next the arc limit ϕ_2 and velocity level v_1 are iterated together to produce an airfoil with $K_S = 0.5$ and $c_{m_0} = -0.2$, as shown in figure 2-17 (b).

Before the desired maximum-thickness ratio t/c is achieved, some remarks should be made regarding the choice of the parameters ϕ_2 and v_1 used for iteration. The value of the leading-edge arc limit ϕ_2 is related indirectly to the range over which the leading-edge stagnation point moves for normal angles of attack. It is well known (e.g., Eppler 1957, 1990; Liebeck 1990) that the leading-edge stagnation point has a dramatic effect on whether or not the airfoil crosses. Consequently, ϕ_2 is selected as

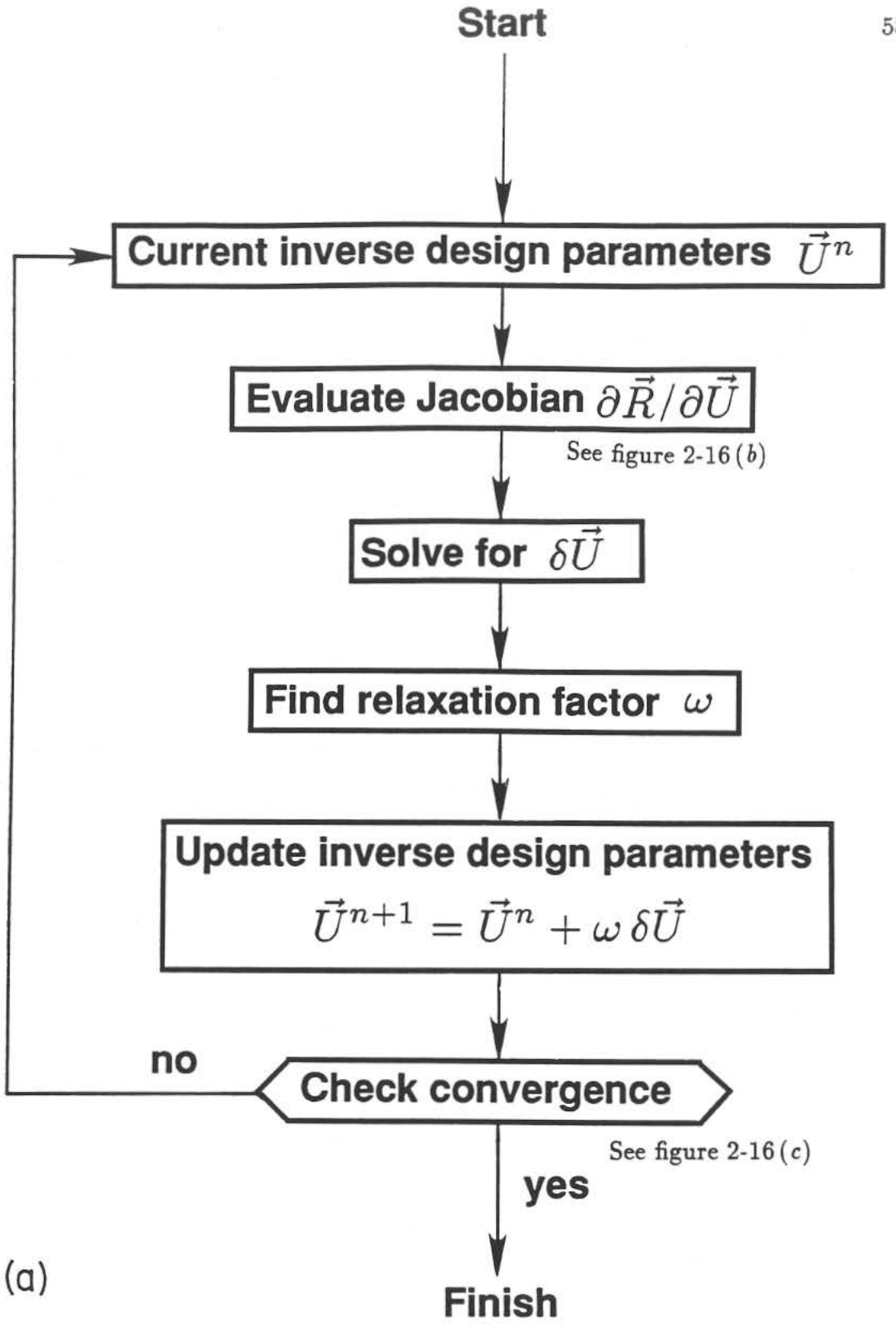

Figure 2-16 Flow chart for Newton iteration: (*a*) basic approach, (*b*) determination of the Jacobian and (*c*) check for convergence.

(figure continues)

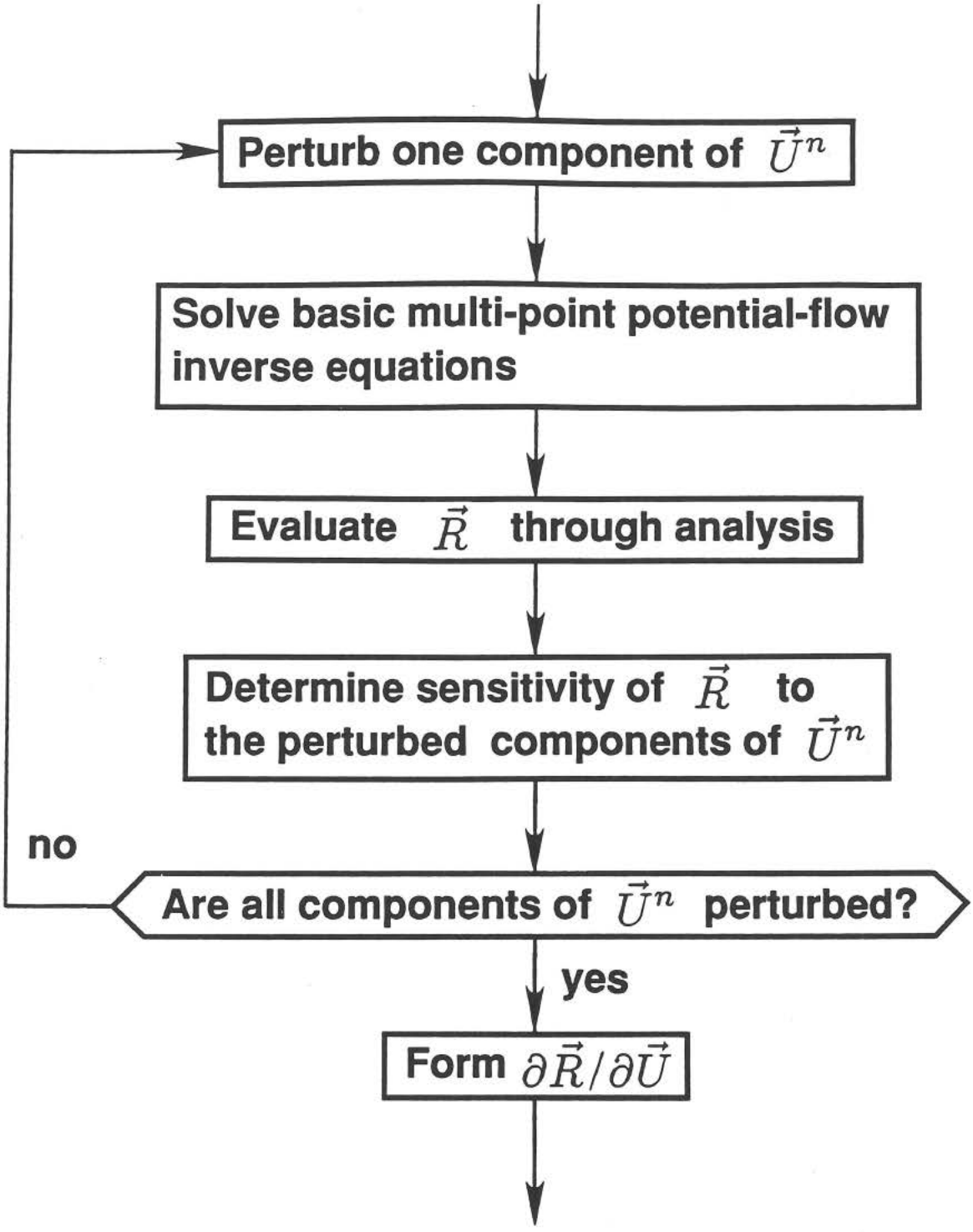

(b)

Figure 2-16 Continued.

(figure continues)

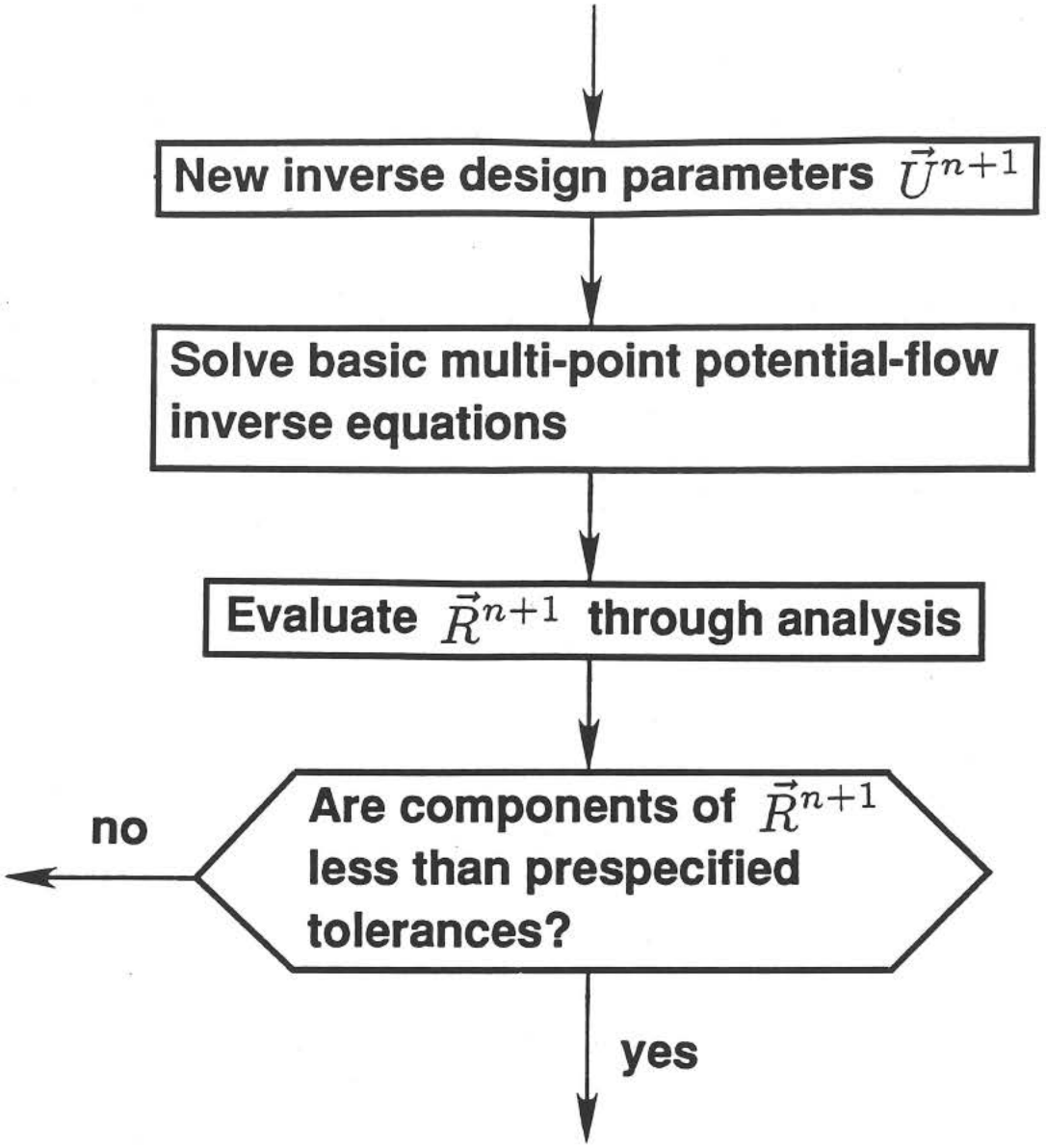

(c)

Figure 2-16 Continued.

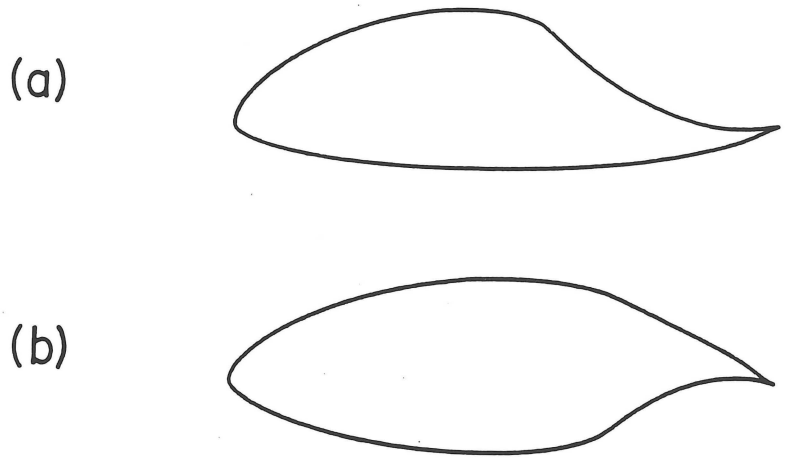

Figure 2-17 Airfoils produced by specifying (a) $K_S = 0.5$, and (b) $K_S = 0.5$, $c_{m_0} = -0.2$.

the parameter to control the trailing-edge thickness parameter K_S. The effect of v_1 on the pitching-moment can be explained by realizing that the adjustment of v_1, in turn, affects all the velocity levels v_2, v_3 and v_4 through equations (2.67*a*–*c*). That is, iteration on the one prescribed velocity level implies having no control over the level of the velocity anywhere. Low-pitching moment airfoils (e.g., Liebeck 1970) are characterized by having a high upper-surface velocity along the forward part of the airfoil, while on the other hand, high-pitching moment airfoils (e.g., Somers 1992) have, in comparison, a relatively low upper-surface velocity along the forward part of the airfoil. This connection between the velocity and the pitching moment is employed by iterating on the one prescribed velocity level to achieve a desired pitching-moment coefficient.

In order to obtain the desired thickness ratio of 15%, it is necessary to identify an inverse design parameter which affects the thickness. For the airfoil shown in figure 2-17(*b*), the forward upper-surface and lower-surface velocity distributions were prescribed to be constant for angles of attack of 0° and 15°, respectively. An increase in the angle of attack above 15° will produce an increasingly severe suction peak on the upper surface at the leading edge which will eventually result in flow separation and stall. Likewise, a decrease in the angle of attack below 0° will produce a suction peak on the lower-surface leading edge, giving rise to flow separation and shortly thereafter negative stall. In approximate terms, the airfoil has a useable operating range from 0° to 15°. A decrease in the upper-surface design angle of attack by 2° to 13° and an increase in the lower-surface design angle of attack by 2° to 2° (while still satisfying $K_S = 0.5$ and $c_{m_0} = -.02$) results in the airfoil shown in figure 2-18. From the foregoing discussion, it follows that this new airfoil will have a useable range from only 2° to 13°. By comparison, this

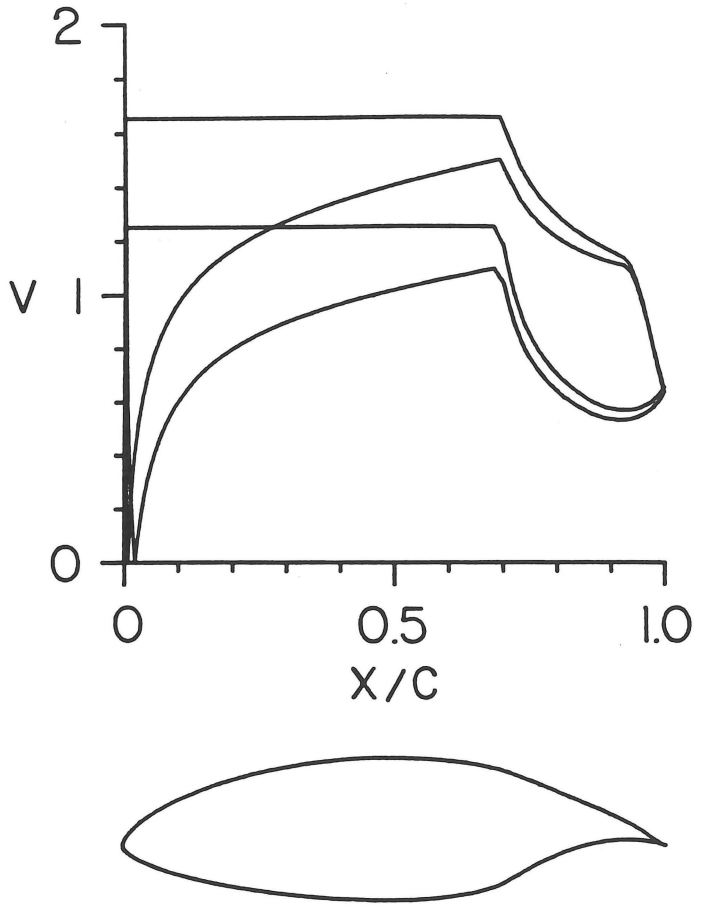

Figure 2-18 Airfoil derived from that shown in figure 2-17(*b*) with different design angles of attack for the upper and lower surfaces.

new airfoil has a narrower operating range and is thinner than the one shown in figure 2-17 (b)—26.4% vs. 32.4%. Consequently, the design angles of attack (which determine the operating range) may be used for iteration to achieve the desired maximum-thickness ratio. In particular, the thickness ratio is obtained by adding an increment $\delta\alpha$ to the upper-surface design angles of attack and subtracting the same increment from the lower-surface design angles of attack. With this approach, the 32.4% thick airfoil shown in figure 2-17 (b) may be modified by iteration on the design angles of attack in the opposite fashion as mentioned in order to produce the desired 15% thick airfoil as shown in figure 2-19.

The Newton iteration procedure is also employed to locate a segment junction in x_i/c and to allow specification of the design velocity distribution in arc length s. In order to specify an x_i/c location (for instance, the beginning of the recovery), the corresponding arc limit ϕ_i is used for iteration. Explicit specification of the velocity distribution $v(s)$ for a segment would be inconsistent with the inverse formulation as presented [equations (2.60a–b)]. Equations (2.67a–c) determine the value of the velocity at the beginning of each segment so it cannot be directly prescribed. Furthermore, the arc length s along a segment is determined as part of the solution. It is consistent, however, to prescribe the relative design velocity $\tilde{v}_i(\tilde{s}_i)$ subject to the condition $\tilde{v}_i(\tilde{s}_i = 0) = 0$ since $\tilde{v}_i(\tilde{\phi}_i = 0) = 0$. A desired distribution $\tilde{v}_i(\tilde{s}_i)$ is obtained through iteration on $\tilde{v}_i(\tilde{\phi}_i)$. The distribution $\tilde{v}_i(\tilde{s}_i)$ is satisfied at collocation points in $\tilde{\phi}_i$ for the particular segment as indicated in figure 2-7. Each collocation point thereby gives rise to another equation in the Newton system. As a practical matter, the relative arc length $\tilde{s}_i$ is normalized by the airfoil chord. The collocation points defining $\tilde{v}_i(\tilde{\phi}_i)$ and employed in the Newton iteration are specified as a percentage of the length of the segment $\phi_i - \phi_{i-1}$. This prescription

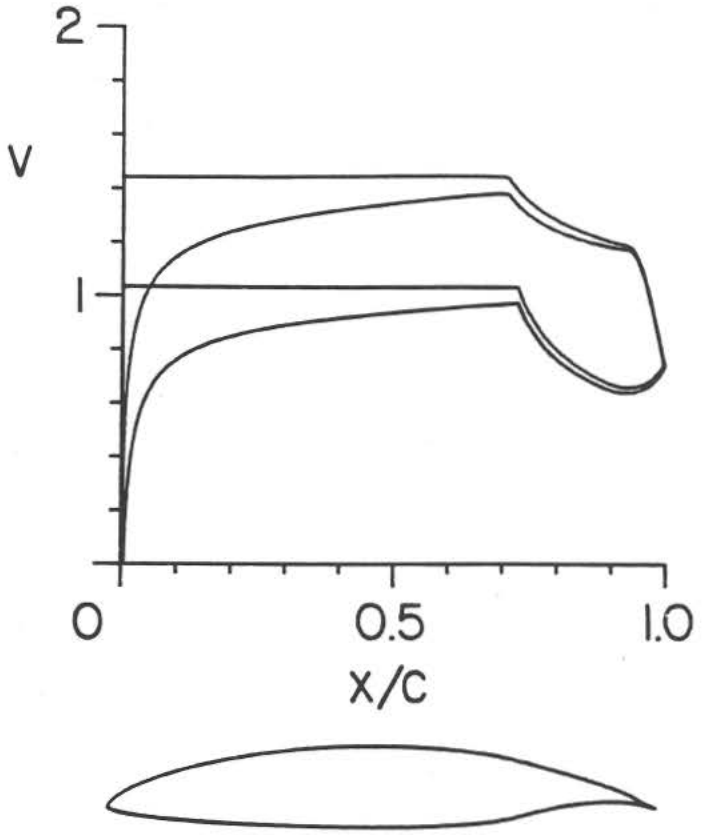

Figure 2-19 Airfoil with $K_S = 0.5$, $c_{m_0} = -0.2$, and $t/c = 15\%$ at $\alpha = 9.96°$ and $5.04°$.

on a percentage basis is necessary since iteration on an arc limit ϕ_i or ϕ_{i-1} will change the length of the segment i.

Another example is presented to illustrate the capability of prescribing the chordwise locations x_i/c and velocity distribution $\tilde{v}_i(\tilde{s}_i)$. For the second and third segments, it is desired that $\tilde{v}_2(\tilde{s}_2) = -0.50\tilde{s}_2$ and $\tilde{v}_3(\tilde{s}_3) = 0.25\tilde{s}_3$, respectively. The upper-surface and lower-surface recovery are prescribed to begin at 50% and 40% of chord, respectively. The airfoil is further constrained by specification of $K_S = 0.3$, $c_{m_0} = -0.05$ and $t/c = 25\%$. Lastly, the trailing-edge angle is specified to be 10° or $\epsilon = 1/18$. Of course, since ϵ appears explicitly in the equations, achievement of a particular trailing-edge angle does not require any iteration. To meet these design goals, iteration is performed on the limits ϕ_1, ϕ_2, ϕ_3, the velocity level v_1, the design angles of attack α_i through $\delta\alpha$ (as previously described) and the relative design velocity distributions $\tilde{v}_2(\tilde{\phi}_2)$ and $\tilde{v}_3(\tilde{\phi}_3)$. Figures 2-20 (*a,b*) show the final velocity distributions at the resulting design angles of attack of 1.20° and 11.80°. As expected, the finite trailing-edge angle leads to zero velocity at the trailing edge. As depicted in figure 2-20 (*b*), showing $v(s)$, the desired relative velocity distributions $\tilde{v}_2(\tilde{s}_2)$ and $\tilde{v}_3(\tilde{s}_3)$ are achieved. The arc length and relative arc lengths are normalized by the airfoil chord giving $s_{max}/c = 2.1$. In figure 2-21, the airfoil profile and velocity distributions show that the desired recovery locations are obtained. Finally, K_S, c_{m_0} and t/c also match the design specifications.

Some further remarks should be made regarding the choice of the inverse design parameters used for iteration in order to achieve a set of airfoil characteristics. In the design of any new airfoil, K_S is usually prescribed to produce an uncrossed airfoil. As in the examples presented, the leading-edge arc limit can usually be iterated to drive K_S to the desired value. Alternatively, however, the single prescribed

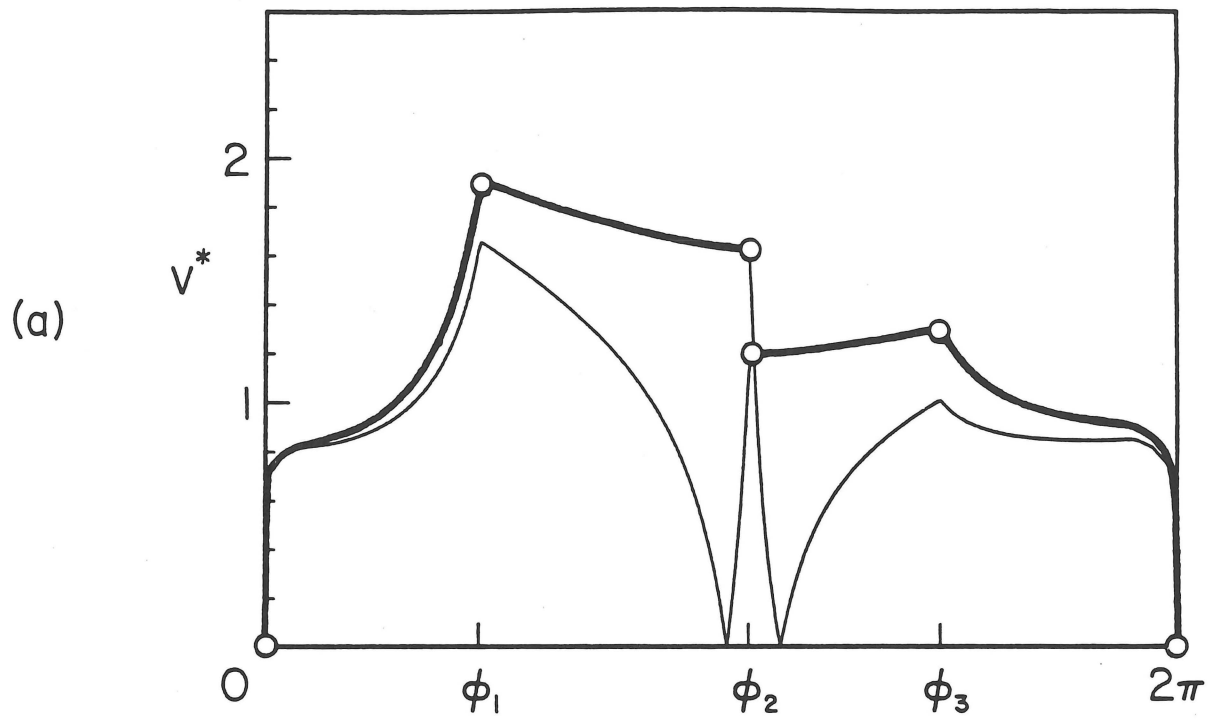

Figure 2-20 Velocity distributions at $\alpha = 1.2°$ and $11.8°$ as a function of (*a*) ϕ and (*b*) s/c.

(figure continues)

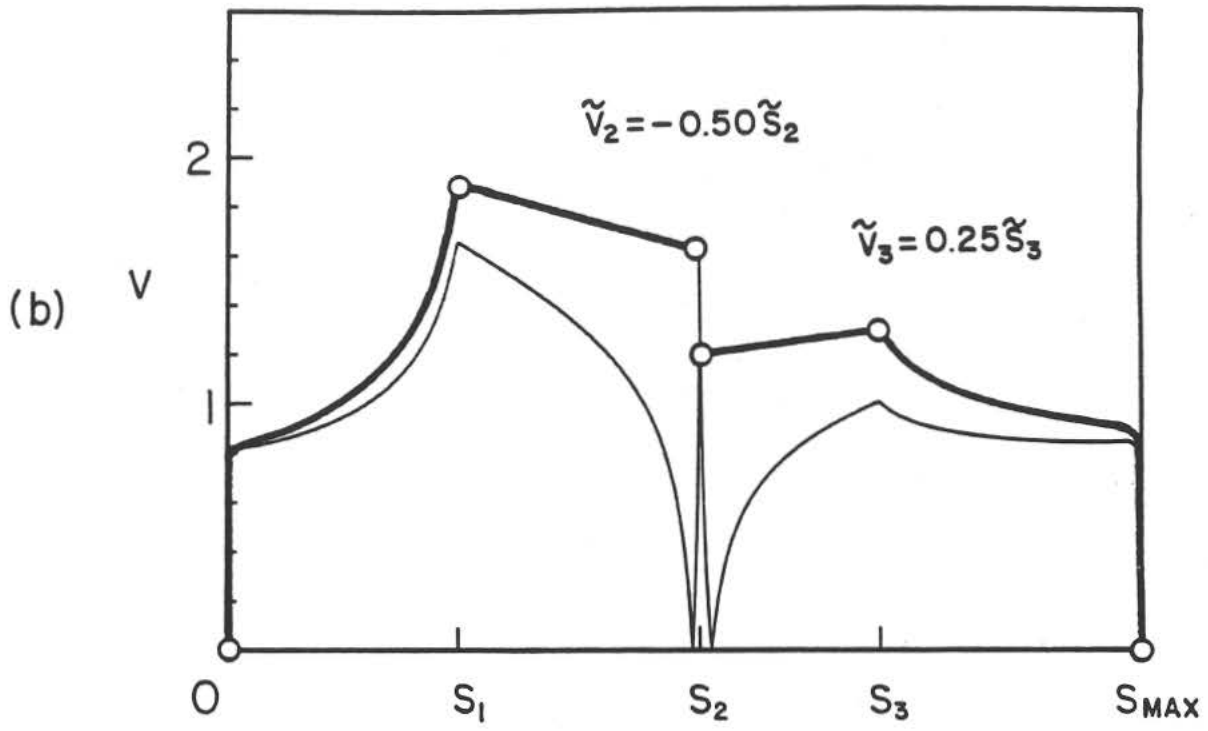

Figure 2-20 Continued.

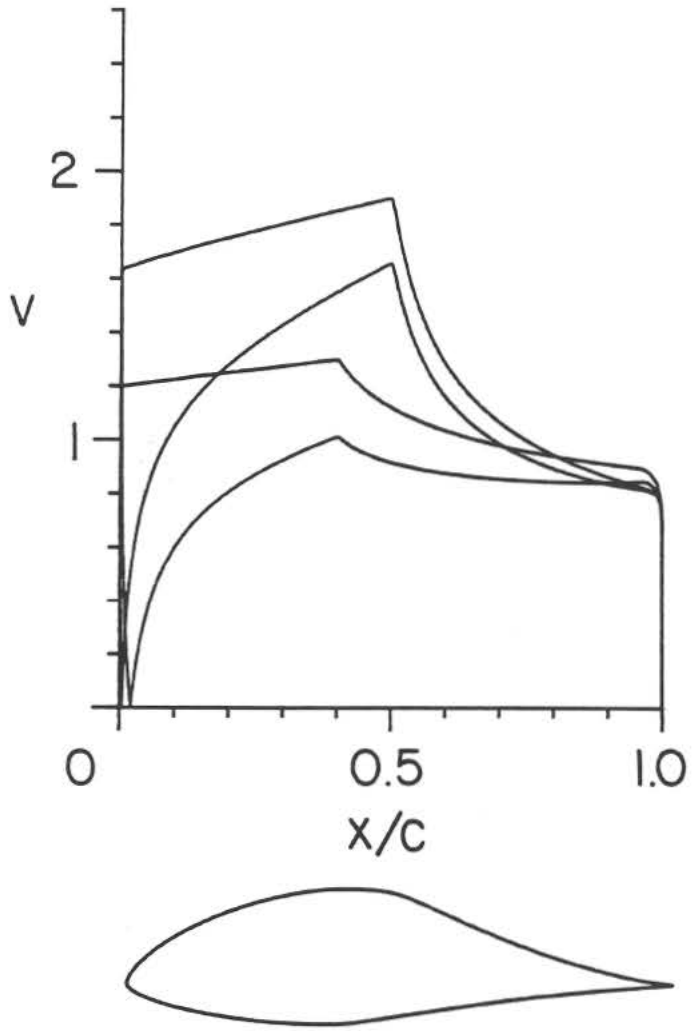

Figure 2-21 Airfoil and velocity distributions at $\alpha = 1.2°$ and $11.8°$.

velocity level or any, all, or part of the design angles of attack may be iterated in an attempt to achieve the desired K_S. Options are also included to change the slope of $\tilde{v}_i(\tilde{\phi}_i)$ along a segment or several segments. Iteration for prescribed thickness ratio or pitching moment is usually successful through adjustments in the velocity level or design angles of attack as shown. Several other options are available, however. The use of $\tilde{v}_i(\tilde{\phi}_i)$ to achieve a given $\tilde{v}_i(\tilde{s}_i)$ is necessary. Also, if a segment junction is to have a specified x_i/c location, the corresponding segment arc limit ϕ_i must be iterated. As a final remark, if the specified design requirements are realistic, convergence is usually assured so long as an appropriate set of inverse design parameters is used for the iteration. In this regard, going in stages, starting with the achievement of the desired K_S, then c_{m_0}, etc., often provides valuable insight into potentially conflicting design requirements and helps to determine which inverse design parameters are best suited for iteration.

2.2 THE VISCOUS DESIGN PROBLEM

2.2.1 Formulation of the Problem

Several schemes have been devised to achieve a desired velocity distribution, but, to achieve a desired boundary-layer development, there are only two common approaches. One approach (e.g., Liebeck 1976; Henderson 1978; Goettsching 1988) is to use an inverse boundary-layer method to determine the velocity distribution which yields the desired boundary-layer development, typically the shape-factor or the skin-friction distribution. The resulting velocity distribution is then used as input to a potential-flow inverse method which provides the corresponding airfoil shape.

The disadvantage of this method is that only single-point design problems can be handled directly. Whether or not the resulting airfoil meets the multi-point design requirements is determined through post-design analysis. If discrepancies do exist, part of the velocity distribution is modified judiciously until the desired goals are achieved eventually. Another difficulty arises when the boundary-layer equations and the auxiliary equations may not be expressed in inverse form, for instance, if it were desired to prescribed the distribution of the linear stability amplification factor n.

Another approach, that may be employed using almost any inverse airfoil method, dispenses entirely with the inverse boundary-layer solution as a driver to the inverse airfoil method. In an interactive, iterative manner, all of the design goals are met by adjusting the velocity distribution provided as input to the inverse method. Based on feedback from successive analyses and with some experience, the velocity distribution may be changed in the direction necessary to bring the airfoil closer to the desired goals.

It is instructive to illustrate this technique within the framework of the inverse method described in section 2.1. For this example, five segments are used as depicted in figure 2-22. Attention, however, is focused on the third and fourth segments (on the lower surface) along which the velocity distribution $v^*(\phi)$ is prescribed for the design angle of attack of 5° [figure 2-23 (a)]. After the specification of the remaining inverse design parameters, the inverse problem is solved to give the airfoil shape. The velocity distribution may then be plotted as a function of the arc length s as shown in figure 2-23 (b). Through the use of a direct boundary-layer method, the shape-factor distribution $H_{12}(s)$ may be computed and then plotted in the relative coordinate system consistent with the prescribed velocity distribution as shown in

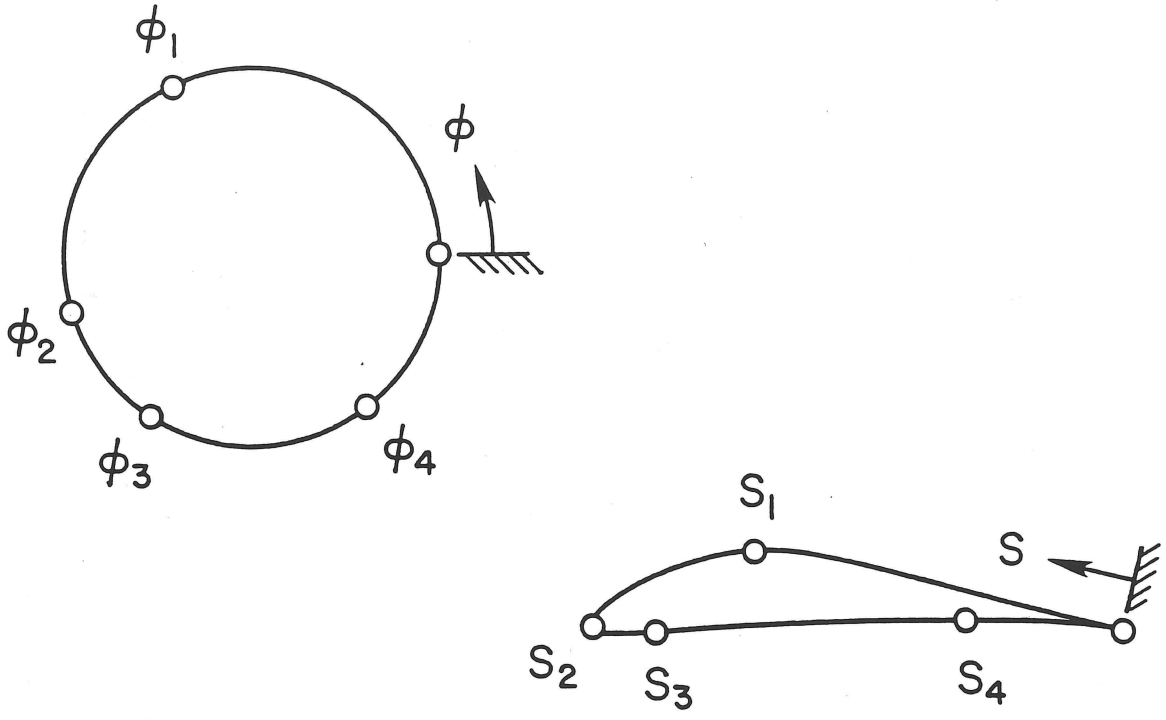

Figure 2-22 Circle divided into five segments and mapped to a five-segment airfoil.

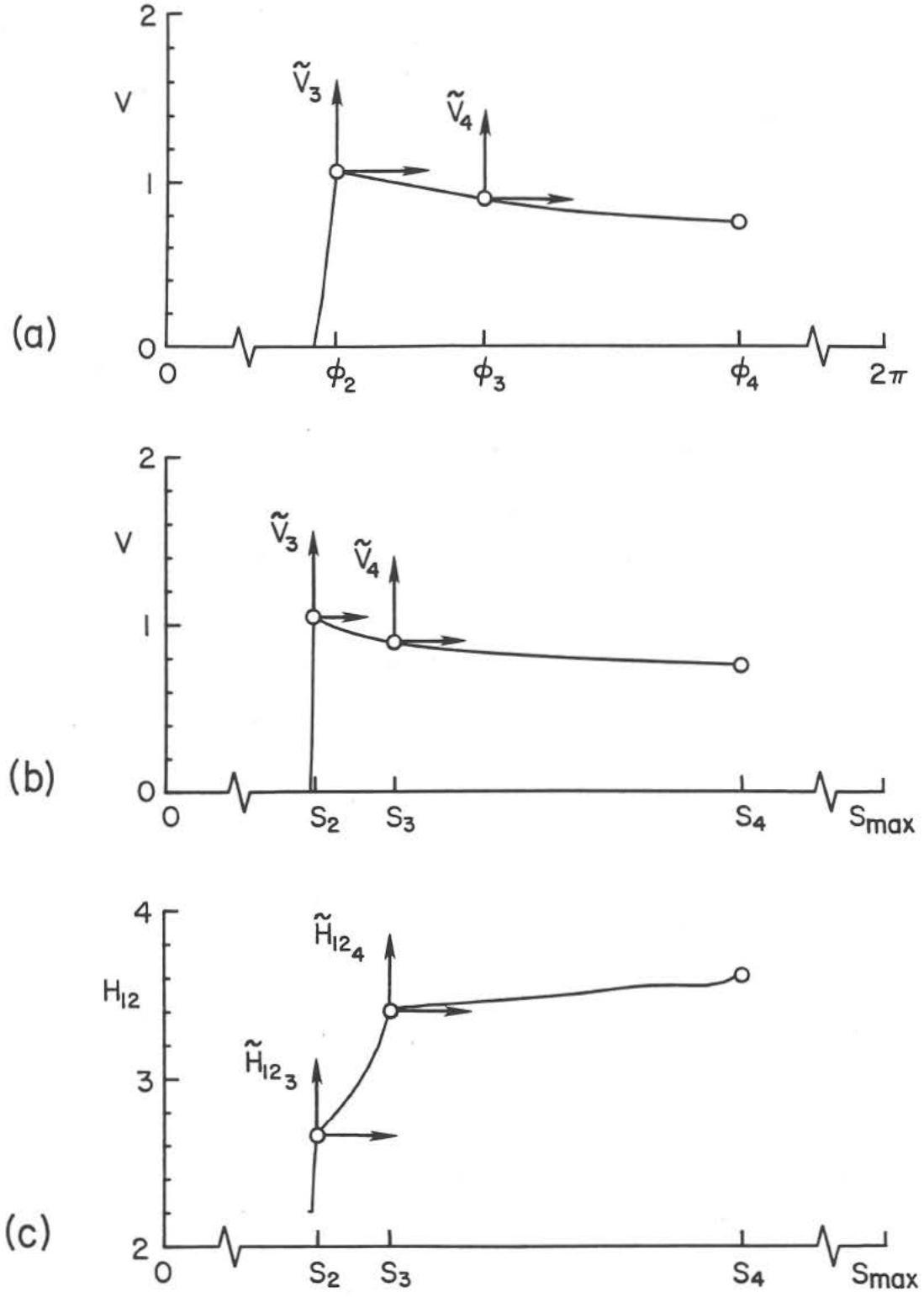

Figure 2-23 Velocity distributions for the third and fourth segments at $\alpha = 5°$ plotted as a function of ϕ and s and the corresponding shape-factor distribution.

figure 2-23 (c).

Now suppose that one of the design goals is to have $H_{12} = 3$ for the fourth segment at the design angle of attack $\alpha = 5°$. As shown in figures 2-24 (a,b), the relative velocity at the end of the third segment may be adjusted to achieve the desired initial condition: $H_{12} = 3$. After having achieved this desired initial condition, attention is turned to the adjustment of the relative velocity distribution on the fourth segment so that H_{12} does not change from the initial condition. Put differently, $\tilde{v}_4(\tilde{\phi}_4)$ is adjusted such that $\tilde{H}_{12_4}(\tilde{s}_4) = 0$. Although it cannot be seen from figures 2-25 (a,b), the solution $\tilde{v}_4(\tilde{\phi}_4)$ for which $\tilde{H}_{12_4}(\tilde{s}_4) = 0$ leads to a slight change in the initial condition. If necessary, this process may be repeated until the shape-factor distribution for the fourth segment is within a set tolerance of the desired value of 3.

From this simple example emerges the basis of a practical, viscous inverse design method. The velocity distribution (defined by the inverse design parameters) is iterated not to achieve a desired velocity distribution $v(s)$ but rather to obtain a desired boundary-layer development. One step in this process involves the performance of several direct boundary-layer analyses to determine the residues in the Newton equations.

2.2.2 Direct Boundary Layer Method

As an overview, once the airfoil is designed through the potential-flow inverse design method described previously, the boundary-layer development may be determined along each segment of the airfoil at the design condition for which some boundary-layer development is prescribed. The results of these calculations are then used to determine the residues necessary for Newton iteration. Depending

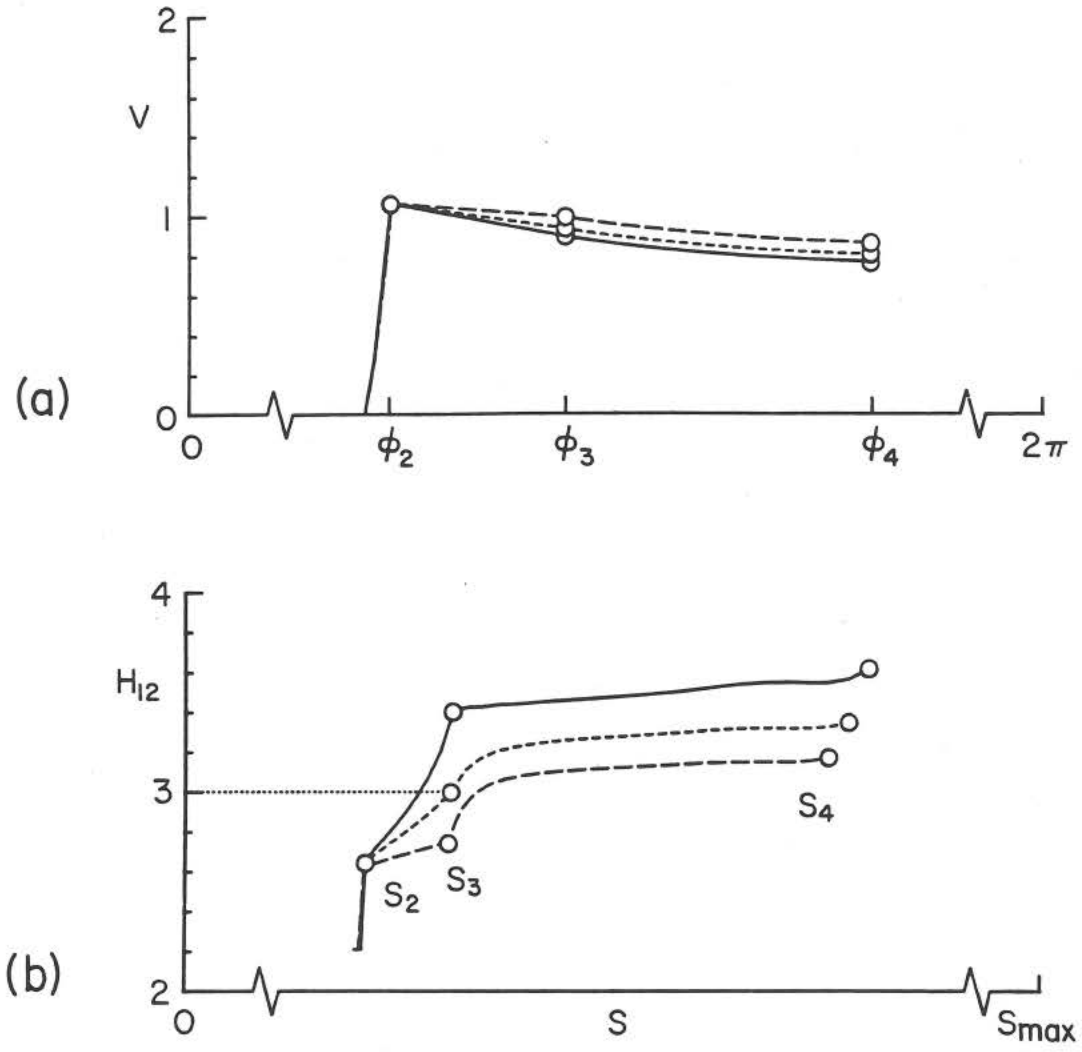

Figure 2-24 Changes in the shape-factor distribution as a results of varying the slope of the velocity distribution on the third segment.

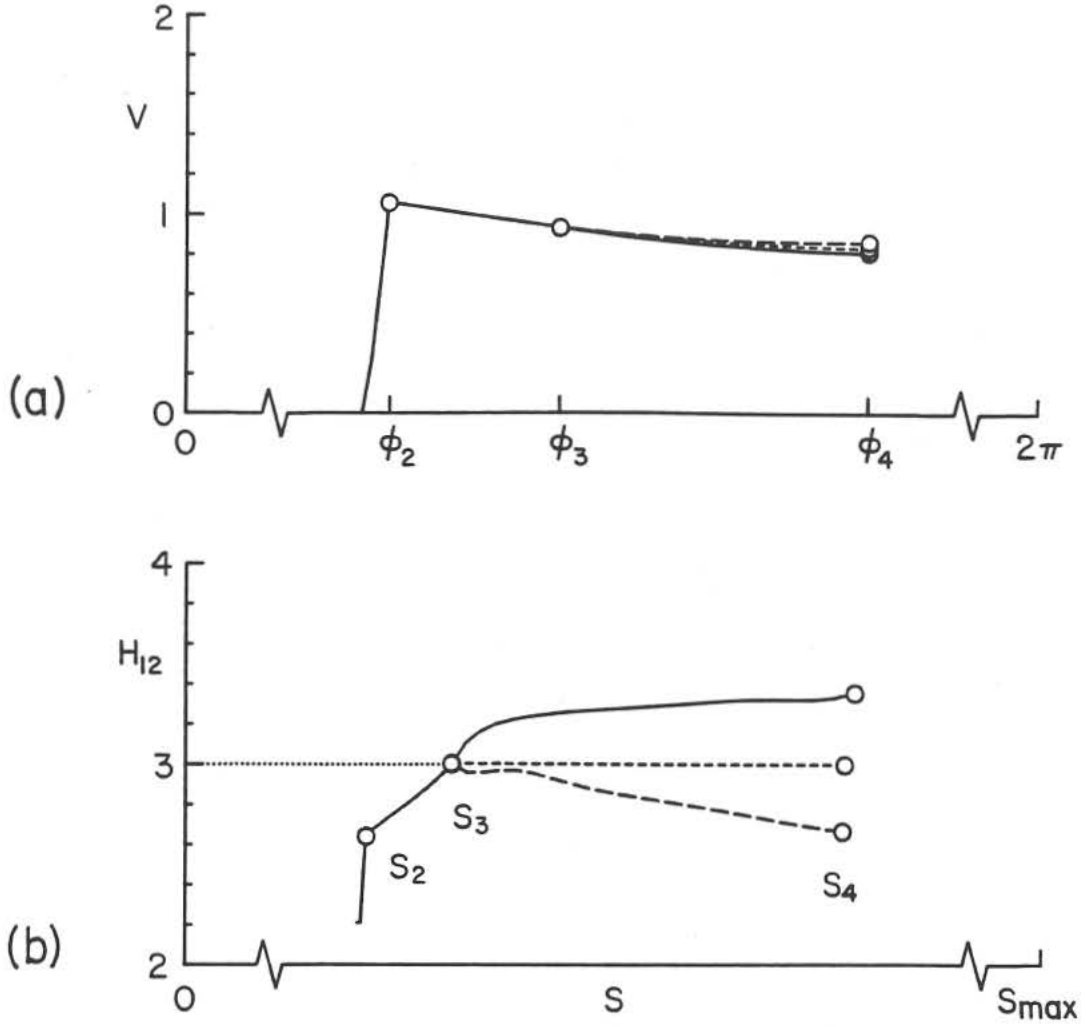

Figure 2-25 Changes in the shape-factor distribution as a result of varying the velocity distribution along the fourth segment.

on the sophistication of the design approach and the design philosophy, a single design session lasting, say, less than an hour could easily involve over 100 direct boundary-layer analyses. In this case, a rapid boundary-layer analysis method is an essential ingredient for efficient interactive design. This requirement is satisfied presently through the use of an integral boundary-layer method, in particular, that based largely on the work of Eppler (1963*a*).

To keep the computational time to a minimum, displacement-thickness effects are ignored and the prescribed boundary-layer developments are limited to those corresponding to attached flows. These restrictions pose no real practical limitations, and the use of an integral boundary-layer method is the only viable option, yet it is certainly not an oversimplification. Airfoils in use on wings, tail surfaces, propellers, etc. operate for the most part as intended in efficient conditions—those for which the boundary layers are thin and attached over most of the surface. Under these circumstances, the displacement thickness has only a small impact on the outer potential flow and hence may be neglected without causing any appreciable discrepancies between predicted and measured performance. Solutions of the integral boundary-layer equations, although rapid, require careful consideration with regard to the choice of the laminar and turbulent boundary-layer correlations if the predicted boundary-layer development is to be an adequate representation of the boundary layer as governed by the Prandtl boundary-layer equations or, more generally, the Navier-Stokes equations.

For the laminar boundary layer, the Falkner-Skan family of profiles are exact solutions to the boundary-layer equations. Laminar boundary-layer solutions of the integral boundary-layer equations based on correlations derived from these similar profiles are found to be in close agreement with both finite difference solutions of

the boundary-layer equations (Drela 1986) and experimental results. For the turbulent boundary layer, no exact solutions to the boundary-layer equations exist. Consequently, the validity of any proposed turbulent boundary-layer correlation is determined ultimately by a comparison with experimental results. The need for great accuracy in the boundary-layer closure correlations is somewhat reduced by the fact that they need be only accurate in the present case for incompressible boundary layers found typically in flows about airfoil shapes. The closure correlations used currently are those due to Eppler (1963*a*). For airfoil flows, Eppler has derived turbulent closure correlations in terms compatible with the solution of the integral boundary-layer equations. These correlations were derived in part based on the work of Weighardt (1948), Ludwieg and Tillmann (1949) and Rotta (1952). As given by Eppler, the extension of this early work is based on empirical results and asymptotic methods.

The prediction of transition from laminar-to-turbulent flow plays a vital role in the determination of the ultimate success of the boundary-layer method as a whole. Two different approaches have been implemented in the present work—an H-R method and an e^n method based on linear stability theory. Fortunately, the reliance on an accurate method of transition prediction is mitigated by the fact that on many airfoils there is a short region over which the adverse pressure gradient changes from mild to severe. Any transition method, no matter how sophisticated, can hardly miss the prediction of transition over such a short distance. The situation is complicated and accuracy is called into question when the pressure gradient is mild (either favorable or adverse) or when laminar separation takes place before turbulent transition is predicted. These are concerns involved mainly in low Reynolds number airfoil applications typical of sailplanes and model aviation. In the case of laminar

separation, transition usually takes place rapidly with reattachment ensuing shortly thereafter. Special considerations are necessary to treat the development of the so-called laminar separation bubble which forms between laminar separation and turbulent reattachment (e.g., Drela 1989; Dini 1990). Careful account of the laminar separation bubble goes beyond the scope of the present investigation. If laminar separation is predicted before transition, transition is assumed to take place at that point—an assumption which is a close approximation to the true physics of the flow so long as the bubble is short. More details of the transition prediction methods are discussed later.

It has been well-established that the combined method gives good predictions of airfoil performance (e.g., Eppler 1963*b*; Maughmer and Somers 1989; Somers 1992). Improvements to the boundary-layer method involve the modelling of the laminar separation bubble (if present), the incorporation of a displacement thickness iteration (Eppler and Somers 1980*b*), the extension of the correlations to compressible flow (Drela and Giles 1986, 1987) or the solution of the boundary-layer equations by a finite difference method. While each of these may be viewed as an improvement to the analysis method, they may simultaneously be viewed as a hindrance which impedes the design process by adding to the level of computation effort which curtails rapid feedback. As stated, rapid feedback is a necessity in design, and the addition of the Newton iteration, while simplifying the work of the designer, may already be viewed as impeding the attainment of this requirement. Further enhancements to the analysis method will await improvements in computer speed.

2.2.2.1 Integral Boundary Layer Equations, Closure Correlations and Transition

The integral momentum and energy equations are used in their standard form,

namely

$$\frac{d\delta_2}{ds} = -(2 + H_{12})\frac{\delta_2}{v}\frac{dv}{ds} + c_f \tag{2.94a}$$

$$\frac{d\delta_3}{ds} = -\frac{3\delta_3}{v}\frac{dv}{ds} + c_D \tag{2.94b}$$

with closure correlations expressed functionally by

$$H_{12} = H_{12}(H_{32}) \tag{2.95a}$$

$$c_f = c_f(H_{12}, R_{\delta_2}) \tag{2.95b}$$

$$c_D = c_D(H_{12}, R_{\delta_2}) \tag{2.95c}$$

for both the laminar and turbulent part of the boundary layer. In particular, for the laminar boundary layer, the Falkner-Skan family of profiles is used to give for attached flow:

$$H_{12} = -5.967105263 + 6.578947368H_{32} - \sqrt{43.2825(0.907 - H_{32})^2 - 16} \tag{2.96a}$$

and for separated flow:

$$H_{12} = -14.9375 + 12.5H_{32} - \sqrt{156.25(1.195 - H_{32})^2 - 16} \tag{2.96b}$$

$$c_f = \frac{\varepsilon^*}{Rv\delta_2} \tag{2.96c}$$

$$c_D = \frac{H_{32}D^*}{Rv\delta_2} \tag{2.96d}$$

where

$$\varepsilon^* = \begin{cases} -0.067 + 0.01977\dfrac{(7.4 - H_{12})^2}{H_{12} - 1}, & H_{12} \leq 7.4 \\ -0.067 + 0.022\left(1 - \dfrac{1.4}{H_{12} - 6}\right)^2, & H_{12} > 7.4 \end{cases} \tag{2.97a, b}$$

$$D^* = \begin{cases} 0.207 + 0.00205(4 - H_{12})^{5.5}, & H_{12} \leq 4 \\ 0.207 - 0.003\dfrac{(4 - H_{12})^2}{1 + 0.02H_{12}^2}, & H_{12} > 4 \end{cases} \qquad (2.98a, b)$$

These correlations, due to Drela and Giles (1986), give essentially the same correlations as those due to Eppler (1963*a*). The difference is that these correlations are valid beyond the point of laminar separation. Although only attached flows are considered in the design method, the need for correlations beyond the point of laminar separation ($H_{12} > 4$) will be discussed later in section 2.2.2.2. It will also be explained there that the shape-factor correlation for separated flows, equation (2.96*b*), must be modified for incorporation into the Newton solution. For the turbulent boundary layer, the correlations developed by Eppler (1963*a*) are used as

$$H_{12} = \frac{11H_{32} + 15}{48H_{32} - 59} \qquad (2.99a)$$

$$c_f = 0.045716[(H_{12} - 1)R_{\delta_2}]^{-0.232}\exp(-1.26H_{12}) \qquad (2.99b)$$

$$c_D = 0.0100[(H_{12} - 1)R_{\delta_2}]^{-1/6} \qquad (2.99c)$$

where it is assumed that turbulent separation takes place when $H_{32} = 1.46$.

For transition, either the short-cut H_{32}-R_{δ_2} method of Eppler (1963*a*, 1969, 1990) or the e^n method of Dini, Selig and Maughmer (1991) is used. Alternatively, transition may be fixed at a point to model transition by a trip strip. A discussion of the H_{32}-R_{δ_2} method is left for Appendix B in which the transition method is used to aid in the design of the NASA NLF(1)-0115 airfoil for general aviation application (Selig, Maughmer and Somers 1990). It should be noted that this airfoil was not designed using the current inverse design method as it was not developed fully at that time. In section 2.2.4, the present e^n method is used in the design of an airfoil, although the airfoil is not intended for practical application. A detailed discussion of the present e^n method is given in Dini, Selig and Maughmer (1991). Briefly,

the linear stability amplification rates over a range of Falkner-Skan profiles have been calculated for a selected range of frequencies at Reynolds numbers up to those typically found on airfoils in application. In the analysis of an airfoil boundary layer via the integral boundary-layer equations, the database of the amplification rates is accessed to simultaneously track the growth of the amplification factors for several frequencies. Based on the envelope of these curves, each corresponding to a different frequency, the envelope may be calculated to give $n(s)$. When $n(s)$ reaches a certain value, typically $n = 9$, transition is assumed to take place.

As a test case, the amplification factor n was evaluated for a Blasius boundary layer at the dimensionless frequencies of 0.000100, 0.000075 and 0.000050 corresponding to those analyzed by Jordinson (1970). Here the reduced frequency F, shown in the figure, is $2\pi f\nu/v^2$ where f is the disturbance frequency, ν the kinematic viscosity and v the boundary-layer edge velocity. As seen in figure 2-26, the comparison indicates that the method does give the proper growth for n vs. R_{δ_1}.

2.2.2.2 Solution Procedure

Equations (2.94a,b) are integrated with a second-order accurate Runge-Kutta scheme for the upper-surface and lower-surface boundary layers from the stagnation point to the trailing-edge, with the potential-flow velocity distribution used as the boundary-layer edge velocity. The stagnation-point conditions, that is, initial conditions on δ_2 and δ_3, are obtained through an asymptotic analysis procedure similar to that given by Eppler (1963a). By the use of equations (2.96c,d), equations (2.94a,b) are expressed alternatively as

$$\frac{d\delta_2}{ds} = -(2 + H_{12})\frac{\delta_2}{v}\frac{dv}{ds} + \frac{\varepsilon^*}{Rv\delta_2} \qquad (2.100a)$$

$$\frac{d\delta_3}{ds} = -\frac{3\delta_3}{v}\frac{dv}{ds} + \frac{H_{32}D^*}{Rv\delta_2} \qquad (2.100b)$$

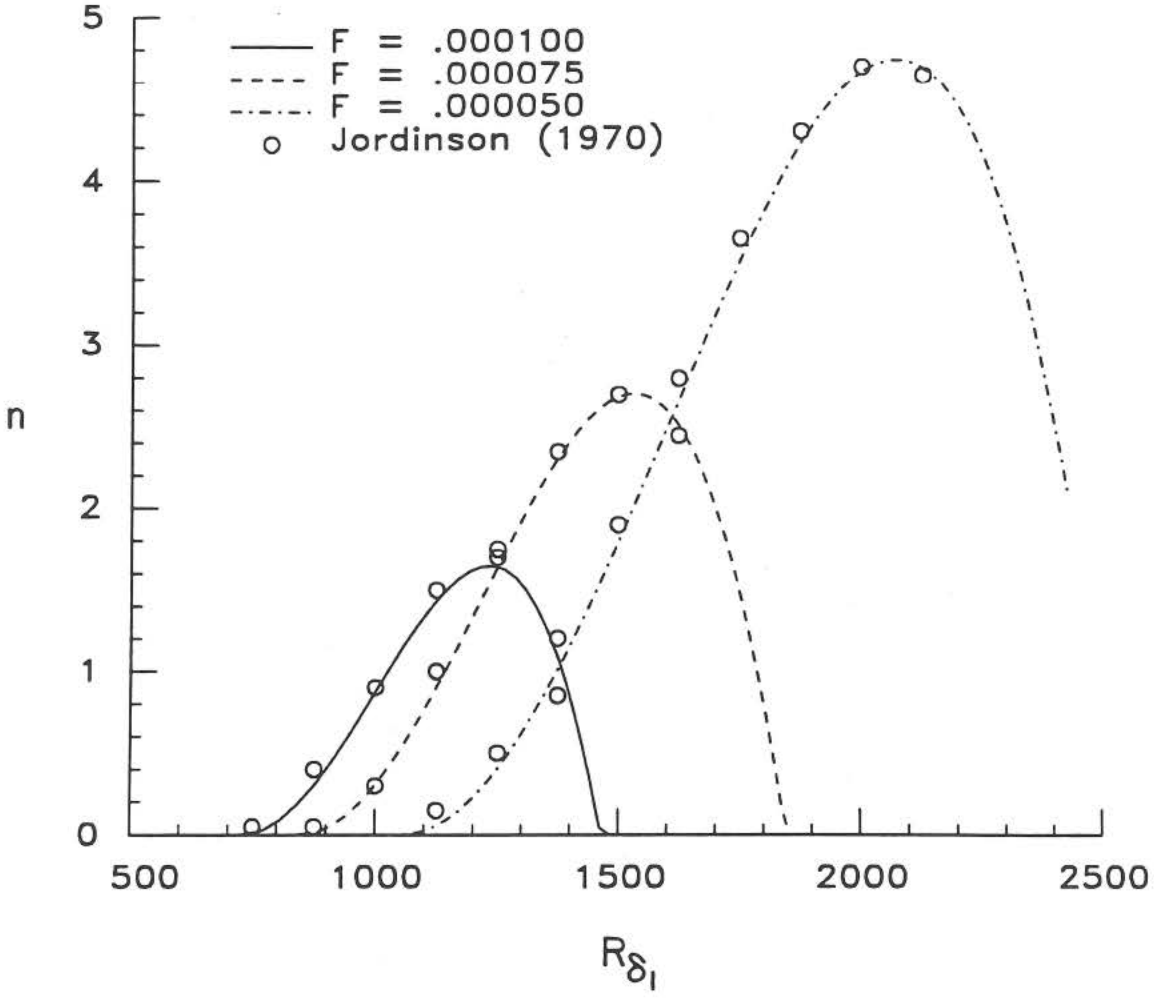

Figure 2-26 Jordinson (1970) amplification factor curves as compared with present results for the Blasius boundary layer.

Equation (2.100a) will be considered for asymptotic analysis first.

Near the stagnation point using the first term of the Taylor series, the velocity may be approximated by

$$v = \Delta s \frac{dv}{ds} \tag{2.101}$$

Substitution of equation (2.101) into (2.100a) gives

$$\Delta s \frac{d\delta_2}{ds} = -(2 + H_{12})\delta_2 + \frac{\varepsilon^*}{R\frac{dv}{ds}\delta_2} \tag{2.102}$$

With justification given later, it is assumed that, near the stagnation point, $d\delta_2/ds$ is negligible. Making this assumption gives

$$(2 + H_{12})\delta_2 = \frac{\varepsilon^*}{R\frac{dv}{ds}\delta_2} \tag{2.103}$$

or

$$\delta_2 = \sqrt{\frac{\varepsilon^*}{(2 + H_{12})R\frac{dv}{ds}}} \tag{2.104}$$

The Reynolds number and the velocity gradient are known. Thus, from equation (2.104), the stagnation-point momentum thickness δ_2 may be found so long as the shape factor H_{12} is known at the stagnation point.

The stagnation value of H_{12} is obtained through both the asymptotic form of the momentum equation (2.104) and the energy equation. The use of expression (2.101) in the energy equation (2.100b) gives

$$\Delta s \frac{d\delta_3}{ds} = -3\delta_3 + \frac{H_{32}D^*}{R\frac{dv}{ds}\delta_2} \tag{2.105}$$

Again, with later justification, $d\delta_3/ds$ is assumed to be negligible, giving

$$3\delta_3 = \frac{H_{32}D^*}{R\frac{dv}{ds}\delta_2} \tag{2.106}$$

Division of equation (2.106) by (2.103) yields,

$$3\varepsilon^* = (2 + H_{12})D^* \tag{2.107}$$

which is a single equation for the value of H_{12} at the stagnation point. The solution of this equation gives $H_{12} = 2.24009159$ which, when used in equation (2.104), provides the initial condition for the momentum thickness, that is,

$$\delta_2 = 0.290352908 \sqrt{\frac{1}{R\frac{dv}{ds}}} \tag{2.108}$$

Through equation (2.96a), with $H_{12} = 2.24009159$, it is found that $H_{32} = 1.62008219$ at the stagnation point. Thus, since $H_{32} \equiv \delta_3/\delta_2$, the initial condition on the energy thickness is given by

$$\delta_3 = 1.62008219\,\delta_2 \tag{2.109}$$

Justification for this asymptotic procedure at the stagnation point is explained as follows. From equation (2.104), it is indeed true that $d\delta_2/ds = 0$ so long as $dH_{12}/ds = 0$. Proof of this comes from equation (2.107) which shows that H_{12} is constant or $dH_{12}/ds = 0$ if $d\delta_3/ds = 0$. From the correlation (2.96a), $dH_{12}/ds = 0$ implies that $dH_{32}/ds = 0$. Since $dH_{32}/ds = (\delta_2^{-1})d\delta_3/ds - (\delta_3\delta_2^{-2})d\delta_2/ds$ together with $d\delta_2/ds = 0$ and $dH_{32}/ds = 0$, it must in fact be true that $d\delta_3/ds = 0$. Consequently all the assumptions are consistent, and equations (2.108) and (2.109) represent a valid asymptotic solution.

Since only attached flows are considered, a special problem is encountered if, at some point in the Newton iteration, laminar separation is reached before transition. An excursion of this sort is entirely conceivable even though the final boundary-layer development will be attached along the design segment at the prescribed design condition. Conventional integral boundary-layer solution techniques at the

point of laminar separation switch from a treatment of the velocity as the independent variable to its treatment as a dependent variable; that is, it follows from the solution. What is given instead of the velocity is another variable, such as the shape of the separation streamline (Ingen 1975) or the distribution of the shape factor (e.g., Dini 1990) which approximates the development of the ensuing laminar separation bubble. The integral boundary-layer equations are then solved in an inverse mode. An entirely different approach is to solve the problem through the inverse boundary-layer equations by specifying a boundary-layer property and calculating the corresponding boundary-layer edge velocity (e.g., Cebeci 1976; Stock 1988; Whitfield *et al.* 1982).

The need to approach the solution in either of these two ways is guided not only by physical observation, in that it would be improper to give the potential-flow velocity distribution beyond separation, but also by clues found in the governing equations. The shape-factor correlations (2.96*a,b*) are only valid for $H_{32} \geq 1.515$ whether or not the flow is attached or separated. Attempting to solve the integral boundary-layer equations beyond the point of separation with a boundary-layer edge velocity given by potential-flow theory will yield a shape factor $H_{32} < 1.515$ which is not within the bounds of the correlations.

To circumvent this difficulty and to integrate in the direct mode beyond the point of laminar separation, the present method replaces equation (2.96*b*) for separated flow with a *fictitious* shape-factor correlation given by

$$H_{12} = 7\sqrt{1.515 - H_{32}} + 4, \qquad H_{32} < 1.515 \tag{2.110}$$

This equation merely serves as a means to continue in the direct mode beyond laminar separation without having to resort to an inverse boundary-layer method. Of course, the solution beyond the point of laminar separation will no longer be a valid

boundary-layer development. Nevertheless, the final solution after iteration will yield the desired, i.e. prescribed, attached boundary-layer development for which the correlations are still perfectly valid.

As a check on the method, the airfoil shown in figure 2-27 was analyzed at $R = 1 \times 10^6$ and $\alpha = 10°$ by the present computer program and the program discussed in Eppler (1988). A comparison of the predicted shape-factor development is shown in figure 2-28. Slight discrepancies, largest near the stagnation point, are most likely due to slight fluctuations in the velocity distribution computed by the panel method as compared with the velocity distribution used as input to the present inverse method. Nevertheless, the agreement is excellent, not only for the shape-factor development (as shown), but also for the other boundary-layer variables.

2.2.3 Multi-Dimensional Newton Iteration in Viscous Design

In the example illustrated in figures 2-22 through 2-25, the shape factor H_{12} at the beginning of the fourth segment ($s = s_3$) is specified as 3. This value is obtained finally by the adjustment of the slope $d\tilde{v}_3/d\tilde{\phi}_3$ through the specification of relative design velocity distribution at the end of the third segment and assuming a linear variation along the segment. In terms of the Newton iteration scheme $d\tilde{v}_3/d\tilde{\phi}_3$ becomes the unknown in order to satisfy the Newton equation

$$d\tilde{v}_3/d\tilde{\phi}_3 \quad \Rightarrow \quad 0 = H_{12}(s_3) - 3 \tag{2.111}$$

where the notation '$\Rightarrow$' means that this inverse design parameter is used for iteration and has a first-order effect on the corresponding Newton equation. It further serves as an aid in keeping an equal number of equations as unknowns.

For the fourth segment, the relative design velocity distribution $\tilde{v}_4(\tilde{\phi}_4)$ is ad-

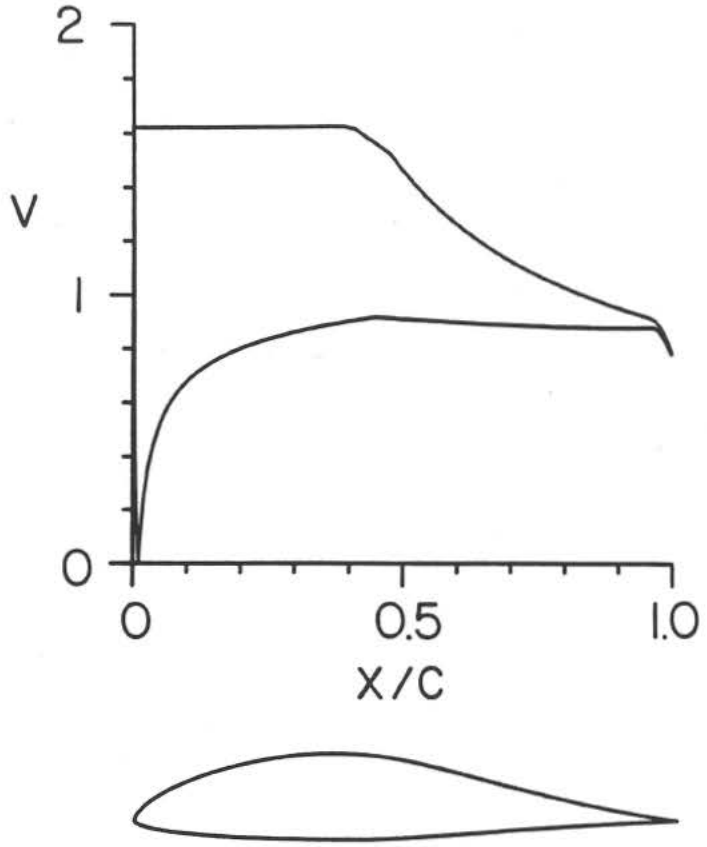

Figure 2-27 Airfoil used for a check on the boundary-layer analysis method.

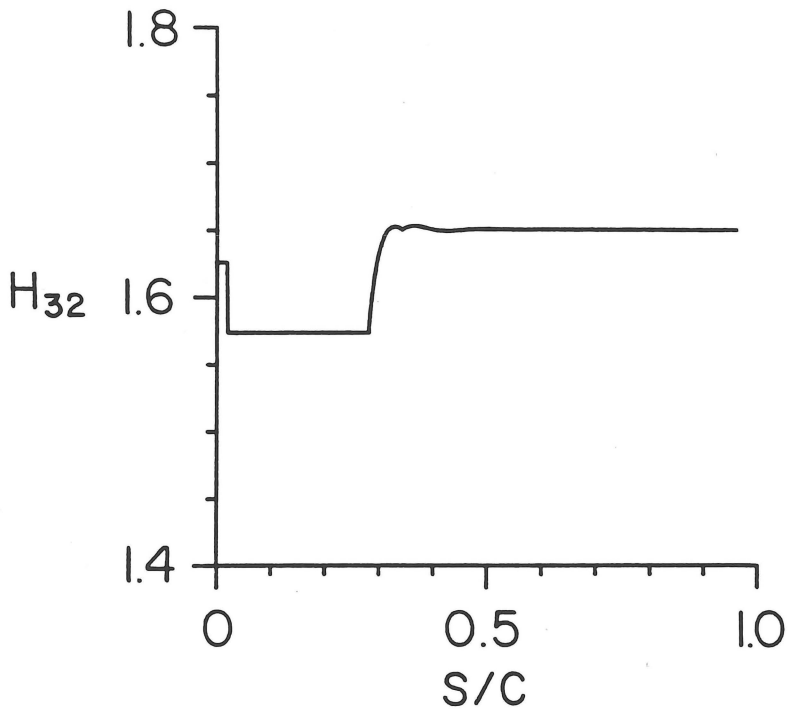

Figure 2-28 Comparison between the shape factor (H_{32}) distribution predicted by the present boundary-layer analysis program and the Eppler program for the airfoil shown in figure 2-27 at $R = 1 \times 10^6$ and $\alpha = 10°$.

justed such that $\tilde{H}_{12_4}(\tilde{s}_4) = 0$, that is, through Newton iteration

$$\tilde{v}_4(\tilde{\phi}_4) \quad \Rightarrow \quad 0 = \tilde{H}_{12_4}(\tilde{s}_4) \tag{2.112}$$

The numerical problem, however, must be discretized for incorporation into the Newton system. The design velocity distribution $\tilde{v}_4(\tilde{\phi}_4)$ is defined by a desired number of moveable spline supports as shown in figure 2-7. For the three nodes shown, the following three equations must be satisfied.

$$\tilde{v}_4(\tilde{\phi}_4 = \tilde{\phi}_4^1) \quad \Rightarrow \quad 0 = \tilde{H}_{12_4}(\tilde{s}_4 = \tilde{s}_4^1) \tag{2.113a}$$

$$\tilde{v}_4(\tilde{\phi}_4 = \tilde{\phi}_4^2) \quad \Rightarrow \quad 0 = \tilde{H}_{12_4}(\tilde{s}_4 = \tilde{s}_4^2) \tag{2.113b}$$

$$\tilde{v}_4(\tilde{\phi}_4 = \tilde{\phi}_4^3) \quad \Rightarrow \quad 0 = \tilde{H}_{12_4}(\tilde{s}_4 = \tilde{s}_4^3) \tag{2.113c}$$

The superscripts indicate the index of the nodes in terms of the arc limit $\tilde{\phi}_4$ and the corresponding nodes in $\tilde{s}_4$.

As discussed in section 2.1.9, an arc limit ϕ_i between two segments can be iterated to correspond to a specified x_i/c (or s_i/c) location as

$$\phi_i \quad \Rightarrow \quad 0 = x_i/c - p \tag{2.114}$$

where p is the value of the generic desired parameter. More generally the arc limit may be adjusted so that a specified boundary-layer property is reached at that location. For example, ϕ_i may be iterated to correspond to the point where the linear stability amplification factor is a value of 9 for a given operating condition, i.e.

$$\phi_i \quad \Rightarrow \quad 0 = n(s_i) - 9 \tag{2.115}$$

The relative design velocity distribution for a segment may be used to control the relative boundary-layer shape-factor distribution as previously mentioned, the

relative velocity distribution in $\tilde{s}_i$ or any one of another desired distributions. For example, either the local geometry may be specified, the n-development, or a curve in the H_{32}-R_{δ_2} diagram used in the Eppler method for predicting transition.

2.2.4 Application of the Method

Two example airfoils are presented to illustrate some of the capabilities of the method. Again, these airfoils serve only as examples of the method and are not intended for practical use. The main design goals, although defined in mathematical detail later, may be stated as follows. Along the forward part of the upper surface of the airfoil, the n-development is prescribed at the design angle of attack and Reynolds number. Following this segment, a linear ramp is introduced for a different angle of attack. On the lower surface, at yet a different angle of attack, the boundary-layer shape-factor distribution is prescribed much like the example of figures 2-23 through 2-25.

These characteristics are obtained by an airfoil with seven segments—four on the upper surface and three on the lower. All of the inverse design parameters are listed in table 2-2 below, with the exception of the trailing-edge angle parameter ϵ.

Table 2-2: Inverse Design Parameters for a Seven-Segment Airfoil

i	ϕ	$\alpha^*(\phi)$	$v^*(\phi)$
1	$[0, \phi_1]$	α_1	$v_1, w(\phi; \phi_{W^-}, \phi_S, \phi_F, \mu, K_H, K)$
2	$[\phi_1, \phi_2]$	α_2	$v_2, \tilde{v}_2(\tilde{\phi}_2)$
3	$[\phi_2, \phi_3]$	α_3	$v_3, \tilde{v}_3(\tilde{\phi}_3)$
4	$[\phi_3, \phi_4]$	α_4	$v_4, \tilde{v}_4(\tilde{\phi}_4)$
5	$[\phi_4, \phi_5]$	α_5	$v_5, \tilde{v}_5(\tilde{\phi}_5)$
6	$[\phi_5, \phi_6]$	α_6	$v_6, \tilde{v}_6(\tilde{\phi}_6)$
7	$[\phi_6, 2\pi]$	α_7	$v_7, \overline{w}(\phi; \overline{\phi}_{W^-}, \overline{\phi}_S, \overline{\phi}_F, \overline{\mu}, \overline{K}_H, \overline{K})$

Many of these parameters are selected as unknowns in the Newton iteration in order to match the design goals, but for those which are left unchanged the following values are used.

$$\alpha_1 = \alpha_2 = 10^\circ \tag{2.116a}$$

$$\alpha_3 = \alpha_4 = 15^\circ \tag{2.116b}$$

$$\alpha_5 = \alpha_6 = \alpha_7 = 8^\circ \tag{2.116c}$$

$$K = \overline{K} = 1 \tag{2.116d}$$

$$\phi_S = 15^\circ, \qquad \overline{\phi}_S = 340^\circ \tag{2.116e}$$

$$\phi_F = 10^\circ, \qquad \overline{\phi}_F = 350^\circ \tag{2.116f}$$

$$\epsilon = 1/18 \tag{2.116g}$$

The value for ϵ is selected to yield a 10° trailing-edge angle and the arc limits ϕ_S, $\overline{\phi}_S$, ϕ_F, and $\overline{\phi}_F$ are set to confine the closure and the finite trailing-edge angle contributions of the pressure recovery to a small region near the trailing edge. The small values for K and $\overline{K}$ which define in part the main pressure recovery [equation 2.61(a)] will give a slightly adverse pressure gradient at the beginning of the recovery on the upper surface and lower surface at the corresponding design angles of attack α_1 and α_7, respectively.

As discussed in section 2.1.9, the design goals are matched in stages. In this example case, the process is taken in the order of increasing complexity. First, the leading-edge arc limit ϕ_4 is iterated to match K_S. The leading-edge arc limit ϕ_4 and the velocity level v_1 are then iterated together to achieve the desired K_S and c_{m_0} as

$$\phi_4 \quad \Rightarrow \quad 0 = K_S - 0.4 \tag{2.117a}$$

$$v_1 \quad \Rightarrow \quad 0 = c_{m_0} + 0.25 \tag{2.117b}$$

Next, the remaining arc limits are iterated to correspond to specified s_i/c locations by

$$\phi_1 \quad \Rightarrow \quad 0 = s_1/c - 0.25 \tag{2.118a}$$

$$\phi_2 \quad \Rightarrow \quad 0 = s_2/c - 0.40 \tag{2.118b}$$

$$\phi_3 \quad \Rightarrow \quad 0 = s_3/c - 0.90 \tag{2.118c}$$

$$\phi_5 \quad \Rightarrow \quad 0 = s_5/c - 1.20 \tag{2.118d}$$

$$\phi_6 \quad \Rightarrow \quad 0 = s_6/c - 1.70 \tag{2.118e}$$

After this, the relative design velocity distribution on the second segment is iterated to produce a linear velocity distribution in s at the design angle of attack $\alpha_2 = 10°$. Specifically,

$$\tilde{v}_2(\tilde{\phi}_2) \quad \Rightarrow \quad 0 = \tilde{v}_2(\tilde{s}_2) + 1.2\tilde{s}_2 \tag{2.119}$$

where now $\tilde{s}_2$ is measured in the direction from s_2 to s_1, that is, $\tilde{s}_2 = s_2 - s$ (opposite to that shown in figure 2-7). Figure 2-29 shows portions of the velocity distribution for the design angles of attack $\alpha = 8°$, $10°$ and $15°$. For the $\alpha = 10°$ case, it is seen in the figure that the desired linear variation (in boldline) is obtained for the second segment. The $\alpha = 8°$ and $15°$ cases are pertinent to the remaining lower-surface and upper-surface design requirements, respectively.

For the lower surface, the boundary-layer shape factor is prescribed to be $H_{12} = 2.8$ for the sixth segment at $\alpha_6 = 8°$. This is achieved as in the illustrated example of figures 2-22 through 2-25 by iterating on the preceding segment to match the desired initial condition at $s = s_5$ and by the adjustment of the relative design velocity distribution along the sixth segment to maintain $H_{12} = 2.8$, that is,

$$d\tilde{v}_5/d\tilde{\phi}_5 \quad \Rightarrow \quad 0 = H_{12}(s_5) - 2.8 \tag{2.120a}$$

$$\tilde{v}_6(\tilde{\phi}_6) \quad \Rightarrow \quad 0 = \tilde{H}_{12_6}(\tilde{s}_6) \tag{2.120b}$$

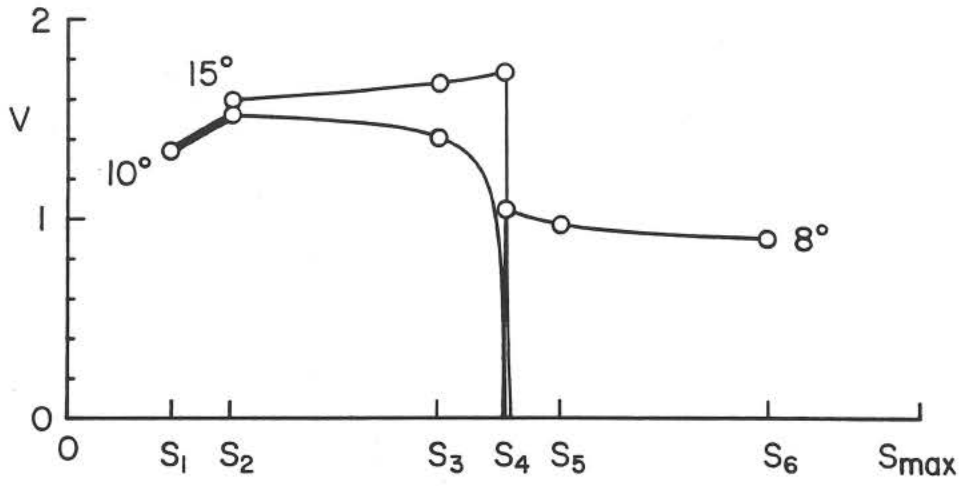

Figure 2-29 Partial velocity distributions corresponding to the design conditions ($s_{max} = 2.067$).

As shown in figure 2-30, this shape-factor distribution is achieved by the velocity distribution shown in figure 2-29 for $\alpha = 8°$.

On the upper surface, the n-development is prescribed for the third segment at the design conditions $\alpha_3 = 15°$ and $R_3 = 1 \times 10^6$. The initial value of $n = 2$ is set by adjusting the velocity distribution of the fourth segment ($s = s_3$), i.e.

$$d\tilde{v}_4/d\tilde{\phi}_4 \quad \Rightarrow \quad 0 = n(s_3) - 2 \tag{2.121}$$

The velocity distribution for the third segment is adjusted to give the desired linearly increasing n-growth given by

$$\tilde{v}_3(\tilde{\phi}_3) \quad \Rightarrow \quad 0 = \tilde{n}_3(\tilde{s}_3) - 14\tilde{s}_3 \tag{2.122}$$

where this time $\tilde{s}_3$ is measured from s_3 to s_2, that is, $\tilde{s}_3 = s_3 - s$.

Since the length of the segment is $s_3 - s_2 = 0.5$ with an initial value of $n = 2$ and slope of $dn/ds = 14$, the value of n at the end of the segment is 9 corresponding to the point of transition. As shown in figure 2-30, this desired n-growth, based on the analysis method of Dini, Selig and Maughmer (1991), is achieved. Finally, the airfoil shape and the velocity distributions at the design angles of attack are shown in figure 2-31.

While the preceeding airfoil illustrates the prescription of laminar boundary-layer developments, this next airfoil is designed for a certain turbulent boundary-layer development. In particular, the upper-surface recovery distribution is prescribed to be near separation as was first studied by Wortmann (1955). The airfoil to be presented employs an upper-surface pressure recovery much like the Stratford pressure recovery used by Liebeck and Ormsbee (1970) and Miley (1974). While it is not suggested that the use of a Stratford distribution is necessarily ideal, such an example does represent an interesting limiting case.

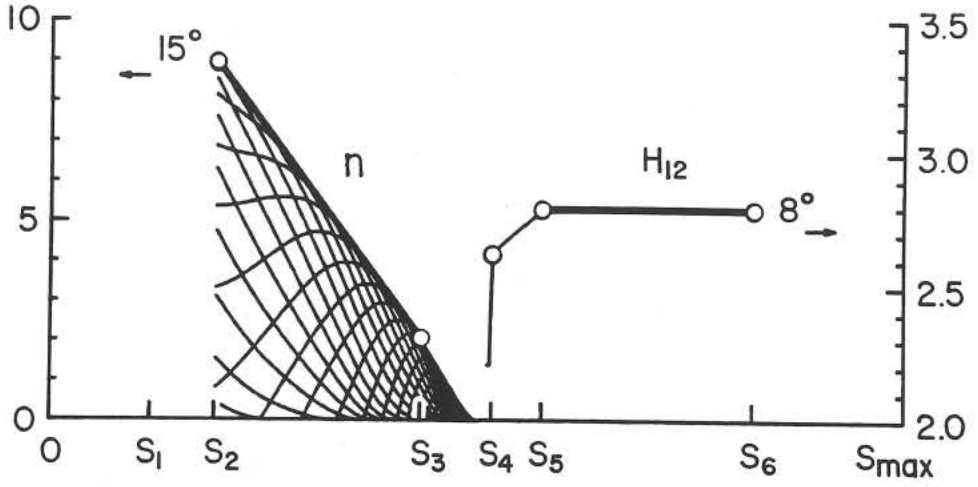

Figure 2-30 Partial boundary-layer developments corresponding to the design conditions ($R = 1 \times 10^6$ for the n-development).

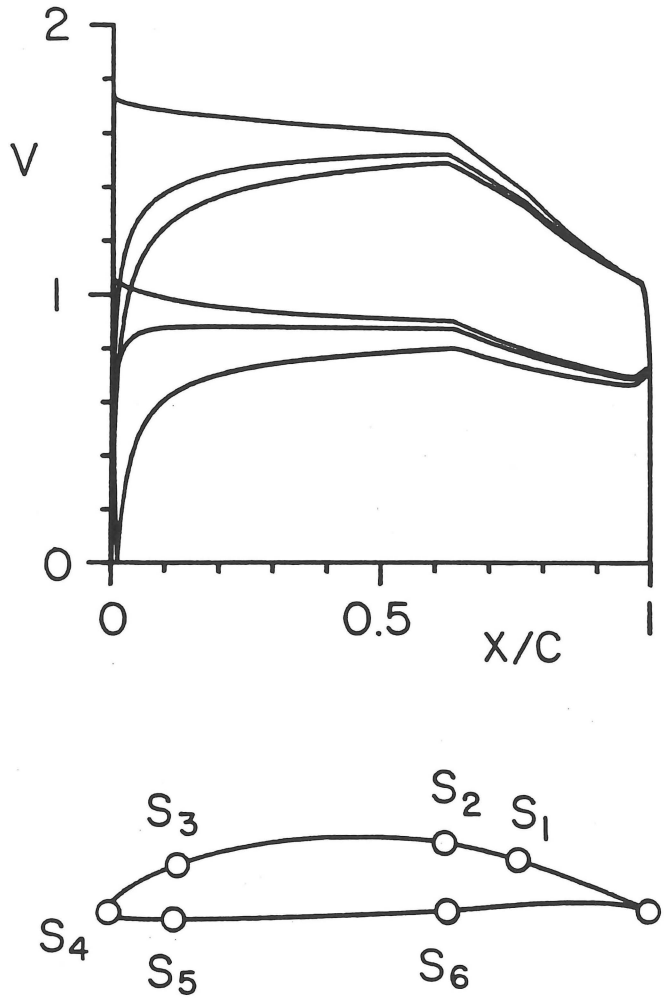

Figure 2-31 Airfoil and velocity distributions for $\alpha = 8°$, $10°$ and $15°$.

Without going into all the details, the airfoil shown in figure 2-32 was designed to have for $\alpha = 18°$ and $R = 1 \times 10^6$, a shape-factor distribution $H_{32} = 1.65$ along the upper-surface pressure recovery from a point just past the flat rooftop to approximately $0.8c$. This distribution was achieved in the same way that the previous example achieved a constant shape-factor distribution $[H_{12}(s)]$ over the forward lower surface. A short segment after the flat rooftop was iterated to make $H_{32} = 1.65$ at its end. Then, the relative design velocity distribution of the following segment extending back to approximately $0.8c$ was iterated so as to keep H_{32} constant (or $\tilde{H}_{32} = 0$). The resulting shape-factor distribution for the upper surface is shown in figure 2-33.

2.3 THE DIRECT ISOLATED AIRFOIL PROBLEM

The direct or analysis problem has been treated in various ways by conformal mapping; however, practically all of these may be traced back to the work of Theodorsen (1931) and Theodorsen and Garrick (1933). The so-called Theodorsen method involves two mappings to go from the airfoil to the circle. First, the inverse Joukowski or Karman-Treffetz mapping is used to take the airfoil into a 'near' circle. A second mapping (determined by iterative means) is then used to take this near circle into an exact circle about which the flow is known. Working backwards, the velocity about the airfoil is finally obtained. To discuss the details of Theodorsen's method would go beyond the scope of the present investigation. Rather, the purpose here is to present a new analysis method which, like Theodorsen's method, uses conformal mapping and involves an iterative solution technique. Other than this, however, the two methods are not similar.

The present analysis method differs from that of Theodorsen's in that the trans-

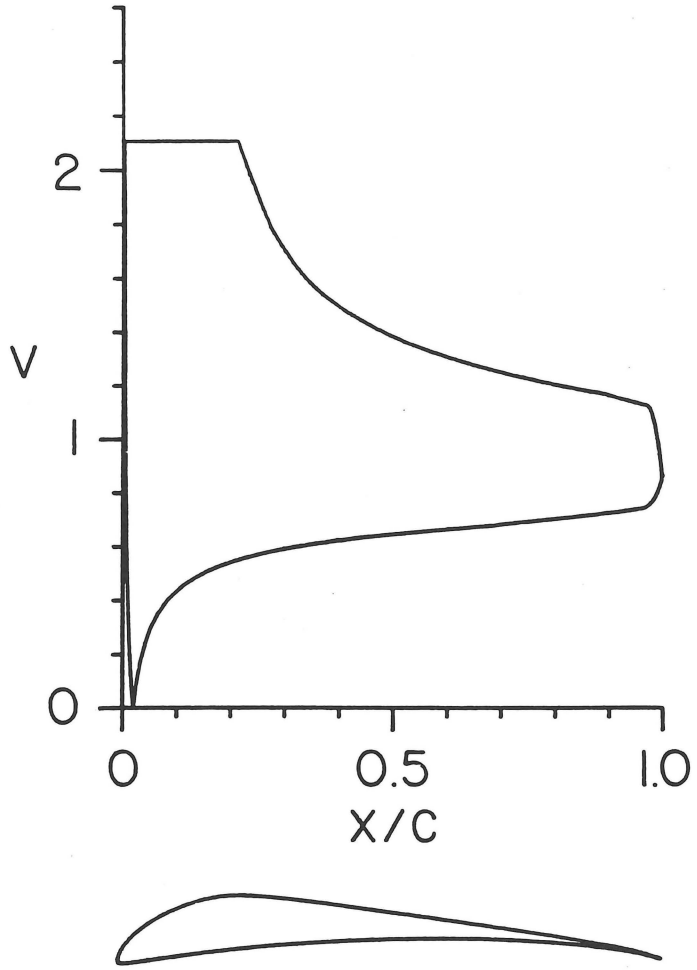

Figure 2-32 Airfoil and velocity distribution for $\alpha = 18°$ for prescribed turbulent boundary-layer development.

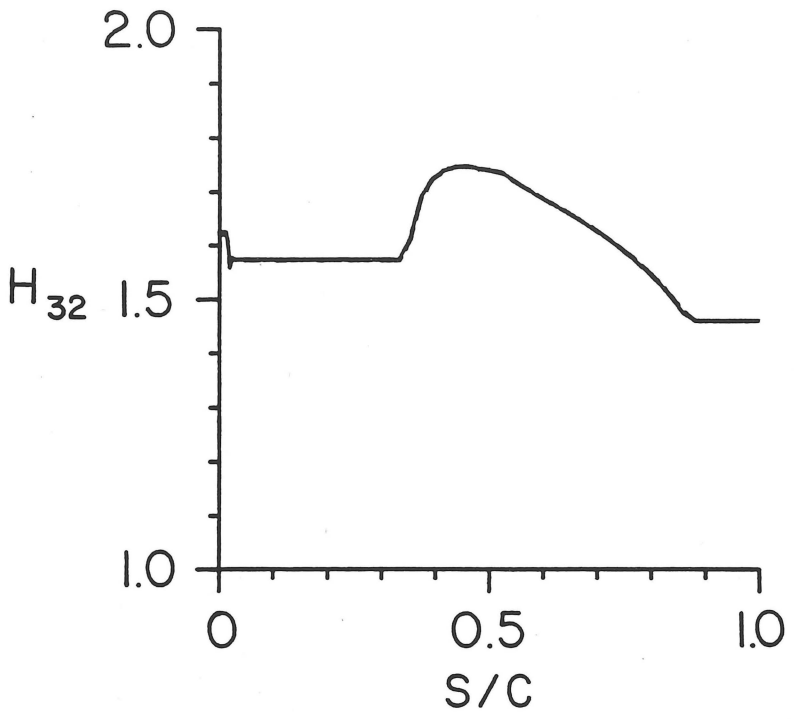

Figure 2-33 Boundary-layer shape factor (H_{32}) for airfoil shown in figure 2-32 ($\alpha = 18°$, $R = 1 \times 10^6$).

formation from the airfoil to the circle is done in one step (rather than two), and the mapping derivative [equation (2.2)] is used (rather than the mapping itself). The analysis procedure begins by considering the conjugate harmonic function $Q(\phi)$ which is repeated from equation (2.20):

$$Q(\phi) = \theta^*(\phi) + \pi^*(\phi) - \phi/2 + \epsilon(\pi/2 - \phi/2) \tag{2.124}$$

As indicated in figure 2-2 and equation (2.15) for a given angle of attack, $\theta^*(\phi)$ jumps by $-\pi$ at the stagnation point while $\pi^*(\phi)$ jumps by π at the stagnation point. In effect, these jumps cancel in which case

$$\theta(\phi) = \theta^*(\phi) + \pi^*(\phi) \tag{2.124}$$

where $\theta(\phi)$ is simply the surface angle about the airfoil contour. Thus, equation (2.123) becomes

$$Q(\phi) = \theta(\phi) - \phi/2 + \epsilon(\pi/2 - \phi/2) \tag{2.125}$$

In the analysis problem, the surface angle $\theta(s)$ about the given airfoil may be computed. If it is known where points about the circle ($\zeta = \zeta_c = e^{i\,\phi}$) map to points about the airfoil, that is, if $s(\phi)$ is known, the surface angle about the airfoil may be expressed as a function ϕ, viz. $\theta(\phi)$. In this case, $Q(\phi)$ is known by equation (2.125) which leads to $P(\phi)$. From $P(\phi)$, the velocity distribution is obtained, and if desired from $P(\phi)$ and $Q(\phi)$ the mapping derivative can be found. Thus, the derivative of the mapping follows directly from $s(\phi)$. Of course, in the analysis problem, $s(\phi)$ is not known a priori, and as a result the mapping derivative is not computed so easily. Consequently, the solution of the problem revolves around $s(\phi)$.

While $s(\phi)$ is not known a priori, it may be estimated as $\hat{s}^i(\phi)$ where the superscript $(\ )^i$ denotes the i-th estimate. The only requirements are that $\hat{s}^i(\phi = 0) = 0$,

$\hat{s}^i(\phi = 2\pi) = s_{max}$ and that $\hat{s}^i(\phi)$ increases monotonically so there is a one-to-one correspondence between points about the airfoil and points about the circle. From this estimate $\hat{s}^i(\phi)$, the surface angle about the airfoil may be estimated as $\hat{\theta}(\phi)$. An estimate of the conjugate harmonic function is then given by

$$\hat{Q}^i(\phi) = \hat{\theta}(\phi) - \phi/2 + \epsilon(\pi/2 - \phi/2) \tag{2.126}$$

To proceed from here by computation of an estimate of $P(\phi)$ as $\hat{P}^i(\phi)$ and then the mapping derivative would ignore the conditions on the mapping coefficients. As a result, the estimates $\hat{P}^i(\phi)$ and $\hat{Q}^i(\phi)$ would not necessarily satisfy the integral constraints in which case the mapping derivative would not necessarily result in a closed airfoil or give a velocity distribution compatible with the freestream.

From the estimate $\hat{Q}^i(\phi)$, a better estimate $\hat{Q}^{i+1}(\phi)$ may be formed in such a way that it satisfies the conditions on the mapping. From equation (2.18), the conjugate harmonic function is expressed as

$$\hat{Q}^i(\phi) = \hat{b}_0^i + \hat{b}_1^i \cos\phi - \hat{a}_1^i \sin\phi + \hat{b}_2^i \sin 2\phi - \hat{a}_2^i \sin 2\phi + \cdots \tag{2.127}$$

By equations (2.5*b*) and (2.7*a*,*b*), the new estimate $\hat{Q}^{i+1}(\phi)$ based on $\hat{Q}^i(\phi)$ must have $\hat{b}_0^i = 0$, $\hat{b}_1^i = 0$ and $\hat{a}_1^i = 1 - \epsilon$. This new estimate may be formed by

$$\hat{Q}^{i+1}(\phi) = \hat{Q}^i(\phi) - \hat{b}_0^i - \hat{b}_1^i \cos\phi + \hat{a}_1^i \sin\phi - (1 - \epsilon)\sin\phi \tag{2.128}$$

where

$$\hat{b}_0^i = \frac{1}{2\pi}\int_0^{2\pi} \hat{Q}^i(\phi)\, d\phi \tag{2.129a}$$

$$\hat{b}_1^i = \frac{1}{\pi}\int_0^{2\pi} \hat{Q}^i(\phi)\cos\phi\, d\phi \tag{2.129b}$$

$$-\hat{a}_1^i = \frac{1}{\pi}\int_0^{2\pi} \hat{Q}^i(\phi)\sin\phi\, d\phi \tag{2.129c}$$

Substitution of equation (2.127) into (2.128) gives for the new estimate

$$\hat{Q}^{i+1}(\phi) = -(1-\epsilon)\sin\phi + \hat{b}_2^i \cos 2\phi - \hat{a}_2^i \sin 2\phi + \cdots \tag{2.130}$$

which now does satisfy the conditions on the coefficients.

Equation (2.130) may be derived through an alternative approach which, in Chapter 3, will prove useful in the analysis of cascades. This alternative approach involves the satisfaction of the conditions on the coefficients by use of the three integral constraints on $Q(\phi)$. The new estimate based on the old estimate is expressed as

$$\hat{Q}^{i+1}(\phi) = \hat{Q}^i(\phi) + k_1 + k_2 \cos + k_3 \sin\phi \tag{2.131}$$

By the integral constraints (2.51a–c), it is required that the new estimate satisfy

$$\frac{1}{2\pi}\int_0^{2\pi} \hat{Q}^{i+1}(\phi)\, d\phi = 0 \tag{2.132a}$$

$$\frac{1}{\pi}\int_0^{2\pi} \hat{Q}^{i+1}(\phi)\cos\phi\, d\phi = 0 \tag{2.132b}$$

$$\frac{1}{\pi}\int_0^{2\pi} \hat{Q}^{i+1}(\phi)\sin\phi\, d\phi = \epsilon - 1 \tag{2.132c}$$

Substitution of equation (2.131) into the integral constraints (2.132) yields three equations for the three unknowns to give

$$k_1 = -\frac{1}{2\pi}\int_0^{2\pi} \hat{Q}^i(\phi)\, d\phi \tag{2.133a}$$

$$k_2 = -\frac{1}{\pi}\int_0^{2\pi} \hat{Q}^i(\phi)\cos\phi\, d\phi \tag{2.133b}$$

$$k_3 = \epsilon - 1 - \frac{1}{\pi}\int_0^{2\pi} \hat{Q}^i(\phi)\sin\phi\, d\phi \tag{2.133c}$$

By comparison with equations (2.129a–c) and (2.128), it is seen that substitution of equations (2.133a–c) into (2.133) yields the same result for $\hat{Q}^{i+1}(\phi)$ as equation (2.130).

With this new estimate $\hat{Q}^{i+1}(\phi)$, $\hat{P}^{i+1}(\phi)$ is obtained. From equation (2.23), the new estimate $\hat{s}^{i+1}(\phi)$ is given from $\hat{P}^{i+1}(\phi)$ by

$$\hat{s}^{i+1}(\phi) = \int (2 \sin \phi/2)^{1-\epsilon} \exp(\hat{P}^{i+1}(\phi))\, d\phi \tag{2.134}$$

Based on this new estimate for $s(\phi)$, the process is repeated until successive estimates cease to show a significant difference.

To illustrate the approach, the airfoil shown in figure 2-27 is analyzed for the velocity distribution at $\alpha = 10°$. In this case, the successive estimates for $s(\phi)$ may be compared with the true solution obtained from the inverse method. The given surface angle for the airfoil shown in figure 2-27 is depicted in figure 2-34. The first estimate for $s(\phi)$ is shown in figure 2-35 by the straight line from (0, 0) to (2π, s_{max}). Also shown in the figure are the successive estimates for the second, fourth and sixth iterations. As may be seen, the sixth iteration agrees almost perfectly with the true solution. As a point of interest, the mapping derivative for the second, fourth and sixth iterations is obtained and used to derive the airfoil corresponding to that stage of the iteration. The results are shown in figure 2-36. For clarity, the successive airfoils and the true airfoil are shown as computed directly from the mapping derivative. As may be seen, the mapping of the circle to the airfoil improves progressively, and after six iterations the airfoil generated is almost coincident with the true airfoil. Twelve iterations were required for convergence of the solution. In figure 2-37, the velocity distribution for $\alpha = 10°$ from the converged solution is compared with the true velocity distribution from the inverse method. As seen from figure 2-37, some discrepancies do exist. It is believed that these differences are caused by an insufficiently accurate integration scheme. Improvements in the integration will most likely lead to better agreement.

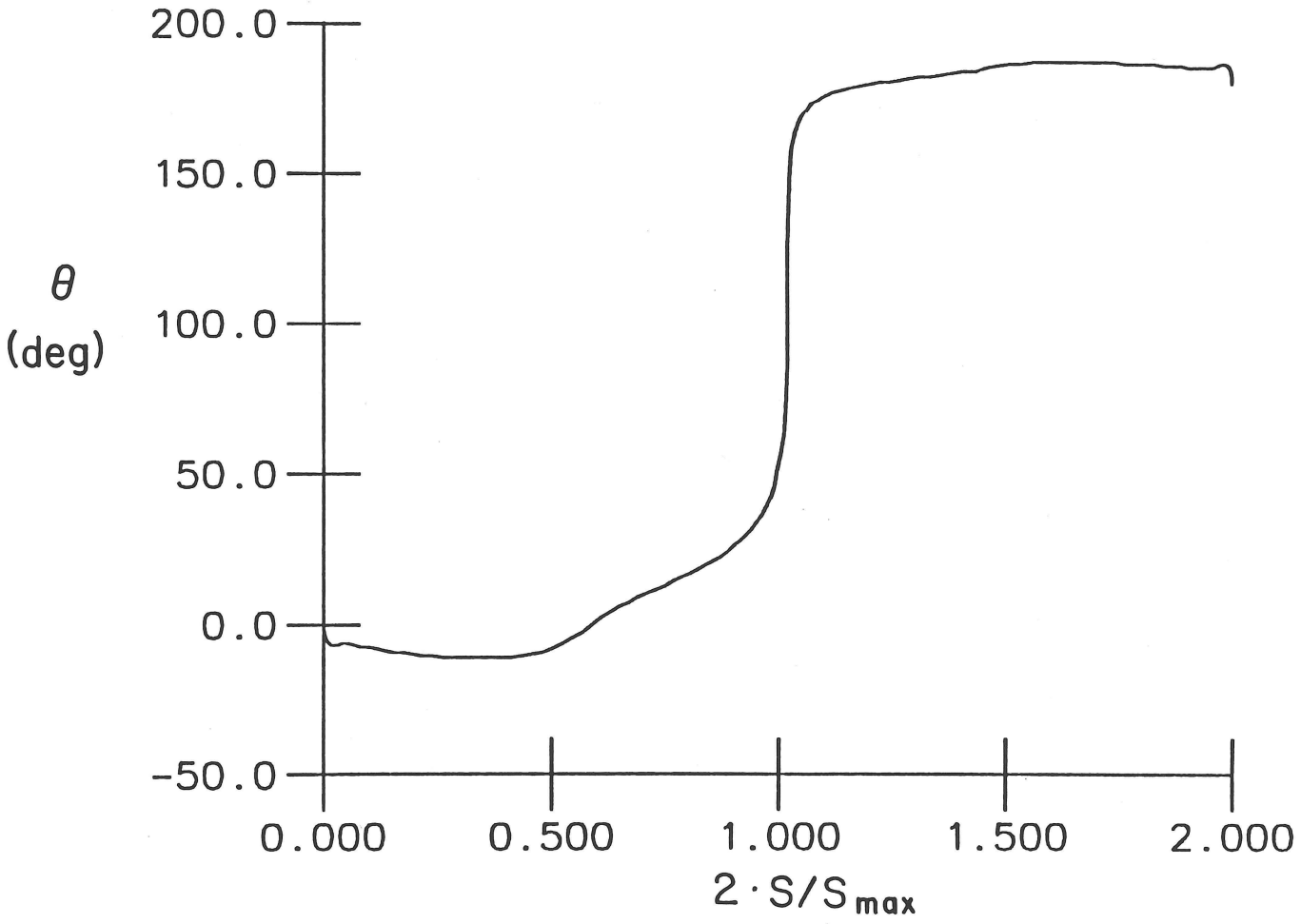

Figure 2-34 Surface angle distribution for airfoil of figure 2-27.

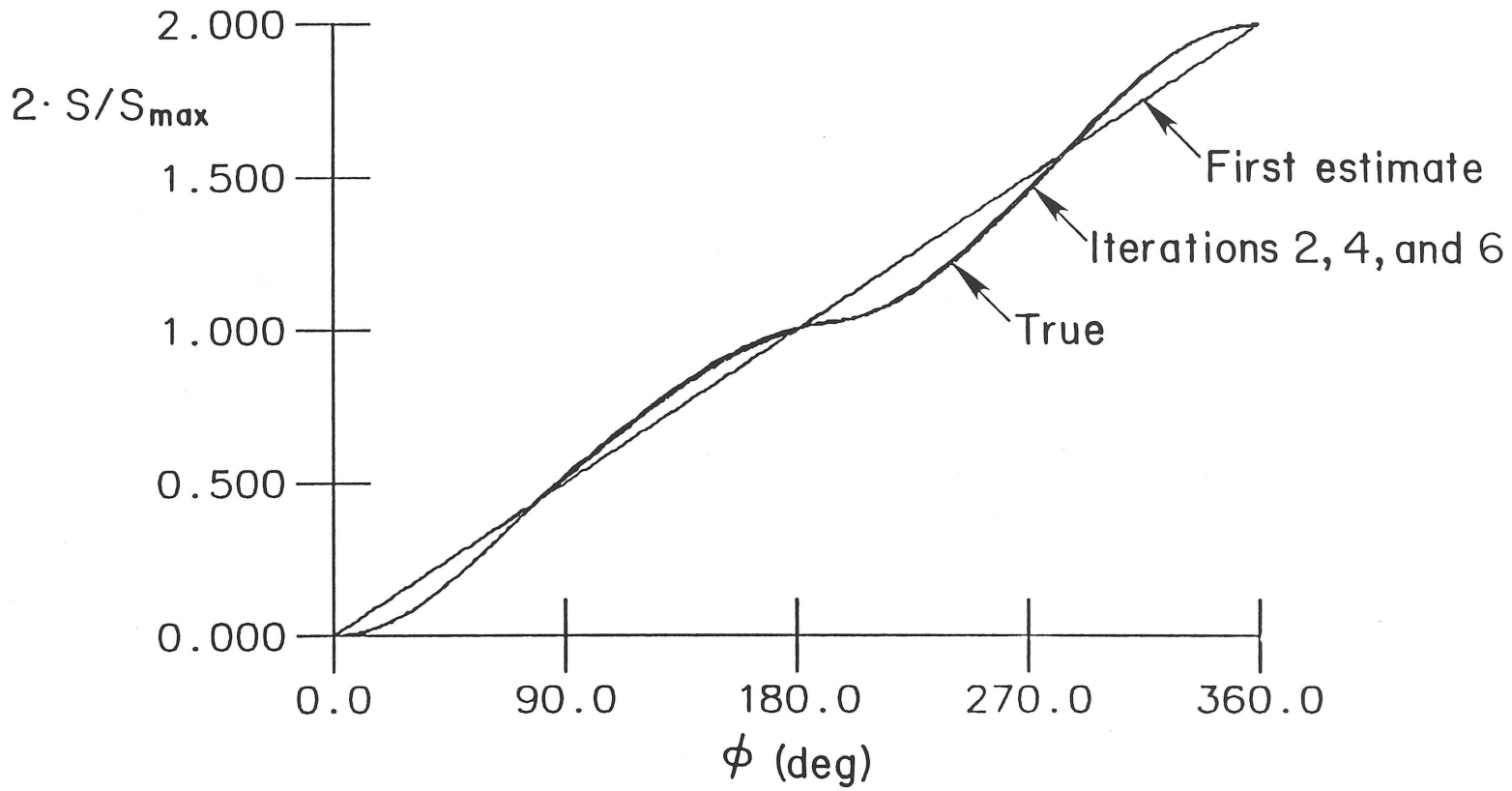

Figure 2-35 Initial estimate of $s(\phi)$, successive estimates for second, fourth and sixth iterations, and true solution for airfoil of figure 2-27.

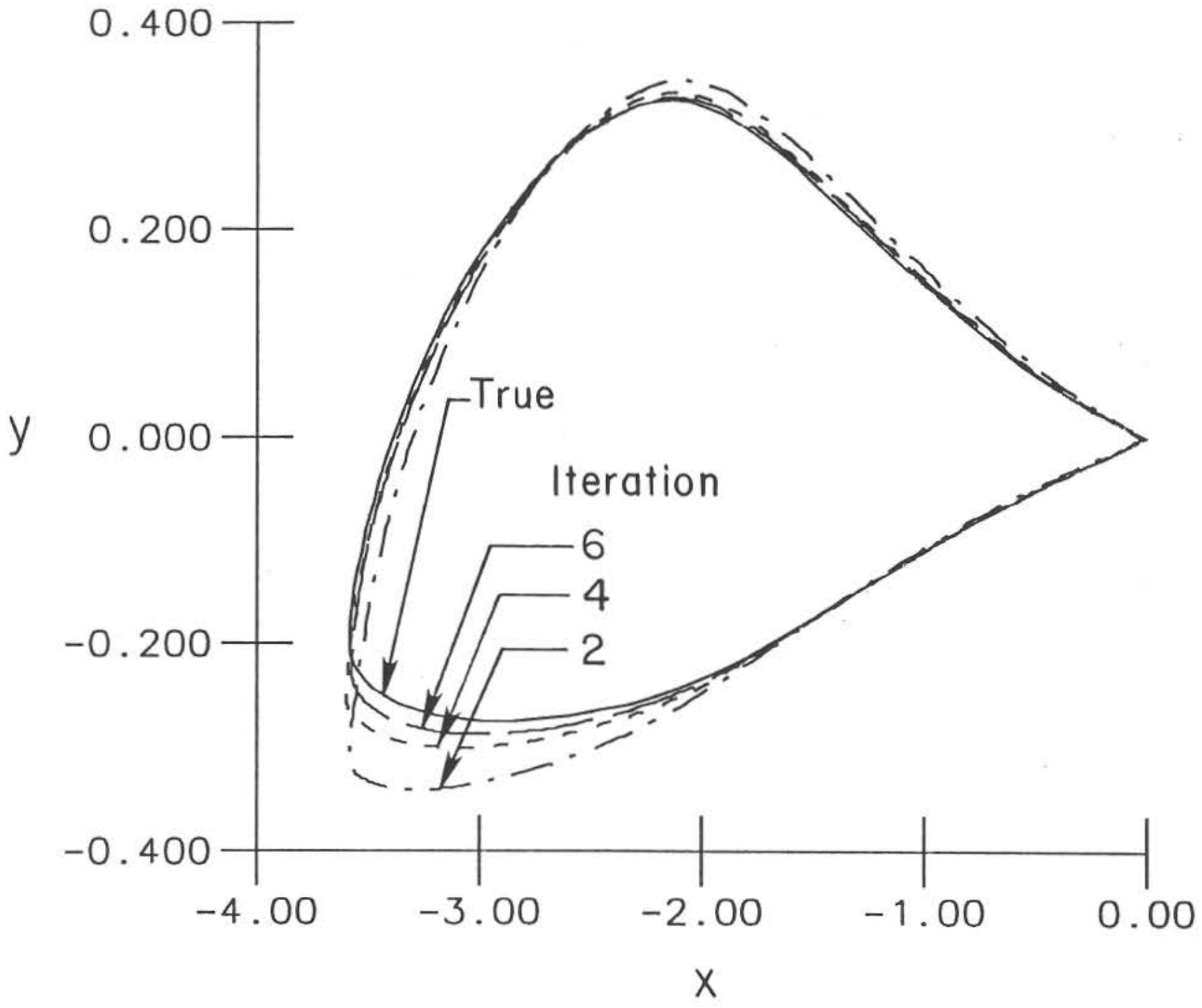

Figure 2-36 Airfoil resulting from the second, fourth and sixth iterations and true airfoil of figure 2-27.

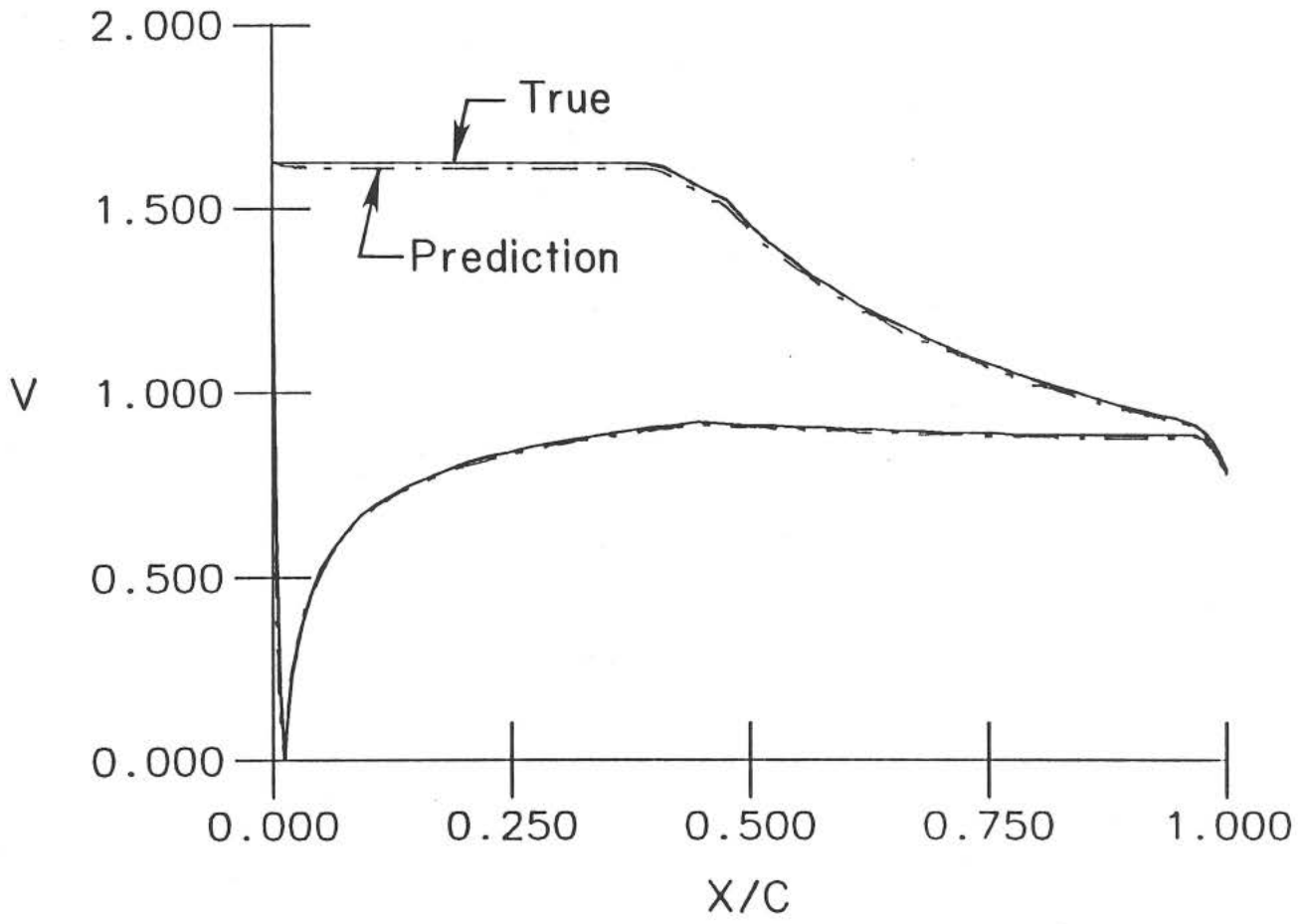

Figure 2-37 Comparison between the velocity distribution for $\alpha = 10°$ from the analysis method and inverse method for the airfoil of figure 2-27.

Chapter 3

INFINITE CASCADES OF AIRFOILS

Conceptually, what has been already been stated with regard to isolated airfoil design is equally applicable to cascade design. Specifically, a multi-point design capability is as important for cascades as it is for isolated airfoils. The same is true of the viscous design aspects of the problem and the need to achieve a given thickness ratio, pitching moment, etc. Of course, with a cascade, there is usually interest in achieving a desired stagger or solidity as defined in figure 3-1. This chapter will present a method that allows for multi-point inverse cascade design in a manner analogous to that presented in chapter 2 for the isolated airfoil. The viscous design part of the problem is, however, left for future extension of this work.

The determination of flows through infinite cascades by means of conformal mapping has developed along lines similar to those of the isolated airfoil. The early work of Joukowski (1916) and Weinig (1935) among others dealt mainly with the generation of exact solutions for flat plates in order to ascertain the basic flow patterns and correlate the turning angles with cascade stagger and solidity. Collar (1941) and Merchant and Collar (1941) were the first to generate exact solutions for cascade blades with finite thickness and camber in a manner somewhat analogous to the Joukowski airfoil problem. Using Theodorsen's method for isolated airfoil analysis, Garrick (1944) and Howell (1948) were among the first to solve the cascade analysis problem. Lighthill (1945*b*), Costello (1950), Costello, Cummings and Sinnette (1952), Rosenblatt and Woods (1956) and Papailiou (1967) have developed inverse methods, yet they allow only for single-point inverse cascade design. The lack of an existing method for multi-point inverse cascade design has provided the

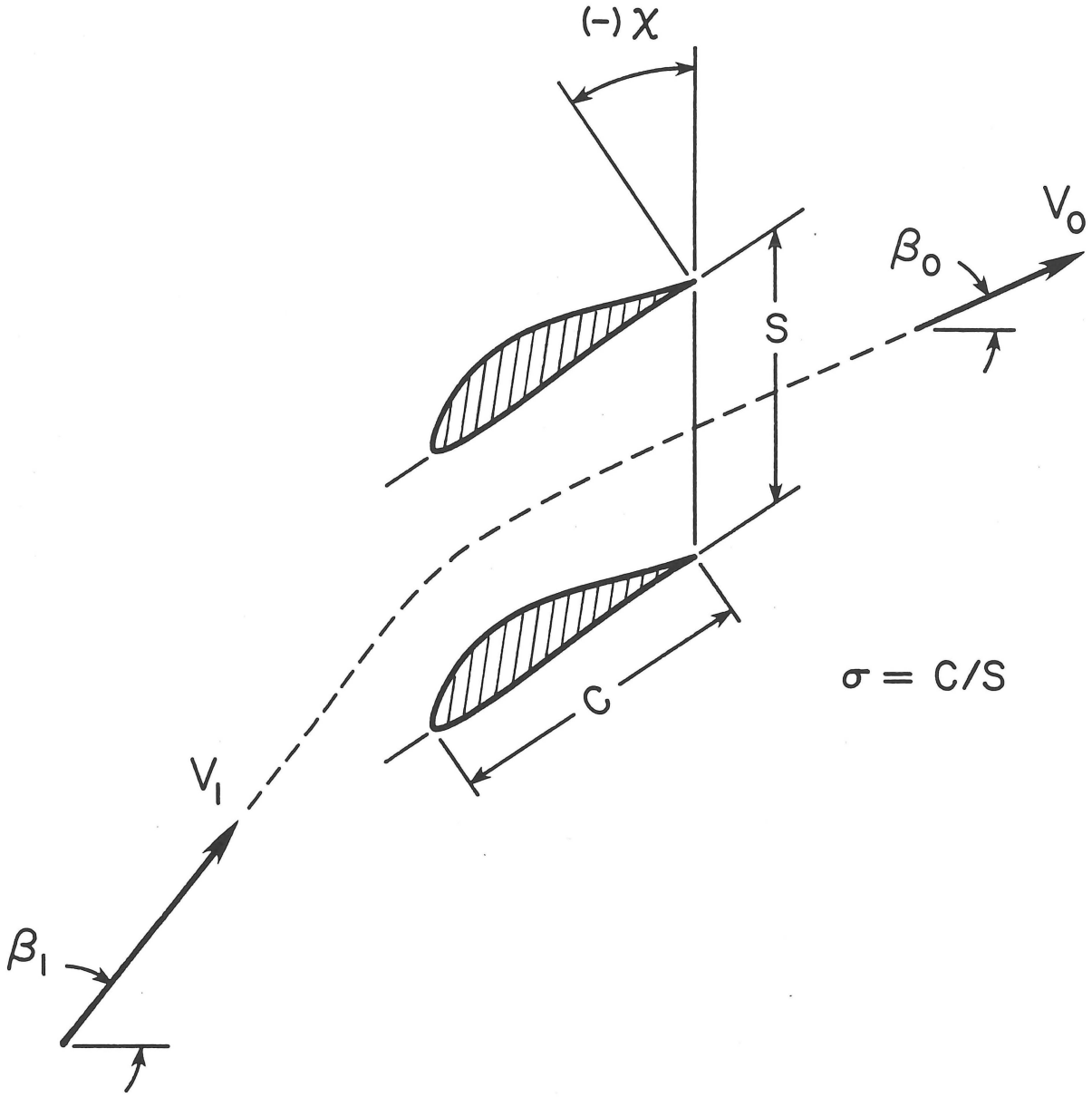

Figure 3-1 Cascade notation for a cascade with negative stagger.

impetus for this initiative.

That it must be possible to do multi-point inverse cascade design by conformal mapping is best illustrated by considering the derivative of the mapping function expressed as

$$\frac{dz}{d\zeta} = \frac{dF/d\zeta}{dF/dz} \tag{3.1}$$

where the z-plane is the physical cascade domain, ζ-plane is the mapped domain, and F is the complex potential function known in the ζ-plane based on conditions in the physical plane. It is important to keep in mind that the mapping only relates the geometry between the two planes (even though in the inverse problem the mapping is ultimately determined from the desired velocity distribution).

First to be discussed is the single-point inverse airfoil design problem in which the circle is mapped to an airfoil. For a given angle of attack α, the airfoil design velocity distribution $v_\alpha(\phi)$ is prescribed. Since dF/dz $[= v(\phi)e^{-i\theta(\phi)}]$ on the airfoil is an analytic function of ϕ, the flow direction $\theta(\phi)$ may be obtained from $v(\phi)$ to form dF/dz. Thus, to prescribe $v(\phi)$ is to prescribe dF/dz, so, for discussion, prescribing the velocity distribution $v(\phi)$ is taken to mean prescribing dF/dz. Of course, the velocity distribution must satisfy the integral constraints which arise from the conditions imposed on the mapping function; however, for the present discussion, it is not necessary to be concerned with this detail. Having prescribed the airfoil velocity distribution for the desired angle of attack, $dF/dz|_{\alpha_1}$, the circle velocity distribution at the same angle of attack is obtained, viz. $dF/d\zeta|_{\alpha_1}$. Taking the ratio of these velocity distributions according the equation (3.1) gives $dz/d\zeta$ from which the airfoil coordinates are then obtained by integration.

For multi-point inverse airfoil design, the key difference is that $dz/d\zeta$ is determined piecewise. For example, suppose that the airfoil upper-surface velocity

distribution is prescribed for α_1 and the lower-surface for α_2. The mapping derivative is then defined in two pieces: $dF/d\zeta|_{\alpha_1}/dF/dz|_{\alpha_1}$ on the upper surface and $dF/d\zeta|_{\alpha_2}/dF/dz|_{\alpha_2}$ on the lower surface. Of course, now dF/dz must satisfy not only the integral constraints for multi-point design but also the continuity conditions at the leading edge and trailing edge so as to maintain a piecewise continuous $dz/d\zeta$. This is another detail which is of no immediate concern. Introducing an additional segment with a new angle of attack only means defining $dz/d\zeta$ by another piece and so on for each new segment.

With respect to multi-point design, the inverse cascade problem and inverse airfoil problem are fundamentally the same. The inlet (or outlet) angle of the cascade may be considered as analogous to the airfoil freestream angle of attack. Thus, in the multi-point design case, the cascade velocity distribution is prescribed at the desired inlet (or outlet) angle for each of the desired number of segments. Taking the ratio of the velocity distribution in the mapped domain at the conditions corresponding to the prescribed cascade velocity distribution for each segment gives the mapping derivative in a piecewise manner from which the cascade blade is determined.

The solution to the inverse cascade design problem by conformal mapping is different from the inverse airfoil problem in that for the cascade no standard approach exists. There are many viable ways to express the mapping and many reasonable domains onto which the cascade can be mapped. Typically, several mappings are used in sequence to take the cascade into a circle or circles. For instance, Garrick (1944), Howell (1948) and Papailiou (1967) first use a suitable periodic mapping, for example, $\tanh z = f(z')$, to take the cascade [figure 3-2 (a)] into a single closed contour in the z'-plane [figure 3-2 (b)]. In this plane, points far upstream and down-

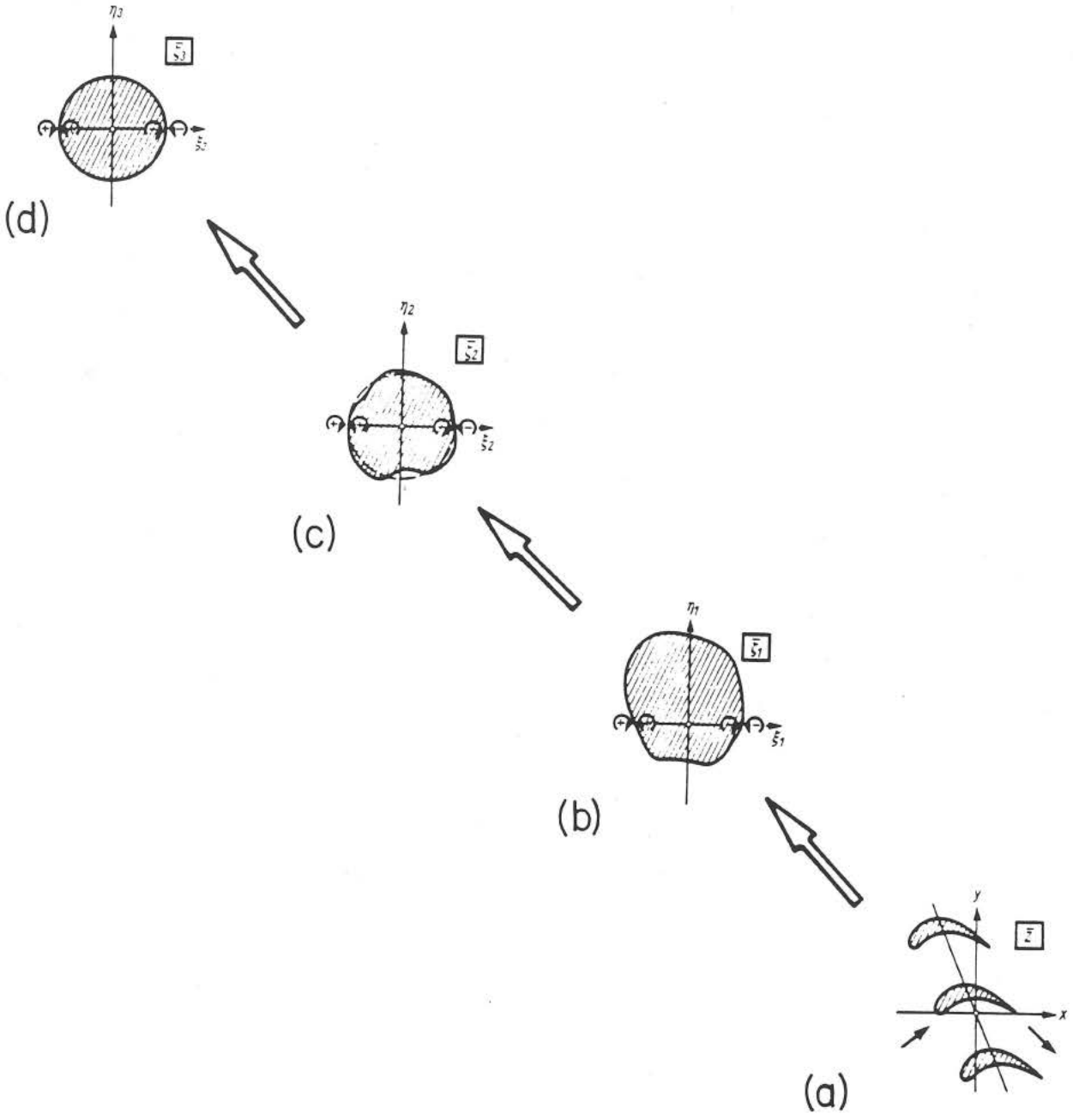

Figure 3-2 Typical mapping sequence used to take a cascade into a circle in the presence of two spirals: (*a*) cascade, (*b*) single closed contour, (*c*) near circle and (*d*) circle.
[Adapted from Scholz (1965).]

stream of the cascade are represented by a vortex-source and vortex-sink (spirals), respectively. Both of these spirals are at a finite distance from the single contour. Then through one or more regular mappings, this closed curve is taken to a nearly circular contour [figure 3-2 (*c*)]. Finally, Theodorsen's method is used to map this near circle [figure 3-2 (*d*)] to an exact circle about which the flow is known analytically. In a similar procedure, Traupel (1945) and Ives and Luitezmoza (1977) solve the problem on the interior of the domain, except Traupel does not go completely to the circle.

In a different approach, Lighthill (1945*b*) uses as a first mapping $e^z = z'$ to map the cascade into a single airfoil in the presence of a single spiral as shown in figure 3-3. In this case, points infinitely far upstream of the cascade are mapped to a vortex-source at a finite distance from the airfoil; whereas, points infinitely far downstream of the cascade are mapped to infinity. In the next step, the mapping derivative is introduced to take the airfoil in the presence of the vortex-source into a circle in the presence of the vortex-source.

For either one of these mapped domains, the cascade stagger and solidity are mainly related to the location of the spirals (figure 3-2) or spiral (figure 3-3) relative to the circle. The single-spiral case is to be considered for discussion, although similar arguments apply to the double-spiral case. In the design problem, the spiral location is specified in order to control (to first order) the stagger and solidity; whereas, in the analysis problem, the spiral location is determined by the geometry of the cascade. As the solidity of the cascade increases, the spiral moves closer to the circle. This may be explained as follows. Consider the cascade spacing to be a constant set by the mapping so that the solidity is changed only by the chord of the cascade blade. Because the spiral is mapped to infinitely far upstream of the

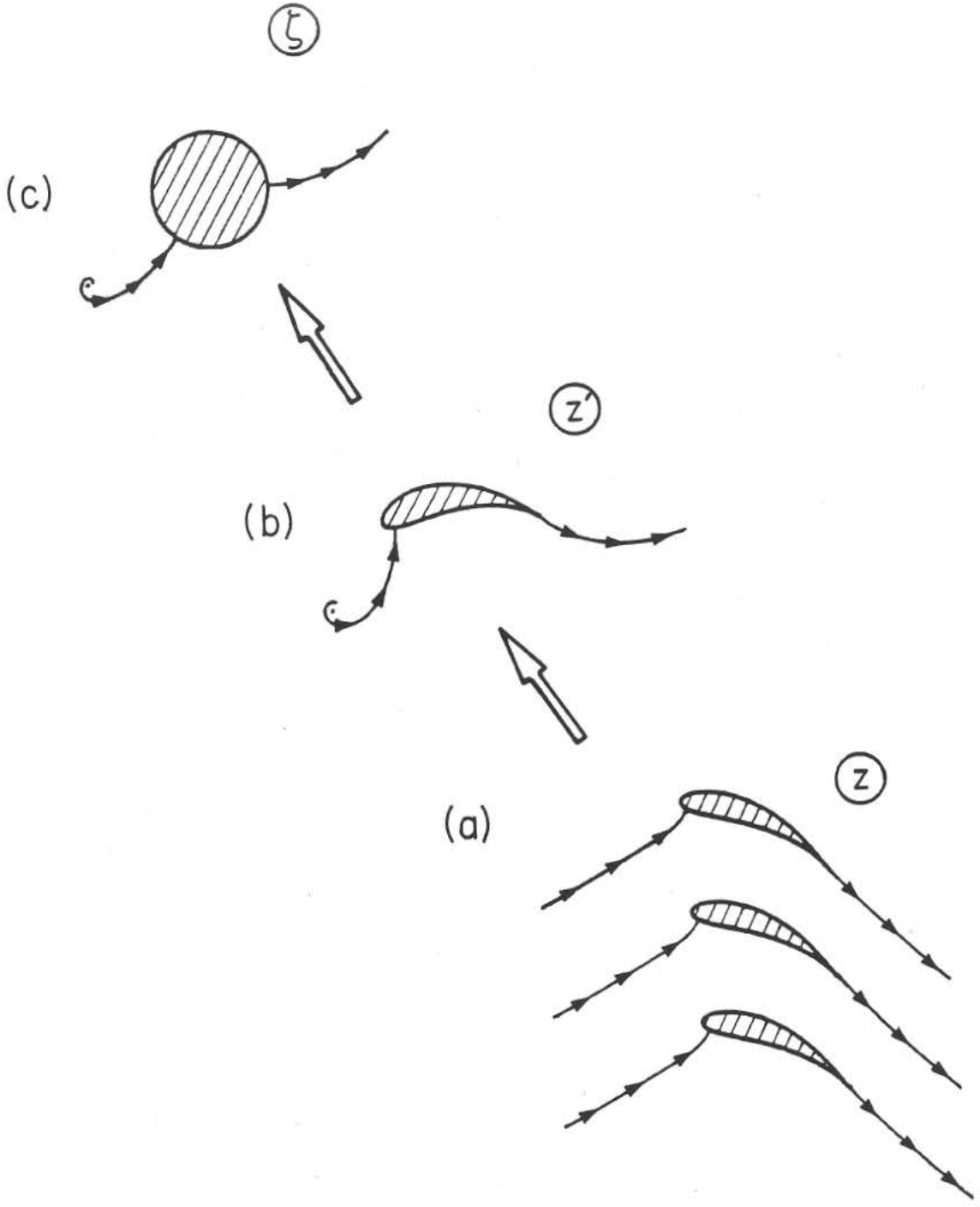

Figure 3-3 Lighthill's mapping sequence used to take a cascade into a circle in the presence of one spiral: (a) cascade, (b) single closed contour and (c) circle.

cascade, points very near the spiral tend to be mapped far upstream. Thus, as the spiral moves closer to the circle, the part of the circle nearest the spiral stretches upstream in the cascade plane; that is, the cascade-blade chord increases which in turn increases the solidity.

There is a practical limit to which the solidity may be increased by moving the spiral closer to the circle. For solidities greater than one (i.e., cascade spacings less than one chord), the spiral must be so close to the circle that the amount of stretching on the circle in the vicinity of the spiral can lead to cascade blades with only a few points left to define the leading edge (assuming that a practical number of equiangular points are used to define the circle). Examples will be presented later. This numerical difficulty renders methods which map to the single circle practical only for solidities up to one.

For solidities greater than one, other mapped domains have been successful. For instance, a suitable mapping is to take a cascade of ovals (Collar 1941; Collar and Merchant 1941; Gostelow 1965*a*,*b*) or circles (Goto and Shirakura 1984) into a cascade of airfoils. In a novel approach, Shirakura (1972) maps the annulus between two concentric circles in the presence of a vortex-source and vortex-sink into the infinite cascade. Another approach was suggested by Sanz (1988, 1991). The region exterior to an ellipse with points at infinity represented by a vortex-source and vortex-sink is mapped into the cascade. The advantage of using the ellipse as opposed to the circle is that the ellipse is elongated and does not therefore require as much stretching as the circle in order to give solidities greater than one. A difficulty associated with each of these methods, except the case of the ovals, is that the complex potential function in the mapped domain must be determined numerically. (Other mathematical difficulties are associated with the use of the ovals in the

inverse problem.) With the single circle, however, the complex potential function is readily obtainable using the Milne-Thomson circle theorem (Milne-Thomson 1958).

In the current approach, the cascade is mapped onto the single circle in the presence of a vortex-source. Therefore, from a practical standpoint in light of the aforementioned remarks, the method is only applicable for the design cascades with solidities up to one due to numerical difficulties that are otherwise encountered. As will be explained in detail later, the mapping is done in one step by introducing a general form of the mapping derivative. Using a single mapping and expressing the mapping in the derivative form greatly facilitates the mathematical formulation of the multi-point inverse design problem and leads to considerable numerical simplification as compared with the (less general) single-point inverse design methods (Lighthill 1945*b*; Costello 1950; Costello, Cummings and Sinnette 1952; Rosenblatt and Woods 1956; Papailiou 1967).

As a preliminary, a new, exact solution of the flow through an infinite cascade of airfoils with finite thickness and camber is presented for two reasons. First, the exact solution is new and considered valuable in itself. Second, the solution helps to establish some of the ideas applied in the inverse problem presented afterwards. Previous to the current approach, the only known exact solution to the flow through a cascade with blades of finite thickness and camber was due to Collar (1941), later extended by Merchant and Collar (1941) and Gostelow (1965*a*,*b*). The method of Collar (1941) is partly analogous to the Joukowski airfoil problem yet three mappings are used. As a result, the mathematical development is lengthy. In contrast, the current solution involves only a single mapping (one which has a very close connection to the Joukowski mapping). Moreover, the mathematical development is substantially simpler.

3.1 EXACT SOLUTIONS TO THE FLOW THROUGH INFINITE CASCADES OF AIRFOILS

It should be mentioned that exact solutions have application in assessing the accuracy of potential flow analysis methods. The most well-known and widely-referenced test case for such analysis methods is due to Gostelow (1965*a*,*b*) wherein tabulated data is provided only for one cascade at one inlet angle. As mentioned, the generation of further exact solutions from the theory of Gostelow is involved. The current approach provides a means of obtaining exact solutions in a relatively straightforward manner. It is surprising to the author that the current approach does not seem to have been done before. Several example cascades are presented to illustrate the method.

3.1.1 Cascade Mapping and Blade Coordinates

Although in the present theoretical development only one mapping is used to take the circle into an infinite cascade of airfoils, it is helpful to first explain this process in terms of its relationship to the Joukowski airfoil problem. A generating circle in the ζ-plane may be mapped to a Joukowski airfoil in the z'-plane by the mapping

$$z' = \zeta + c_0 + \frac{c_1}{\zeta} \tag{3.2}$$

where the circle passes through the point $\zeta = \zeta_T$ in which case c_1 is found to be ζ_T^2 in order to map the point $\zeta = \zeta_T$ to a cusp. The constant c_0, although arbitrary in the Joukowski airfoil problem, has a special effect through the application of a second mapping. As mentioned, Lighthill (1945*b*) uses the mapping

$$e^z = z' \tag{3.3}$$

to map an infinite cascade of airfoils in the z-plane onto a single airfoil in the z'-plane. By applying this mapping in the inverse sense, the single Joukowski airfoil in the z'-plane can be mapped into an infinite cascade of airfoils in the z-plane. Points infinitely far downstream ($z = x + iy \rightarrow \infty$) of the cascade in the z-plane are mapped to infinity in the z'-plane, and points infinitely far upstream ($z = x + iy \rightarrow -\infty$) of the cascade are mapped to the origin. Infinitely far upstream and downstream, the y-coordinate is arbitrary since the mapping is periodic in y. As a result, the geometry of the cascade (mainly stagger and solidity) is largely dictated by the placement of the Joukowski airfoil with respect to the origin as determined by the constant c_0 in equation (3.2)

The Joukowski mapping and the Lighthill mapping may be combined into a single mapping. Substituting equation (3.2) into (3.3) gives

$$e^z = \zeta + c_0 + \frac{c_1}{\zeta} \tag{3.4}$$

As with the Joukowski airfoil problem, the generating circle is in this case centered on or to the left of the η-axis and is required to pass through the point $\zeta = \zeta_T$ as indicated in figure 3-4, which shows the mapping from the circle to the cascade.

Two conditions on the mapping are used to determine the coefficients c_0 and c_1. First, in order to make the infinite cascade an infinite cascade of airfoils, the point $\zeta = \zeta_T$ must be a critical point of the mapping. Equation (3.4) gives

$$\frac{dz}{d\zeta} = \frac{\left(1 - \frac{\sqrt{c_1}}{\zeta}\right)\left(1 + \frac{\sqrt{c_1}}{\zeta}\right)}{\zeta + c_0 + \frac{c_1}{\zeta}} \tag{3.5}$$

Therefore, the condition that $\zeta = \zeta_T$ be a critical point is satisfied only when

$$c_1 = \zeta_T^2 \tag{3.6}$$

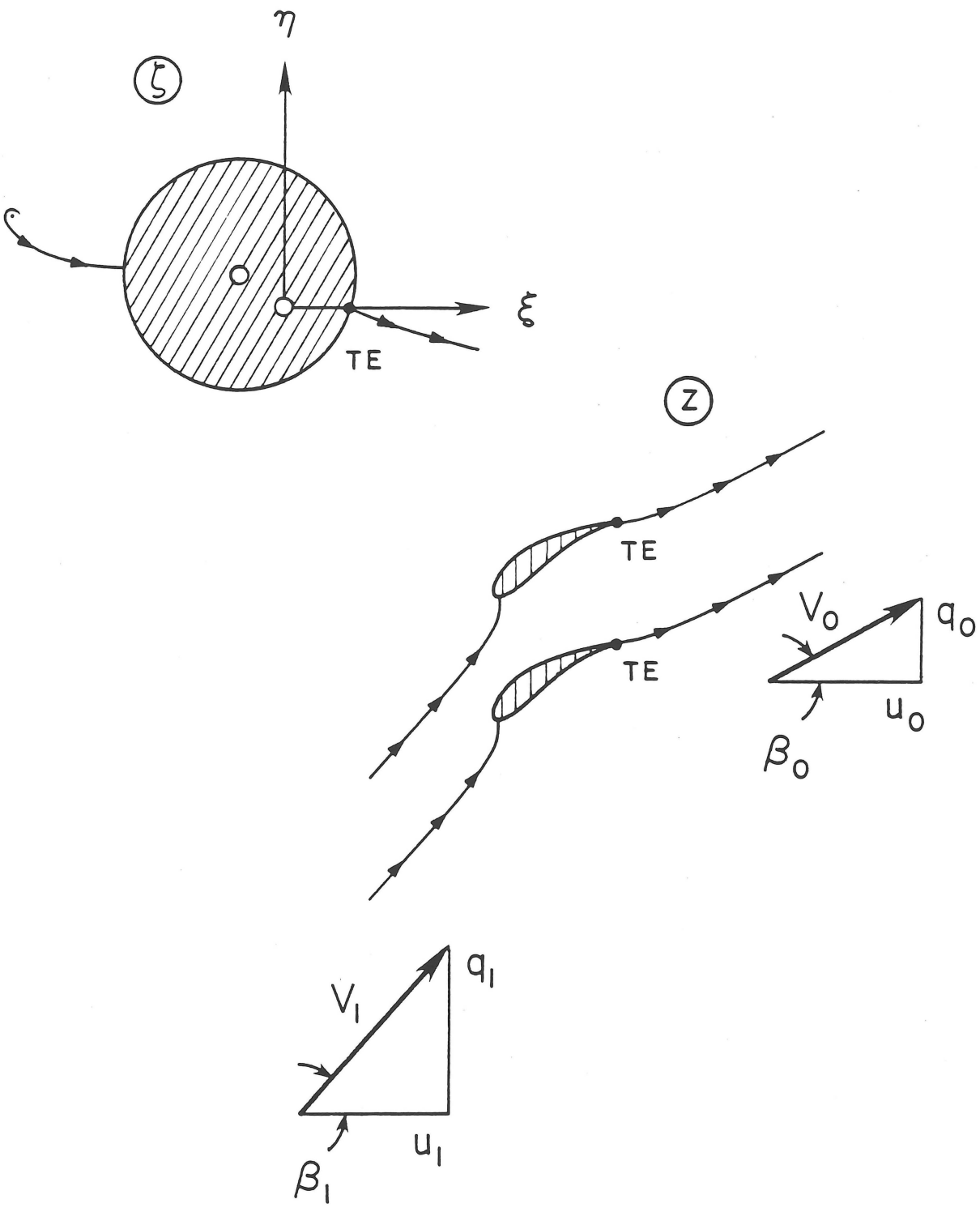

Figure 3-4 Mapping from the offset circle to the infinite cascade.

By inspection, then, the point $\zeta = \zeta_T$ is mapped to a cusp as anticipated. A second condition is that points infinitely far upstream of the cascade must map to the point $\zeta = a$ outside of the circle, that is,

$$\lim_{z \to -\infty} e^z = \lim_{\zeta \to a} \left[\zeta + c_0 + \frac{c_1}{\zeta} \right] \tag{3.7}$$

or

$$0 = a + c_0 + \frac{c_1}{a} \tag{3.8}$$

which together with equation (3.6) gives

$$c_0 = -a - \frac{\zeta_T^2}{a} \tag{3.9}$$

With equations (3.6) and (3.9), the mapping (3.4) and its derivative (3.5) are given by

$$e^z = \zeta - a - \frac{\zeta_T^2}{a} + \frac{\zeta_T^2}{\zeta} = (\zeta - a)\left(1 - \frac{\zeta_T^2}{a\zeta}\right) \tag{3.10}$$

and

$$\frac{dz}{d\zeta} = \frac{\left(1 - \frac{\zeta_T}{\zeta}\right)\left(1 + \frac{\zeta_T}{\zeta}\right)}{(\zeta - a)\left(1 - \frac{\zeta_T^2}{a\zeta}\right)} = \frac{a(\zeta - \zeta_T)(\zeta + \zeta_T)}{\zeta(\zeta - a)(a\zeta - \zeta_T^2)} \tag{3.11}$$

To summarize, the single mapping (3.10) does in one step what would otherwise take two steps. It remains to determine the cascade geometry and ultimately the cascade velocity distribution.

In order to express the equations in the simplest form, two coordinate systems are used in the circle plane as shown in figure 3-5. The ζ'-coordinate system is centered on the generating circle which is offset from the ζ-origin by the constant μ such that points ζ' and ζ are related by

$$\zeta = \xi + i\eta = \zeta' + \mu \tag{3.12}$$

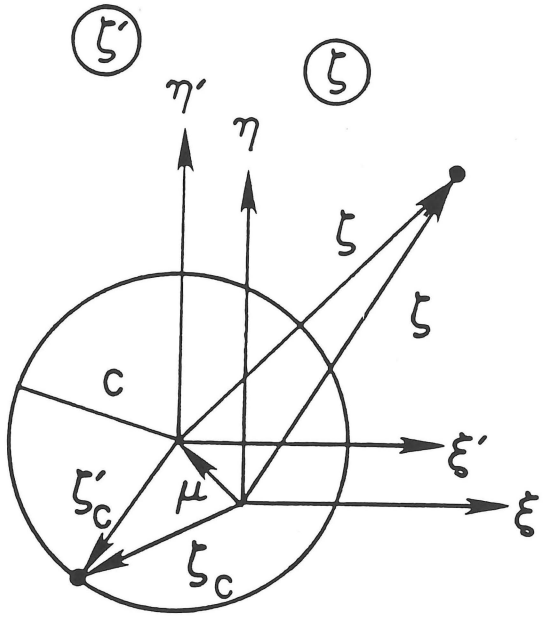

Figure 3-5 Generating circle indicating coordinate systems and circle orientation.

On the boundary of the circle

$$\zeta = \zeta_c = \xi_c + i\,\eta_c = \zeta_c' + \mu \tag{3.13}$$

where the subscript 'c' is used to denote coordinates defining the circle. The mapping is defined once the point $\zeta = a$ is specified to determine $c_0 = a_0 + i\,b_0$ according to equation (3.9). With the generating circle and the mapping known, the cascade blade coordinates $z_c = x_c + i\,y_c$ are defined by

$$e^{x_c + i\,y_c} = \xi_c + i\,\eta_c + a_0 + i\,b_0 + \frac{\zeta_T^2}{\xi_c + i\,\eta_c} \tag{3.14}$$

which gives

$$\tan y_c = \frac{\eta_c + b_0 - \dfrac{\zeta_T^2\,\eta_c}{\xi_c^2 + \eta_c^2}}{\xi_c + a_0 + \dfrac{\zeta_T^2\,\xi_c}{\xi_c^2 + \eta_c^2}} \tag{3.15a}$$

and

$$e^{x_c} = \frac{\xi_c + a_0 + \dfrac{\zeta_T^2\,\xi_c}{\xi_c^2 + \eta_c^2}}{\cos y_c} \tag{3.15b}$$

Equation (3.15a) is used to find y_c which is then used in equation (3.15b) to give x_c. As seen through the mapping (3.4) or (3.15a) the blade spacing is set at $2\pi i$.

3.1.2 Complex Potential Function

In order to determine the cascade velocity distribution, it is first necessary to find the complex potential $F(\zeta)$ in the circle plane. To this end, the complex velocity in the circle plane is expressed as

$$\frac{dF}{d\zeta} = \frac{dF}{dz}\frac{dz}{d\zeta} \tag{3.16}$$

As indicated in figure 3-4 by the inlet flow and outlet flow, the complex velocity far upstream of the cascade is known to be

$$\lim_{z\to-\infty}\frac{dF}{dz} = u_I - i\,q_I \tag{3.17a}$$

while downstream

$$\lim_{z\to\infty}\frac{dF}{dz} = u_O - i\,q_O \tag{3.17b}$$

The corresponding complex velocity at these points in the circle plane is expressed as

$$\lim_{\zeta\to a}\frac{dF}{d\zeta} = \lim_{z\to-\infty}\frac{dF}{dz}\cdot\lim_{\zeta\to a}\frac{dz}{d\zeta} \tag{3.18a}$$

and

$$\lim_{\zeta\to\infty}\frac{dF}{d\zeta} = \lim_{z\to\infty}\frac{dF}{dz}\cdot\lim_{\zeta\to\infty}\frac{dz}{d\zeta} \tag{3.18b}$$

In the limit, these equations give with equations (3.11) and (3.17a,b)

$$\lim_{\zeta\to a}\frac{dF}{d\zeta} = \frac{u_I - i\,q_I}{\zeta - a} \tag{3.19a}$$

and

$$\lim_{\zeta\to\infty}\frac{dF}{d\zeta} = \frac{u_O - i\,q_O}{\zeta} \tag{3.19b}$$

Thus, there exists outside the circle two spirals—one at $\zeta = a$ and another at $\zeta \to \infty$.

In a partly heuristic manner, the complex potential characterized by the two singularities indicated in equations (3.19a,b) is obtained by considering the flow depicted in figure 3-6. The spiral at $\zeta = a$, which in reference to the ζ'-plane is at $\zeta' = b$ as shown in figure 3-7, must have its reflection inside the circle. Likewise, the spiral at $\zeta \to \infty$ must have its reflection inside the circle, in particular at $\zeta' = 0$. Since the spiral at $\zeta = a$ corresponds to the inlet flow, it acts as a vortex-source,

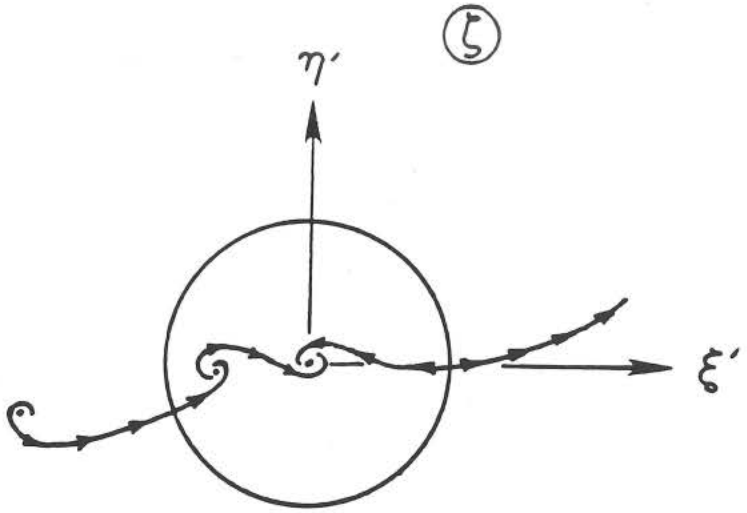

Figure 3-6 Flow in the circle plane due to the spirals at $\zeta' = b$ and $\zeta' \to \infty$ exterior to the circle with reflection interior to the circle.

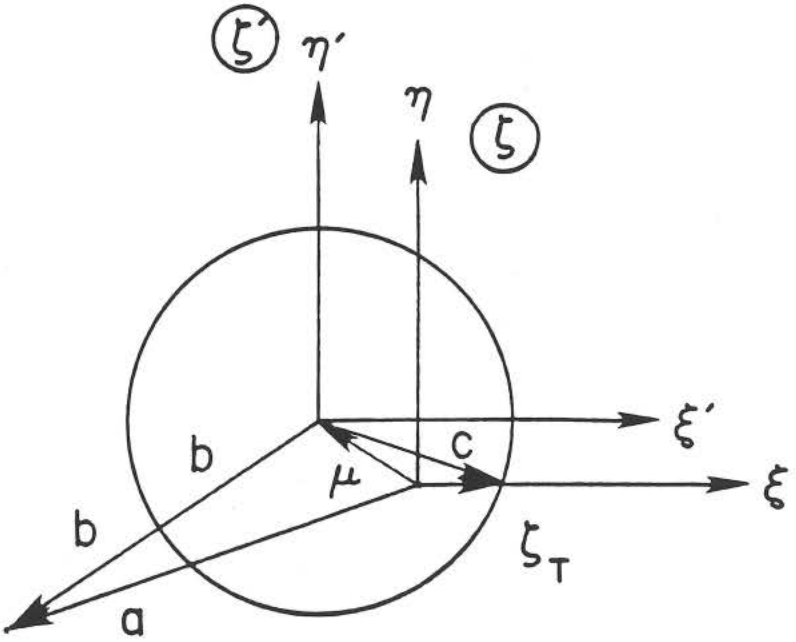

Figure 3-7 Circle offset, spiral locations and trailing-edge image as referenced in the ζ- and ζ'-coordinate systems.

and its reflection must be a vortex of opposite sign and a source of equal strength. This source interior to the circle must flow to the origin under the action of a sink of equal strength so as to maintain continuity of flow within the circle.

As shown in figure 3-8, a circle centered on the ζ'-plane origin is to be added to the flow produced by a vortex-source at the point $\zeta' = b$ so as to represent the image of the cascade inlet flow. For the vortex-source by itself, the complex potential is expressed as

$$F(\zeta) = Q \ln(\zeta' - b) - i\,\Gamma_I \ln(\zeta' - b) \tag{3.20}$$

Using the Milne-Thomson circle theorem (Milne-Thomson 1958), the complex potential with the circle added is found to be

$$\begin{aligned} F(\zeta) = {} & Q[\ln(\zeta' - b) + \ln(c\bar{c} - \bar{b}\zeta') - \ln \zeta'] \\ & - i\,\Gamma_I[\ln(\zeta' - b) + \ln(c\bar{c} - \bar{b}\zeta') - \ln \zeta'] \end{aligned} \tag{3.21}$$

As a result of adding the circle to the flow, the reflection of the source at $\zeta' = b$ is found at $\zeta' = c\bar{c}/b$ within the circle. This source inside the circle flows to the sink at the origin which is the reflection of the sink at infinity. Similarly, a vortex of strength Γ_I at $\zeta' = c\bar{c}/b$ is the reflection of the vortex of strength $-\Gamma_I$ at $\zeta' = b$. Likewise, a vortex of strength Γ_I at the origin is the reflection of a vortex of strength $-\Gamma_I$ at infinity. By equation (3.19*b*), however, the vortex strength at infinity is related to q_O while the vortex strength at $\zeta' = b$ is related to q_I. To allow for this type of dependence in the complex potential, the vortex at the origin is subtracted from the complex potential (3.21) and a vortex of strength $-\Gamma_O$ is added to the origin. Under this operation, the streamfunction on the circle remains a constant, so the circle remains a streamline of the flow as is required. In this case, the complex potential becomes

$$F(\zeta') = Q[\ln(\zeta' - b) + \ln(c\bar{c} - \bar{b}\zeta') - \ln \zeta']$$

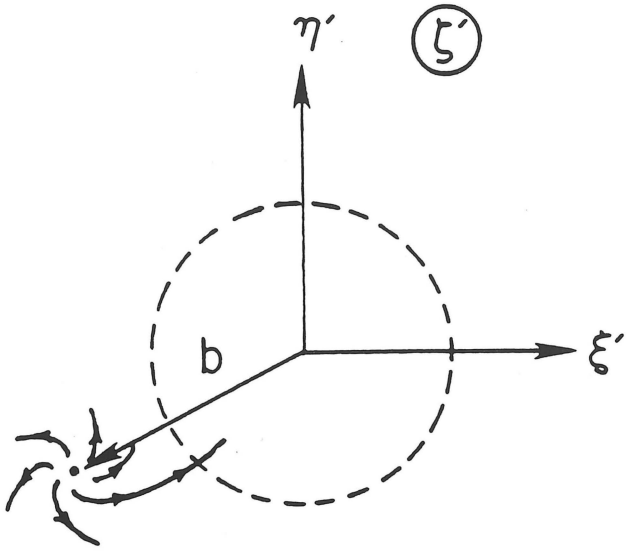

Figure 3-8 Outline of the circle which is to be made a streamline of the flow due to a spiral at $\zeta' = b$.

$$- i\,\Gamma_I[\ln(\zeta' - b) + \ln(c\bar{c} - \bar{b}\zeta')]$$

$$- i\,\Gamma_O[\ln \zeta'] \tag{3.22}$$

3.1.3 Kutta Condition

The point on the circle $\zeta = \zeta_T$ which maps to the trailing edge is made a stagnation point of the flow by the condition that

$$\left.\frac{dF}{d\zeta}\right|_{\zeta=\zeta_T} = 0 \tag{3.23}$$

or using the chain rule

$$\left.\frac{dF}{d\zeta'}\frac{d\zeta'}{d\zeta}\right|_{\zeta'=c} = 0 \tag{3.24}$$

where $c = \zeta_T - \mu$ according to equation (3.12) and as seen in figure 3-7. Since $d\zeta'/d\zeta = 1$, the Kutta condition becomes

$$\left.\frac{dF}{d\zeta'}\right|_{\zeta'=c} = 0 \tag{3.25}$$

Through equation (3.22), it is found that

$$\frac{dF}{d\zeta'} = \frac{Q[bc\bar{c} - \bar{b}\zeta'^2] - i\,\Gamma_I[\zeta'(c\bar{c} - b\bar{b})] - i\,\Gamma_O[(\zeta' - b)(c\bar{c} - \bar{b}\zeta')]}{\zeta'(\zeta' - b)(c\bar{c} - \bar{b}\zeta')} \tag{3.26}$$

Applying the Kutta condition (3.25) requires

$$i\,\Gamma_I = \frac{Q(b\bar{c} - \bar{b}c) - i\,\Gamma_O(c - b)(\bar{c} - \bar{b})}{c\bar{c} - b\bar{b}} \tag{3.27}$$

Substituting equation (3.27) back into (3.26) gives

$$\frac{dF}{d\zeta'} = \frac{Q[c(bc\bar{c} - \bar{b}\zeta'^2) - \zeta'(bc\bar{c} - \bar{b}c^2)] - i\,\Gamma_O[c(\zeta' - b)(c\bar{c} - \bar{b}\zeta') - \zeta'(c - b)(c\bar{c} - \bar{b}c)]}{c\zeta'(\zeta' - b)(c\bar{c} - \bar{b}\zeta')} \tag{3.28}$$

or in its most convenient form

$$\frac{dF}{d\zeta'} = -\left(1 - \frac{c}{\zeta'}\right) \frac{b(Q + i\,\Gamma_o)\bar{c} + \bar{b}(Q - i\,\Gamma_o)\zeta'}{(\zeta' - b)(c\bar{c} - \bar{b}\zeta')} \tag{3.29}$$

3.1.4 Inlet and Outlet Conditions

The outlet flow condition yields

$$\lim_{z\to\infty} \frac{dF}{dz} = \lim_{\zeta\to\infty} \frac{dF/d\zeta}{dz/d\zeta} = \frac{\lim\limits_{\zeta'\to\infty} dF/d\zeta'}{\lim\limits_{\zeta\to\infty} dz/d\zeta} \tag{3.30}$$

where $d\zeta'/d\zeta = 1$ has been used. After substituting in equations (3.11), (3.19b), and (3.29) and realizing that $\zeta' - b = \zeta - a$, equation (3.30) gives in the limit

$$u_o - i\,q_o = Q - i\,\Gamma_o \tag{3.31}$$

which yields

$$Q = u_o \qquad \text{and} \qquad \Gamma_o = q_o \tag{3.32a, b}$$

In a similar procedure, the inlet flow condition gives

$$\lim_{z\to-\infty} \frac{dF}{dz} = \frac{\lim\limits_{\zeta'\to b} dF/d\zeta'}{\lim\limits_{\zeta\to a} dz/d\zeta} \tag{3.33}$$

Taking the limit yields

$$u_I - i\,q_I = -\left(1 - \frac{c}{b}\right) \frac{b(u_o + i\,q_o)\bar{c} + \bar{b}(u_o - i\,q_o)b}{c\bar{c} - b\bar{b}} \tag{3.34}$$

or

$$u_I - i\,q_I = u_o + \frac{-u_o(b\bar{c} - \bar{b}c) + i\,q_o(c - b)(\bar{c} - \bar{b})}{c\bar{c} - b\bar{b}} \tag{3.35}$$

By comparison with the Kutta condition (3.27) and equation (3.32a,b), it is found by inspection that

$$u_I = u_o \qquad \text{and} \qquad \Gamma_I = q_I \tag{3.36}$$

In view of this result, the complex velocity becomes taking $u_I = u_O = u$

$$\frac{dF}{d\zeta'} = -\left(1 - \frac{c}{\zeta'}\right)\frac{b(u + i\,q_O)\bar{c} + \bar{b}(u - i\,q_O)\zeta'}{(\zeta' - b)(c\bar{c} - \bar{b}\zeta')} \tag{3.37}$$

Not only is equation (3.35) important in the determination of the vortex strength Γ_I, it also relates the flow variables u, q_I, and q_O. If u is known, q_O can be determined from q_I, and visa versa. This relationship can be clearly expressed by letting

$$c = Ce^{i\omega} \qquad \text{and} \qquad b = Be^{i\psi} \tag{3.38a, b}$$

$$\gamma = \psi - \omega \tag{3.38c}$$

$$\tan\beta_I = \frac{q_I}{u} \qquad \text{and} \qquad \tan\beta_O = \frac{q_O}{u} \tag{3.38d, e}$$

Using these relations and observing that

$$b\bar{c} - \bar{b}c = 2iBC\sin\gamma \tag{3.39a}$$

$$(c - b)(\bar{c} - \bar{b}) = C^2 - 2BC\cos\gamma + B^2 \tag{3.39b}$$

$$c\bar{c} - b\bar{b} = C^2 - B^2 \tag{3.39c}$$

equation (3.35) becomes

$$2BC\sin\gamma - (C^2 - B^2)\tan\beta_I - (C^2 - 2BC\cos\gamma + B^2)\tan\beta_O = 0 \tag{3.40}$$

As a result, depending on the circle and spiral location, if the inlet flow angle β_I is known, β_O is uniquely related, and visa versa. In the special case for which there is no turning through the cascade (the zero-lift case), $\beta_I = \beta_O = \beta_{ZL}$ which through equation (3.40) is found from

$$\tan\beta_{ZL} = \frac{B\sin\gamma}{C - B\cos\gamma} \tag{3.41}$$

3.1.5 Cascade Velocity Distribution

Finally, with the complex potential function defined in terms of the cascade flow variables, the complex velocity in the cascade plane is obtained from

$$\frac{dF}{dz} = \frac{dF/d\zeta}{dz/d\zeta} = \frac{(dF/d\zeta')(d\zeta'/d\zeta)}{dz/d\zeta} = \frac{dF/d\zeta'}{dz/d\zeta} \tag{3.42}$$

together with equations (3.11) and (3.37). In particular, the magnitude of the velocity distribution about the cascade is given by

$$\left|\frac{dF}{dz}\right|_{z=z_c} = \frac{|dF/d\zeta'|_{\zeta'=\zeta'_c}}{|dz/d\zeta|_{\zeta=\zeta_c}} \tag{3.43}$$

except at the trailing edge for which the above equation is indeterminate by the factor $0/0$. As will be shown, the trailing-edge velocity can be obtained by applying L'Hopital's Rule.

On the circle where $\zeta' = \zeta'_c = Ce^{i\phi}$, the complex velocity from equation (3.37) is

$$\left.\frac{dF}{d\zeta'}\right|_{\zeta'=\zeta'_c} = -\left(1 - \frac{c}{\zeta'}\right)\left.\frac{b(u + i\,q_o)\bar{c} + \bar{b}(u - i\,q_o)\zeta'}{(\zeta' - b)(c\bar{c} - \bar{b}\zeta')}\right|_{\zeta'=\zeta'_c} \tag{3.44}$$

As may be shown

$$\left.\left(1 - \frac{c}{\zeta'}\right)\right|_{\zeta'=\zeta'_c} = 2ie^{i\omega/2}e^{-i\phi/2}\sin(\phi/2 - \omega/2) \tag{3.45a}$$

$$b(u + i\,q_o)\bar{c} + \bar{b}(u - i\,q_o)\zeta'|_{\zeta'=\zeta'_c} =$$

$$2BCV_o(\beta_o)e^{-i\omega/2}e^{i\phi/2}\cos(\psi + \beta_o - \omega/2 - \phi/2) \tag{3.45b}$$

$$(\zeta' - b)(c\bar{c} - \bar{b}\zeta')|_{\zeta'=\zeta'_c} = Ce^{i\phi}(C^2 - 2BC\cos(\psi - \phi) + B^2) \tag{3.45c}$$

which when substituted into (3.44) gives

$$\left.\frac{dF}{d\zeta'}\right|_{\zeta'=\zeta'_c} = \frac{4BV_o(\beta_o)\sin(\phi/2 - \omega/2)\cos(\psi + \beta_o - \omega/2 - \phi/2)}{C^2 - 2BC\cos(\psi - \phi) + B^2}\,\frac{e^{i\phi}}{i} \tag{3.46}$$

In exponential form, this becomes

$$\left.\frac{dF}{d\zeta'}\right|_{\zeta'=\zeta_c'} = \frac{4BV_o(\beta_o)\sin(\phi/2-\omega/2)|\cos(\psi+\beta_o-\omega/2-\phi/2)|}{C^2-2BC\cos(\psi-\phi)+B^2}\, e^{i(\phi-\pi/2-\pi^*(\phi))} \tag{3.47}$$

where

$$\pi^*(\phi) = \begin{cases} 0, & \omega \le \phi \le 2(\psi+\beta_o)-\pi-\omega \\ \pi, & 2(\psi+\beta_o)-\pi-\omega \le \phi \le 2\pi+\omega \end{cases} \tag{3.48}$$

The mapping derivative $dz/d\zeta$ on the circle $\zeta = \zeta_c$ is found numerically to give $|dz/d\zeta|_{\zeta=\zeta_c}$. With this and $|dF/d\zeta'|_{\zeta'=\zeta_c'}$ from equation (3.47), the velocity distribution (excluding the trailing-edge point) is obtained by equation (3.43).

At the trailing-edge of the cascade blade, z_T, the velocity is found by

$$\lim_{z\to z_T}\frac{dF}{dz} = \frac{-\left.\dfrac{b(u+i\,q_o)\bar{c}+\bar{b}(u-i\,q_o)\zeta'}{(\zeta'-b)(c\bar{c}-\bar{b}\zeta')}\right|_{\zeta'=c}}{\left.\dfrac{a(\zeta+\zeta_T)}{(\zeta-a)(a\zeta-\zeta_T^2)}\right|_{\zeta=\zeta_T}} \cdot \frac{\lim\limits_{\zeta'\to c}\left(1-\dfrac{c}{\zeta'}\right)}{\lim\limits_{\zeta\to\zeta_T}\left(1-\dfrac{\zeta_T}{\zeta}\right)} \tag{3.49}$$

From L'Hopital's rule

$$\frac{\lim\limits_{\zeta'\to c}\left(1-\dfrac{c}{\zeta'}\right)}{\lim\limits_{\zeta\to\zeta_T}\left(1-\dfrac{\zeta_T}{\zeta}\right)} = \frac{\zeta_T}{c} \tag{3.50}$$

Using this result, equations (3.45*a,b*) and

$$|\zeta_T-a|^2 = \zeta_T^2-2A\zeta_T\cos\alpha+A^2 \tag{3.51}$$

where $a = Ae^{i\,\alpha}$ eventually gives

$$\left|\frac{dF}{dz}\right|_{z=z_T} = v_T|_{\beta_o} = \frac{\zeta_T BV_o(\beta_o)(\zeta_T^2-2A\zeta_T\cos\alpha+A^2)|\cos(\psi+\beta_o-\omega)|}{AC(C^2-2BC\cos(\psi-\omega)+B^2)} \tag{3.52}$$

An important result is found from equation (3.43) applied at two different outlet angles β_{o1} and β_{o2}. Since $dz/d\zeta$ does not depend on the flow conditions, it is

obtained that

$$\frac{v(\phi)|_{\beta_{o2}}}{v(\phi)|_{\beta_{o1}}} = \frac{|dF/dz|_{\beta_{o2}}}{|dF/dz|_{\beta_{o1}}} = \frac{V_{o2}(\beta_{o2})|\cos(\psi+\beta_{o2}-\omega/2-\phi/2)|}{V_{o1}(\beta_{o1})|\cos(\psi+\beta_{o1}-\omega/2-\phi/2)|} \tag{3.53}$$

Thus, if the velocity is known for one outlet angle β_{ob}, it is known for any other outlet angle β_{o2}. It can be shown that the trailing-edge velocity behaves in the same way, that is,

$$\frac{v_T|_{\beta_{o2}}}{v_T|_{\beta_{o1}}} = \frac{V_{o2}(\beta_{o2})|\cos(\psi+\beta_{o2}-\omega/2)|}{V_{o1}(\beta_{o1})|\cos(\psi+\beta_{o1}-\omega/2)|} \tag{3.54}$$

3.1.6 Application of the Exact Solution for Cascade Flows

Choosing a circle offset of $\mu = -0.02$ with $\zeta_T = 1$ and a spiral location of $a = 1.15\,e^{i175^\circ}$ results in the cascade geometry ($\chi = -11.4^\circ$, $\sigma = 0.829$) shown in figure 3-9. The corresponding velocity distributions for $\beta_I = 20^\circ$, 30°, and 40° are shown in figure 3-10, and the velocity distribution for $\beta_{z_L} = 2.67^\circ$ is shown in figure 3-11.

As previously mentioned, the main effect of changing the distance between the spiral and the circle is to change the solidity, although there is as well some change in stagger and cascade blade thickness and camber. Using the offset $\mu = -0.07 + i\,0.1$ and $a = 1.5\,e^{i175^\circ}$ and $a = 3\,e^{i175^\circ}$ results in the two cascades shown in figure 3-12. Changing the argument of a mainly effects the stagger as shown in figure 3-13 for $a = 1.5\,e^{i175^\circ}$ and $a = 1.5\,e^{i160^\circ}$ with $\mu = -0.05 + i\,0.1$. Finally, as with the Joukowski airfoil, moving the generating circle up increases blade camber and moving it to the left increases the thickness.

With regard to the spiral being close to the generating circle, the points near the blade leading edge become sparse as compared with points near the trailing edge in the case of equiangular points around the circle. To demonstrate this effect,

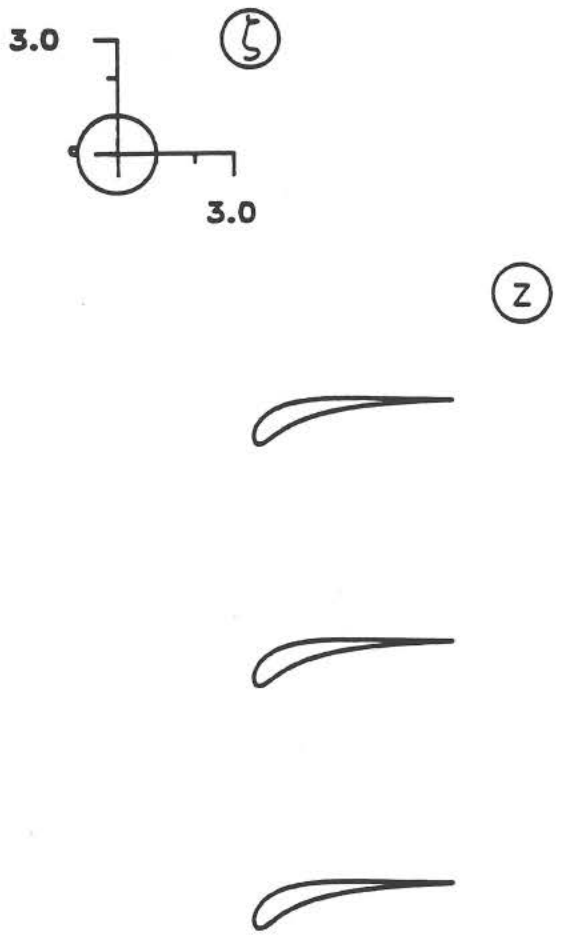

Figure 3-9 Example cascade for a circle offset of $\mu = -0.02$ and a spiral location of $a = 1.15\, e^{i\,175^\circ}$.

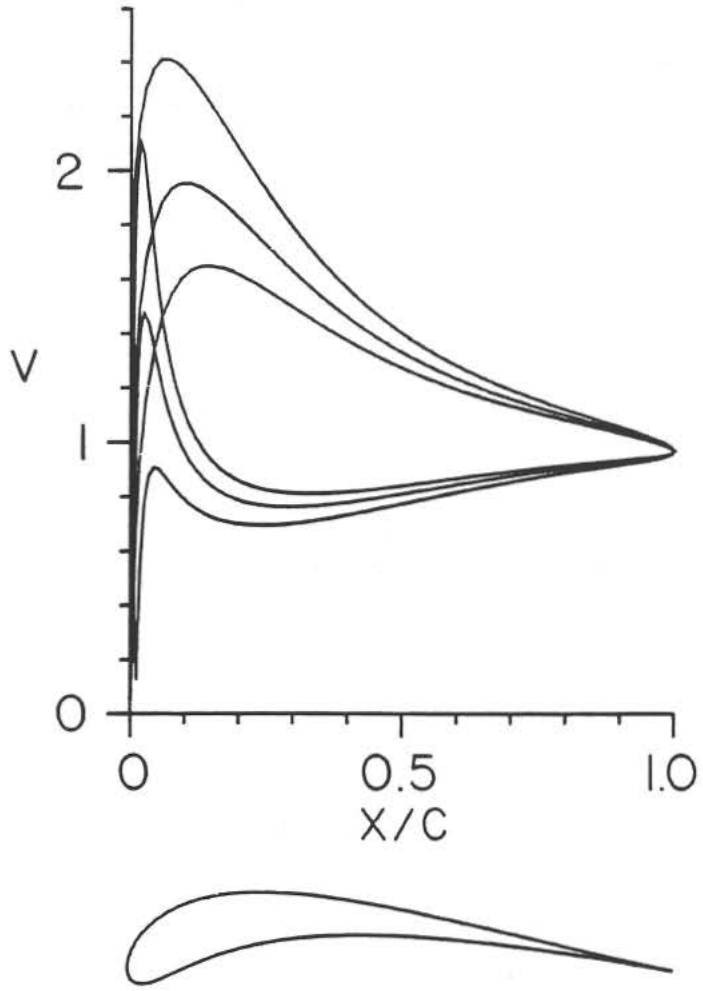

Figure 3-10 Velocity distributions for cascade shown in figure 3-9 ($\beta_1 = 20°$, $30°$ and $40°$).

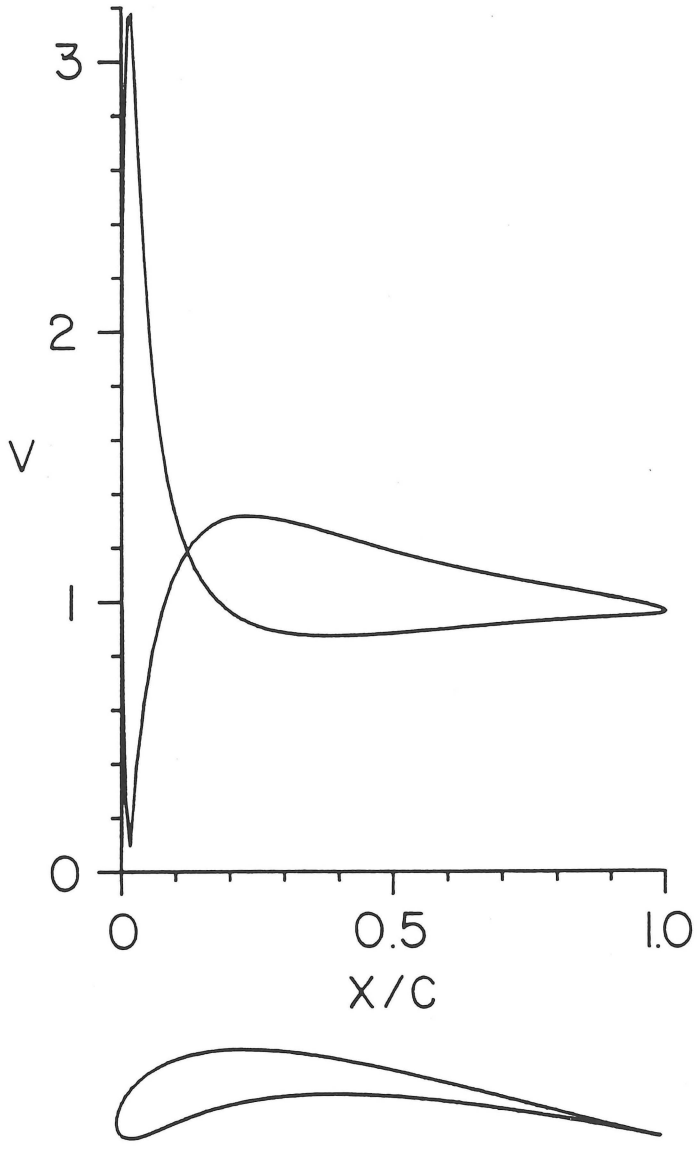

Figure 3-11 Zero-lift velocity distributions for cascade shown in figure 3-9 ($\beta_1 = \beta_{zL} = 2.67°$).

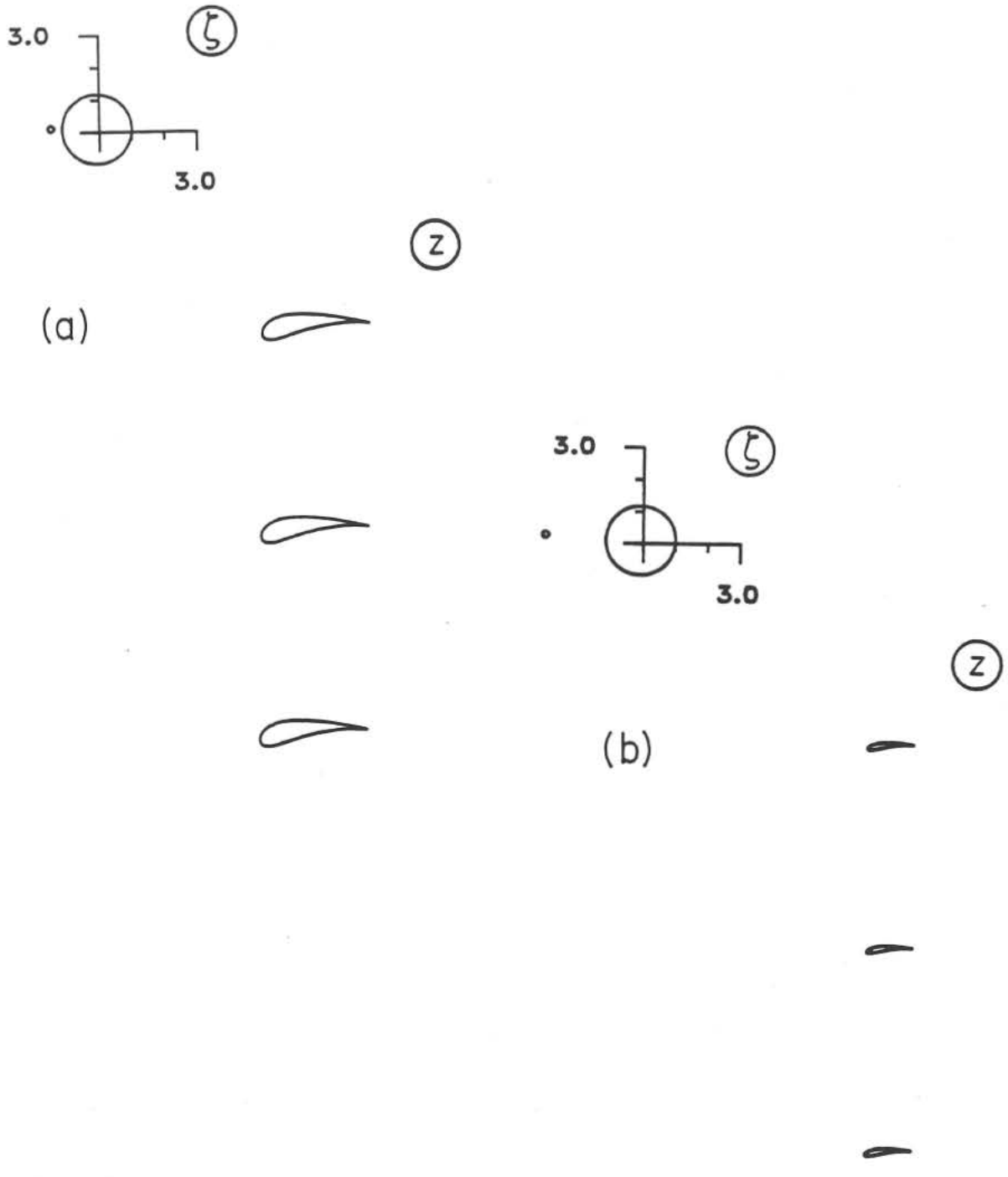

Figure 3-12 Example cascades for a circle offset of $\mu = -0.07 + i\,0.1$ and spiral locations of (a) $a = 1.5\,e^{i\,175^\circ}$ and (b) $a = 3\,e^{i\,175^\circ}$.

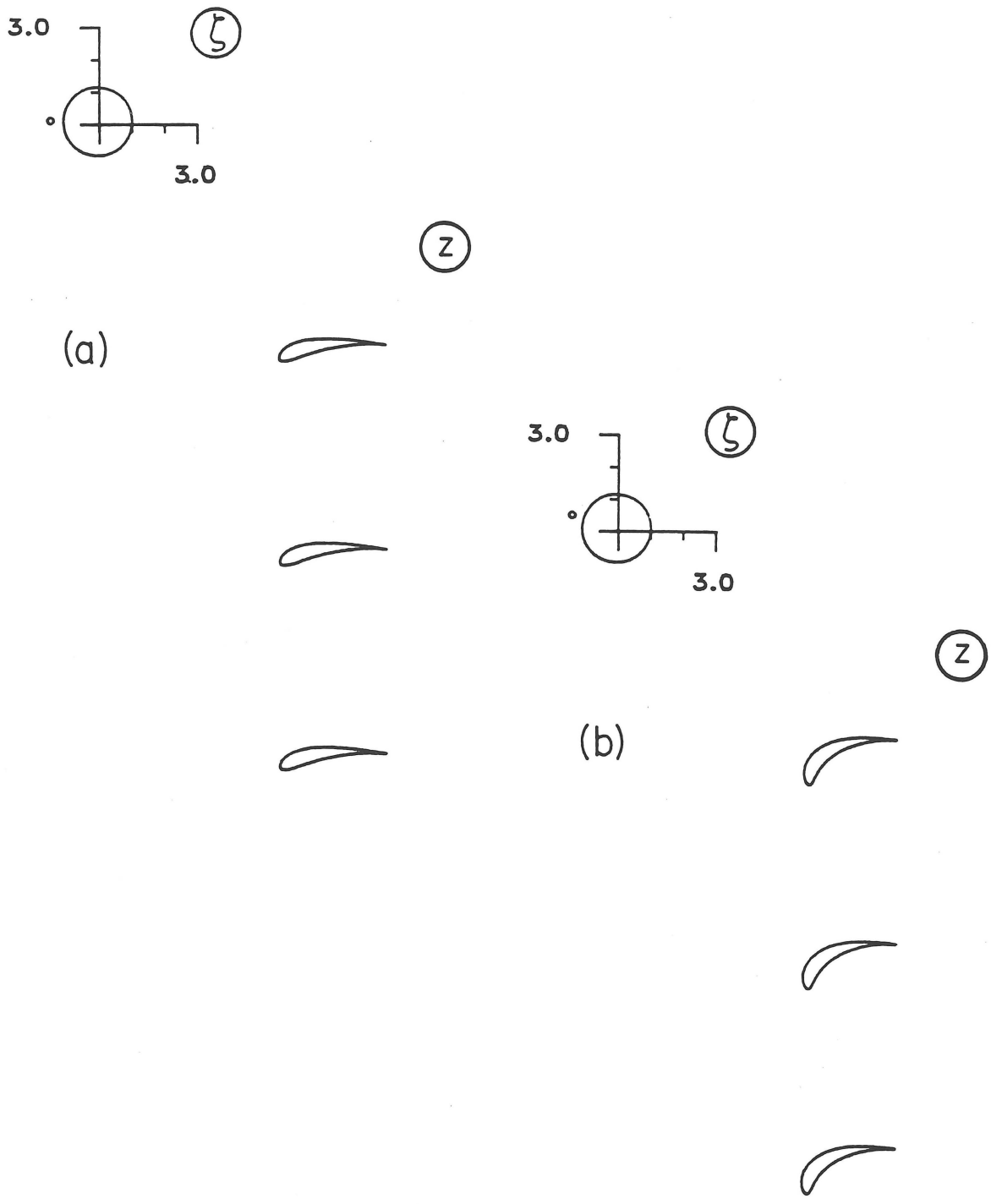

Figure 3-13 Example cascades for a circle offset of $\mu = -0.05 + i\,0.1$ and spiral locations of (a) $a = 1.5\,e^{i\,175^\circ}$ and (b) $a = 3\,e^{i\,160^\circ}$.

the values $a = 1.1\,e^{i\,180^\circ}$ and $\mu = -0.025$ with 500 equiangular points around the circle have been selected to produce the symmetric cascade shown in figure 3-14. Symbols are used to indicate the points as mapped from the circle. In the generation of exact solutions, this stretching is not a limitation since better resolution around the leading-edge may be obtained by carefully selecting points on the circle to be mapped to the cascade. As shown in figure 3-15 for $a = 1.1\,e^{i\,150^\circ}$ and $\mu = -0.01 - i\,0.4$, another effect of having the spiral close to the circle is that as the argument of a is changed from 180° in an effort to have moderate stagger the cascade profiles tend to become S-shaped. Nevertheless, while such profiles are not practical, the solutions may be used as test cases for analysis methods as was originally intended.

3.1.7 Alternative Mappings for Exact Solutions

Instead of using the mapping (3.4), the mapping may be introduced as

$$e^{-z} = \zeta + c_0 + \frac{c_1}{\zeta} \tag{3.55}$$

In this case, the inlet flow ($z \to -\infty$) maps to infinity in the circle plane while the outlet flow ($z \to \infty$) maps to the point $\zeta = a$ given by

$$0 = a + c_0 + \frac{c_1}{a} \tag{3.56}$$

Thus, in the circle plane a vortex-sink exists at the point $\zeta = a$ while at the point $\zeta \to -\infty$ there is a vortex-source, opposite to the exact theory previously presented. For this mapping, the steps taken to obtain the cascade geometry and velocity distributions follow along the same lines as presented in sections 3.1.1 through 3.1.5 except that it is most convenient to express the equations finally in terms of the inlet flow parameters. More generally, the mapping (3.4) or (3.55) need not be

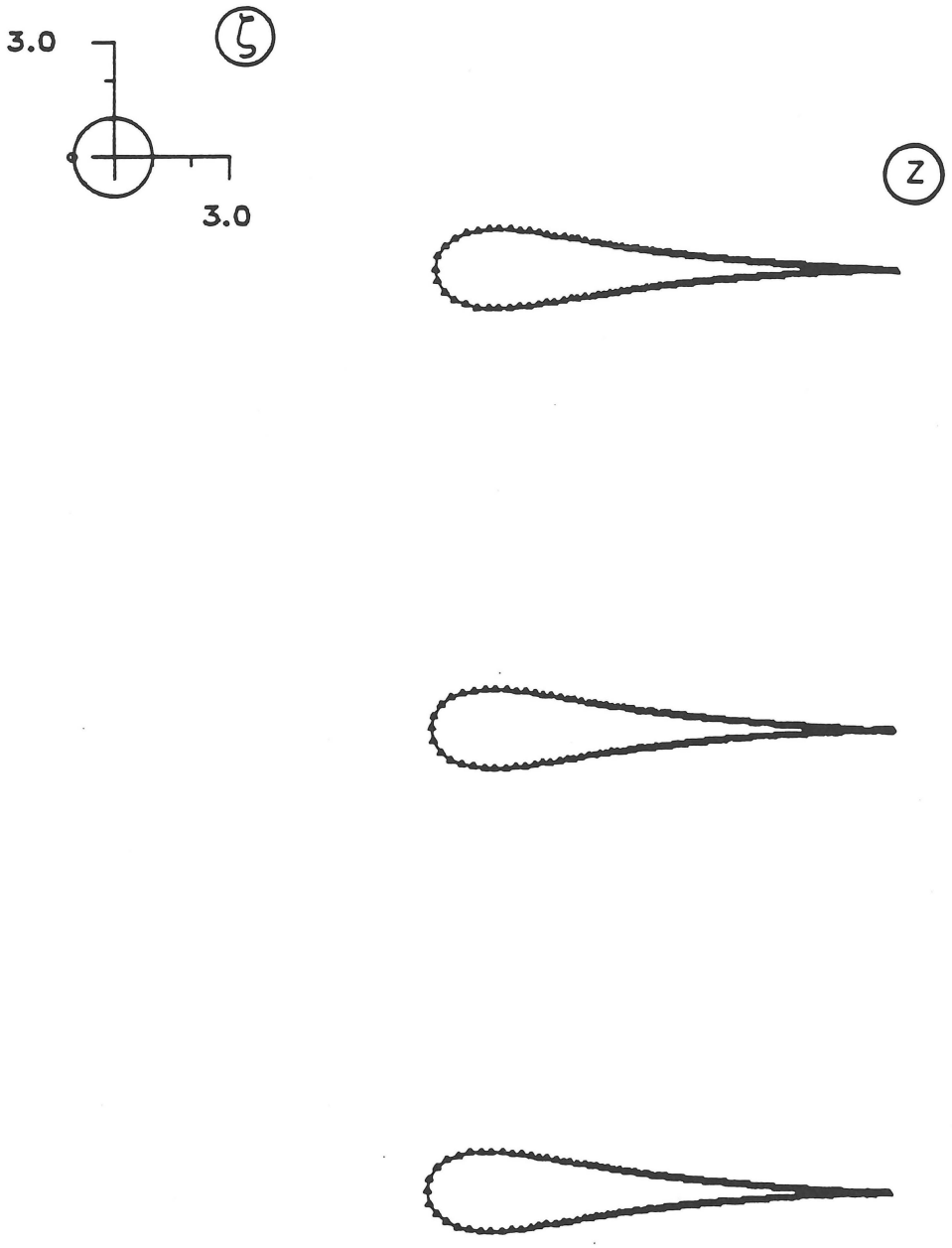

Figure 3-14 Example cascade for a circle offset of $\mu = -0.025$ and a spiral location of $a = 1.1\, e^{i\,180^\circ}$.

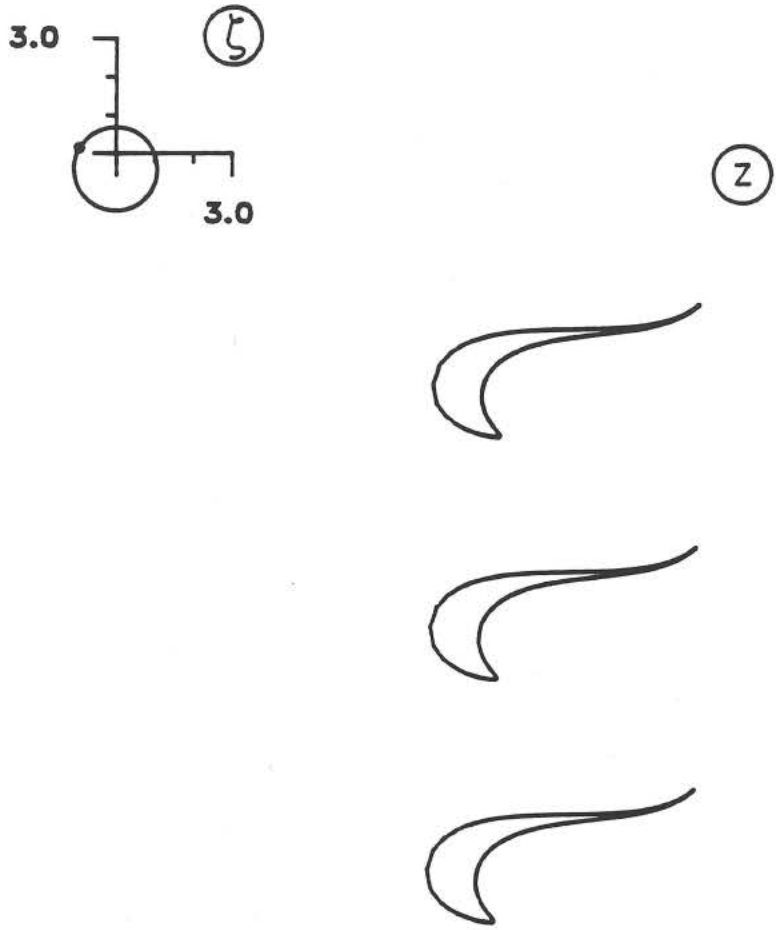

Figure 3-15 Example cascade for a circle offset of $\mu = -0.01 - i\,0.4$ and a spiral location of $a = 1.1\,e^{i\,150^\circ}$.

truncated to three terms. In general, the mapping may have an infinite number of terms as considered in the next section.

3.2 MULTI-POINT INVERSE DESIGN OF AN INFINITE CASCADE OF AIRFOILS

In this section, a theory for multi-point inverse design of cascades is presented and two examples are illustrated. As mentioned, the current approach for cascades is similar to the multi-point inverse airfoil design approach of section 2.1. Aside from the similarity, the significant difference between the present cascade and the airfoil problem is that the cascade mapping is singular at a point exterior to the circle; whereas, with the airfoil the mapping is regular at all points exterior to the circle. It will be shown, as with the isolated airfoil, that the specified velocity distribution about the cascade blade is not entirely arbitrary. Two integral constraints arise in order to ensure closure of the cascade blades. These two integral constraints are analogous to the two integral constraints ensuring closure of the isolated airfoil. For the isolated airfoil, one additional integral constraint ensures compatibility with the freestream flow. For the cascade, however, two more constraints arise to guarantee compatibility with both the inlet and outlet flow. One of these constraints appears in the form of an integral constraint and the other as an algebraic relation. For multi-point design, continuity conditions on the velocity distribution are imposed so that at any single inlet or outlet angle the velocity distribution is continuous. Finally, in what follows where there is a close similarity to the multi-point inverse airfoil design formulation as given in section 2.1, the discussion will be brief since details have already been presented there.

3.2.1 General Cascade Mapping Function

The solution proceeds from a generalization of the mapping (3.4), viz.

$$e^{z(2\pi i/s)} = \zeta + c_0 + \frac{c_1}{\zeta} + \frac{c_2}{\zeta^2} + \cdots \tag{3.57}$$

which takes the unit circle centered on the origin in the ζ-plane into the infinite cascade in the z-plane as shown in figure 3-16. In this case, the spacing between the cascade is given by the complex parameter s. As may be seen by equation (3.57), the outlet flow ($z \to \infty$) maps to infinity, and the inlet flow ($z \to -\infty$) maps to $\zeta = a$ according to

$$\lim_{z \to -\infty} e^z = \lim_{\zeta \to a} \left[\zeta + c_0 + \frac{c_1}{\zeta} + \frac{c_2}{\zeta^2} + \cdots \right] \tag{3.58}$$

or

$$0 = a + c_0 + \frac{c_1}{a} + \frac{c_2}{a^2} + \cdots \tag{3.59}$$

Since the velocity is to be specified, it is most convenient to work not with the mapping (3.57) but with its derivative. From equation (3.57), the mapping derivative is found to be

$$\frac{dz}{d\zeta} = \frac{1 - \frac{c_1}{\zeta^2} - \frac{2c_2}{\zeta^3} - \cdots}{\zeta + c_0 + \frac{c_1}{\zeta} + \frac{c_2}{\zeta^2} + \cdots} \tag{3.60}$$

Through equation (3.60), it is observed that $dz/d\zeta$ is singular outside of the circle at the point $\zeta = a$. Expanding about this point reveals

$$\frac{dz}{d\zeta} = \left(\frac{1}{\zeta - a} \right) \left(1 - \frac{c_0 + a}{\zeta} + \cdots \right) \tag{3.61}$$

in which case the singularity at $\zeta = a$ is a first-order pole—a fact which could have been anticipated from the mapping derivative (3.11).

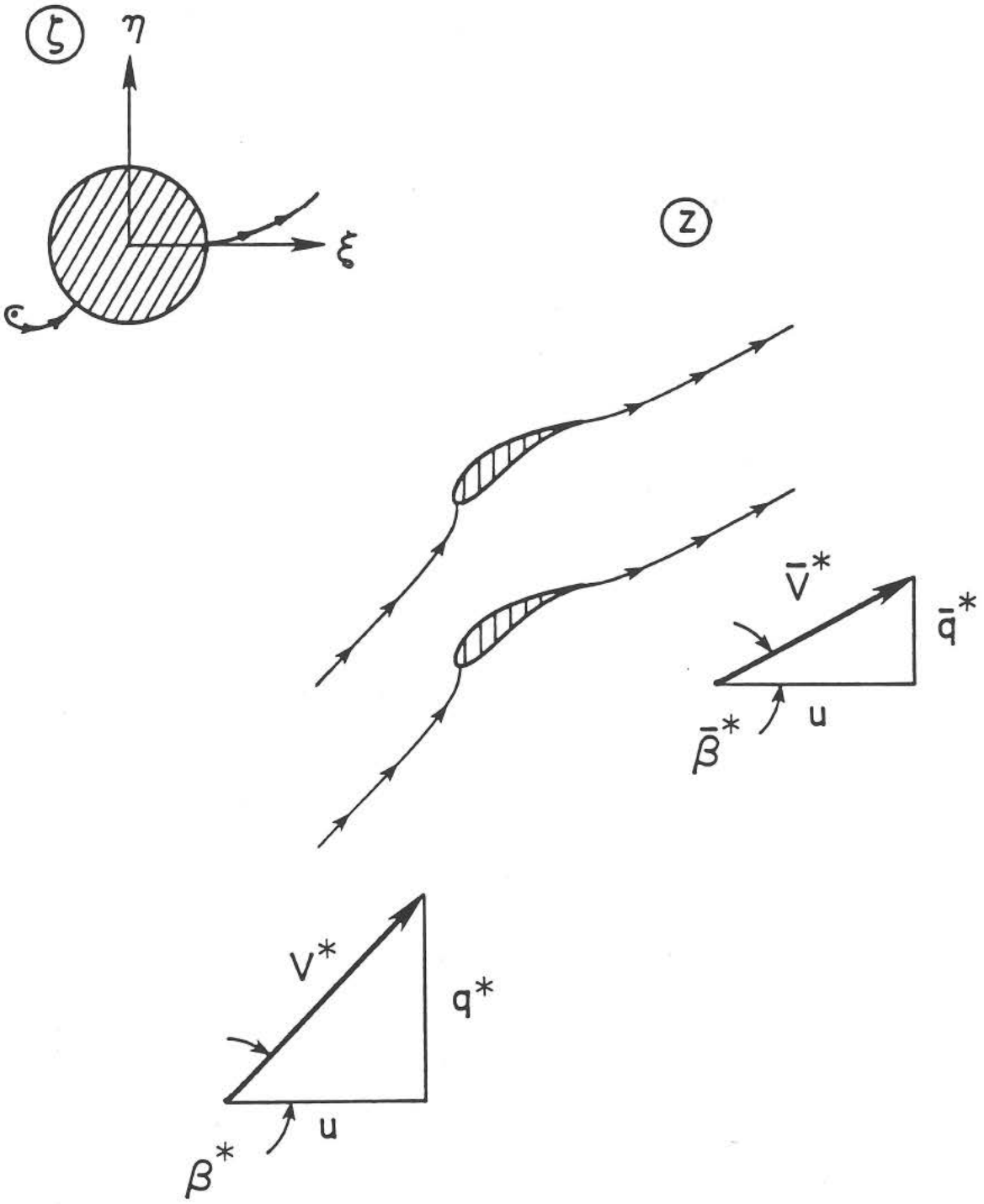

Figure 3-16 Mapping from the unit circle to the cascade plane.

To aid in the inverse formulation, the derivative of the mapping is best expressed as

$$\frac{dz}{d\zeta} = \left(\frac{1}{\zeta - a}\right)\left(1 - \frac{1}{\zeta}\right)^{1-\epsilon} e^{f(\zeta)} \tag{3.62}$$

where the factor $e^{f(\zeta)}$ is a regular non-zero function for $|\zeta| > 1$ and has no zeros, poles or discontinuities on $|\zeta| = 1$. The factor $(1 - 1/\zeta)^{1-\epsilon}$ is introduced to map the point $\zeta = 1$ to the cascade-blade trailing edge with an angle $\pi\epsilon$. Finally, the required first-order pole is included as the first factor. The function $f(\zeta = re^{i\phi})$ is expressed as

$$f(\zeta) = P(r,\phi) + i\,Q(r,\phi) = \sum_{m=0}^{\infty} r^{-m}(a_m + i\,b_m)e^{-m\phi} \tag{3.63}$$

where $P(r,\phi)$ and $Q(r,\phi)$ are real functions, and the series converges for $|\zeta| \geq 1$. On the unit circle, $\zeta = e^{i\phi}$, $f(\zeta)$ becomes

$$P(\phi)+i\,Q(\phi) \equiv \sum_{m=0}^{\infty}(a_m \cos m\phi + b_m \sin m\phi) + i \sum_{m=0}^{\infty}(b_m \cos m\phi - a_m \sin m\phi) \tag{3.64}$$

3.2.2 Closure Condition, Cascade Blade Spacing and Blade Coordinates

As with the isolated airfoil, one objective is to find conditions on the mapping which ensure closure of the cascade blades. To start with, it is best to consider as depicted in figure 3-17 a closed contour C_0 about the unit circle which is mapped into a closed contour B_0 about each cascade blade. For any given blade, then, it must be true that

$$\oint_{B_0} dz = 0 \tag{3.65}$$

For any arbitrary contour C mapped to B, the following relation holds:

$$\oint_B dz = \oint_C \frac{dz}{d\zeta} d\zeta \tag{3.66}$$

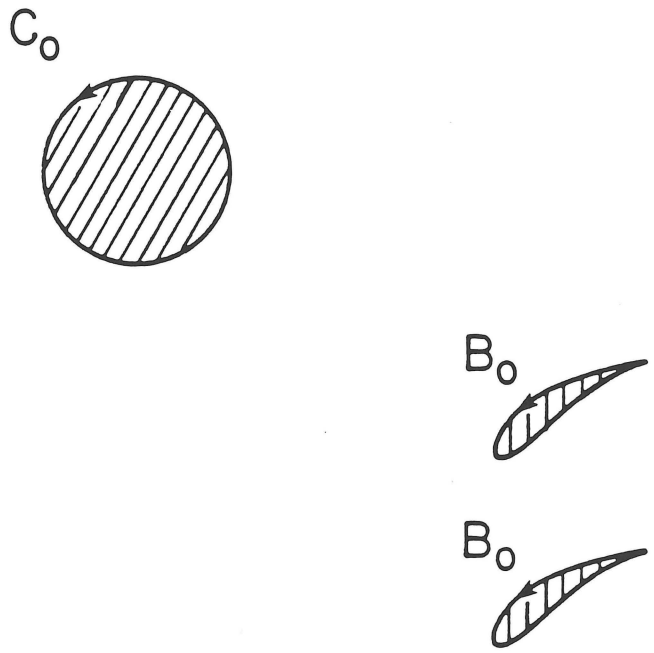

Figure 3-17 Contour about the circle as mapped to the infinite cascade.

Therefore, it follows that

$$\oint_{C_0} \frac{dz}{d\zeta} d\zeta = 0 \tag{3.67}$$

Consider now the contour $C_1+C_2+C_3+C_4$ mapped to $B_1+B_2+B_3+B_4$ as shown in figure 3-18. The stagnation streamlines of the flow are presented to provide a physical interpretation of the contours. Also, the paths which run parallel to these stagnation streamlines off the circle and off the cascade cancel upon integration and hence need not be considered further. Since there are no singularities within the contour, the Cauchy-Goursat theorem gives

$$\int_{C_1} \frac{dz}{d\zeta} d\zeta + \int_{C_2} \frac{dz}{d\zeta} d\zeta + \int_{C_3} \frac{dz}{d\zeta} d\zeta + \int_{C_4} \frac{dz}{d\zeta} d\zeta = 0 \tag{3.68}$$

Using

$$\int_{C_2} \frac{dz}{d\zeta} d\zeta + \int_{C_4} \frac{dz}{d\zeta} d\zeta = -\int_{C_0} \frac{dz}{d\zeta} d\zeta = 0 \tag{3.69}$$

gives

$$\int_{C_1} \frac{dz}{d\zeta} d\zeta + \int_{C_3} \frac{dz}{d\zeta} d\zeta = 0 \tag{3.70}$$

In the limit that C_3 shrinks to the point $\zeta = a$ and C_4 expands out to C_5 as shown in figure 3-18, the integral about C_5 which encloses the singularity at $\zeta = a$ becomes by the residue theorem

$$\oint_{C_5} \frac{dz}{d\zeta} d\zeta = 2\pi i \,\mathrm{Res}(a) = \int_{B_5} dz = s \tag{3.71}$$

The last quantity $\int_{B_5} dz$ is simply the cascade spacing s used in equation (3.57). Taking the spacing to be

$$s = 2\pi i \tag{3.72}$$

requires

$$\mathrm{Res}(a) = 1 \tag{3.73}$$

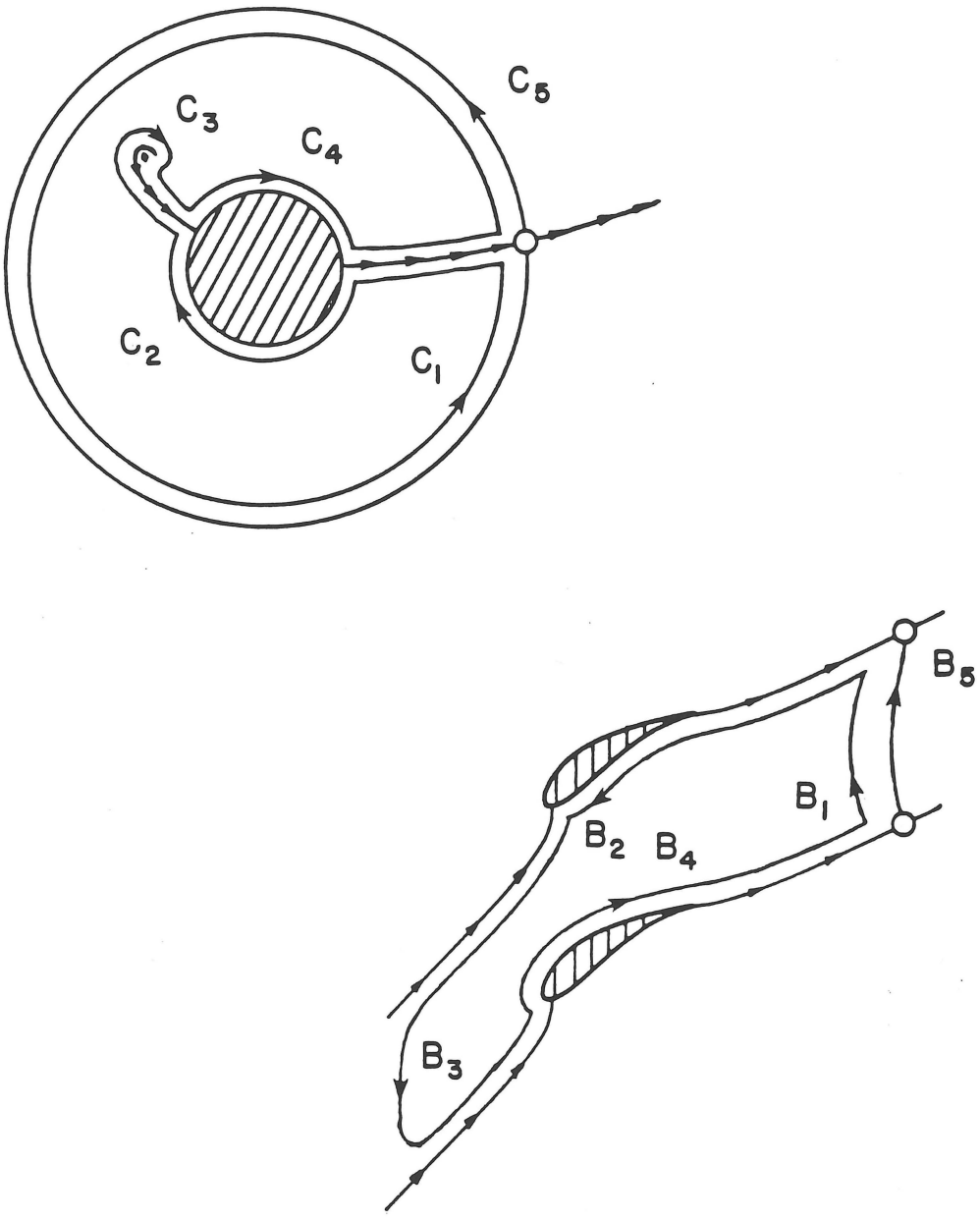

Figure 3-18 Contours in the circle plane as mapped to the cascade plane.

Using this result and substituting equation (3.62) into (3.71) yields

$$\frac{1}{2\pi i}\oint_{C_5}\frac{\left(1-\frac{1}{\zeta}\right)^{1-\epsilon}e^{f(\zeta)}}{\zeta-a}d\zeta=1 \tag{3.74}$$

The integral (3.74) is evaluated by means of the Cauchy integral formula:

$$\frac{1}{2\pi i}\oint_{C}\frac{g(\zeta)}{\zeta-a}\,d\zeta=g(a) \tag{3.75}$$

where $g(\zeta)$ is regular and the contour C encloses the singularity at $\zeta = a$. By comparison with the integral (3.74), it is required that

$$\left(1-\frac{1}{a}\right)^{1-\epsilon}e^{f(a)}=1 \tag{3.76}$$

Separating this result into the real and imaginary parts and taking $a = Ae^{i\alpha}$ yields the conditions

$$P(A,\alpha) = (1-\epsilon)\ln\left(\frac{A}{\sqrt{1-2A\cos\alpha+A^2}}\right) \tag{3.77a}$$

$$Q(A,\alpha) = -(1-\epsilon)\arg(A-e^{-i\alpha}) \tag{3.77b}$$

To summarize, when these conditions are satisfied, the cascade blades will be closed, and the spacing by equation (3.72) will be $s = 2\pi i$. Although the cascade spacing is fixed, the cascade chord (and hence the solidity) is effected by changing the location of the singularity at $\zeta = a$ as done in the exact solution of section 3.1. Examples will be illustrated later.

Coordinates are obtained by integrating the mapping about the unit circle as

$$z|_{z=z_c} = \int \frac{dz}{d\zeta}\,d\zeta\bigg|_{\zeta=\zeta_c} \tag{3.78}$$

Taking

$$z = z_c = x(\phi) + i\,y(\phi) \tag{3.79a}$$

$$\zeta = \zeta_c = e^{i\,\phi} \qquad\qquad d\zeta = i\,e^{i\,\phi}\,d\phi \tag{3.79b, c}$$

$$\left.\frac{dz}{d\zeta}\right|_{\zeta=\zeta_c} = \left(\frac{1}{e^{i\,\phi} - a}\right)(1 - e^{i\,\phi})^{1-\epsilon} e^{P(\phi)+i\,Q(\phi)} \tag{3.79d}$$

$$= \frac{(2\sin\phi/2)^{1-\epsilon} e^{P}(\phi)}{\sqrt{1 - 2A\cos(\alpha - \phi) + A^2}}\; e^{i[(1-\epsilon)(\pi/2-\phi/2) - \arg(e^{i\,\phi}-a) + Q(\phi)]} \tag{3.79e}$$

since

$$e^{i\,\phi} - a = \sqrt{1 - 2A\cos(\alpha - \phi) + A^2}\; e^{i\arg(e^{i\,\phi}-a)} \tag{3.80a}$$

$$1 - e^{-i\,\phi} = 2(\sin\phi/2)\, e^{i\,(\pi/2-\phi/2)} \tag{3.80b}$$

gives

$$x(\phi) + i\,y(\phi) = -\int \frac{(2\sin\phi/2)^{1-\epsilon} e^{P}(\phi)}{\sqrt{1 - 2A\cos(\alpha - \phi) + A^2}}\; e^{i[\phi/2 - \epsilon(\pi/2-\phi/2) - \arg(e^{i\,\phi} - Ae^{i\,\alpha}) + Q(\phi)]}\, d\phi \tag{3.81}$$

3.2.3 Complex Potential Function

As done in section 3.1.2, it may be shown that two spirals exist outside the circle. The inlet flow denoted by the flow quantities $(\;)^*$ corresponds to a vortex-source at $\zeta = a$, and the outlet flow denoted by the quantities $(\overline{\;})^*$ (not to be confused with taking the conjugate) corresponds to a vortex-sink at $\zeta \to \infty$. As a result for the unit circle, the complex potential becomes [from equation (3.22) with $\mu = 0$, $b = a$, $c = 1$, and $\zeta' = \zeta$]

$$F(\zeta) = Q[\ln(\zeta - a) + \ln(1 - \overline{a}\zeta) - \ln\zeta]$$

$$- i\,\Gamma^*(\phi)\,[\ln(\zeta - a) + \ln(1 - \overline{a}\zeta)]$$

$$- i\,\overline{\Gamma}^*(\phi)\,[\ln \zeta] \tag{3.82}$$

At the present point in the development, the inlet and outlet circulation strengths $\Gamma^*(\phi)$ and $\overline{\Gamma}^*(\phi)$ may be thought of as constants. As will be seen later, however, considering the circulation strengths to be functions of ϕ is analogous to considering the airfoil angle of attack in the multi-point inverse airfoil design problem to be a function of ϕ, that is, $\alpha^*(\phi)$. By imposing the Kutta condition which requires $\zeta = 1$ to be a stagnation point, it is found [from equation (3.27)] that

$$i\,\Gamma^*(\phi) = \frac{Q(a - \overline{a}) - i\,\overline{\Gamma}^*(\phi)\,(1 - a)(1 - \overline{a})}{1 - a\overline{a}} \tag{3.83}$$

to yield [from equation (3.29)]

$$\frac{dF}{d\zeta} = -\left(1 - \frac{1}{\zeta}\right)\frac{a(Q + i\,\overline{\Gamma}^*(\phi)) + \overline{a}(Q - i\,\overline{\Gamma}^*(\phi))\zeta}{(\zeta - a)(1 - \overline{a}\zeta)} \tag{3.84}$$

3.2.4 Inlet and Outlet Conditions

As indicated in figure 3-16, the outlet flow is given by

$$\lim_{z\to\infty}\frac{dF}{dz} = u - i\,\overline{q}^*(\phi) = \lim_{\zeta\to\infty}\frac{dF/d\zeta}{dz/d\zeta} \tag{3.85}$$

$$= \lim_{\zeta\to\infty}\left\{\frac{-\left(1 - \frac{1}{\zeta}\right)\frac{a(Q + i\,\overline{\Gamma}^*(\phi)) + \overline{a}(Q - i\,\overline{\Gamma}^*(\phi))\zeta}{(\zeta - a)(1 - \overline{a}\zeta)}}{\left(\frac{1}{\zeta - a}\right)\left(1 - \frac{1}{\zeta}\right)^{1-\epsilon} e^{f(\zeta)}}\right\} \tag{3.86}$$

In the limit

$$u - i\,\overline{q}^*(\phi) = \frac{Q - i\,\overline{\Gamma}^*(\phi)}{\lim\limits_{\zeta\to\infty} e^{f(\zeta)}} \tag{3.87}$$

By requiring that

$$\lim_{\zeta \to \infty} e^{f(\zeta)} = 1 \tag{3.88}$$

it is found that

$$Q = u \qquad \text{and} \qquad \overline{\Gamma}^*(\phi) = \overline{q}^*(\phi) \tag{3.89a, b}$$

in which case equation (3.84) becomes

$$\frac{dF}{d\zeta} = -\left(1 - \frac{1}{\zeta}\right) \frac{a(u + i\,\overline{q}^*(\phi)) + \overline{a}(u - i\,\overline{q}^*(\phi))\zeta}{(\zeta - a)(1 - \overline{a}\zeta)} \tag{3.90}$$

An additional condition on the mapping is provided by the condition (3.88) which, when separated into the real and imaginary parts, gives

$$\lim_{r \to \infty} P(r, \phi) = 0 \qquad \text{and} \qquad \lim_{r \to \infty} Q(r, \phi) = 0 \tag{3.91a, b}$$

Proceeding in a similar manner for the inlet flow gives

$$\lim_{z \to -\infty} \frac{dF}{dz} = u - i\,q^*(\phi) = \lim_{\zeta \to a} \frac{dF/d\zeta}{dz/d\zeta} \tag{3.92a}$$

$$= \frac{-\left(1 - \frac{1}{a}\right) \frac{a(u + i\,\overline{q}^*(\phi)) + \overline{a}(u - i\,\overline{q}^*(\phi))a}{(1 - a\overline{a})}}{\left(1 - \frac{1}{a}\right)^{1-\epsilon} e^{f(a)}} \tag{3.93}$$

and becomes through condition (3.76)

$$= -\left(1 - \frac{1}{a}\right) \frac{a(u + i\,\overline{q}^*(\phi)) + \overline{a}(u - i\,\overline{q}^*(\phi))a}{(1 - a\overline{a})} \tag{3.94}$$

Thus,

$$-i\,q^*(\phi) = \frac{-u(a - \overline{a}) + i\,\overline{q}^*(\phi)(1 - a)(1 - \overline{a})}{1 - a\overline{a}} \tag{3.95}$$

which by comparison with the Kutta condition (3.83) gives

$$\Gamma^*(\phi) = q^*(\phi) \tag{3.96}$$

Expressing equation (3.95) as

$$u(a-\overline{a}) - i\,q^*(\phi)(1-a\overline{a}) - i\,\overline{q}^*(\phi)(1-a)(1-\overline{a}) = 0 \tag{3.97}$$

and using the relations

$$\tan\beta^*(\phi) = \frac{q^*(\phi)}{u} \qquad \text{and} \qquad \tan\overline{\beta}^*(\phi) = \frac{\overline{q}^*(\phi)}{u} \tag{3.98a}$$

$$a - \overline{a} = 2i\,A\sin\alpha \tag{3.98b}$$

$$1 - a\overline{a} = 1 - A^2 \tag{3.98c}$$

$$(1-a)(1-\overline{a}) = 1 - 2A\cos\alpha + A^2 \tag{3.98d}$$

yields

$$2A\sin\alpha - (1-A^2)\tan\beta^*(\phi) - (1-2A\cos\alpha+A^2)\tan\overline{\beta}^*(\phi) = 0 \tag{3.99}$$

Consequently, once the spiral location $\zeta = a$ is selected, the inlet angle $\beta^*(\phi)$ may be determined from the outlet angle $\overline{\beta}^*(\phi)$ and visa versa. The flow angle β_{zL} for which there is no turning becomes

$$\tan\beta_{zL} = \frac{A\sin\alpha}{1 - A\cos\alpha} \tag{3.100}$$

3.2.5 Integral Constraints

The conditions on the mapping [in particular $f(\zeta)$] at points $\zeta = a$ and $\zeta \to \infty$ as expressed by equations (3.77a,b) and (3.91a,b) may be related to integrals involving the value of the mapping [in particular $P(\phi)$ and $Q(\phi)$] about the unit circle. By the

Gauss mean value theorem applied exterior to the unit circle, the outlet conditions (3.91a,b) give

$$\lim_{r\to\infty} P(r,\phi) = \frac{1}{2\pi}\int_0^{2\pi} P(\phi)\,d\phi = 0 \tag{3.101a}$$

$$\lim_{r\to\infty} Q(r,\phi) = \frac{1}{2\pi}\int_0^{2\pi} Q(\phi)\,d\phi = 0 \tag{3.101b}$$

Using the Poisson integral formulas exterior to the unit circle gives for the closure conditions (3.77a,b)

$$-P(A,\alpha) = \frac{1}{2\pi}\int_0^{2\pi} P(\phi)\frac{1-A^2}{1-2A\cos(\alpha-\phi)+A^2}\,d\phi$$
$$= -(1-\epsilon)\ln\left(\frac{A}{\sqrt{1-2A\cos\alpha+A^2}}\right) \tag{3.102a}$$

$$-Q(A,\alpha) = \frac{1}{\pi}\int_0^{2\pi} P(\phi)\frac{A\sin(\alpha-\phi)}{1-2A\cos(\alpha-\phi)+A^2}\,d\phi$$
$$= (1-\epsilon)\arg(A-e^{-i\alpha}) \tag{3.102b}$$

or alternatively

$$-P(A,\alpha) = -\frac{1}{\pi}\int_0^{2\pi} Q(\phi)\frac{A\sin(\alpha-\phi)}{1-2A\cos(\alpha-\phi)+A^2}\,d\phi$$
$$= -(1-\epsilon)\ln\left(\frac{A}{\sqrt{1-2A\cos\alpha+A^2}}\right) \tag{3.103a}$$

$$-Q(A,\alpha) = \frac{1}{2\pi}\int_0^{2\pi} Q(\phi)\frac{1-A^2}{1-2A\cos(\alpha-\phi)+A^2}\,d\phi$$
$$= (1-\epsilon)\arg(A-e^{-i\alpha}) \tag{3.103b}$$

Lastly, by the Poisson integral, $P(\phi)$ and $Q(\phi)$ are related as

$$P(\phi)+iQ(\phi) = -\frac{1}{2\pi}\int_0^{2\pi} Q(\psi)\cot\frac{\psi-\phi}{2}\,d\psi + i\,\frac{1}{2\pi}\int_0^{2\pi} P(\psi)\cot\frac{\psi-\phi}{2}\,d\psi \tag{3.104}$$

The three integral constraints (3.101a) and (3.102a,b) involving $P(\phi)$ and the three integral constraints (3.101b) and (3.103a,b) involving $Q(\phi)$ are analogous in

many ways to those integral constraints found for the isolated airfoil [equations (2.50a-c) and (2.51a-c) respectively]. The essential difference (besides the fact that the equations themselves are obviously different) is that for the cascade there are in a sense two freestream flows—the inlet and outlet flows. The outlet flow gives rise to the integral constraints (3.101a,b) much like in the isolated airfoils problem the freestream gives rise to the integral constraints (2.50a) and (2.51a). For the cascade an additional constraint arises. This constraint is due to the inlet flow condition which leads to an algebraic condition (3.99) relating the inlet and outlet angles. In order for these integral constraints to be useful for inverse design, it is necessary to relate to mapping [defined by $P(\phi)$ and $Q(\phi)$] to the complex velocity.

3.2.6 Relation between the Mapping and the Complex Velocity

Up to now, there has been no connection to the inverse design problem as classically posed through the specification of the velocity distribution. The necessary mapping conditions which ensure closure and compatibility with the inlet and outlet flow have been presented. These special conditions may be satisfied by any number of suitably selected mapping functions from which the cascade can be derived and the velocity distribution determined. Of course, the objective here is not to specify the mapping function per se, but rather to specify the velocity distribution and from that derive the mapping which then gives the cascade. With this in mind, the functions $P(\phi)$ and $Q(\phi)$ appearing in the integral constraints must be related to the complex velocity so that the velocity distribution may be explicitly involved in the integral constraints. After having satisfied the integral constraints by a suitably specified velocity distribution, the mapping may be defined by $P(\phi)$ and $Q(\phi)$ in terms of this velocity distribution. From this mapping, then, the coordinates are finally obtained.

In a manner similar to that presented in section 2.1.2, the complex velocity on the cascade $z = z_c$ is given by

$$\left.\frac{dF}{dz}\right|_{z=z_c} = \frac{dF/d\zeta|_{\zeta=\zeta_c}}{dz/d\zeta|_{\zeta=\zeta_c}} \tag{3.105}$$

where $\zeta = \zeta_c = e^{i\,\phi}$ on the unit circle. In exponential form, the complex velocity on the cascade is expressed as

$$\left.\frac{dF}{dz}\right|_{z=z_c} = v^*(\phi)e^{-i\,\theta^*(\phi)} \tag{3.106}$$

while on the circle the complex velocity becomes

$$\left.\frac{dF}{d\zeta}\right|_{\zeta=\zeta_c} = \frac{2A\,\overline{V}^*(\phi)\,(2\sin\phi/2)\,|\cos(\alpha+\overline{\beta}^*(\phi)-\phi/2)|\,e^{-i\,(\phi-\pi/2-\pi^*(\phi))}}{1-2A\cos(\alpha-\phi)+A^2} \tag{3.107}$$

where

$$\pi^*(\phi) = \begin{cases} 0, & 0 \le \phi \le 2(\alpha+\overline{\beta}^*(\phi)) - \pi \\ \pi, & 2(\alpha+\overline{\beta}^*(\phi)) - \pi \le \phi \le 2\pi \end{cases} \tag{3.108}$$

Using equations (3.105) and (3.106) together with the mapping derivative (3.79*b*), equation (3.105) yields after taking the natural logarithm and separating into the real and imaginary parts

$$P(\phi) = -\ln\left\{\frac{(2\sin\phi/2)^{-\epsilon}\sqrt{1-2A\cos\alpha+A^2}\,v^*(\phi)}{2A\,\overline{V}^*(\phi)\,|\cos(\alpha+\overline{\beta}^*(\phi)-\phi/2)|}\right\} \tag{3.109a}$$

$$Q(\phi) = \theta^*(\phi)+\pi^*(\phi)-\phi/2+\epsilon(\pi/2-\phi/2)+\arg(e^{i\,\phi}-Ae^{i\,\alpha}) \tag{3.109b}$$

which relates the velocity distribution $v^*(\phi)$ and the outlet angle distribution $\overline{\beta}^*(\phi)$ to $P(\phi)$ and the cascade-blade flow-angle direction $\theta^*(\phi)$ to $Q(\phi)$. Thus, the mapping is defined through $P(\phi)$ in terms of the velocity distribution as intended.

3.2.7 Multi-Point Design Capability of the Theory

The discussion given in section 2.1.5 applies equally well to the cascade. The function $P(\phi)$ defined by equation (3.109*a*) is specified in terms of $v^*(\phi)$ and $\overline{\beta}^*(\phi)$

(and $\overline{V}^*(\phi)$ which is related to $\overline{\beta}^*(\phi)$). For multi-point design, the cascade blade is divided into the desired number of segments over each of which the design velocity distribution $v^*(\phi)$ is prescribed together with the desired outlet angle $\overline{\beta}^*(\phi)$ (considered constant over any given segment). For this desired outlet angle $\overline{\beta}^*(\phi)$, the prescribed design velocity distribution will be achieved. Alternatively, for a given segment, the desired inlet angle $\beta^*(\phi)$ may be given from which the corresponding $\overline{\beta}^*(\phi)$ is obtained by equation (3.99).

3.2.8 Continuity Constraints

The requirement that $e^{f(\zeta)}$ be continuous on the boundary of the circle requires that $P(\phi)$ be continuous. In this case at the junction between any two segments

$$P_+(\phi_i) = P_-(\phi_i) \tag{3.110}$$

Thus, for each junction on the cascade blade, a continuity condition arises which ultimately ensures that for any given inlet or outlet angle the velocity distribution about the cascade blade is continuous.

3.2.9 Limiting Behavior of the Velocity Distribution in the Vicinity of the Stagnation Points

By equation (3.109a), the design velocity distribution is expressed as

$$v^*(\phi) = \frac{2A\,\overline{V}^*(\phi)\,(2\sin\phi/2)^\epsilon\,|\cos(\alpha+\overline{\beta}^*(\phi)-\phi/2)|}{\sqrt{1-2A\cos\alpha+A^2}}\,e^{-P(\phi)} \tag{3.111}$$

As may be seen, stagnation points occur first at $\phi = 0$ and $\phi = 2\pi$ which correspond to the trailing edge and second at $\phi = \gamma = 2(\alpha + \overline{\beta}^*(\phi)) - \pi$. Consequently, the design velocity distribution at the trailing edge goes to zero as

$$\lim_{\phi_+ \to 0} v^*(\phi) \sim (\sin\phi/2)^\epsilon\, g_+(\phi) \tag{3.112a}$$

$$\lim_{\phi_- \to 2\pi} v^*(\phi) \sim (\sin \phi/2)^{\epsilon}\, g_-(\phi) \qquad (3.112b)$$

while at the forward stagnation point γ the velocity distribution goes to zero as

$$\lim_{\phi_+ \to \gamma} v^*(\phi) \sim |\cos(\alpha + \overline{\beta}^*(\phi) - \phi/2)|\, h_+(\phi) \qquad (3.113a)$$

$$\lim_{\phi_- \to \gamma} v^*(\phi) \sim |\cos(\alpha + \overline{\beta}^*(\phi) - \phi/2)|\, h_-(\phi) \qquad (3.113b)$$

and where $g_+(\phi)$, $g_-(\phi)$, $h_+(\phi)$, and $h_-(\phi)$ are positive, non-zero functions.

3.2.10 Numerical Implementation

As an overview, the solution proceeds along lines similar to those presented for the isolated airfoil. The differences are that the location of the vortex-source $\zeta = a$ must be specified, and the velocity distribution over any segment of the cascade blade must be given together with the corresponding outlet angle. For simplicity, the velocity distribution normal to the cascade front, u, is taken as one. If it is desired to specify the segment velocity distribution for a desired inlet angle, it becomes necessary to solve equation (3.99) to find the corresponding outlet angle so as to define $P(\phi)$ by $v^*(\phi)$ and $\overline{\beta}^*(\phi)$. Since there are three integral constraints on $P(\phi)$, three free parameters must be introduced. Then, for each segment of the cascade blade for which there is a corresponding continuity equation, an additional free parameter must be introduced. Having solved for the free parameters, $P(\phi)$ is defined from which $Q(\phi)$ is obtained. Together $P(\phi)$ and $Q(\phi)$ are then used to obtain the cascade blade coordinates. To obtain the cascade velocity distribution for any arbitrary outlet angle β_o, the harmonic function $P(\phi)$ is used to give from equation (3.111)

$$v(\phi)|_{\beta_o} = \frac{2A\, V_o(\beta_o)\, (2\sin \phi/2)^{\epsilon}\, |\cos(\alpha + \beta_o - \phi/2)|}{\sqrt{1 - 2A\cos\alpha + A^2}}\, e^{-P(\phi)} \qquad (3.114)$$

Briefly, the design velocity distribution and outlet angle distribution are defined as

$$\begin{aligned} v^*(\phi) &= v_1\, w(\phi) \\ \overline{\beta}^*(\phi) &= \overline{\beta}_1 \qquad 0 \le \phi \le \phi_1 \end{aligned} \tag{3.115a}$$

$$\begin{aligned} v^*(\phi) &= v_i \\ \overline{\beta}^*(\phi) &= \overline{\beta}_i \qquad \phi_{i-1} \le \phi \le \phi_i \qquad i = 2,3,\ldots,I-1 \end{aligned} \tag{3.115b}$$

$$\begin{aligned} v^*(\phi) &= v_I\, \overline{w}(\phi) \\ \overline{\beta}^*(\phi) &= \overline{\beta}_I \qquad \phi_{I-1} \le \phi \le 2\pi \end{aligned} \tag{3.115c}$$

where I is the total number of segments. As may be seen, the velocity distribution over each intermediate segment is specified as constant; however, as in section 2.1.7.1, the velocity distribution may be defined as a function of ϕ by the addition of the relative velocity distributions $\tilde{v}_i(\tilde{\phi}_i)$. The recovery functions $w(\phi)$ and $\overline{w}(\phi)$ are as defined in section 2.1.7.1 by equations (2.61) and (2.62*a*–*c*).

After forming $P(\phi)$ and substituting this into the integral constraints (3.101*a*) and (3.102*a*,*b*) and the continuity equation (3.110) at the trailing edge, it follows that

$$a_{11}\mu + a_{12}\overline{\mu} + a_{13}K_H + a_{14}\overline{K}_H = b_1 \tag{3.116a}$$

$$a_{21}\mu + a_{22}\overline{\mu} + a_{23}K_H + a_{24}\overline{K}_H = b_2 \tag{3.116b}$$

$$a_{31}\mu + a_{32}\overline{\mu} + a_{33}K_H + a_{34}\overline{K}_H = b_3 \tag{3.116c}$$

$$a_{41}\mu + a_{42}\overline{\mu} + a_{43}K_H + a_{44}\overline{K}_H = b_4 \tag{3.116d}$$

where expressions for the coefficients a_{jk} and b_j are given in Appendix D. At all

other junctions, the continuity equation gives

$$\frac{v_i}{\overline{V}_i|\cos(\alpha+\overline{\beta}_i-\phi_i/2)|}=\frac{v_{i+1}}{\overline{V}_{i+1}|\cos(\alpha+\overline{\beta}_{i+1}-\phi_i/2)|}\qquad i=1,2,\ldots,I-1 \tag{3.117}$$

These equations are solved by letting μ, $\overline{\mu}$, K_H, and $\overline{K}_H$ and all the velocity levels v_i except one be the unknowns or free parameters. First, equation (3.117) is solved in order to determine all the velocity levels v_i. Next, the coefficients a_{jk} and b_j are determined according to the equations given in Appendix D, and the system (3.116*a–d*) is then solved. These parameters finish defining $P(\phi)$ from which $Q(\phi)$ is found by the method discussed in section 2.1.7.3, except in the present implementation only the leading-edge corner (which is by far the largest) is split-off of $P(\phi)$ before forming $Q(\phi)$ as the sum of contributions due to the smooth part of $P(\phi)$ and the part with the sharp leading-edge corner. As may be shown from $dP(\phi)/d\phi$, the function $S(\phi)$ [equations (2.68) and (2.76)] to be split-off of $P(\phi)$ has the strength k given as

$$k=\frac{1}{2}[\tan(\alpha+\overline{\beta}_{i\,L}-\phi_{i\,L}/2)-\tan(\alpha+\overline{\beta}_{i\,L+1}-\phi_{i\,L}/2)] \tag{3.118}$$

where iL is used to mean the leading-edge segment.

3.2.11 Example Cascades with Multi-Dimensional Newton Iteration

Having specified the location of the spiral and the velocity distribution according to equations (3.115) along with the velocity normal to the cascade front ($u=1$ in the examples to follow), the governing equations (3.116*a–b*) and (3.117) may be solved. In all likelihood, the resulting cascade blade will be either bulbous (as, for example, in figure 3-19), crossed or unrecognizable. The problem again stems from the values determined for K_H and $\overline{K}_H$ which control the shape of the velocity

Figure 3-19 Example cascade derived by the inverse method without Newton iteration ($K_H = 7.652$, $\overline{K}_H = 8.656$).

distribution near the trailing edge. Newton iteration may be used to remedy the situation as was done for the isolated airfoil (section 2.1.9).

For the cascade shown in figure 3-19, the single prescribed velocity level and the leading-edge arc limit are iterated to achieve $K_H = 0.25$ and $\overline{K}_H = 0.25$ resulting in the cascade shown in figure 3-20. For this cascade made up of seven segments, the following values are used to specify the spiral location and the velocity distribution:

$$\begin{aligned}
a &= 1.5\, e^{i\,135^\circ} \\
\phi_1 &= 109.735^\circ & \beta_1 &= 50^\circ \\
\phi_2 &= 124.473^\circ & \beta_2 &= 50^\circ \\
\phi_3 &= 133.090^\circ & \beta_3 &= 53^\circ \\
\phi_4 &= 140.304^\circ & \beta_4 &= 56^\circ \\
 & & \beta_5 &= 59^\circ \\
\phi_6 &= 109.735^\circ & \beta_6 &= 45^\circ \\
\phi_7 &= 360^\circ & \beta_7 &= 45^\circ \\
K &= 1 & \overline{K} &= 1 \\
\phi_W &\equiv \phi_1 & \overline{\phi}_W &\equiv \phi_6 \\
\phi_S &= 40^\circ & \overline{\phi}_S &= 320^\circ \\
\epsilon &= 0
\end{aligned} \tag{3.119}$$

From the given inlet angles, the outlet angles ($\overline{\beta}_1 = 33.912^\circ$, $\overline{\beta}_2 = 33.912^\circ$, $\overline{\beta}_3 = 35.136^\circ$, $\overline{\beta}_4 = 36.500^\circ$, $\overline{\beta}_5 = 38.034^\circ$, $\overline{\beta}_6 = 32.115^\circ$, and $\overline{\beta}_7 = 32.115^\circ$) are computed according to equation (3.99) in order to define $P(\phi)$ in terms of the outlet angle distribution. With this and Newton iteration as

$$\phi_5 \quad \Rightarrow \quad 0 = K_H - 0.25, \qquad v_1 \quad \Rightarrow \quad 0 = \overline{K}_H - 0.25 \tag{3.120}$$

the following solution is obtained:

$$\phi_5 = 157.238^\circ, \quad v_1 = 2.517, \quad v_2 = 2.517, \quad v_3 = 2.736$$

Figure 3-20 Example cascade designed by the inverse method with Newton iteration ($K_H = 0.25$, $\overline{K}_H = 0.25$).

$$v_4 = 3.056, \quad v_5 = 3.533, \quad v_6 = 1.121, \quad v_7 = 1.121 \tag{3.121}$$

The pertinent cascade parameters computed from the solution are

$$\sigma = 0.425, \quad \chi = -35.259°, \quad \beta_{zL} = 27.235°, \quad t/c = 0.200 \tag{3.122}$$

For the cascade shown in figure 3-19, the values $\phi_5 = 156.745°$ and $v_1 = 2.543$ were used. By comparison with equations (3.121) the changes necessary to result in a the normal cascade of figure 3-20 are only very slight. The resulting velocity distributions at the design inlet angles of $\beta_I = 45°, 50°, 53°, 56°$, and $59°$ are shown in figure 3-21. As may be seen, the first four segments on the upper surface and the first segment on the lower surface each have a constant velocity at the corresponding design inlet angle. Standard practice is to normalize the velocity distribution for a given inlet angle by the inlet flow speed $V_O(\beta_O)$ as shown in figure 3-22.

For code validation purposes, the cascade shown in figure 3-20 was analyzed using the recently added cascade option of the Eppler program (1988, 1990). Figure 3-23 shows a comparison between an exact solution and the predicted results for a cascade generated by the theory of section 3.1 with the chosen values $\mu = -0.07 + i\,0.2$ and $a = 3\,e^{i\,175°}$ to give $\sigma = 0.223$, $\chi = -5.242°$, and $t/c = 0.121$. The comparison is made at the zero-lift angle of $\beta_{zL} = -1.589°$ and results in an RMS difference of 0.000163. For the cascade shown in figure 3-20, the comparison shown in figure 3-24 is made at the zero-lift angle and gives again good agreement with an RMS difference of 0.000478. It may be concluded that the Eppler program gives correct results and that the inverse code gives the correct cascade geometry for a specified velocity distribution.

As a last example, a cascade with positive stagger and four segment is presented. Taking the values

$$\arg(a) = 280°$$

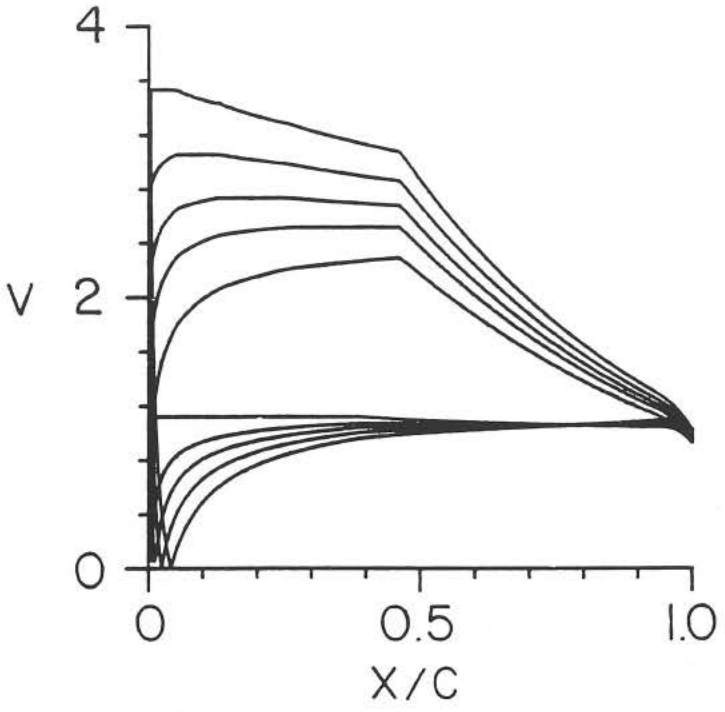

Figure 3-21 Velocity distributions for $\beta_1 = 45°$, 50°, 53°, 56° and 59° corresponding to the design inlet angles for the cascade shown in figure 3-20. (Each velocity distribution normalized by the flow speed normal to the cascade front.)

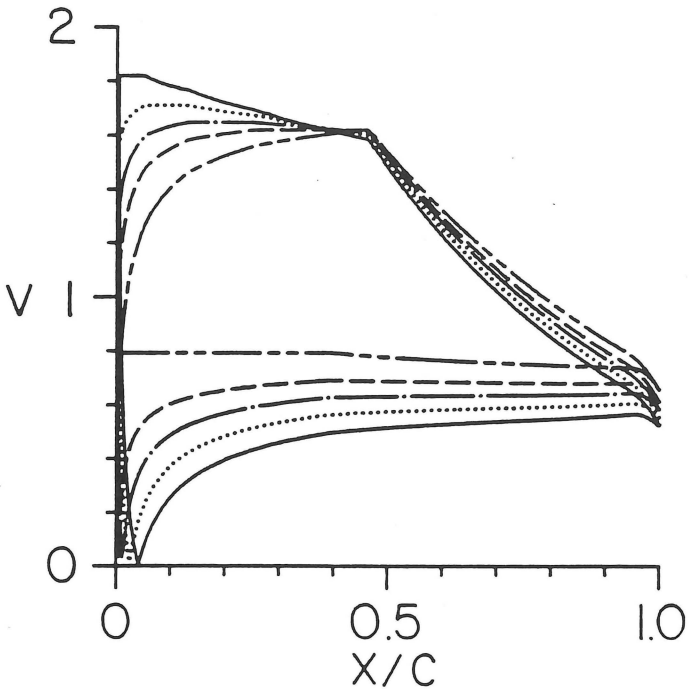

Figure 3-22 Velocity distributions for $\beta_1 = 45°$, 50°, 53°, 56° and 59° corresponding to the design inlet angles for the cascade shown in figure 3-20. (Each velocity distribution normalized by the inlet flow speed.)

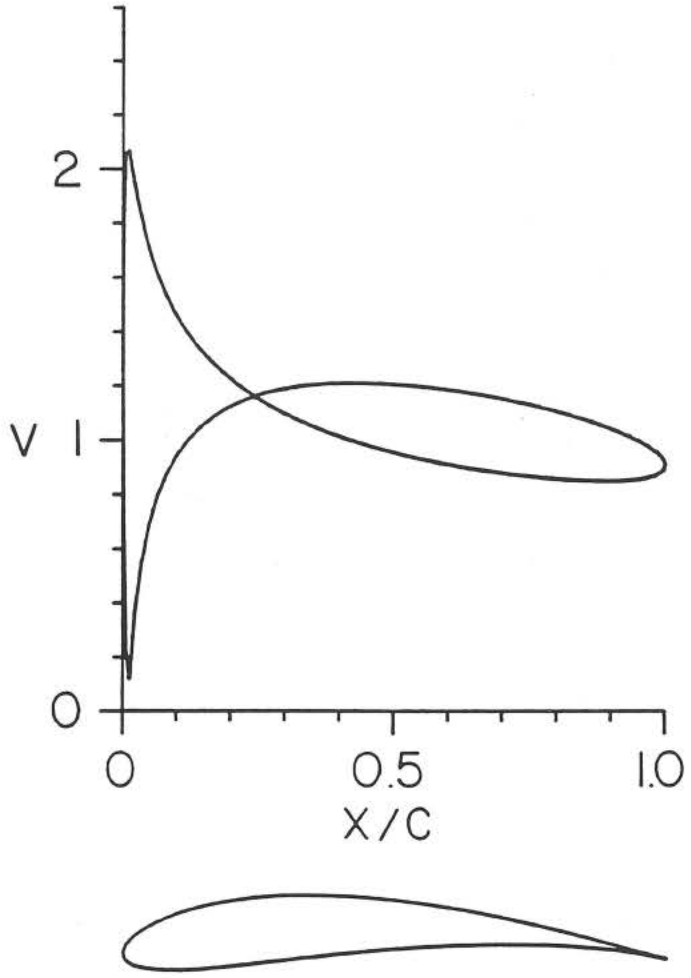

Figure 3-23 Comparison between the exact velocity distribution and the velocity distribution predicted by the Eppler program for $\beta_1 = \beta_{z_L} = -1.589°$ for a cascade generated by the theory of section 3.1. (Velocity distribution normalized by the inlet flow speed.)

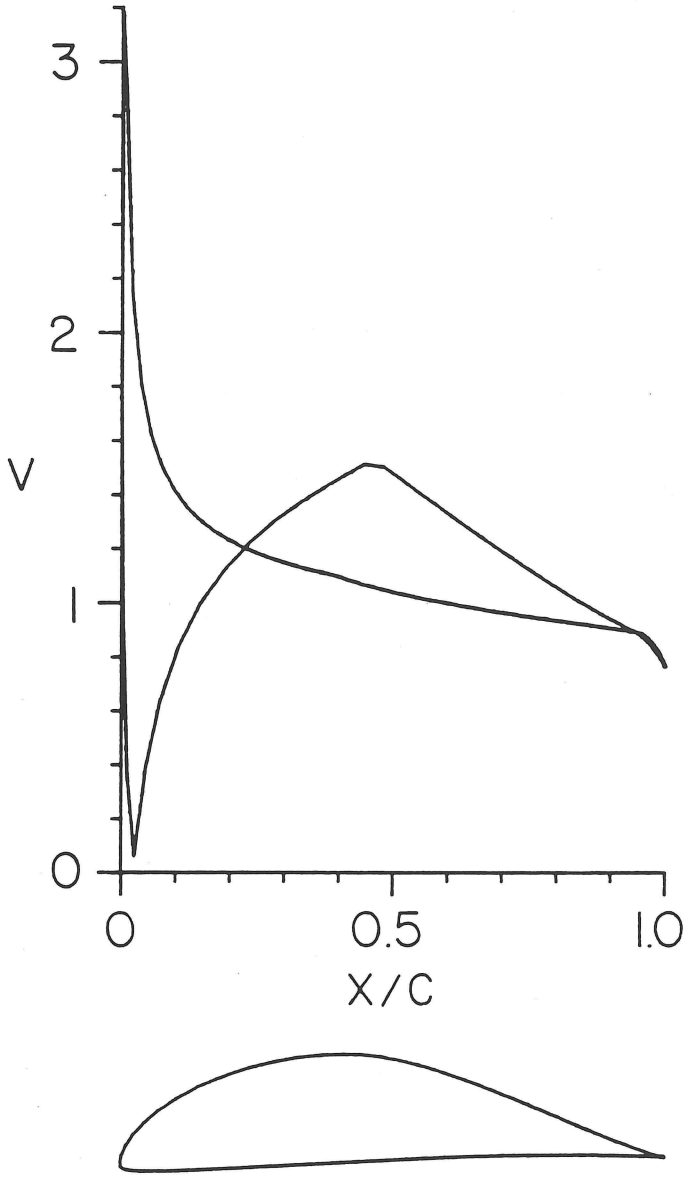

Figure 3-24 Comparison between the velocity distribution of figure 3-21 and the velocity distribution predicted by the Eppler program for $\beta_1 = \beta_{zL} = -1.589°$ for the cascade shown in figure 3-20. (Velocity distribution normalized by the inlet flow speed.)

Taking the values

$$\begin{aligned}
\arg(a) &= 280^\circ \\
\phi_1 &= 159.792^\circ & \beta_1 &= -30^\circ \\
& & \beta_2 &= -30^\circ \\
\phi_3 &= 290.449^\circ & \beta_3 &= -40^\circ \\
\phi_4 &= 360^\circ & \beta_4 &= -40^\circ \\
K &= 1 & \overline{K} &= 1 \\
\phi_{TE} &\equiv \phi_1 & \overline{\phi}_{TE} &\equiv \phi_3 \\
\phi_S &= 40^\circ & \overline{\phi}_S &= 320^\circ \\
\phi_F &= 10^\circ & \overline{\phi}_F &= 330^\circ \\
\epsilon &= 1/9
\end{aligned} \tag{3.123}$$

and iterating as

$$|a| = A \quad \Rightarrow \quad 0 = \sigma - 1, \qquad \phi_2 \quad \Rightarrow \quad 0 = K_H - 1, \qquad v_1 \quad \Rightarrow \quad 0 = \overline{K}_H \tag{3.124}$$

results in

$$A = 1.040, \quad \phi_2 = 278.456, \quad v_1 = 1.757$$

$$v_2 = 1.757, \quad v_3 = 1.419, \quad v_4 = 1.419 \tag{3.125}$$

In this case, the cascade parameters computed from the solution are

$$\chi = 41.023^\circ, \quad \beta_{zL} = -51.339^\circ, \quad t/c = 0.106 \tag{3.126}$$

Figures 3-25 and 3-26 (a–c) show that cascade geometry and velocity distributions for $\beta_l = -30^\circ$ and -40° respectively. For this cascade 500 points were used to find the cascade-blade shape, and as seen in figure 3-27 (where the points are shown as symbols) the stretching about the leading edge is extreme.

Figure 3-25 Cascade design with a solidity of one.

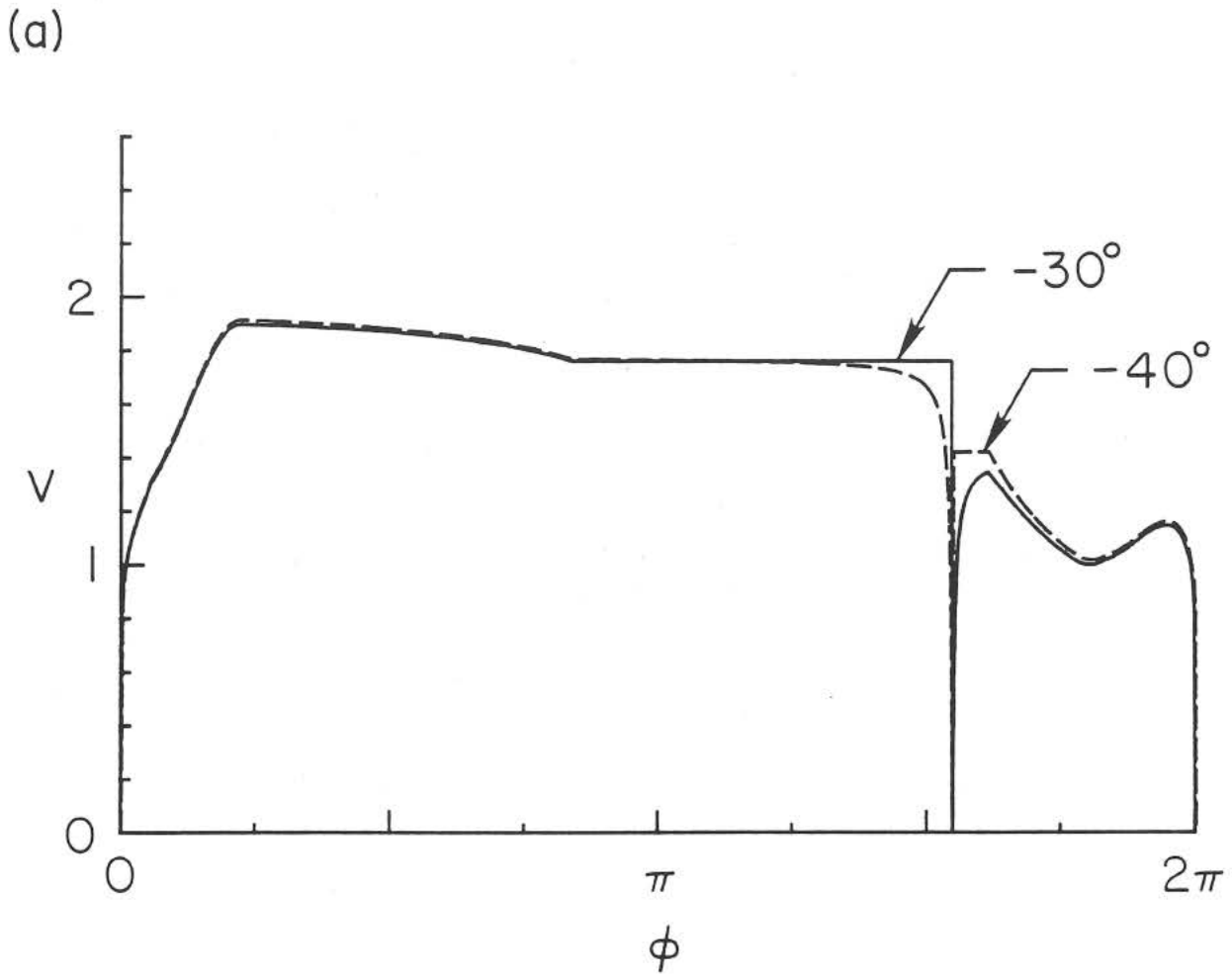

Figure 3-26 Velocity distributions for $\beta_1 = -30°$ and $-40°$ corresponding to the cascade shown in figure 3-25. (Each velocity distribution normalized by the flow speed normal to the cascade front.)

(figure continues)

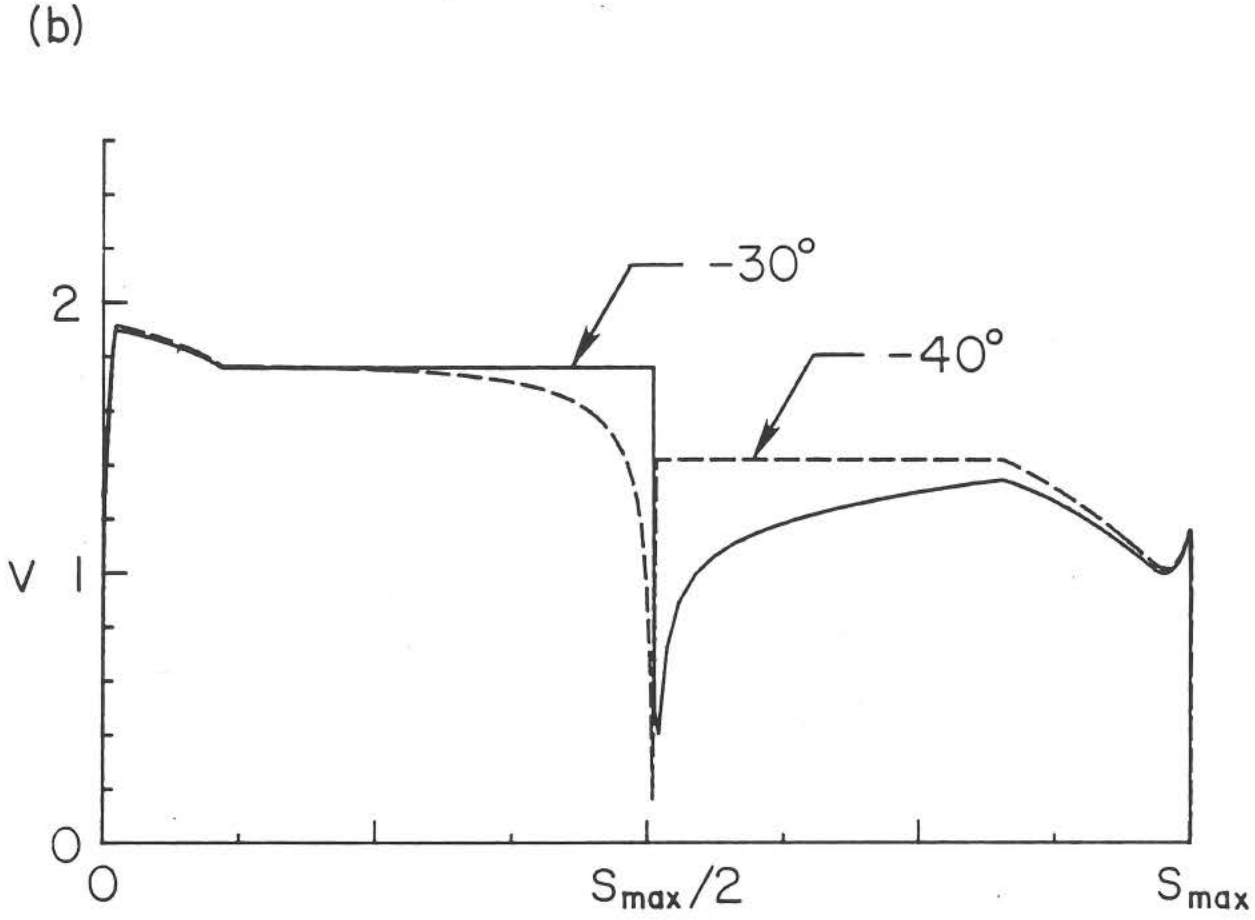

Figure 3-26 Continued.

(figure continues)

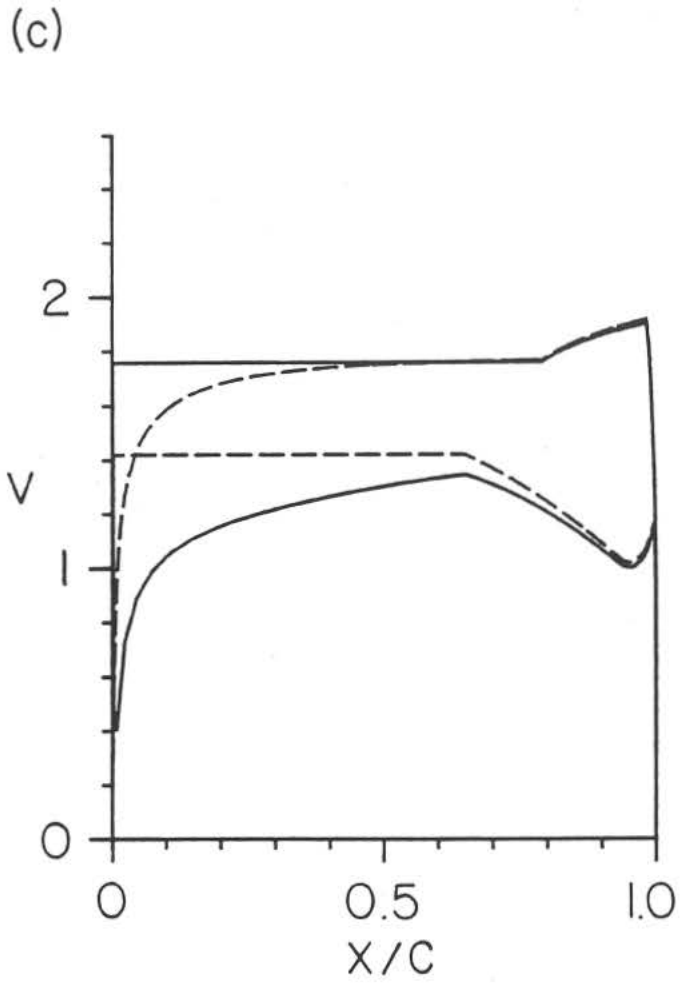

Figure 3-26 Continued.

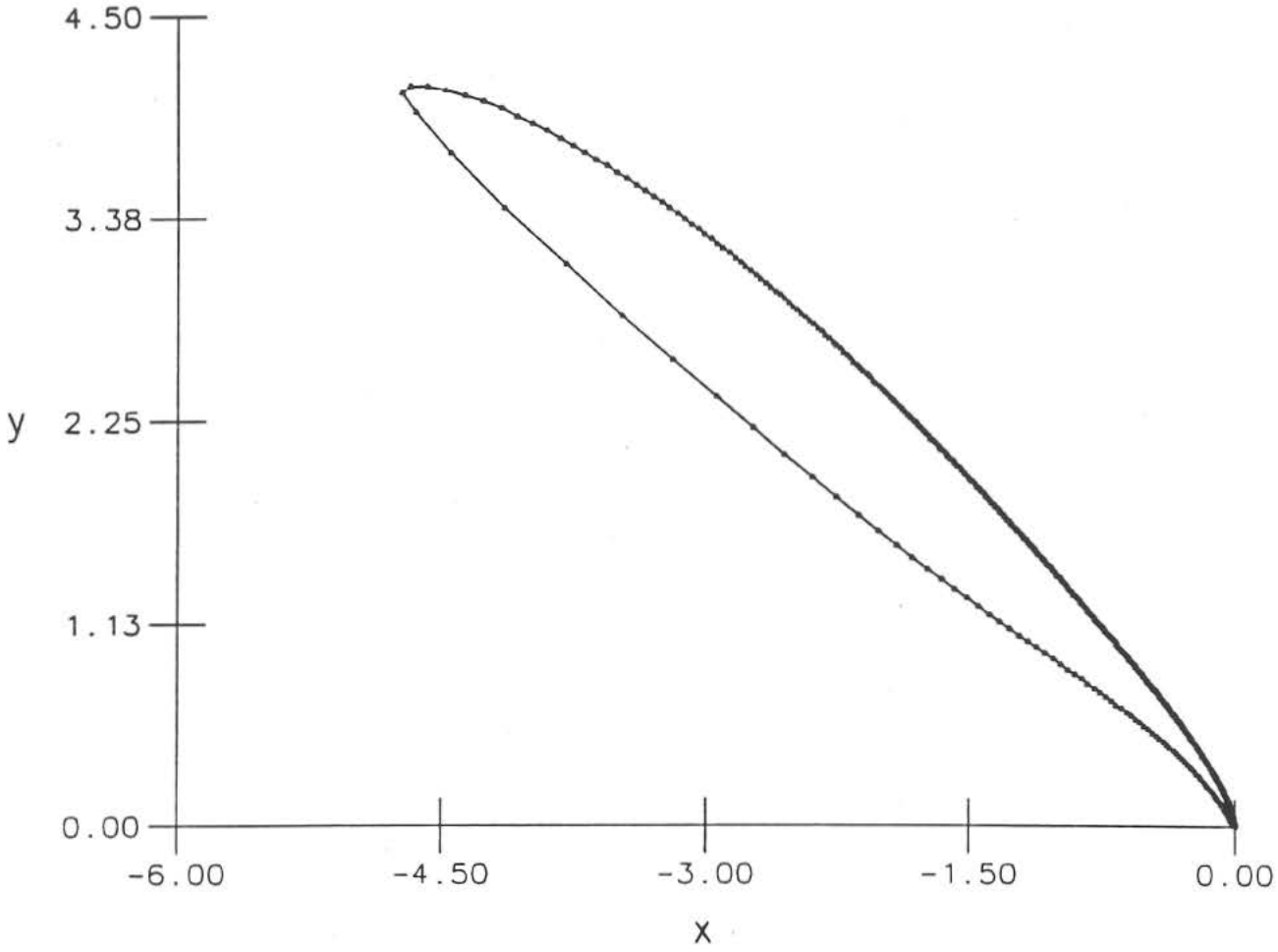

Figure 3-27 Cascade blade for cascade shown in figure 3-25 with symbols plotted at each of the 500 points about the cascade blade to illustrate the stretching near the leading edge.

This last example illustrates the practical limitation of the method as previously discussed. Attempting to obtain solidities much greater that one results in stretching so severe about the leading edge that the integration of the cascade-blade coordinates by equation (3.81) leads to numerical inaccuracies resulting in a cascade blade which does not close on itself. This aside, the method should prove valuable in the design of cascades for solidities up to one.

3.3 ANALYSIS OF AN INFINITE CASCADE OF AIRFOILS

One approach to solving the analysis problem for cascades by conformal mapping is to map the infinite cascade first to a single body. Then, this single body, through subsequent mappings, is taken to a circle. By far the most common approach to determining the last mapping is to use Theodorsen's method (e.g., Garrick 1944; Howell 1948; Hall and Thwaites 1963). The current analysis method differs significantly from previous methods in two ways. First, the mapping from the infinite cascade to the circle is done in one step. Second, rather than solving for the mapping itself, the mapping derivative is determined from which the velocity distribution is directly obtained.

The current analysis method for cascades draws on the analysis method for isolated airfoils as discussed in section 2.3. In application of that method to cascades, it is necessary to determine not only $s(\phi)$ but also $a = A\,e^{i\,\alpha}$. From these quantities follow $Q(\phi)$, then $P(\phi)$ and finally the velocity distribution. To this end, an iterative technique must be employed to determine $s(\phi)$, A and α from the known surface angle $\theta(s)$, solidity σ and stagger χ for a given cascade. As to be discussed, the method determines estimates of $s(\phi)$ from the known $\theta(s)$ and from the estimates of A and α. In this process, a two-dimensional Newton iteration is performed to

determine the correct values for A and α which give rise to σ and χ for the given cascade.

Starting from the estimates $\hat{s}^i(\phi)$, $\hat{A}^i$ and $\hat{\alpha}^i$, the estimate $\hat{Q}^i(\phi)$ is determine by [equation (3.109b)]

$$\hat{Q}^i(\phi) = \hat{\theta}^i(\phi) - \phi/2 + \epsilon(\pi/2 - \phi/2) + \arg[\exp(i\,\phi) - \hat{A}^i \exp(i\,\hat{\alpha}^i)] \qquad (3.127)$$

This estimate for $Q(\phi)$ will not necessarily satisfy the integral constraints (3.101b) and (3.103a,b). A correction, however, can be applied in a manner similar to that discussed in section 2.3 for the isolated airfoil. It is not possible to correct $\hat{Q}^i(\phi)$ by the simple and intuitive procedure used for the isolated airfoil—that procedure which involves subtracting-off quantities in order to satisfy the conditions on the mapping coefficients. Simple conditions on the coefficients do not exist for the cascade; however, integral constraints for the cascade are known and may be used to determine the correction as done in the alternative approach for the isolated airfoil (section 2.3).

The new estimate for $Q(\phi)$ is given by

$$\hat{Q}^{i+1}(\phi) = \hat{Q}^i(\phi) + k_1 + k_2 \cos\phi + k_3 \sin\phi \qquad (3.128)$$

Substitution of $\hat{Q}^{i+1}(\phi)$ into the three integral constraints on $Q(\phi)$ leads to three linear equations for the three unknowns k_1, k_2 and k_3. After solving for these three coefficients, $\hat{Q}^i(\phi)$ may be corrected according to (3.128). The new estimate $\hat{P}^{i+1}(\phi)$ is then determine from $\hat{Q}^{i+1}(\phi)$ which together define the mapping derivative about the circle. The cascade-blade coordinates may then be obtained through equation (3.81). Based on the resulting cascade geometry, the corresponding σ and χ are determined.

Using the same initial estimates for $\hat{s}^i(\phi)$ and $\hat{\alpha}^i$, a perturbation is added to $\hat{A}^i$, and the process is repeated for the corresponding σ and χ. From this perturbation and the changes in σ and χ, the sensitivities of σ and χ to changes in $\hat{A}^i$ are computed. Next, using $\hat{s}^i(\phi)$ and $\hat{A}^i$, a perturbation is added to $\hat{\alpha}^i$, and the sensitivities of σ and χ to changes in $\hat{\alpha}^i$ are determined by repeating the process again. Based on the resulting Jacobian, the current σ and χ from the unperturbed solution, and the known σ and χ for the given cascade, the corrections $\delta\hat{A}$ and $\delta\hat{\alpha}$ are determined to give the new estimates $\hat{A}^{i+1} = \hat{A}^i + \delta\hat{A}$ and $\hat{\alpha}^{i+1} = \hat{\alpha}^i + \delta\hat{\alpha}$. With these new estimates and the estimate $\hat{s}^{i+1}(\phi)$ from the unperturbed solution, the entire process is repeated. When successive estimates $\hat{s}^i(\phi)$ and $\hat{s}^{i+1}(\phi)$ cease to differ significantly, the solution has converged, and the velocity distribution may be computed for any flow angle according to equation (3.114). Whether or not the proposed method proves feasible awaits practical implementation of the theory.

Chapter 4

SUGGESTIONS FOR FUTURE WORK

The inverse airfoil and inverse cascade design problems as presented belong to a class of solutions which involve mapping the physical flow into the flow about the circle. For the isolated airfoil problem, the flow in the circle plane results from a vortex-source infinitely far upstream and a vortex-sink infinitely far downstream which inside the circle form an image represented by a doublet and vortex at the circle center. When one of these spirals at infinity is brought to a point at a finite distance from the circle, the flow may be mapped into a cascade so long as the mapping is singular (by a first-order pole) at the location of the spiral. The cascade need not be an infinite cascade as presented in Chapter 3. By introducing $z^{1/N} = \zeta + c_0 + c_1/\zeta + \cdots$, the circle may be mapped into a radial cascade with N blades.

If instead the vortex-sink infinitely far downstream of the circle is brought to a point on the circle (in which case the vortex-sink becomes simply a sink), this point may be mapped infinitely far downstream by again introducing a first-order pole in the mapping derivative at the location of the sink. Such a flow in the physical plane would correspond to the flow about a semi-infinite body. If the vortex-source infinitely far upstream is then brought to a point at a finite distance from the circle and another first-order pole is introduced into the mapping at the location of the vortex-source, the flow may be mapped into an infinite cascade of semi-infinite bodies. Moving the vortex-source from off the circle to a point on the circle so that a source and sink exist on the circle results in a flow which may be mapped to the flow about a channel or more importantly the flow within a channel. This channel

may be curved depending on the location of the source and sink.

It is not strictly necessary that there exist on the boundary of the circle just one source and one sink. These singularities may be split into any number so long as the sum of the strengths of the sources and sinks is zero. The mapping then must contain first-order poles at the locations of each source and each sink which may then be mapped into a channel with as many branches as there are singularities. These singularities may also be combined into a single doublet which may then be mapped into the flow over (or under) a mound.

For each of these flow problems, all resulting from the flow about a circle derivable from the Milne-Thomson circle theorem, there will be conditions on the mapping for the inverse design problem. Depending on the particular problem, these conditions may ensure closure (airfoils, infinite and radial cascades) or may set the spacing between adjacent bodies (cascades), the gap width (semi-infinite bodies, cascades of semi-infinite bodies, channels), or the flow direction at infinity (airfoils, cascades, semi-infinite bodies, channels, mounds). By far the two most important problems of this class are airfoils and cascades which have both been presented in this thesis.

The airfoil design method presented in this thesis could be further improved to allow for the prescription of additional boundary-layer variables, for instance, c_f and δ_2. This would enhance the utility of the method. Sometimes it is not always clear what is the best distribution of a particular boundary-layer parameter that gives rise to a desired airfoil performance. In this case, the design effort must rely on practical experience. Further studies are suggested to ascertain what type of boundary-layer distribution is needed for a desired airfoil performance.

Chapter 5

CONCLUSIONS

5.1 ISOLATED AIRFOILS

In this thesis, an inverse airfoil design technique has been developed by coupling a potential-flow multi-point inverse airfoil design method with a direct boundary-layer method. It has been shown that satisfying the integral constraints, continuity constraints, and stagnation point velocity relationships for the potential-flow inverse problem does not guarantee a normal airfoil shape, let alone one which matches all of the design requirements. The myriad of possible design requirements may, however, be selectively satisfied (so long as they are compatible) by reformulating the solution and solving the equations by multi-dimensional Newton iteration. This approach makes it possible to specify single parameters such as maximum thickness, enclosed area, pitching moment, and also distributions of velocity and boundary-layer flow physics along segments of the airfoil for the given conditions such as angle of attack and Reynolds number. Although the current approach makes use of an incompressible-flow inverse method for airfoil design, a compressible-flow inverse method could be used in place of the present method. Likewise, the boundary-layer method could be replaced. As it stands, fairly sophisticated airfoil design studies can now be made with relative ease, and this should ultimately lead to improvements in new airfoil designs.

5.2 INFINITE CASCADES

For the infinite cascade, there exists a wide variety of conformal mapping solution techniques because there are many alternative domains onto which the cascade may be mapped. These solution techniques differ further by the way in which the cascade is ultimately mapped into the final domain. Typically, a sequence of mappings is used to take the cascade into first an intermediate domain in order to either remove the cascade-blade trailing-edge sharp corner or reduce the cascade to a single body or both. From this domain, further intermediate mappings may be used to eventually take the cascade into the plane in which the flow is easily determined. In the present method, this task has been greatly simplified by employing just one mapping to go from the infinite cascade to a single circle in the presence of a single spiral. It has been shown that exact solutions for the infinite cascade may be derived in a way almost perfectly analogous to the exact Joukowski airfoil solution.

The single mapping used to generate exact solutions may be generalized to allow for multi-point inverse design of an infinite cascade of airfoils. All previously existing inverse methods for cascade design are only capable of solving the single-point inverse design problem. The current approach is almost perfectly analogous to the inverse method for isolated airfoil design as presented. As discussed, the mapping is introduced in its derivative form which is singular at a point exterior to the circle. From this point in the cascade plane there emanates a vortex-source which is the image of the inlet flow in the cascade plane. In forming the complex velocity in the cascade plane, this vortex-source and the singularity of the mapping cancel and thereby leave the complex velocity in the cascade plane regular at all points exterior to the cascade as required. From this key step of expressing the mapping derivative in its general form there follows all the necessary conditions for

the potential-flow inverse design problem. In the process, it is readily seen that multi-point design is a natural outcome of the formulation.

As demonstrated, solutions to the inverse problem for the cascades are unwieldy unless Newton iteration is employed to permit the specification of parameters which ultimately dictate in large part whether or not the cascade blades are crossed or uncrossed. Iteration may also be performed to control cascade solidity and stagger in addition to parameters of interest in the isolated airfoil design problem. Although the current implementation of the inverse cascade design theory does not take full advantage of the ideas expressed and illustrated in the isolated airfoil design problem, there are no fundamental limitations which prevent this extension of the method. The method, however, is limited by the fact that numerical errors are encountered if an attempt is made to design a cascade with a solidity greater than one. In that case, let it be said that there is no difficulty with the method in designing cascades with solidities up to one.

REFERENCES

Abbott, I. H. (1980), "Airfoils: Significance and Early Development," in *The Evolution of Aircraft Wing Design*, AIAA Symposium, pp. 23–24.

Abbott, I. H., Von Doenhoff, A. E. and Stivers, L. S., Jr. (1945), "Summary of Airfoil Data," NACA Rept. 824.

Abbott, I. H. and Von Doenhoff, A. E. (1959), "Theory of Wing Sections," Dover, New York.

Arlinger, G. (1970), "An Exact Method of Two-Dimensional Airfoil Design," Saab, SAAB TN 67, October.

Barger, R. L. (1974), "A Modified Theodorsen ϵ-Function Airfoil Design Procedure," NASA TN D-7741.

Barger, R. L. (1975 *a*), "Procedures for the Design of Low-Pitching-Moment Airfoils," NASA TN D-7982.

Barger, R. L. (1975 *b*), "Adaptation of the Theodorsen Theory to the Representation of an Airfoil as a Combination of a Lifting Line and a Thickness Distribution," NASA TN D-8117.

Betz, A. (1934), "Änderung der Profilform zur Erzielung einer vorgegebenen Änderung der Druckverteilung," *Luftfahrtforschung*, Vol. 11, No. 6, pp. 158–164. (Also NACA Translation TM-767, 1935.)

Cebeci, T. (1976), "An Inverse Boundary-Layer Method for Compressible Laminar and Turbulent Boundary Layers," *J. Aircraft*, Vol. 13, No. 9, pp. 709–717.

Costello, G. R. (1950), "Method of Designing Cascade Blades with Prescribed Velocity Distributions in Compressible Potential Flows," NACA Rept. 978.

Costello, G. R., Cummings, R. L. and Sinnette, J. T. Jr. (1952), "Detailed Computational Procedure for Design of Cascade Blades with Prescribed Velocity Distributions in Compressible Potential Flows," NACA Rept. 1060.

Collar, A. R. (1941), "The Flow of a Perfect Fluid through Cascades of Aerofoils," *J. Royal Aeronautical Society*, May, pp. 183–213.

Crooks, P. V. and Howard, W. (1954), "Low Speed Tests on Three Aerofoil Cascades Designed for Prescribed Surface Velocity Distributions," Aust. Aeronautical Research Laboratories, Mechanical Engineering Note 76, June.

Dini, P. (1990), "A Computationally Efficient Modelling of Laminar Separation Bubbles," Ph.D. Thesis, Department of Aerospace Engineering, The Pennsylvania State University, August.

Dini, P., Selig, M. S. and Maughmer, M. D. (1991), "A Simplified e^n Method for Separated Boundary Layers," AIAA Paper 91-3285.

Drela, M. (1988), "Low-Reynolds-Number Airfoil Design for the M.I.T. Daedalus Prototype: A Case Study," *J. Aircraft*, Vol. 25, No. 8, pp. 724–732.

Drela, M. (1989), "XFOIL: An Analysis and Design System for Low Reynolds Number Airfoils," in *Lecture Notes in Engineering: Low Reynolds Number Aerodynamics*, T. J. Mueller (ed.), Vol. 54, Springer-Verlag, New York, June.

Drela, M. (1990 *a*), "Viscous and Inviscid Inverse Schemes Using Newton's Method," in *AGARD-FPD-VKI Lecture Series on Inverse Methods in Airfoil Design for Aeronautical and Turbomachinery Applications*, May.

Drela, M. (1990 *b*), "Elements of Airfoil Design Methodology," in *Progress in Astronautics and Aeronautics: Applied Computational Aerodynamics*, P. A. Henne (ed.), Vol. 125, AIAA, Washington, D.C., pp. 167–189.

Drela, M. and Giles, M.B. (1986), "Viscous-Inviscid Analysis of Transonic and Low Reynolds Number Airfoils," AIAA Paper 86-1186.

Drela, M. and Giles, M.B. (1987), "Viscous-Inviscid Analysis of Transonic and Low Reynolds Number Airfoils," *J. Aircraft*, Vol. 25, No. 10, pp. 1347–1355.

Eppler, R. (1957), "Direkte Berechnungvon Tragflügelprofilen aus der Druckverteilung," *Ingenieur-Archive*, Vol. 25, No. 1, pp. 32–57. (Translated as "Direct Calculation of Airfoils from Pressure Distribution," NASA TT F-15, 417, 1974.)

Eppler, R. (1960), "Ergebnisse gemeinsamer Anwendung vo Grenzschicht- und Potentialtheorie," *Zeitschrift für Flugwissenschaften*, Vol. 8, No. 9, pp. 247–260. (Translated as "Results of the Combined Application of Boundary Layer and Profile Theory," NASA TT F-15, 416, March 1974.)

Eppler, R. (1963 *a*), "Praktische Berechnung laminarer und turbulenter Absaugegrenzchichten," *Ingenieur-Archive*, Vol. 32, No. 4, pp. 221–245. (Translated as "Practical Calculation of Laminar and Turbulent Bled-Off Boundary Layers," NASA TM 7-75328, September 1978.)

Eppler, R. (1963 *b*), "Vergleich theoretischer und experimenteller Profil-Widerstande," *Schweizer Aero-Review*, Vol. 38, No. 10, pp. 593–595. (Translated as "Comparison of Theoretical and Experimental Profile Drags," NASA TT F-16981, April 1976.)

Eppler, R. (1991), "Airfoil Program System, User's Guide," Institut A für Mechanik, Universität Stuttgart, March.

Eppler, R. (1990), *Airfoil Design and Data*, Springer-Verlag, New York.

Eppler, R. and Somers, D. M. (1979), "Low Speed Airfoil Design and Analysis," NASA CP 2045, Vol. 1, Part 1, pp. 73–99.

Eppler, R. and Somers, D. M. (1980 *a*), "A Computer Program for the Design and Analysis of Low-Speed Airfoils," NASA TM-80210, August.

Eppler, R. and Somers, D. M. (1980 *b*), "Supplement to: A Computer Program for the Design and Analysis of Low-Speed Airfoils," NASA TM-81862, December.

Garrick, I. E. (1944), "On the Plane Potential Flow Past a Lattice of Arbitrary Airfoils," NACA Rept. 788.

Garrick, I. E. (1952), "Conformal Mapping in Aerodynamics, with Emphasis on the Method of Successive Conjugates," in *National Bureau of Standards Applied Mathematics Series 18: Constructions and Application of Conformal Maps*, Washington.

Ghielmi, L., Marazzi, R. and Baron, A. (1989), "A Tool for Automatic Design of Airfoils in Different Operating Conditions," in *Computational Methods for Aerodynamic Design (Inverse) and Optimization*, AGARD CP-463.

Glauert, M. B. (1947), "The Application of the Exact Method of Aerofoil Design," Aeronautical Research Council, R&M 2683, October.

Goettsching, L. (1988), "Designs of Profiles for Cascades," NASA TT-20161, April. (Translated from *Thermodynamic and Flow Mechanical Problems in Aircraft and Spacecraft Drives*, Stuttgart University, West Germany, April 1986, pp. 243–267.)

Gostelow, J. P. (1965 *a*), "Potential Flow through Cascades - A Comparison between Exact and Approximate Solutions," Aeronautical Research Council, C.P. No. 807.

Gostelow, J. P. (1965 *b*), "Potential Flow through Cascades - Extensions to an Exact Theory," Aeronautical Research Council, C.P. No. 808.

Goto, A. and Shirakura, M. (1984), "Compressor Cascade Optimization based on Inverse Boundary Layer Method and Inverse Cascade Method (1st Report, An Inverse Cascade Method for Incompressible Two-Dimensional Potential Flow)," *Bulletin of JSME*, Vol. 27, No. 226, pp. 653–659.

Hall, W. S. and Thwaites, B. (1963), "On the Calculation of Cascade Flows," Aeronautical Research Council 24,367.

Hansen, J. R. (1987), *Engineer in Charge*, NASA SP-4305.

Henderson, M. L. (1978), "Inverse Boundary-Layer Technique for Airfoil Design," NASA CP-2045, Part 1, Vol. 1, pp. 383–397.

Hicks, R. M. and Vanderplaats, G. N. (1977), "Application of Numerical Optimization to the Design of Supercritical Airfoils without Drag-Creep," SAE Paper 760477.

Howell, A. R. (1948), "A Theory of Arbitrary Aerofoils in Cascade," *Phil. Mag.*, Vol. 39, No. 299, pp. 913–927.

Ingen, J. L. van (1969), "A Program for Airfoil Section Design Utilizing Computer Graphics," in *AGARD-VKI Short Course on High Reynolds Number Subsonic Aerodynamics*, AGARD LS-37-70, April.

Ingen, J. L. van (1975), "On The Calculation of Laminar Separation Bubbles in Two-Dimensional Incompressible Flow," AGARD CP-168.

Ives, D. C. and Liutermoza, J. F. (1977), "Analysis of Transonic Cascade Flow Using Conformal Mapping and Relaxation Techniques," *AIAA Journal*, Vol. 15, No. 5, pp. 647–650.

Jacobs, E. N., Ward, K. E. and Pinkerton, R. M. (1933), "The Characteristics of 78 Related Airfoil Sections from Tests in the Variable-Density Wind Tunnel," NACA Rept. 460.

Jacobs, E. N. (1939), "Preliminary Report on Laminar-Flow Airfoils and New Methods Adopted for Airfoil and Boundary-Layer Investigations," NACA WR L-345.

James, R. M. (1971), "A General Class of Airfoils Conformally Mapped from a Circle," Douglas Aircraft Corp., Rept. MDC J5108, Long Beach, Calif., May.

Joukowski, N. E. (1916), *Aerodynamique*, Gauthier-Villars, Paris.

Johnson, C. H. J. (1954), "Aerofoils in Cascade with Boundary Layer Control," Aust. Aeronautical Research Laboratories, Note 222, July.

Jordinson, R. (1970), "The Flat Plate Boundary Layer. Part 1. Numerical Integration of the Orr-Sommerfeld Equation," *Journal of Fluid Mechanics,* Vol. 43, Part 4, pp. 801–811.

Kolesar, C. E. (1987), "Design and Test of a Natural Laminar Flow / Large Reynolds Number Airfoil with a High Design Cruise Lift Coefficient," in *Research in Natural Laminar Flow and Laminar-Flow Control,* J. N. Hefner and F. E. Sabo (eds.), NASA CP-2487, Part3, March, pp. 727–751.

Lewis, R. I. (1982), "A Method for Inverse Aerofoil and Cascade Design by Surface Vorticity," ASME Paper 82-GT-154.

Liebeck, R. H. and Ormsbee, A. I. (1970), "Optimization of Airfoils for Maximum Lift," *J. Aircraft*, Vol. 7, No. 5, pp. 409-415.

Liebeck, R. H. (1976), "On the Design of Subsonic Airfoils for High Lift," AIAA Paper 76-406.

Liebeck, R. H. (1978), "Design of Subsonic Airfoil for High Lift," *J. Aircraft*, Vol. 15, No. 9, pp. 547–561.

Liebeck, R. H. (1990), "Subsonic Airfoil Design," in *Progress in Astronautics and Aeronautics: Applied Computational Aerodynamics*, P. A. Henne (ed.), Vol. 125, AIAA, Washington, D.C., pp. 133–165.

Lighthill, M. J. (1945 *a*), "A New Method of Two-Dimensional Aerodynamic Design," Aeronautical Research Council, R&M 2112, April.

Lighthill, M. J. (1945 *b*), "A Mathematical Method of Cascade Design," Aeronautical Research Council, R&M 2104, June.

Ludwieg, H. and Tillmann, W. (1949), "Untersuchungen üder die Wandschubspannung in Turbulenten Reibungsschichten," *Ingenieur-Archive*, Vol. 17, pp. 288–299. (Translated as "Investigations of the Wall-Shearing Stress in Turbulent Boundary Layers," NACA TM 1285.)

Mangler, W. (1938), "Die Berechnung eines Tragflügelprofiles mit vorgeschreibener Druckverteilung", *Jahrbuch der deutschen Luftfahrtforschung*, Vol. 1, pp 46–53. (Translated as Air Ministry of London, Translation No. 932, 1940.)

Maughmer, M. D. and Somers, D. M. (1989), "Design and Experimental Results for a High-Altitude, Long-Endurance Airfoil," *J. Aircraft*, Vol. 26, No. 2, pp. 148–153.

McMasters, J. H. and Henderson, M. L. (1979), "Low-Speed Single-Element Airfoil Synthesis," NASA SP-2085, pp. 1–31.

Merchant, W. and Collar, A. R. (1941), "Flow of an Ideal Fluid Past a Cascade of Blades (Part II)," Aeronautical Research Council, R&M 1893, May.

Miley, S. J. (1974), "On the Design of Airfoils for Low Reynolds Numbers," AIAA Paper 74-1017.

Milne-Thomson, L. M. (1958), *Theoretical Aerodynamics*, Dover, New York.

Nonweiler, T. R. F. (1968), "A New Series of Low-Drag Aerofoils," Aeronautical Research Council, R&M 3618, March.

Ormsbee, A. I. and Maughmer, M. D. (1985), "A Class of Airfoils Having Finite Trailing Edge Pressure Gradients," AIAA Paper 85-0206.

Papailiou, K. (1967), "Blade Optimization Based on Boundary Layer Concepts," Von Karman Institute for Fluid Dynamics, Course Note 60, March.

Peebles, G. H. (1947), "A Method for Calculating Airfoil Sections from Specifications on the Pressure Distributions," Journal of the Aeronautical Sciences, Vol. 4, No. 8., pp. 451–456.

Peebles, G. H. and Parkin, B. R. (1956), "Calculation of Hydrofoil Sections for Prescribed Pressure Distributions," Society of Naval Architects and Marine Engineers, Technical and Research Bulletin No. 1–17, December. (Reprinted March 1966.)

Polito, L. (1974), "Un Metodo Esatto per il Progetto di Profili Alari in Corrente Incompressibile Aventi un Prestabilito Andamento della Velocità sul Contorno," Universita degli Studi di Pisa, Pisa, Italy, Rept. 42.

Rosenblatt, S. and Woods, L. C. (1956), "A Method of Cascade Design for Two-Dimensional Incompressible Flow," Aust. Aeronautical Research Committee, Rept. ACA-58, March.

Rotta, J. (1952), "Schubspannungsverteilung und Energiedissipation bei turbulenten Grenzschichten," *Ingenieur-Archive*, Vol. 20, pp. 195–207.

Ruzicka, M. and Spacek, L. (1981), "A Mathematical Method for Design of Turbine Blade Cascades for Small Subsonic Mach Numbers," National Research Institute for Machine Design, Monographs and Memoranda, No. 29, Bechovice.

Sanz, M. J. (1988), "Automated Design of Controlled Diffusion Blades," ASME Paper 88-GT-139.

Sanz, M. J. (1991), private communications.

Schwering, W. (1970), "Design of Cascades for Incompressible Plane Potential Flows with Prescribed Velocity Distribution," ASME Paper 70-GT-87.

Selig, M. S. and Maughmer, M. D. (1991 *a*), "A Multi-Point Inverse Airfoil Design Method Based on Conformal Mapping," AIAA Paper 91-0069.

Selig, M. S. and Maughmer, M. D. (1991 *b*), "Generalized Multi-Point Inverse Airfoil Design," AIAA Paper 91-3333.

Selig, M. S., Maughmer, M. D. and Somers, D. M. (1989), "An Airfoil for General Aviation Applications," Presented at Techfest XVI, Wichita Section AIAA, Wichita, KS, November.

Selig, M. S., Maughmer, M. D. and Somers, D. M. (1990), "An Airfoil for General Aviation Applications," in *Proceedings of the 1990 AIAA/FAA Joint Symposium on General Aviation Systems*, DOT/FAA/CT-90/11, May, pp. 280–291.

Shen, Y. T. and Eppler, R. (1981), "Wing Sections for Hydrofoils–Part 2: Nonsymmetrical Profiles," *J. Ship Research*, Vol. 25, No. 3, pp. 191–200.

Shirakura, M. (1972), "Potential Flow about Arbitrary Thick Blades of Large Camber in Cascade," in *The Second International JSME Symposium, Fluid Machinery and Fluidics*, Tokyo, pp. 71–82.

Scholtz, N. (1965), *Aerodynamik der Schaufelgitter*, Verlag G. Braun, Karlsruhe, p. 320.

Sobieczky, H. (1989), "Progress in Inverse Design and Optimization in Aerodynamics," in *Computational Methods for Aerodynamic Design (Inverse) and Optimization*, AGARD CP-463.

Somers, D. M. (1981), "Design and Experimental Results for a Flapped Natural-Laminar-Flow Airfoil for General Aviation Applications," NASA TP-1865.

Somers, D. M. (1992), "Subsonic Natural-Laminar-Flow Airfoils," in *Natural Laminar Flow and Laminar Flow Control*, R. W. Barnwell and M. Y. Hussaini (eds.), Springer-Verlag, New York.

Somers, D. M. and Horstmann, K. H. (1985), "Design of a Medium-Speed, Natural-Laminar-Flow Airfoil for Commuter Aircraft Applications," Institut fur Entwurfsaerodynamik, Braunschweig, IB 129-85/26, April.

Sorensin, T. (1991), "Airfoil Optimization with Efficient Gradient Calculations," in *Third International Conference on Inverse Design Concepts and Optimization in Engineering Sciences*, G. S. Dulikravich (ed.), Washington, October, pp. 433-444.

Stock, H. W. (1988), "An Inverse Boundary-Layer Method for Turbulent Flows on Infinite Swept Wings," *Z. Flugwiss. Weltraumforsch.*, Vol. 12, pp. 51–62.

Strand, T. (1973), "Exact Method of Designing Airfoil with Given Velocity Distribution in Incompressible Flow," *J.of Aircraft*, Vol. 10, No. 11, pp. 651–659.

Stratford, B. S. (1959), "An Experimental Flow with Zero Skin Friction throughout Its Region of Pressure Rise," *J. Fluid Mechanics*, Vol. 5, No. 17, pp. 1–16.

Theodorsen, T. (1931), "Theory of Wing Sections of Arbitrary Shape," NACA TR-411.

Theodorsen, T. and Garrick, I. E. (1933), "General Potential Theory of Arbitrary Wing Sections," NACA Rept. 452.

Theodorsen, T. (1944), "Airfoil-Contour Modifications Based on ϵ-Curve Method of Calculating Pressure Distribution," NACA WR L-135. (Formerly NACA ARR L4G05.)

Timman, R. (1951), "The Direct and Inverse Problem of Airfoil Theory. A Method to Obtain Numerical Solutions," Rept. F.16, National Aeronautical Research Inst., Amsterdam.

Traupel, W. (1945), "Die Berechnung der Strömung durch Schaufelgitter," *Sulzer Tech. Rundschau*, Nr. 1, pp. 25–42.

Viken, J. K. (1983), "Aerodynamic Design Considerations and Theoretical Results for a High Reynolds Number Natural Laminar Flow Airfoil," M.S. Thesis, George Washington University, January.

Watson, E. J. (1945), "Formulæ for the Computation of the Functions Employed for Calculating the Velocity Distribution about a Given Aerofoil," Aeronautical Research Council, R&M 2176, May.

Weinig, F. (1929), "Widerstands- und Tragflügelprofile mit vorgeschriebener Geschwindigkeitsverteilung an der Oberfläche," *Z. angew. Math. Mech.*, Vol. 9, 1929, pp. 507–513.

Weinig, F. (1935), *Die Strömung um die Schaufeln von Turbomashinen*, Johann Ambreosius Barth, Liepzig.

Wieghardt, K. (1948), "Über einen Energiesatz zur Berechnung Laminarer Grenzschichten," *Ingenieur-Archive*, Vol. 16, No. 1, pp. 21–242.

Whitfield, D. L., Swafford, T. W. and Donegan, T. L. (1982), "An Inverse Integral Computational Method for Compressible Turbulent Boundary Layers," in *Recent Contributions to Fluid Mechanics*, W. Haase (ed.), Springer-Verlag, New York.

Wilkinson, D. H. (1969), "Analysis and Design of Aerofoils and Cascades in Incompressible Flow," *J. Science and Technology*, Vol. 36, No. 2, pp. 99–104.

Wortmann, F. X. (1955), "Ein Beitrag zum Entwurf von Laminarprofilen für Segelflugzeuge und Hubschrauber," *ZFW*, Vol. 3, No. 10, pp. 333–345. (Translated as British M.O.S. translation TIL/T A903, 1960.)

Wortmann, F. X. (1957), "Experimentelle Untersuchungen an neuen Laminarprofilen für Segelflugzeuge und Hubschrauber," *ZFW*, Vol. 5, No. 8, pp. 228–243. (Translated as British M.O.S. translation TIL/T A906, 1960.)

Wortmann, F. X. (1961), "Progress in the Design of Low Drag Airfoils," in *Boundary Layer and Flow Control*, G.V. Lachmann (ed.), Pergamon Press, London, pp. 748-770.

Appendix A

CONTINUITY CONSTRAINTS

The condition that the mapping must be continuous (excluding the trailing-edge point) about the circle may be viewed without regard to the harmonic function $P(\phi)$. It is only necessary to state that $|dz/d\zeta|$ is continuous. This condition of continuity leads to a condition on the design velocity distribution as follows.

Consider as depicted in figure A-1 the velocity distribution about the circle. Two velocity distributions $w(\phi)$ for α_1 and α_2 are shown. Shown in figure A-2 are the velocity distributions $v(\phi)$ about the airfoil for the same two angles of attack. The velocity distribution about the circle is known. With regard to the airfoil, the velocity level v_1 is known for α_1. The question is to find v_2 for α_2.

To this end, it may be written that

$$\left|\frac{dz}{d\zeta}\right| = \left|\frac{dF/d\zeta}{dF/dz}\right| = \frac{w}{v} \tag{A.1}$$

This quantity may be expressed at $\phi = \phi_i$ for $\alpha = \alpha_1$, that is,

$$\left|\frac{dz}{d\zeta}\right|_{\phi=\phi_i} = \frac{w_1}{v_1} \tag{A.2}$$

or for $\alpha = \alpha_2$, that is,

$$\left|\frac{dz}{d\zeta}\right|_{\phi=\phi_i} = \frac{w_2}{v_2} \tag{A.3}$$

Since $|dz/d\zeta|$ is continuous, it must be true from equations (A.2) and (A.3) that

$$\frac{w_1}{v_1} = \frac{w_2}{v_2} \tag{A.4}$$

Rearrangement gives the desired velocity level v_2, i.e.,

$$v_2 = v_1 \frac{w_2}{w_1} \tag{A.5}$$

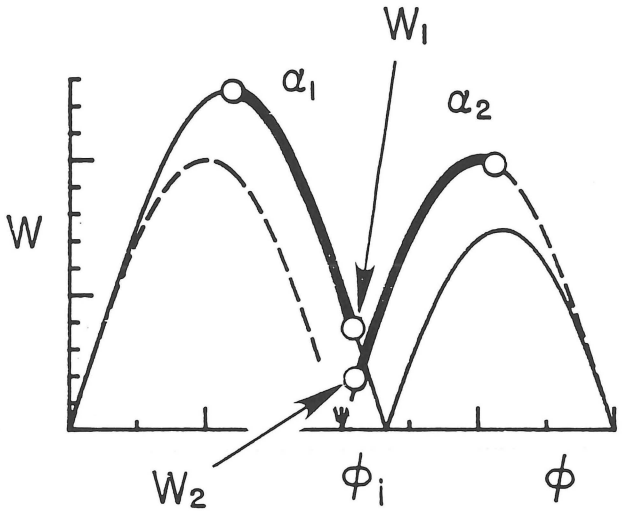

Figure A-1 Velocity distribution about circle for α_1 and α_2.

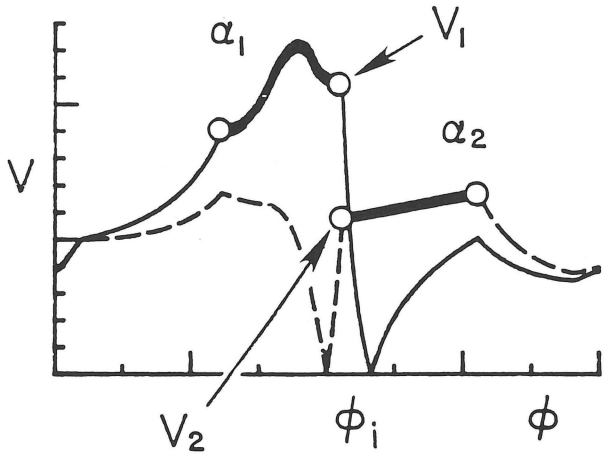

Figure A-2 Velocity distribution about airfoil for α_1 and α_2.

More physically from equation (A.4), it follows that

$$\frac{w_2}{w_1} = \frac{v_2}{v_1} \tag{A.6}$$

As seen in the figures A-1 and A-2, the ratios of the jump in the velocity on the circle and on the airfoil are equal as indicated by equation (A.6).

Appendix B

COEFFICIENTS FOR ISOLATED AIRFOILS

The coefficients a_{jk} and b_j found in equations (2.66*a*–*d*) are determined by substituting the expressions for $v^*(\phi)$ and $\alpha^*(\phi)$ [equations (2.60*a*–*b*)] into the three integral constraints on $P(\phi)$ and the trailing-edge continuity constraint given by

$$\int_{\phi_0}^{\phi_I} P(\phi)\, d\phi = 0 \tag{B.1a}$$

$$\int_{\phi_0}^{\phi_I} P(\phi) \cos\phi\, d\phi = \pi(1-\epsilon) \tag{B.1b}$$

$$\int_{\phi_0}^{\phi_I} P(\phi) \sin\phi\, d\phi = 0 \tag{B.1c}$$

$$P(\phi_0) = P(\phi_I) \tag{B.1d}$$

where $\phi_0 \equiv 0$ and $\phi_I \equiv 2\pi$. For an arbitrary number of segments, $v^*(\phi)$ and $\alpha^*(\phi)$ may be expressed as

$$\begin{aligned} v^*(\phi) &= v_1\, w(\phi) \\ \alpha^*(\phi) &= \alpha_1 \qquad\qquad \phi_0 \le \phi \le \phi_W \end{aligned} \tag{B.2a}$$

$$\begin{aligned} v^*(\phi) &= v_i\left(1 + \frac{\tilde{v}_i(\tilde{\phi}_i)}{v_i}\right) \\ \alpha^*(\phi) &= \alpha_i \qquad\qquad \phi_{i-1} \le \phi \le \phi_i \qquad i = 2,3,\ldots,I-1 \end{aligned} \tag{B.2b}$$

$$\begin{aligned} v^*(\phi) &= v_I\, \overline{w}(\phi) \\ \alpha^*(\phi) &= \alpha_I \qquad\qquad \overline{\phi}_W \le \phi \le \phi_I \end{aligned} \tag{B.2c}$$

which upon substitution into equation (2.20) leads to

$$P(\phi) = -\ln\left\{ \frac{(2\sin\phi/2)^{-\epsilon}}{2|\cos(\phi/2 - \alpha_1)|}\, v_1 w(\phi) \right\} \qquad 0 \le \phi \le \phi_W \tag{B.3a}$$

$$P(\phi) = -\ln\left\{\frac{(2\sin\phi/2)^{-\epsilon}}{2|\cos(\phi/2-\alpha_i)|}\, v_i\left(1+\frac{\tilde{v}_i(\tilde{\phi}_i)}{v_i}\right)\right\} \qquad \phi_{i-1}\le\phi\le\phi_i \quad i=2,3,\ldots,I-1 \qquad (B.3b)$$

$$P(\phi) = -\ln\left\{\frac{(2\sin\phi/2)^{-\epsilon}}{2|\cos(\phi/2-\alpha_1)|}\, v_I\overline{w}(\phi)\right\} \qquad \overline{\phi}_{W^-}\le\phi\le\phi_I \qquad (B.3c)$$

For later use, the following functions are defined

$$T(\phi,i) \equiv \ln|\cos(\phi/2-\alpha_i)| \qquad (B.4a)$$

$$T(i,j) \equiv \ln|\cos(\phi_i/2-\alpha_i)| \qquad (B.4b)$$

$$U(\phi,i) \equiv \ln\left(1+\frac{\tilde{v}_i(\tilde{\phi}_i)}{v_i}\right) \qquad (B.4c)$$

$$U(i) \equiv \ln\left(1+\frac{\tilde{v}_i(\tilde{\phi}_i=\phi_i-\phi_{i-1})}{v_i}\right) \qquad (B.4d)$$

where $\phi_{i-1}\le\phi\le\phi_i$ and $\tilde{\phi}_i=\phi-\phi_{i-1}$.

With these expressions for $P(\phi)$ and the functions defined above, the first integral constraint [equation (2.66a)] leads to

$$a_{11}\mu + a_{12}\overline{\mu} + a_{13}K_H + a_{14}\overline{K}_H = b_1 \qquad (B.5)$$

where

$$a_{11} = -\int_{\phi_0}^{\phi_{W^-}} \ln w_{W^-}(\phi)\, d\phi \qquad (B.6a)$$

$$a_{12} = -\int_{\overline{\phi}_{W^-}}^{\phi_I} \ln \overline{w}_{W^-}(\phi)\, d\phi \qquad (B.6b)$$

$$a_{13} = \int_{\phi_0}^{\phi_S} \ln w_S(\phi)\, d\phi \qquad (B.6c)$$

$$a_{14} = \int_{\overline{\phi}_S}^{\phi_I} \ln \overline{w}_S(\phi)\, d\phi \qquad (B.6d)$$

and

$$b_1 = 2\pi \ln 2 + \sum_{i=1}^{I} \left[(\phi_{i-1} - \phi_i) \ln v_i + \int_{\phi_{i-1}}^{\phi_i} T(\phi, i)\, d\phi \right]$$

$$- \sum_{i=2}^{I-1} \int_{\phi_{i-1}}^{\phi_i} U(\phi, i)\, d\phi$$

$$+ \epsilon \left[(\phi_F - \phi_0) \ln(2 \sin \phi_F/2) + (\phi_I - \overline{\phi}_F) \ln(2 \sin \overline{\phi}_F/2) + \int_{\phi_F}^{\overline{\phi}_F} \ln(2 \sin \phi/2)\, d\phi \right] \tag{B.7}$$

Evaluating the second integral constraint [equation (2.66b)] gives

$$a_{21}\mu + a_{22}\overline{\mu} + a_{23}K_H + a_{24}\overline{K}_H = b_2 \tag{B.8}$$

where

$$a_{21} = -\int_{\phi_0}^{\phi_W} \cos\phi \, \ln w_W(\phi)\, d\phi \tag{B.9a}$$

$$a_{22} = -\int_{\overline{\phi}_W}^{\phi_I} \cos\phi \, \ln \overline{w}_W(\phi)\, d\phi \tag{B.9b}$$

$$a_{23} = \int_{\phi_0}^{\phi_S} \cos\phi \, \ln w_S(\phi)\, d\phi \tag{B.9c}$$

$$a_{24} = \int_{\overline{\phi}_S}^{\phi_I} \cos\phi \, \ln \overline{w}_S(\phi)\, d\phi \tag{B.9d}$$

and

$$b_2 = -\pi(1-\epsilon) + \sum_{i=1}^{I} \left\{ \frac{1}{2}(\phi_i - \phi_{i-1}) \cos 2\alpha_i + \sin 2\alpha_i [T(i,i) - T(i-1,i)] \right\}$$

$$+ \sum_{i=2}^{I-1} \left[U(i) \sin\phi_i - \int_{\phi_{i-1}}^{\phi_i} U(\phi, i) \cos\phi \, d\phi \right]$$

$$+ \epsilon \left[(\sin\phi_F - \sin\phi_0) \ln(2 \sin \phi_F/2) \right.$$

$$+(\sin\phi_I - \sin\overline{\phi}_F)\ln(2\sin\overline{\phi}_F/2) + \int_{\phi_F}^{\overline{\phi}_F} \cos\phi \ln(2\sin\phi/2)\,d\phi\Bigg] \quad (B.10)$$

The third integral constraint [equation (2.66c)] becomes

$$a_{31}\mu + a_{23}\overline{\mu} + a_{33}K_H + a_{34}\overline{K}_H = b_3 \quad (B.11)$$

where

$$a_{31} = -\int_{\phi_0}^{\phi_W} \sin\phi\ \ln w_W(\phi)\,d\phi \quad (B.11a)$$

$$a_{32} = -\int_{\overline{\phi}_W}^{\phi_I} \sin\phi\ \ln \overline{w}_W(\phi)\,d\phi \quad (B.11b)$$

$$a_{33} = \int_{\phi_0}^{\phi_S} \sin\phi\ \ln w_S(\phi)\,d\phi \quad (B.11c)$$

$$a_{34} = \int_{\overline{\phi}_S}^{\phi_I} \sin\phi\ \ln \overline{w}_S(\phi)\,d\phi \quad (B.11d)$$

and

$$b_3 = \sum_{i=1}^{I}\left\{\frac{1}{2}(\phi_i - \phi_{i-1})\sin 2\alpha_i - (1+\cos 2\alpha_i)[T(i,i) - T(i-1,i)]\right\}$$
$$+\sum_{i=2}^{I-1}\left[U(i)(1-\cos\phi_i) - \int_{\phi_{i-1}}^{\phi_i} U(\phi,i)\sin\phi\,d\phi\right]$$
$$+\epsilon\Bigg[(-\cos\phi_F + \cos\phi_0)\ln(2\sin\phi_F/2)$$
$$(-\cos\phi_I + \cos\overline{\phi}_F)\ln(2\sin\overline{\phi}_F/2) + \int_{\phi_F}^{\overline{\phi}_F} \sin\phi\ \ln(2\sin\phi/2)\,d\phi\Bigg] \quad (B.12)$$

The integrals for the a_{2k} and a_{3k} coefficients are determined using the closed-form expressions given by Eppler (1957). Also, the closed-form expressions for the integrals

$$I = \int \cos\phi\ \ln|\cos(\phi/2 - \alpha_i)|\,d\phi \quad \text{and} \quad J = \int \sin\phi\ \ln|\cos(\phi/2 - \alpha_i)|\,d\phi \quad (B.13a,b)$$

given by Eppler (1957) were used to determine some of the terms in b_2 and b_3. The integrals involving the terms $\cos\phi \ln(2\sin\phi/2)$ and $\sin\phi \ln(2\sin\phi/2)$ are determined using the closed-form expressions

$$\int \cos\phi \ln(2\sin\phi/2)\, d\phi = \sin\phi\,[\ln(2\sin\phi/2) - 1/2] - \phi/2 \qquad (B.14a)$$

$$\int \sin\phi \ln(2\sin\phi/2)\, d\phi = \cos\phi\,[1/2 - \ln(2\sin\phi/2)] + \ln\sin\phi/2 \qquad (B.14b)$$

All the remaining integrals are not expressible in closed form and are evaluated numerically using Simpson's rule.

Finally, continuity of $P(\phi)$ at the trailing edge [equation $(2.66d)$] results in

$$a_{41}\mu + a_{42}\overline{\mu} + a_{43}K_H + a_{44}\overline{K}_H = b_4 \qquad (B.15)$$

where

$$a_{41} = \ln w_W(\phi_0) \qquad (B.16a)$$

$$a_{42} = -\ln \overline{w}_W(\phi_I) \qquad (B.16b)$$

$$a_{43} = -\ln w_S(\phi_0) \qquad (B.16c)$$

$$a_{44} = \ln \overline{w}_S(\phi_I) \qquad (B.16d)$$

and

$$b_4 = T(I,I) - T(0,1) + \ln\frac{v_1}{v_I} + \epsilon \ln\left(\frac{\sin\overline{\phi}_F/2}{\sin\phi_F/2}\right) \qquad (B.17)$$

Appendix C

THE NASA NLF(1)-0115 GENERAL AVIATION AIRFOIL

Through the use of modern, composite structures in general aviation aircraft, it has become possible for some time now to produce wings with a surface finish on a level capable of sustaining long runs of laminar flow. As a result, the use of laminar-flow airfoils has increased, but such use has not been completely successful in all instances. Chief among the difficulties is the sometimes substantial reduction in the maximum lift coefficient $c_{l_{max}}$ due to surface contamination (e.g., bug strikes, rain droplets, exhaust spray). A decrease in the maximum lift coefficient produces an increase in the stall speed which is critical information needed by the pilot during take-off and landing. Not knowing the stall speed (i.e., not knowing the degree of contamination and its influence on $c_{l_{max}}$) puts the pilot in jeopardy in these low-speed flight regimes. Another problem is the fact that many laminar-flow airfoils have been designed with a long, favorable pressure gradient on the upper surface in order to sustain laminar flow over the greatest possible distance. While this design approach is sound from a flow physics standpoint, it leads to aft loading on the airfoil which in turn leads to a large nose-down pitching-moment coefficient. The trouble is that for some applications the large moment results in unacceptable trim-drag penalties. Furthermore, if such airfoils are used over sections of the wing with control surfaces, large control stick forces can exist and the control surfaces can have a tendency to 'float.'

This section discusses the development of a new, laminar-flow airfoil designated the NASA NLF(1)-0115 and designed at NASA Langley Research Center by the author in collaboration with D. M. Somers and M. D. Maughmer. The new air-

foil yields the performance gains usually associated with laminar flow but without the aforementioned drawbacks often erroneously attributed to having laminar flow. First, the specific design goals are outlined in the context of two NACA airfoils traditionally used in general-aviation applications. Next, the Eppler and Somers design method (Eppler and Somers 1980*a*,*b*) used in the development of this new airfoil is discussed. Finally, a discussion of the design approach is presented.

C.1 AIRFOIL DESIGN OBJECTIVES AND CONSTRAINTS

Many of the design requirements for a modern general-aviation airfoil can be derived from other successful general-aviation airfoils. Most notably, the turbulent-flow NACA 23015 airfoil (Abbott and Von Doenhoff 1959) has been a popular choice for general-aviation applications for many years. This fact stems not only from a broad lift range and low pitching-moment coefficient but also from small loss in $c_{l_{max}}$ due to surface contamination. The laminar-flow NACA 63_2-215 airfoil (Abbott and Von Doenhoff 1959) has also had wide appeal owing to its low-drag, yet it suffers from a narrow usable lift range as compared with the NACA 23015.

In light of these two airfoils, the principal goal of this airfoil-design effort is to maintain a broad lift range like that of the NACA 23015 while realizing low-drag characteristics like those of the NACA 63_2-215. In particular, low profile drag is desired over the range from $c_l = 0.1$ at $R = 9 \times 10^6$ (the cruise condition) to $c_l = 0.6$ at $R = 4 \times 10^6$ (the climb condition) where the fact has been used that general-aviation aircraft typically have a wing loading in the range 718 to 958 N/m^2 (15 to 20 lb/ft^2). While the new airfoil could employ flaps, it is required that without flaps $c_{l_{max}} \geq 1.5$ at $R = 2.6 \times 10^6$ (the takeoff and landing condition). In case of surface contamination, the loss in $c_{l_{max}}$ should be no larger than 14%—the

same as that suffered by the NACA 23015. To minimize trim-drag penalties, it is desired that $c_{m_0} \geq -0.055$. Furthermore, for a control surface of 20% of chord, the hinge-moment coefficient should be no less than that of the NACA 63_2-215, that is, $c_H \geq -0.0022$. In this case, control stick forces and control-surface 'float' will not be excessive. Lastly, the airfoil maximum thickness should be 15%.

C.2 INVERSE AIRFOIL DESIGN METHOD

The airfoil design process was performed using the Eppler and Somers Computer Program for the Design and Analysis of Low Speed Airfoils (Eppler 1990, 1991; Eppler and Somers 1980*a*,*b*). Briefly, the inverse design method employs conformal mapping as discussed in section 2.1 in order to obtain the airfoil shape through the specification of the design velocity and angle of attack distribution in a multi-point manner. The method only allows for the design velocity distribution to be prescribed as constant over a given intermediate segment of the airfoil, that is, $\tilde{v}(\tilde{\phi}) = 0$. A one-dimensional Newton iteration scheme is used to allow for the specification of the trailing-edge thickness parameter K_S. Consequently, achievement of all of the design goals can be rather tedious since only K_S can be prescribed from the outset. For instance, the design of the NASA NLF(1)-0115 airfoil required two months of effort, although some of this time was spent in developing the design philosophy apart from working with the actual computer program. Incidentally, this rather tedious design process provided part of the motivation to develop the inverse design method as detailed previously in sections 2.1 and 2.2. Finally, the viscous analysis method implemented in the program uses integral boundary-layer equations to predict airfoil performance, and transition is predicted by the H_{32}-R_{δ_2} method of Eppler (1990) to be discussed shortly.

C.3 AIRFOIL DESIGN APPROACH

The result of the design effort is the NASA NLF(1)-0115, shown in figure C-1 along with three inviscid velocity distributions corresponding to the key flight conditions: cruise, climb, and takeoff and landing. The accompanying theoretical airfoil characteristics are shown in figure C-2 for $R = 9 \times 10^6$ and 4×10^6, the cruise and climb conditions, respectively. The zero-lift pitching-moment and hinge-moment coefficients are within the design specifications: $c_{m_0} = -0.055$ and $c_H = -0.0022$ for a 20% of chord control surface. The airfoil thickness is 15% as desired.

A comparison between the airfoil characteristics of the NASA NLF(1)-0115 and those of the NACA 23015 at the cruise flight Reynolds number is presented in figure C-3. As seen, the design goal of obtaining a broad lift range like that of the NACA 23015 has been obtained. The effects of surface contamination are shown in figure C-4 for the takeoff and landing Reynolds number of 2.6×10^6. It is observed that the predicted value of $c_{l_{max}}$ for the NASA NLF(1)-0115 airfoil is not overly sensitive to surface roughness. In fact, the lift loss due to contamination is only 11% as compared with 14% for the NACA 23015.

In order to have limited sensitivity to surface roughness, the NASA NLF(1)-0115 airfoil embodies upper-surface velocity distributions which behave as generally depicted in figure C-5. The velocity distribution for $c_l = 0.6$ (the upper limit of the low-drag range at $R = 4 \times 10^6$) is prescribed such that with increasing angles of attack the transition point moves rapidly forward to the leading edge. Thus, for $c_l < 0.6$, the pressure gradients confine transition to the short instability region just upstream of the main pressure recovery. For $c_l > 0.6$, however, the adverse pressure gradient over the forward portion of the airfoil moves transition to very near the leading edge. Consequently, because transition naturally happens early

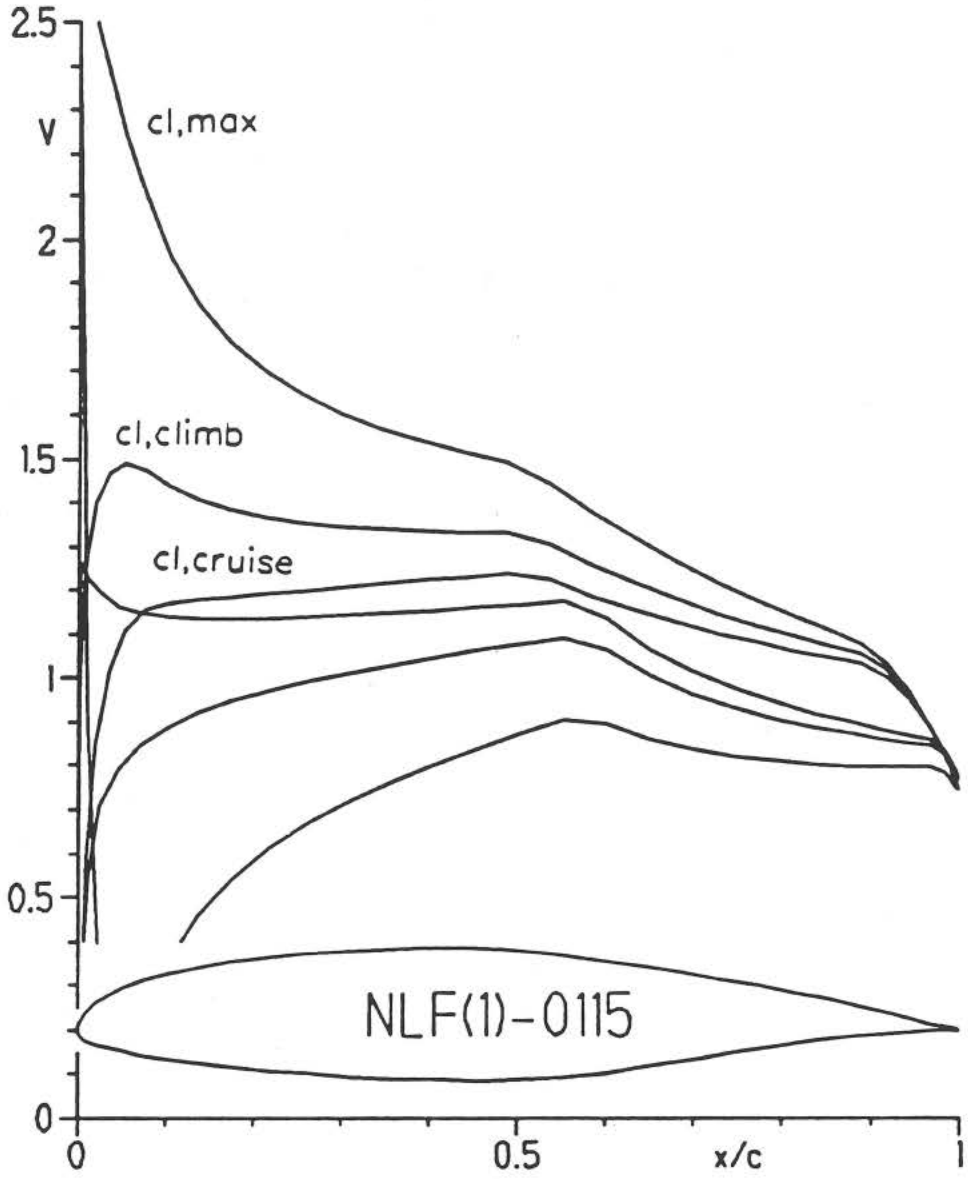

Figure C-1 NASA NLF(1)-0115 airfoil and three inviscid velocity distributions.

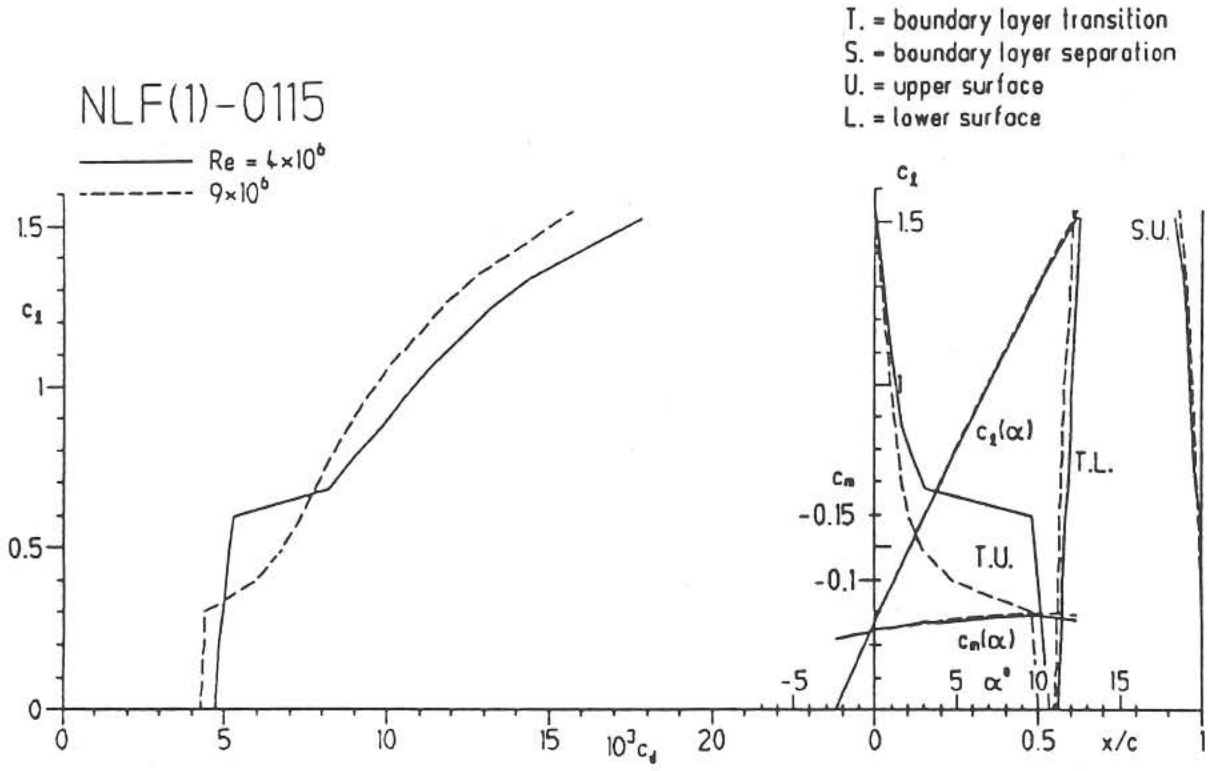

Figure C-2 Theoretical airfoil characteristics for the NASA NLF(1)-0115 airfoil.

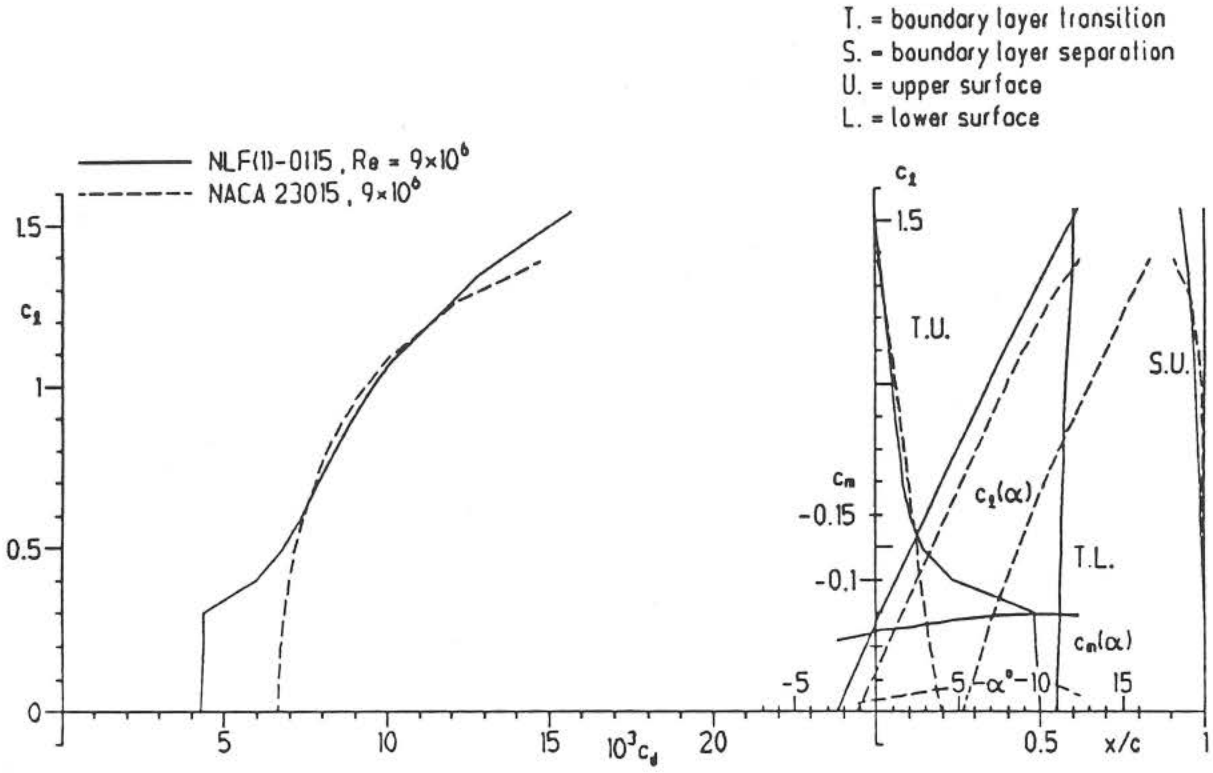

Figure C-3 Comparison of the NASA NLF(1)-0115 and NACA 23015 theoretical airfoil characteristics for $R = 9 \times 10^6$.

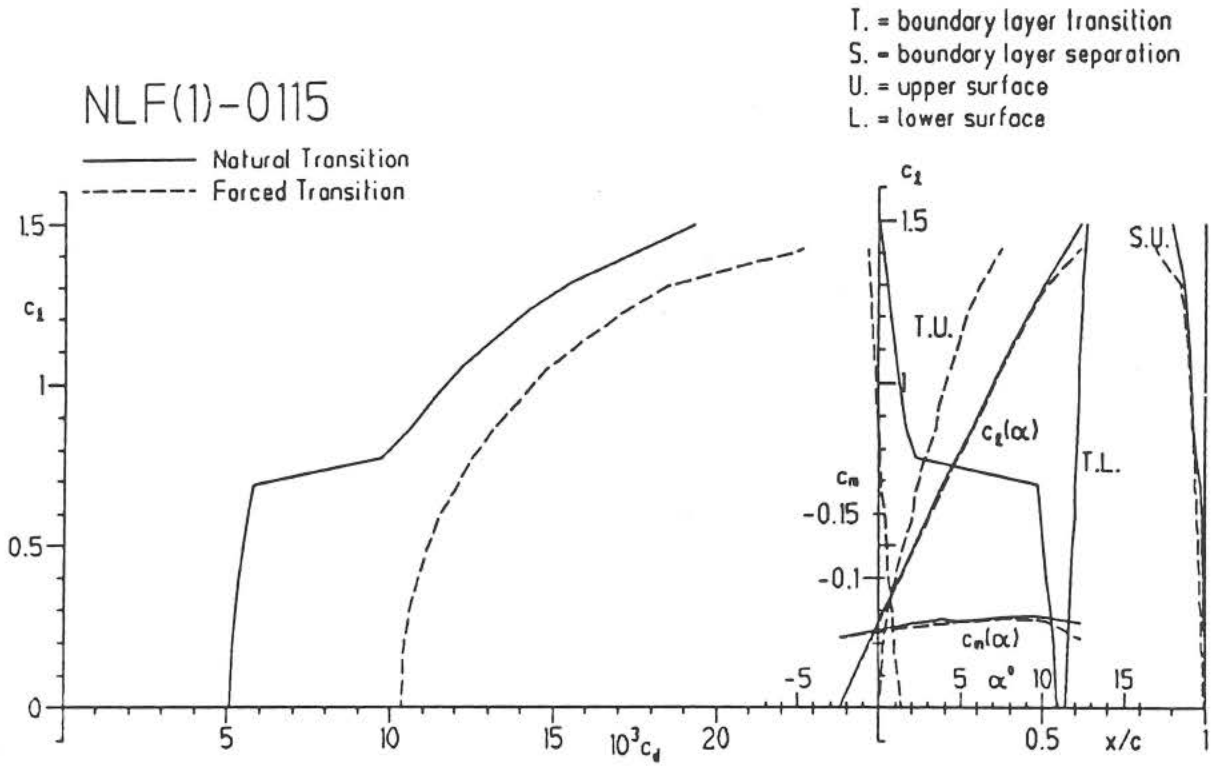

Figure C-4 The effects of surface roughness on the theoretical airfoil characteristics of the NASA NLF(1)-0115 airfoil for $R = 2.6 \times 10^6$.

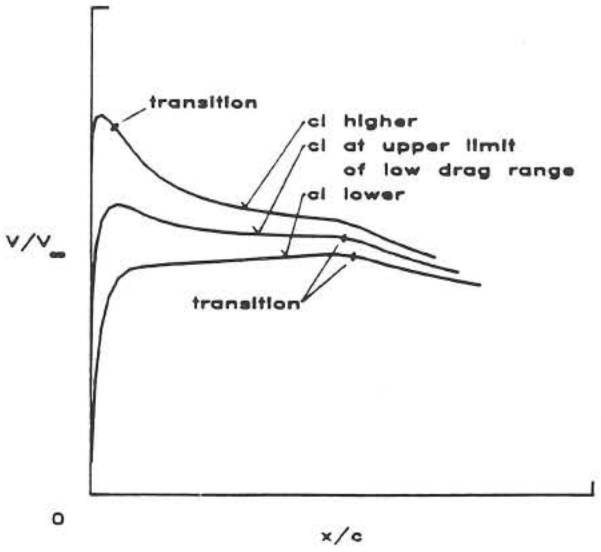

Figure C-5 Behavior of the upper-surface velocity distribution that limits $c_{l,max}$ sensitivity to surface roughness.

on the upper surface at the maximum lift coefficient, $c_{l_{max}}$ is not dramatically influenced by surface roughness.

In figure C-6, a comparison is made between the airfoil characteristics of the NASA NLF(1)-0115 and those of the NACA 63_2-215 at $R = 9 \times 10^6$. At the cruise condition ($c_l = 0.1$), the NASA NLF(1)-0115 airfoil has 25% less drag than the NACA 63_2-215, and this advantage is maintained over most of the operational envelope. Although both airfoils are designed to have significant runs of laminar flow, significant differences exist in the way in which this is achieved. These differences are best interpreted using the boundary-layer development plot as shown in figure C-7 (a,b) Some preliminary discussion is required.

In figure C-7 (a,b), the local momentum thickness Reynolds number R_{δ_2} is plotted vs. the shape factor H_{32}. The Reynolds number R_{δ_2} increases monotonically downstream. Due to the logarithmic scale in R_{δ_2}, the initial development of the boundary layer takes up a considerable portion of the plot while further downstream, as R_{δ_2} increases, equally spaced points on the airfoil appear very closely spaced in the boundary-layer development plot. The shape factor H_{32} can vary significantly with certain values of H_{32} corresponding to specific laminar boundary-layer phenomena: $H_{32} = 1.620$ corresponds to stagnation, 1.573 to the flat-plate Blasius boundary layer, and 1.515 to laminar separation. It is noted that while H_{32} decreases from the stagnation point toward laminar separation, H_{12} increases.

The Eppler method of predicting transition is based on the local values of H_{32} and R_{δ_2}. To the right of the dotted-line boundaries given in figure C-7 (a), the flow is assumed to be laminar. The vertical boundary on the left corresponds to laminar separation ($H_{32} = 1.515$). If the boundary-layer development curve for a given condition intersects this boundary, laminar separation is assumed to take

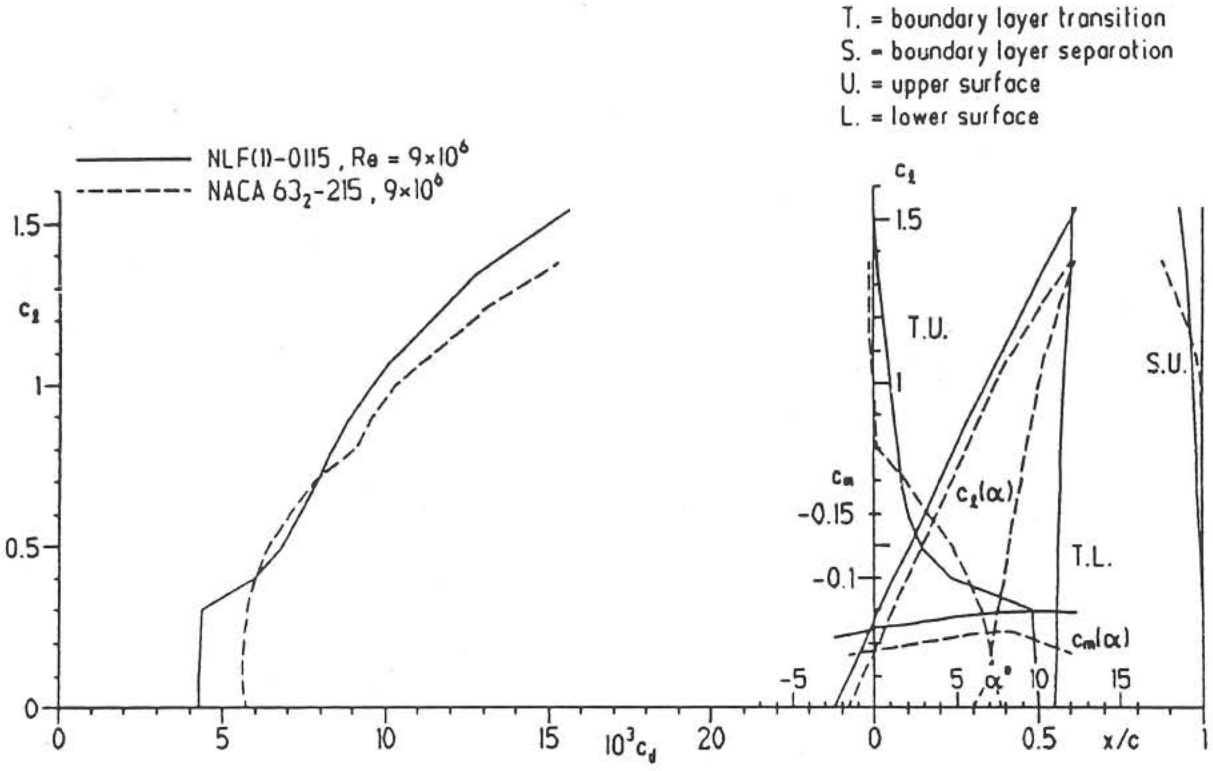

Figure C-6 Comparison of the NASA NLF(1)-0115 and NACA 63_2-215 theoretical airfoil characteristics for $R = 9 \times 10^6$.

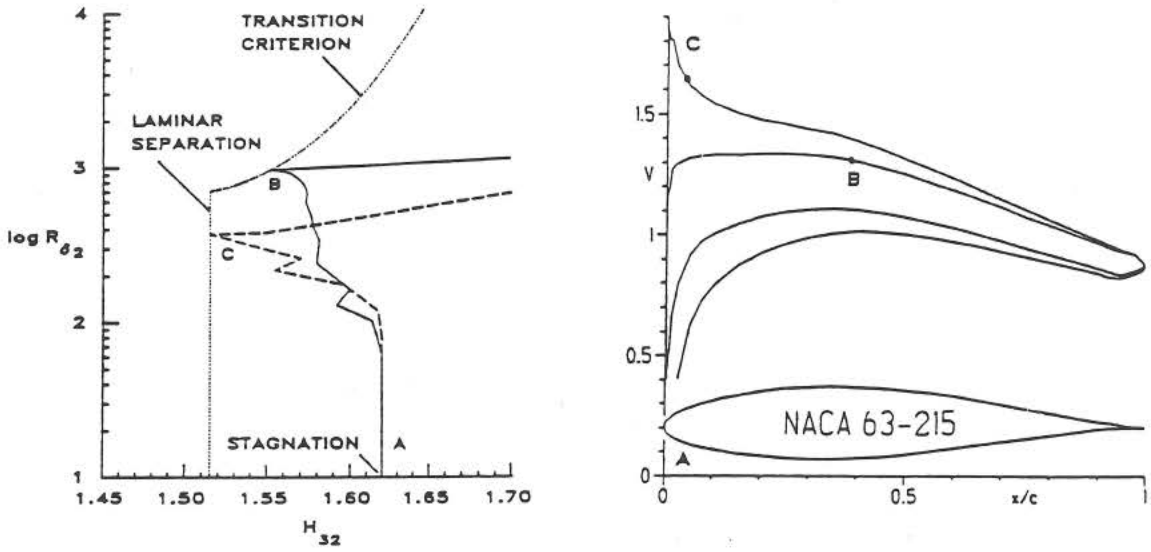

Figure C-7 Theoretical boundary-layer development for the NACA 63_2-215 airfoil lower surface at (a) $c_l = 0.4$ (solid-line) and (b) 0.8 (dotted-line) for $R = 4 \times 10^6$.

place at that point. For the Reynolds numbers considered here, transition in the free shear layer happens quickly enough that transition can be assumed to take place at the point of laminar separation. The upper boundary corresponds to natural boundary-layer transition. This curve was empirically derived from wind tunnel and flight test data and should therefore be considered as a band since it is merely a fairing through the experimental data points. Once transition is predicted, the method switches to the turbulent boundary-layer equations.

The two boundary-layer developments shown in figure C-7 (a) correspond to the two upper-surface velocity distributions of the NACA 63_2-215 at $c_l = 0.4$ and 0.8 with $R = 4 \times 10^6$. In figure C-7 (a), both boundary-layer developments begin at the stagnation point (point A in the figure). For $c_l = 0.4$, transition is predicted to occur at point B via natural boundary-layer transition. As the angle of attack increases, the upper-surface boundary-layer development curve skews toward the left as the pressure gradient becomes steeper. For $c_l = 0.8$, the steep adverse pressure gradient immediately downstream of the velocity peak near the leading edge results in a more rapid decrease in H_{32} and causes transition to be predicted by laminar separation at point C.

When the boundary-layer data is provided in this format, it reveals valuable information related to transition and thereby offers clues as to how to sustain laminar flow in the design of a new airfoil. For example, referring back to figure C-7 (a) at $c_l = 0.8$, transition is predicted to occur shortly downstream of the stagnation point. If the adverse pressure gradient in the region were reduced through modification of the velocity distribution, transition would be postponed. By adjusting the velocity distribution based on the boundary-layer development plot, laminar flow can be extended further back on the airfoil and is limited only by boundary-layer

separation or one of the design constraints. As discussed by Somers (1992) and first suggested by Eppler (1990), the widest possible low-drag range is achieved when the laminar boundary layer is held on the verge of laminar separation and then on the verge of boundary-layer transition. Such a scenario would be characterized by a boundary-layer development that follows the dotted lines in figure C-7(a). While certainly not suitable in all situations, this concept has been exploited in the design of other airfoils, such as those presented by Somers (1981), Somers and Horstmann (1985), and Maughmer and Somers (1989) and is now employed in the NASA NLF(1)-0115.

Figure C-8 shows the boundary-layer development for the lower surface of the NASA NLF(1)-0115 at $c_l = 0.0$ and $R = 9 \times 10^6$ and corresponds to the lower limit of the low-drag range (as seen in figure C-2). First, the laminar-separation limit is approached quickly and is followed for a short distance up to point A. The boundary-layer development then essentially follows the transition-criterion curve. The beginning of the pressure recovery at point B causes the transition criterion to be satisfied which, in turn, invokes the turbulent boundary-layer calculations.

For the upper surface, the critical design condition occurs at the upper limit of the low-drag range. The corresponding boundary-layer development is shown in figure C-9 for $c_l = 0.6$ and $R = 4 \times 10^6$. Unlike the design of the lower surface, the upper surface is not designed to rapidly approach laminar separation. Rather from the stagnation point to 10% of chord, the design of the upper surface is dictated by $c_{l_{max}}$ and surface roughness considerations as previously discussed. From 10% to 50% of chord, however, the boundary layer is again forced to be everywhere on the verge of transition.

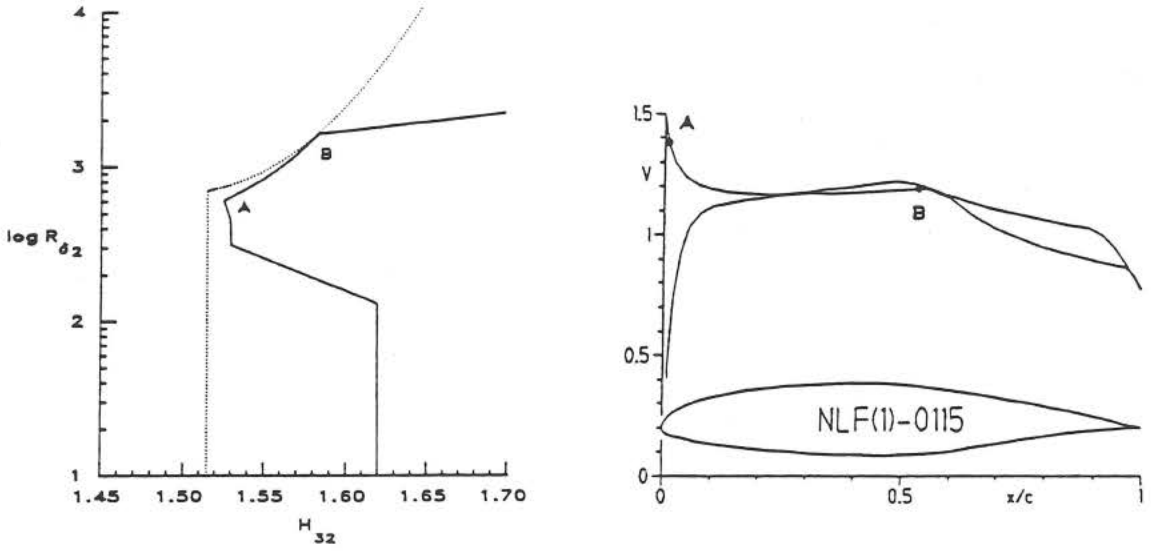

Figure C-8 Theoretical boundary-layer development for the NASA NLF(1)-0115 airfoil lower surface at $c_l = 0$ and $R = 9 \times 10^6$.

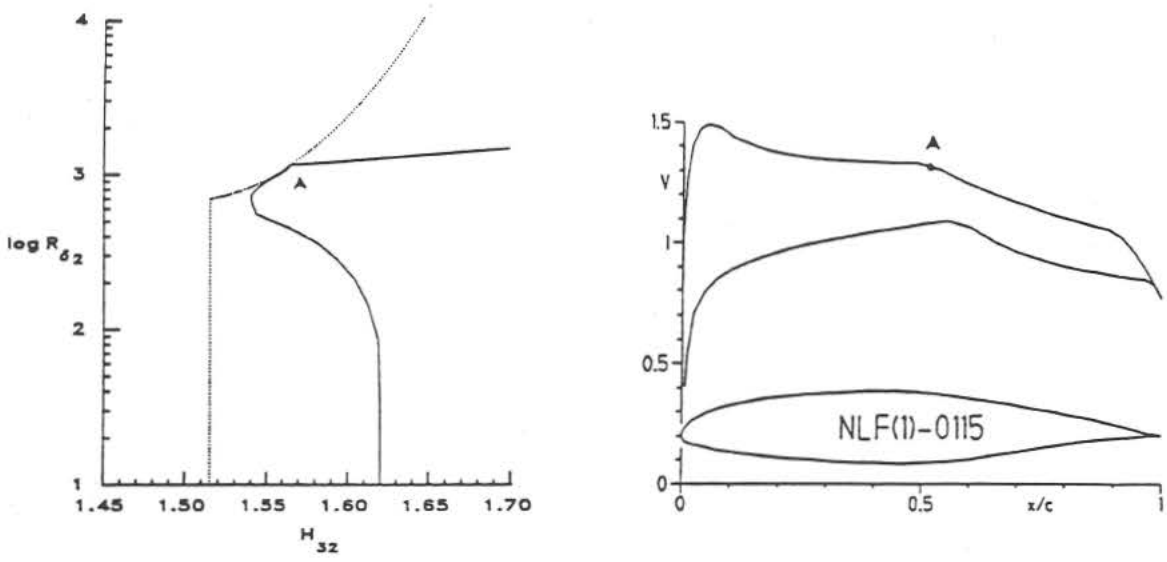

Figure C-9 Theoretical boundary-layer development for the NASA NLF(1)-0115 airfoil upper surface at $c_l = 0.4$ and $R = 4 \times 10^6$.

In summary, the NASA NLF(1)-0115 airfoil is the latest in a series of natural laminar-flow airfoils designed at NASA Langley. It is specifically intended for use in general-aviation applications where high-speed, long-range performance is paramount. Incorporated into this design are favorable features derived from several previously existing successful airfoils. These features, coupled with significant drag reductions made possible through the use of extended lengths of laminar flow, should prove to make the NASA NLF(1)-0115 airfoil successful in application to general-aviation aircraft.

Appendix D

COEFFICIENTS FOR INFINITE CASCADES

The coefficients a_{jk} and b_j found in equations (3.116a–d) are determined by substituting the expressions for $v^*(\phi)$ and $\overline{\beta}^*(\phi)$ [equations (3.115a–c)] into the three integral constraints on $P(\phi)$ [equations (3.101a) and (3.102a,b)] and the trailing-edge continuity constraint [equation (3.110)] expressed as

$$-\int_{\phi_0}^{\phi_I} \sigma_j P(\phi)\, d\phi = \rho_j \qquad j = 1,2,3 \qquad (D.1a)$$

$$P(\phi_0) = P(\phi_I) \qquad (D.1b)$$

where

$$\sigma_j = \begin{Bmatrix} 1 \\ \dfrac{1}{\tau(\phi)} \\ \dfrac{\sin(\alpha-\phi)}{\tau(\phi)} \end{Bmatrix} \quad \text{and} \quad \rho_j = \begin{Bmatrix} 0 \\ \dfrac{2\pi(1-\epsilon)}{1-A^2} \ln\left(\dfrac{A}{\sqrt{1-2A\cos\alpha+A^2}}\right) \\ \dfrac{-\pi(1-\epsilon)}{A} \arg(A - e^{-i\alpha}) \end{Bmatrix} \qquad (D.2a, b)$$

and

$$\tau(\phi) = 1 - 2A\cos(\alpha-\phi) + A^2 \qquad (D.3)$$

The harmonic function $P(\phi)$ is expressed as

$$-P(\phi) = \ln(2\sin\phi/2)^{-\epsilon} \nu(\phi)\, v^*(\phi) \qquad (D.4)$$

where

$$\nu(\phi) = \frac{\sqrt{\tau(\phi)}}{2A\overline{V}^*(\phi)|\cos(\alpha+\overline{\beta}^*(\phi)-\phi/2)|} \qquad (D.5)$$

Upon substitution and simplification the following results are obtained for the coefficients a_{jk} and b_j $(j = 1, 2, 3)$:

$$a_{j1} = -\int_{\phi_0}^{\phi_W} \sigma_j \ln w_W(\phi)\, d\phi \qquad (D.6a)$$

$$a_{j2} = -\int_{\overline{\phi}_W}^{\phi_I} \sigma_j \ln \overline{w}_W(\phi)\, d\phi \qquad (D.6b)$$

$$a_{j3} = \int_{\phi_0}^{\phi_S} \sigma_j \ln w_S(\phi)\, d\phi \qquad (D.6c)$$

$$a_{j4} = \int_{\overline{\phi}_S}^{\phi_I} \sigma_j \ln \overline{w}_S(\phi)\, d\phi \qquad (D.6d)$$

and

$$\begin{aligned} b_j = \rho_j &- \ln(2\sin\phi_F/2)^{-\epsilon} \int_{\phi_0}^{\phi_F} \sigma_j\, d\phi \;-\; \ln(2\sin\overline{\phi}_F/2)^{-\epsilon} \int_{\overline{\phi}_F}^{\phi_I} \sigma_j\, d\phi \\ &- \int_{\phi_F}^{\phi_W} \sigma_j \ln(2\sin\phi/2)^{-\epsilon}\, d\phi \;-\; \int_{\overline{\phi}_W}^{\overline{\phi}_F} \sigma_j \ln(2\sin\phi/2)^{-\epsilon}\, d\phi \\ &- \int_{\phi_0}^{\phi_W} \sigma_j \ln[v_1\, \nu(\phi)]\, d\phi \;-\; \int_{\overline{\phi}_W}^{\phi_I} \sigma_j \ln[v_I\, \nu(\phi)]\, d\phi \\ &- \sum_{i=1}^{I-1} \int_{\phi_i}^{\phi_{i+1}} \sigma_j \ln[(2\sin\phi/2)\, \nu(\phi)\, v^*(\phi)]\, d\phi \end{aligned} \qquad (D.7)$$

Continuity at the trailing edge gives $(j = 4)$

$$a_{41} = \ln w_W(\phi_0) \qquad (D.8a)$$

$$a_{42} = -\ln \overline{w}_W(\phi_I) \qquad (D.8b)$$

$$a_{43} = -\ln w_S(\phi_0) \qquad (D.8c)$$

$$a_{44} = \ln \overline{w}_S(\phi_I) \qquad (D.8d)$$

and

$$b_4 = \ln\left\{ \frac{\overline{V}_I |\cos(\alpha + \overline{\beta}_I - \phi_I/2)|\, v_1\, (\sin\overline{\phi}_F/2)^{\epsilon}}{\overline{V}_1 |\cos(\alpha + \overline{\beta}_1 - \phi_0/2)|\, v_I\, (\sin\phi_F/2)^{\epsilon}} \right\} \qquad (D.9)$$

All integrals are evaluated by Simpson's rule.